



PACIFIC EARTHQUAKE ENGINEERING RESEARCH CENTER

Using OpenSees for Performance-Based Evaluation of Bridges on Liquefiable Soils

Steven L. Kramer

University of Washington

Pedro Arduino

University of Washington

HyungSuk Shin

Kleinfelder, Inc.
Seattle, Washington

Using OpenSees for Performance-Based Evaluation of Bridges on Liquefiable Soils

Steven L. Kramer

Department of Civil and Environmental Engineering
University of Washington, Seattle

Pedro Arduino

Department of Civil and Environmental Engineering
University of Washington, Seattle

HyungSuk Shin

Kleinfelder, Inc., Seattle

PEER Report 2008/07
Pacific Earthquake Engineering Research Center
College of Engineering
University of California, Berkeley

November 2008

ABSTRACT

By virtue of their locations, bridges that cross bodies of water are particularly likely to be damaged by lateral spreading of liquefied soils. The behavior of these soils can cause unusual forms of seismic demands on bridges and their foundations, ranging from rapid modifications of input motion amplitudes and frequency contents to high levels of kinematic loading associated with permanent deformations of the supporting soils. This report describes the application of the PEER methodology of performance-based earthquake engineering to a bridge structure founded on liquefiable soils. In this investigation, the response of the soil-foundation-structure system was computed using detailed nonlinear inelastic analyses. The computer program, OpenSees, was used to model liquefiable and non-liquefiable soils, pile foundations, abutments, and the bridge superstructure. The detailed model enabled direct prediction of the response of critical bridge elements, hence the more accurate estimation of resulting physical damage and loss. The report presents a detailed description of the site, the analytical model and its validation, the computed response under various loading conditions, and the resulting damage and loss estimates. The response and losses under conditions where the bridge is supported on non-liquefiable soils and on rock are also computed and compared with the liquefaction case.

ACKNOWLEDGMENTS

This work was supported primarily by the Earthquake Engineering Research Centers Program of the National Science Foundation under award number EEC-9701568 through the Pacific Earthquake Engineering Research (PEER) Center. Any opinions, findings, and conclusions or recommendations expressed in this material are those of the author(s) and do not necessarily reflect those of the National Science Foundation.

CONTENTS

ABSTRACT	iii
ACKNOWLEDGMENTS	iv
TABLE OF CONTENTS	v
LIST OF FIGURES	xi
LIST OF TABLES	xvii
1 INTRODUCTION	1
1.1. Background	1
1.2. Performance-Based Earthquake Engineering.....	2
1.3. Objectives of the Study	3
1.4. Organization	3
2 PERFORMANCE-BASED EARTHQUAKE ENGINEERING	5
2.1 Introduction	5
2.2 PEER Framework.....	5
2.3 Response Prediction	7
2.4 Damage Prediction	8
2.5 Loss Prediction	9
2.6 Summary	9
3 SEISMIC SOIL-PILE-STRUCTURE INTERACTION	11
3.1 Introduction	11
3.2 Soil-Pile Interaction Modeling	11
3.2.1 Static and Dynamic Beam-on-Nonlinear-Winkler-Foundation (BNWF) Models	12
3.3 P-y Curves	13
3.3.1 Conventional p-y Curves for Piles Subjected to Static and Cyclic Loading.....	13
3.3.1.1 Back-Calculated p-y Curves for Sand, Stiff Clay, and Soft Clay	14
3.3.1.2 Initial Stiffness of p-y Curves	16
3.3.1.3 Ultimate Resistance of p-y Curves.....	18
3.3.2 p-y Curves for Liquefiable Soil.....	21

3.3.2.1	Back-Calculated p-y Curves for Piles in Level Ground Liquefiable Soils	21
3.3.2.2	Lateral Soil Pressure on Piles due to Lateral Spreading	22
3.3.2.3	Approximation of Liquefiable p-y Curves	25
3.4	Pile Response to Lateral Loads	26
3.4.1	Pile Response due to Static/Cyclic Lateral Load and Load Transmission.....	27
3.4.2	Pile Response under Pile Head Load	27
3.4.3	Pile Response during Lateral Spreading	28
3.5	Pile Group Response to Lateral Loads	29
3.5.1	Group Effect.....	29
3.5.2	Pile Cap Resistance	31
3.5.3	Response of Pile Groups Subjected to Earthquake Loading.....	35
3.6	Axially Loaded Single Pile.....	36
3.6.1	Ultimate Skin Resistance (t_{ult}) and Ultimate Point Resistance (q_{ult}) for Sands.....	38
3.7	SPSI and Structural Stiffness	41
3.7.1	SPSI Effect on Structural Response	41
3.7.2	Other Factors That Influence Structural Response	42
3.8	Soil-Abutment-Bridge Interaction.....	42
3.9	Summary	45
4	CHARACTERISTICS OF A TESTBED HIGHWAY BRIDGE.....	47
4.1	Introduction	47
4.2	Testbed Bridge System.....	47
4.2.1	Soil Conditions.....	48
4.2.2	Bridge and Abutments.....	51
4.2.3	Pile Foundations.....	51
4.3	Summary	52
5	OPENSEES MODEL OF TESTBED HIGHWAY BRIDGE	53
5.1	Introduction	53
5.2	Soil Conditions.....	53
5.3	Bridge Structure	58

5.4	Pile Foundations	58
5.4.1	Pile p-y Springs	59
5.4.2	Pile Cap Passive Earth Pressure Springs.....	62
5.5	Abutment Interface Springs.....	62
5.6	Summary	63
6	RESPONSE OF TESTBED HIGHWAY BRIDGE	65
6.1	Introduction	65
6.2	Model Validation Analyses	65
6.2.1	Soil Response	65
6.2.2	Pinning Effect and Soil Element Out-of-Plane Thickness	70
6.2.3	Global Behavior of Bridge System	72
6.2.4	Bridge Pier Response	73
6.2.5	Abutment Response.....	76
6.2.6	Pile and p-y Spring Response.....	80
6.3	Summary of Response in Validation Exercises.....	83
7	ESTIMATION OF EDP-IM RELATIONSHIPS FOR TESTBED HIGHWAY BRIDGE.....	85
7.1	Introduction	85
7.2	Analyses for EDP IM Evaluation	85
7.2.1	Input Motions and Intensity Measures	86
7.2.2	EDPs of Bridge System.....	92
7.2.3	Uncertainties in Inputs to Response Analyses	94
7.2.4	Record-to-Record Uncertainty	95
7.2.5	Model Parameter Uncertainty	99
7.2.5.1	List of Model Parameters	100
7.2.5.2	Tornado Diagrams.....	100
7.2.5.3	First-Order Second-Moment (FOSM) Analysis	102
7.2.6	Spatial Variability Effects	105
7.2.6.1	Spatial Variability within Homogeneous Soil Deposits	105
7.2.6.2	Generation of Gaussian Random Fields.....	107
7.2.6.3	Effects of Spatial Variability.....	109
7.2.6.4	Relative Contributions to Total Uncertainty	112

7.2.7	Results of Analyses with Ground Motion Database	112
7.2.7.1	Lateral Soil Deformations	113
7.2.7.2	Vertical Soil Deformations	118
7.2.7.3	Structural Response.....	118
7.2.7.4	Simplified EDP-IM Model.....	122
7.3	Summary	123
8	FOUNDATION DAMAGE AND LOSS	125
8.1	Introduction	125
8.2	Damage and Loss Probability Matrix Approach	125
8.2.1	Methodology	126
8.2.2	Estimated Damage and Loss Probabilities	128
8.3	Estimated Foundation Damage	129
8.4	Estimated Foundation Losses	130
8.5	Summary	133
9	BRIDGE DAMAGE AND LOSS.....	135
9.1	Introduction	135
9.2	Damage Models.....	135
9.2.1	Columns	136
9.2.2	Expansion Joints.....	137
9.2.3	Bearings.....	138
9.2.4	Back Walls	138
9.2.5	Approach Slabs	139
9.2.6	Deck Segments.....	139
9.2.7	Pile Foundations.....	140
9.3	Repair Methods and Costs.....	141
9.4	Estimated Repair Costs	143
9.4.1	Estimation of Total Repair Costs	143
9.4.1.1	Repair Cost Hazard Curves.....	144
9.4.1.2	Deaggregation of Repair Cost.....	145
9.4.2	Sensitivity of Bridge Losses to Soil Conditions.....	147
9.4.2.1	Losses for Non-Liquefiable Soil Conditions	147
9.4.2.2	Losses for Fixed-Base Conditions	150

9.4.2.3	Summary	152
9.4.3	Sensitivity of Bridge Losses to Uncertainty.....	153
9.4.4	Implications for Simplified Response Analyses	155
9.5	Summary	157
10	SUMMARY AND CONCLUSIONS	159
10.1	Summary	160
	REFERENCES.....	163
	APPENDIX: IMPLEMENTATION OF PBEE.....	A-1
A.1	Introduction	A-1
A.2	The PEER PBEE Process	A-1
A.3	The Procedure.....	A-3

LIST OF FIGURES

Figure 3.1	Static and dynamic beam-on-nonlinear-Winkler-foundation (BNWF) model.....	12
Figure 3.2	Back-calculated p-y curves for sand from field tests (after Reese et al. 1975)	15
Figure 3.3	Back-calculated p-y curves for stiff clay from field tests (after Reese et al. 1974)	15
Figure 3.4	Cyclic response of rigid pile in soft clay (after Matlock 1970).....	16
Figure 3.5	Comparison of ultimate soil resistance of soft clay (Matlock 1971) and sand (Reese et al. 1974)	20
Figure 3.6	Suggested ultimate soil resistance for cohesionless soil	20
Figure 3.7	Back-calculated p-y behavior during shaking (after Wilson et al. 2000).....	22
Figure 3.8	Relationship between residual strength and corrected SPT resistance (Seed and Harder 1990).....	24
Figure 3.9	Pile foundation failure of Yachiyo bridge due to kinematic loading (after Hamada 1992).....	28
Figure 3.10	Schematic of pile alignment in group.....	30
Figure 3.11	Design chart for p-multipliers (after Mokwa 1999)	31
Figure 3.12	Schematic of rotational soil resistance due to pile cap rotation	32
Figure 3.13	Illustration of axial load transfer in a pile (after Vijayvergiya 1997).....	32
Figure 3.14	Illustration of axial load transfer mechanism in a pile (after Vijayvergiya 1997)...	36
Figure 3.15	Typical load-movement characteristics of an axially loaded pile (after Vijayvergiya 1997)	37
Figure 3.16	Normalized t-z (or f-z) curve for clay and sand (after Vijayvergiya 1997).....	39
Figure 3.17	Normalized q-z curve for sand and clay (after Vijayvergiya 1997)	40
Figure 3.18	Lateral stiffness of column with and without rotational restraint at top.....	41
Figure 3.19	Schematic of seat-type abutment structural components and bridge deck-abutment-soil interaction	44
Figure 3.20	Simplified abutment load-deflection characteristic using initial stiffness and ultimate resistance in Caltrans's guideline (after SDC 2004)	45
Figure 4.1	Testbed bridge configuration (dimensions in meters)	48
Figure 4.2	Layer definition and identification	49
Figure 4.3	SPT profiles of loose sand layer below both embankments.....	50

Figure 4.4	Variation of undrained shear strength of clay layer across bridge	50
Figure 4.5	Structure configuration	51
Figure 5.1	Recommended loose sand material parameters in OpenSees and interpolations	55
Figure 5.2	Modeling of soil-structure interaction in OpenSees	58
Figure 5.3	p-y spring parameters: ultimate lateral resistance (P_{ult})	60
Figure 5.4	p-y spring parameters: y_{50}	61
Figure 5.5	Modeling of bridge deck-abutment–soil interaction in OpenSees	63
Figure 6.1	Horizontal and vertical displacements of bridge and pore pressure ratio in soil following earthquake—Northridge motion. Displacements magnified by factor of 20	66
Figure 6.2	Horizontal and vertical displacements of bridge and pore pressure ratio in soil following earthquake—Erzincan motion. Displacements magnified by factor of 20	67
Figure 6.3	Variation of shear strain with time and depth: (a) below left abutment and (b) below right abutment—Northridge motion	67
Figure 6.4	Variation of shear strain with time and depth: (a) below left abutment, and (b) below right abutment—Erzincan motion.....	67
Figure 6.5	Pore pressure ratio time histories in liquefiable soil.....	69
Figure 6.6	Spatial and temporal variation of pore pressure profile below right abutment in liquefiable soil—Northridge motion	70
Figure 6.7	Effect of soil element out-of-plane thickness on slope toe and pile cap lateral displacement—Erzincan motion.....	71
Figure 6.8	Schematic drawing of 3-D embankment deformation.....	72
Figure 6.9	(a) Displacement of each bridge column at top and bottom and (b) drift ratios (column height = 6.7 m)—Erzincan motion.....	74
Figure 6.10	Acceleration time histories and response spectra at soil base and pile cap—Northridge motion	75
Figure 6.11	Abutment and bridge deck movements: (a) Northridge, California 1994, $a_{max}=0.25$ g, (b) Erzincan, Turkey 1992, $a_{max}=0.70$ g.....	77
Figure 6.12	Bridge deck and abutment interaction force-displacement—Erzincan motion.....	79
Figure 6.13	Residual pile bending moments and lateral soil resistance during earthquake—Erzincan motion.....	81

Figure 6.14	p-y time histories during earthquake excitation—Erzincan motion.	82
Figure 6.15	p-y curves during earthquake excitation—Erzincan motion.	82
Figure 6.16	Pile cap resistance curves—Erzincan motion.	83
Figure 7.1	Example of input motion used in comprehensive bridge study—Erzincan motion.	86
Figure 7.2	PGA hazard curve.	89
Figure 7.3	Implied hazard curves for different IMs.	91
Figure 7.4	Correlation between lateral pile cap displacement and curvature from simulations for Northridge 1994, 0.2557 g; unit of curvature = 1/m	93
Figure 7.5	Components of total uncertainty in EDP estimation	94
Figure 7.6	EDP-IM relationships for right abutment slope residual vertical settlement	96
Figure 7.7	EDP-IM relationships for Pier 4 maximum drift.	97
Figure 7.8	Relative efficiencies of different IMs.	98
Figure 7.9	Tornado diagrams for four maximum EDPs: Temblor 1966 motion at Parkfield ($a_{\max} = 0.47$ g)	102
Figure 7.10	Inherent soil variability (after Phoon and Kulhawy 1999)	106
Figure 7.11	Example of generated Gaussian fields.	107
Figure 7.12	Development of random field for friction angle in loose, saturated sand layer; (a) mean friction angle, (b) residual friction angle, (c) total friction angle.	109
Figure 7.13	Variation of horizontal subsurface displacements for ground motions with (a) 15-yrs return period, (b) 72-yrs return period, (c) 475-yrs return period, and (d) 2475-yrs return period.	114
Figure 7.14	Horizontal displacements at tops and bottoms of Piers 1 and 4. Note that absolute displacement of Pier 4 (bottom) is larger than that of Pier 1, but difference between the top and bottom displacements is larger at Pier 1 than Pier 4.	115
Figure 7.15	Relationship between PGV and (a) expansion joint displacement at left abutment, (b) expansion joint displacement at right abutment.	116
Figure 7.16	Relationship between PGV and pile cap horizontal displacement for (a) Pier 0 (left abutment), (b) Pier 1, (c) Pier 2, and (d) Pier 3, (e) Pier 4, and (f) Pier 5 (right abutment).	117

Figure 7.17	Relationship between CAV_5 and (a) vertical gap at left abutment and (b) vertical gap at right abutment.	118
Figure 7.18	Relationship between PGV and column drift for (a) Pier 1, (b) Pier 2, (c) Pier 3, and (d) Pier 4.	119
Figure 7.19	Location of maximum pile bending moment in Pile 0 at left abutment	120
Figure 7.20	Location of maximum pile curvatures in Pile 4 and Pile 5 at right abutment	121
Figure 7.21	Variation of median pier drift with PGV.....	122
Figure 8.1	Mean annual rates of exceedance of repair cost ratio, RCR, for different pile groups: (a) left abutment, (b)–(e) interior columns, and (f) right abutment. DM hazard curves for each pile group obtained considering most efficient IM: (a) CAV_5 , (b) PGV, (c) CAV_5 , (d) PGA, (e) Ia, (f) CAV_5	132
Figure 9.1	PGV hazard curve for highway testbed bridge site.	144
Figure 9.2	Distribution of DV IM (16th, 50th, and 84th percentile curves shown) for highway testbed bridge site for liquefaction case.....	144
Figure 9.3	Total repair cost ratio hazard curve for liquefaction case obtained from convolution of relationships shown in Figures 9.1 and 9.2.	145
Figure 9.4	Deaggregated conditional repair costs for testbed highway bridge in liquefaction case.	146
Figure 9.5	Deaggregated conditional repair costs for testbed highway bridge for 475-yrs return period in liquefaction case.	146
Figure 9.6	Distribution of DV IM for highway testbed bridge site for non-liquefaction case.	148
Figure 9.7	Total repair cost ratio hazard curve for non-liquefaction case.	148
Figure 9.8	Deaggregated conditional repair costs for testbed highway bridge in non-liquefaction case.	149
Figure 9.9	Deaggregated conditional repair costs for testbed highway bridge for 475-yrs return period in non-liquefaction case.	149
Figure 9.10	Distribution of DV IM for highway testbed bridge site for fixed-base case	150
Figure 9.11	Total repair cost ratio hazard curve for fixed-base case.....	151
Figure 9.12	Deaggregated conditional repair costs for testbed highway bridge in fixed-base case.	151

Figure 9.13	Deaggregated conditional repair costs for testbed highway bridge for 475-yr return period.	152
Figure 9.14	Effect of different soil conditions on total repair cost ratio hazard curves.....	153
Figure 9.15	DV IM relationship for liquefaction case with different fractions of actual uncertainty.	154
Figure 9.16	DV IM relationship for non-liquefaction case with different fractions of actual uncertainty.	154
Figure 9.17	Effects of different levels of uncertainty in DV IM on loss hazard for liquefaction case.	154
Figure 9.18	Effects of different levels of uncertainty in DV IM on loss hazard for liquefaction case.	154
Figure A.1	Schematic illustration of PEER PBEE components.	A-1
Figure A.2	Variation of right abutment vertical displacement with (I-r) peak ground velocity, Arias intensity, and CAV_5	A-5
Figure A.3	Variation of Pier 4 maximum drift with (I-r) peak ground velocity, Arias intensity, and CAV_5	A-5
Figure A.4	Fragility surface for testbed bridge. White lines indicate fragility curves for repair cost ratios of 20%, 40%, 60%, 80%, and 90%.	A-7
Figure A.5	Loss curve for testbed bridge.	A-8

LIST OF TABLES

Table 3.1	Representative values of ϵ_{50} for normally consolidated clays—Peck et al. (1974) (after Reese and Van Impe 2001).	17
Table 3.2	Representative values of ϵ_{50} for overconsolidated clays (after Reese and Van Impe 2001).	17
Table 3.3	Representative values of k_{py} for sand (after Reese and Van Impe 2001).	18
Table 3.4	Recommended p-multipliers for pseudo-static analysis (after Brandenberg 2005).	26
Table 3.5	Typical values of soil adhesion factor, a (after NAVFAC 1982).	35
Table 3.6	Recommended parameters for cohesionless siliceous soil (after API 1993).	39
Table 4.1	Soil types and properties.	49
Table 4.2	SPT profiles below embankments	50
Table 5.1	Summary of PIMY material parameter values used for cohesive soil	56
Table 5.2	Summary of PDMY material parameter values used for granular soils.	57
Table 7.1	Magnitude-corrected PGA.	87
Table 7.2	I-880 input motion characteristics (four hazards).	88
Table 7.3	Intensity measures	90
Table 7.4	IM hazard curve coefficients for I-880 input motions.	91
Table 7.5	EDP list.	92
Table 7.6	Summary of EDP median coefficients and record-to-record uncertainty for power-law median response model, $EDP = a IM^b$	99
Table 7.7	Input parameter uncertainties	100
Table 7.8	Correlation coefficients for uncertain input parameters.	104
Table 7.9	Summary of parametric uncertainty	105
Table 7.10	Summary of spatial variability uncertainty (loose sand plus clay).	110
Table 7.11	Summary of spatial variability uncertainty (loose sand)	111
Table 7.12	Summary of spatial variability uncertainty (clay)	112
Table 7.13	Summary of EDP hazard curve: exponential coefficient	123
Table 8.1	Damage probability matrix.	126
Table 8.2	Loss probability matrix.	127

Table 8.3	EDP ranges corresponding to different damage states; where EDP=foundation lateral displacement	128
Table 8.4	Damage probabilities.....	129
Table 8.5	Loss probabilities.....	129
Table 8.6	Tabular listing of mean annual rates of exceedance and return period for various damage states.....	130
Table 8.7	Estimated loss levels.....	131
Table 9.1	Performance groups and associated EDPs.....	136
Table 9.2	Column damage states based on maximum tangential drift ratio.....	137
Table 9.3	Column damage states based on residual tangential drift ratio.	137
Table 9.4	Expansion joint damage states.....	138
Table 9.5	Bearing damage states.	138
Table 9.6	Abutment backwall damage states.	139
Table 9.7	Approach slab damage states.....	139
Table 9.8	Bridge deck damage states.	140
Table 9.9	Pile foundation damage states.	140
Table 9.10	Column repair methods and costs.....	141
Table 9.11	Expansion joint repair methods and costs.	142
Table 9.12	Bearing repair methods and costs.....	142
Table 9.13	Abutment backwall repair methods and costs.	142
Table 9.14	Approach slab repair methods and costs.	142
Table 9.15	Bridge deck repair methods and costs.	142
Table 9.16	Pile foundation repair methods and costs.....	143

1 Introduction

1.1 BACKGROUND

The performance of bridges has a strong effect on emergency response, economic loss, and recovery of urban regions struck by strong earthquakes. History has provided numerous examples of situations in which earthquake-induced bridge failures have kept ambulances, fire trucks, and aid vehicles from reaching those who need them in a timely manner. Earthquake-caused bridge failures have led to expensive repair and replacement costs, and to even more expensive indirect losses associated with shipping delays, congestion, and other indirect consequences of their loss of function. Because bridges are complicated structures that are frequently located in difficult environments, their repair and/or replacement is frequently so time-consuming that their unavailability can impact regions for months or years.

Many bridges cross bodies of water and are therefore in geologic and hydrologic environments that produce significant deposits of loose, saturated sand near and beneath sloping ground surfaces. These types of deposits are frequently susceptible to liquefaction, so the bridges require support on deep foundations. The sloping ground condition leads to the potential for lateral spreading, which can cause severe damage to bridge foundations and abutments and, in severe cases, lead to bridge collapse. In seismically active regions, the provision of adequate levels of safety with respect to these effects can dominate the design of bridges and add substantially to their design and construction cost.

1.2 PERFORMANCE-BASED EARTHQUAKE ENGINEERING

Most bridges are “owned” (i.e., designed, financed, constructed, operated, and maintained) by public agencies that are responsible for multiple bridges and the network of roadways that connect them. Such agencies need to evaluate the potential seismic performance of their entire transportation systems in order to determine which elements of the system are most vulnerable to earthquake damage. To an owner, measures of performance in economic terms are most useful in providing guidance with respect to decisions on investment in repair or replacement of bridges.

The concept of performance-based earthquake engineering (PBEE) provides a framework for direct, quantitative estimation of losses due to earthquake shaking. PBEE allows an integrated assessment of earthquake ground shaking hazards, bridge system response, physical bridge damage, and resulting economic loss. By explicitly considering the various uncertainties in ground motion, response, damage, and loss estimation, a PBEE analysis can provide an unbiased, objective, and quantifiable estimate of earthquake risk. The results of such analyses can be used to evaluate economic exposure, and to evaluate the relative costs and benefits of various mitigation/retrofit measures (including the option of no mitigation or retrofit).

The Pacific Earthquake Engineering Research (PEER) Center has developed a PBEE framework that allows estimation of response, damage, and loss to be made in a modular manner. This framework has numerous advantages including the ability to allow the loss estimation process to be divided into discipline-specific components with relatively clear indications of required interdisciplinary interactions, as well as the ability to track the main factors that contribute to estimated losses. The framework is probabilistic in nature, i.e., it requires identification and characterization of all uncertainties involved in response, damage, and loss estimation, and propagates those uncertainties in a manner that reflects their effects on estimated losses. The expected losses in a given exposure period can be shown to increase with increasing levels of uncertainty; as a result, reduction of uncertainty in different components of the PBEE evaluation can lead to reductions in expected losses.

Response and damage estimation are among the most prominent activities of earthquake engineers in the PBEE process. Geotechnical and structural engineers are usually involved in the estimation of bridge response and damage due to different levels of earthquake ground motion. Various approaches to response prediction are used, for example, in geotechnical engineering

practice. These range from very simple prescriptive models to somewhat more complicated empirical models to simplified analytical models to complicated analytical models. In concept, the uncertainties in predicted response for these different models should decrease with increasing level of model rigor. The current state of geotechnical engineering practice, however, has not advanced to the point where these uncertainty levels can be accurately quantified. As a result, the relative benefits and drawbacks of performing more rigorous response analyses have not been demonstrated.

1.3 OBJECTIVES OF THE STUDY

The objective of the investigation described in this report was to apply the PEER PBEE methodology to the evaluation of a bridge founded on liquefiable soils subject to lateral spreading. This investigation used high-level finite element-based soil-foundation-structure interaction analyses to predict bridge system response, and then used that response to predict physical damage and economic loss. A parallel investigation, conducted at UC Berkeley (Ledezma and Bray 2007), used simplified response analyses to estimate physical damage and then economic loss.

The investigation was intended to document the procedures used to apply the PEER methodology when a rigorous response analyses is performed, and to identify the costs and benefits of performing such analyses.

1.4 ORGANIZATION

The report is organized in a manner that should allow a practicing engineer to understand the PEER PBEE framework and its application to the problem of estimating bridge performance.

Following the introduction, Chapter 2 provides a review of PBEE and introduces the PEER PBEE framework with descriptions of response, damage, and loss estimation. Chapter 3 describes basic concepts of soil-pile-structure interaction analysis. The notion of p-y curves and their characteristics for both non-liquefiable and liquefiable soils is described, as is their use in analysis of laterally loaded piles and pile groups. Similar rheological elements for vertically loaded piles and for abutments are also introduced. The characteristics of a testbed bridge in a hypothetical (but realistic) soil profile are described in Chapter 4. Chapter 5 describes the

development of a detailed finite element model of the soil profile, foundations, abutments, and bridge superstructure. Chapter 6 describes a series of validation analyses of the finite element model, and then goes on to describe the results of an extensive series of response analyses for different input ground motions. In Chapter 7 variations of median response level for numerous response metrics are presented, and the dispersion of computed responses about those median values are characterized. The effects of uncertainties in model parameters and of spatial variability are also described. The performance of the bridge foundations are expressed in terms of damage states and loss levels in a discrete framework described in Chapter 8. Chapter 9 describes damage and loss for the entire bridge in a continuous framework. The loss levels for cases in which liquefaction is allowed to occur and not allowed to occur, and for the case in which the bridge is essentially assumed to be founded on rock, are all described and compared. The effects of uncertainty in the response model on predicted losses are also discussed. Finally, Chapter 10 summarizes the investigation and the conclusions that can be drawn from it.

2 Performance-Based Earthquake Engineering

2.1 INTRODUCTION

Performance-based earthquake engineering (PBEE) refers to an emerging paradigm in which the “performance” of a system of interest can be quantified and predicted on a discrete or continuous basis. The notion of performance means different things to different stakeholders, and an important goal of PBEE is to allow performance to be expressed using terms and quantities that are of interest and meaning to a wide range of earthquake professionals and decision-makers.

Implicit in the development of PBEE is the idea that performance can be quantified and predicted with sufficient accuracy to allow decisions regarding design, repair, retrofit, and replacement to be made with confidence. Continuing developments in the field of earthquake engineering are providing engineers with the tools necessary to make such predictions. The full development of PBEE will allow performance to be expressed in terms of “risk” i.e., in terms that reflect both the direct and indirect losses associated with the occurrence of earthquakes. Such losses can be expressed in terms of casualties, economic losses, and lost time.

2.2 PEER FRAMEWORK

PBEE is generally formulated in a probabilistic framework to account for the many uncertainties involved in estimating the risk associated with earthquake hazards at a particular site. The term “risk” is used in this report to denote loss, which can be expressed in terms of cost, fatalities, or other measures. The term “hazard” is used to describe levels of ground shaking, system response, and/or physical damage, but has no specific connotation of loss. Minimizing the uncertainty in hazard and risk estimates requires minimizing the uncertainties in the variables and the relationships between the variables that go into their calculation.

The PBEE framework developed by the Pacific Earthquake Engineering Research Center (PEER) computes risk as a function of ground shaking through the use of several intermediate

variables. The ground motion is characterized by an intensity measure, IM , which could be any one of a number of ground motion parameters (e.g., PGA, Arias intensity, S_a , etc.). The effects of the IM on a system of interest are expressed in terms that make sense to engineers in the form of engineering demand parameters, or $EDPs$ (e.g., interstory drift, settlement, etc.). The physical effects associated with the $EDPs$ are expressed in terms of damage measures, or DMs (e.g., crack width, spalling). Finally, the risk associated with the DM is expressed in a form that is useful to decision-makers by means of decision variables, DV (e.g., repair cost). The mean annual rate of exceedance of various DV levels, λ_{DV} , can be expressed in terms of the other variables as

$$\lambda_{DV} = \sum_{k=1}^{N_{DM}} \sum_{j=1}^{N_{EDP}} \sum_{i=1}^{N_{IM}} P[DV | DM_k] P[DM_k | EDP_j] P[EDP_j | IM_i] \Delta \lambda_{IMi} \quad (2.1)$$

where $P[a|b]$ describes the probability of exceeding a given b , and where N_{DM} , N_{EDP} , and N_{IM} are the number of increments of DM , EDP , and IM , respectively; with accuracy increasing with increasing number of increments.

The PEER framework has the important benefit of being modular. The framing equation (Eq. 2.1) can be broken down into a series of components, e.g.,

$$\lambda_{EDP}(edp) = \sum_{i=1}^{N_{IM}} P[EDP > edp | IM = im_i] \Delta \lambda_{IMi} \quad (2.2a)$$

$$\lambda_{DM}(dm) = \sum_{j=1}^{N_{EDP}} P[DM > dm | EDP = edp_j] \Delta \lambda_{EDPj} \quad (2.2b)$$

$$\lambda_{DV}(dv) = \sum_{k=1}^{N_{DM}} P[DV > dv | DM = dm_k] \Delta \lambda_{DMk} \quad (2.2c)$$

The problem of performance evaluation can therefore be broken into four basic components: evaluation of ground motion hazard, evaluation of system response to the ground motions, evaluation of physical damage resulting from the system response, and evaluation of losses associated with the physical damage. The problem requires identification of appropriate metrics of ground motion, system response, physical damage, and losses, which are denoted by the previously described IM , EDP , DM , and DV terms; which in view of the desire to account for uncertainty are treated as random variables. It also requires, however, the ability to predict $EDPs$ in response to $IM(s)$, $DM(s)$ in response to $EDP(s)$, and $DV(s)$ in response to $DM(s)$. These are accomplished by response models, damage models, and loss models, respectively. In the PEER

framework, these models are all formulated probabilistically—for example, the response model must be able to predict the probability distribution of an *EDP* for a given *IM* value.

2.3 RESPONSE PREDICTION

Currently, the structural and geotechnical engineers' primary contributions to the PBEE process come primarily in the evaluation of $P[EDP|IM]$ as indicated in Equation (2.2a). This process involves establishing an appropriate *IM*, which should be one that the *EDP*(s) of interest are closely related to (furthermore, the *EDP*(s) of interest should be the ones that the *DM*(s) of interest are closely related to, and the *DM*(s) of interest should be the ones that the *DV*(s) of interest are closely related to). Luco and Cornell (2001) defined efficient intensity measures as those that produced little dispersion in *EDP* for a given *IM*. In other words, an efficient *IM* is one for which the uncertainty in $EDP|IM$ is low. The efficiency of *IM*(s) varies from one type of problem to another, and can also vary from one *EDP* to another. Selection of efficient *IM*(s) is critical to the reliable and economical implementation of PBEE procedures. Luco and Cornell (2001) also described sufficient *IM*(s) as those for which the use of additional ground motion information does not reduce the uncertainty in $EDP|IM$. A perfectly sufficient *IM* would be one that tells an engineer all he/she needs to know about the motion's potential for producing a certain response in a system of interest.

The notions of efficiency and sufficiency are important for the performance-based evaluation of structures affected by liquefaction hazards because conventional procedures for evaluating liquefaction potential are based on an *IM* (PGA) that is moderately efficient but distinctly insufficient. The moderate efficiency comes from the fact that liquefaction potential is evaluated using peak ground acceleration, which is a measure of the high-frequency content of a ground motion. The generation of excess porewater pressure, however, is clearly related to shear strain amplitude, which basic wave propagation concepts (in a linear system) indicate is proportional to particle velocity. Because of the smoothing effects of integration (from acceleration to velocity), strain amplitude is more closely related to intermediate frequencies (often in the range of 1–2 Hz). The insufficiency comes from the fact that excess pore pressures increase incrementally during an earthquake; hence the duration of a ground motion, which is not reflected in peak acceleration alone, affects excess porewater pressure generation. In the earliest modern procedures for liquefaction potential evaluation, the effects of duration were accounted

for by the introduction of a magnitude scaling factor. The need for the magnitude scaling factor is, in and of itself, evidence that peak acceleration is insufficient for the prediction of liquefaction potential.

Structural response is generally less sensitive to duration than liquefaction, so *IMs* that reflect anticipated peak response can be relatively efficient. First-mode spectral acceleration, $S_a(T_o)$, is frequently used as a scalar *IM* for structural response evaluation. For structures of intermediate fundamental period, peak velocity often correlates strongly to $S_a(T_o)$ and can therefore serve as an efficient *IM* that is computed directly from the ground motion (rather than through the filter of SDOF system response on which $S_a(T_o)$ is based).

2.4 DAMAGE PREDICTION

Prediction of the physical damage associated with various levels of system response is a relatively new and difficult task. Physical damage is generally associated with nonlinear, inelastic response; ground shaking that produces only linear, elastic response is unlikely to cause physical damage to a structure or its foundations, although it is possible that some damage to contents could occur.

Damage is estimated through the use of damage models, which can be continuous or discrete. A continuous damage model would define damage in terms of some continuous variable, e.g., crack width in a concrete column or beam. By defining some capacity in terms of a limiting level of response that produces a given amount of damage and characterizing the uncertainty in damage, Equation (2.2b) can be used to convolve a continuous damage function with an *EDP* hazard curve to obtain a damage hazard curve.

For many forms of damage, however, specific capacity distributions are not available. In such cases, damage can be divided into several discrete categories, or damage states. Discrete damage states can be defined by quantitative ranges of some *DM*, for example, crack widths of 0–1 mm, 1–2 mm, 2–4 mm, etc. Alternatively, damage states can be defined qualitatively, e.g., low, medium, or high. The expression of damage states is often performed heuristically based on experience, intuition, and engineering judgment. In the absence of detailed, quantitative damage data, it may be necessary to use expert opinion to identify damage states. Upsall (2006) polled two groups of geotechnical engineers—a group of random practitioners in the Seattle, Washington, area and a group of experienced post-earthquake reconnaissance leaders—and

found significant differences in their estimates of the levels of permanent deformations required to produce different qualitative damage states.

2.5 LOSS PREDICTION

The estimation of earthquake-induced losses, whether expressed in terms of casualties, direct and/or indirect losses, or downtime) is also in a relatively undeveloped state. Loss estimation is typically best performed by persons other than those who are best suited to evaluating response and physical damage. Construction estimators, insurance adjustors, real estate appraisers, and others who deal with damaged structures are more likely to be capable of accurate loss estimation than typical design engineers. The advancement of PBEE will clearly require increased interaction between engineers and loss estimators.

The estimation of even direct economic losses, which are arguably the easiest types of losses to estimate, is far from simple. In addition to the effects of such uncertain variables as future material, labor, and capital costs, loss functions are also discontinuous. For example, repair costs associated with epoxying of cracks in a bridge girder would suddenly drop to zero if damage is sufficiently high that the girder would be replaced. Many repair/replacement costs are highly correlated, but studies that would better define the relationships between various damage/loss variables for both simple and complex structures have not yet been performed.

In the absence of detailed loss estimation procedures, it is often necessary to use expert opinion to develop working loss models. The quality of the resulting loss estimates should consider the efficiencies and sufficiencies of the variables used to estimate losses.

2.6 SUMMARY

The PEER framework for performance-based earthquake engineering provides a useful, rational, and modular approach to performance prediction. Implementation of the framework involves the identification of suitable parameters for describing ground motion system response, physical damage, and losses. It also requires the prediction of response given ground motion, physical damage given response, and loss given physical damage. The framework further requires that uncertainty in these parameters, and the relationships between them, be characterized and properly accounted for in the analyses.

3 Seismic Soil-Pile-Structure Interaction

3.1 INTRODUCTION

Typical bridges consist of the bridge structure, pile/drilled shafts or spread footing foundations, abutment structures, and the supporting soil. During earthquakes, the individual components interact with each other and affect the global response of the bridge. In this chapter, relevant aspects related to lateral soil-pile interaction and soil-abutment-bridge interaction are briefly reviewed and discussed. Since p-y curves are important in modeling soil-pile-structure interaction, this topic is covered in more detail. Other topics reviewed in this chapter include the lateral response of piles and pile groups, soil-pile-structure interaction associated with structural stiffness, and soil-abutment-bridge interaction.

3.2 SOIL-PILE INTERACTION MODELING

Soils and pile foundations interact with each other under both static and dynamic loading conditions. The interaction is complex, and complete evaluation requires resources that are rarely available to practicing engineers. As a result, simplified models, which attempt to capture the main aspects of soil-pile interaction, have been developed. These models have been shown to work well for static and relatively slow cyclic loads (such as wave loads, typically encountered in pile-supported offshore structures), and can also be applied, with consideration of inertial effects, to problems including seismic soil-pile interaction. Among these models, those based on the static/dynamic beam-on-nonlinear-Winkler-foundation (BNWF) method, often referred to as the p-y method, are commonly used to model soil-pile interaction problems and deserve special attention.

3.2.1 Static and Dynamic Beam-on-Nonlinear-Winkler-Foundation (BNWF) Models

The analysis of laterally loaded piles is complicated due to the long and slender configuration of piles, the nonlinear response of the surrounding continuous soils, and the interface where the soil is in contact with the pile. Rigorous simulation of the interaction problem requires three-dimensional (3-D) finite element models (FEM), which are computationally expensive, and require the use of advanced constitutive models to capture localized soil response. They also require the use of robust contact elements to capture soil and pile interaction effects such as gapping and sliding (e.g., Petek 2006). As an alternative, Winkler foundation models have been widely used in practice. In these models the pile is treated as a beam supported on a Winkler spring foundation, i.e., a series of independent horizontal and vertical nonlinear springs distributed along the pile. For this reason, these models are often referred to as beam-on-nonlinear-Winkler-foundation (BNWF) models. Figure 3.1(a) shows a schematic of a BNWF model.

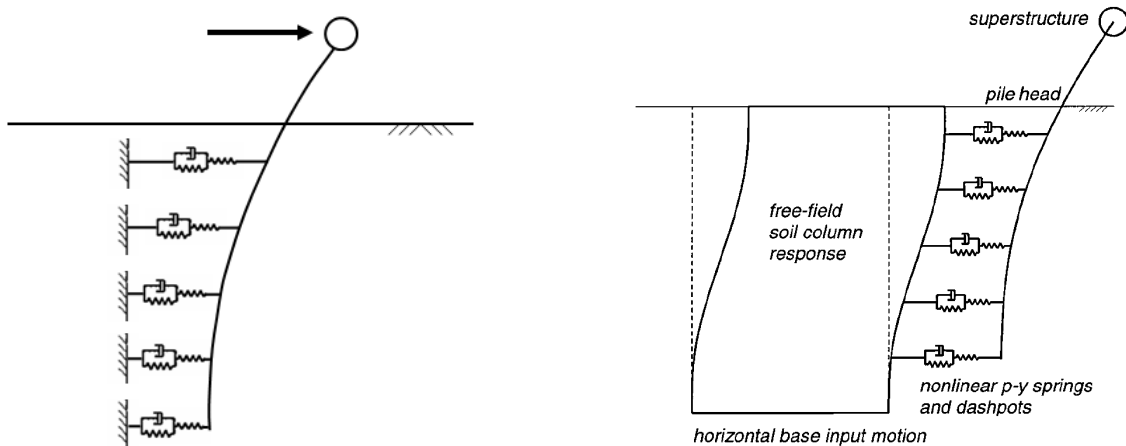


Fig. 3.1 Static and dynamic beam-on-nonlinear-Winkler-foundation (BNWF) model.

During earthquakes, shear waves propagate through the soil applying kinematic forces to the pile foundation. The foundation shaking induces inertial forces in the superstructure. The inertial forces affect the foundation response and the soil movement. The soil motion around the pile, where soil-pile interaction occurs, is referred to as near-field motion. The soil motion recorded far from the pile is referred to as far-field or free-field motion. In coupled simulations,

where the pile and soil are connected by interface springs, it is assumed that a soil column provides the free-field motion and that the soil-pile-structure interaction occurs at the interface springs. Alternatively, free-field motions can be calculated separately along the pile depth and the corresponding displacement time histories can be applied to p-y springs. This idea is illustrated in the dynamic Beam-on-nonlinear-Winkler-foundation (BNWF) model shown in Figure 3.1(b).

3.3 p-y CURVES

To completely define the BNWF model it is important to establish accurate p-y curves. In this section two cases are considered: (1) a pile subjected to monotonic and cyclic loads at the pile head and (2) a pile embedded in liquefiable soil and subjected to earthquake excitations and lateral spreading. To analyze the first case, conventional p-y curves are introduced. For the earthquake problem, since there are not yet well-established p-y curves for liquefiable soil, several experimental observations are discussed.

3.3.1 Conventional p-y Curves for Piles Subjected to Static and Cyclic Loading

To capture the lateral response of piles, soil reaction force versus pile displacement (i.e., p-y) relationships are commonly used together with beam elements in static and dynamic BNWF models. In general these curves are based on field tests, laboratory model tests, and analytical solutions. The pile displacement (y) and soil-resisting force per unit length (p) can be back-calculated from measured or calculated bending moments by double-differentiating and double-integrating the governing equilibrium differential equation. That is,

$$p = \frac{d^2}{dz^2} M(z) \tag{3.1}$$

and, assuming linear bending behavior,

$$\frac{d^2}{dz^2} y = \frac{M(z)}{EI} \tag{3.2}$$

where p is the lateral resistance on the pile, y is the relative lateral pile displacement, M is the pile bending moment, EI is the flexural rigidity of the pile, and z is the vertical distance measured along the pile. Many researchers have performed static and cyclic lateral load tests on full-scale and model piles in different soils with the purpose of evaluating p - y curves, e.g., Matlock (1970) for soft clay, Reese (1974) for sand, Reese et al. (1975) for stiff clay below the ground water table, and Reese et al. (1981) for stiff clays above the ground water tables. As a result, several p - y curve criteria have been proposed for sands and clays. Additional field load tests and analytical and numerical evaluation of p - y response have increased confidence in the use of these curves (Reese et al. 1981). Although there is some criticism of the BNWF model due to its limitations for capturing all soil continuum effects (in particular the coupling between p - y and t - z springs), the back-calculated p - y curves themselves reflect the continuum condition and have been successfully used in many projects. Wang and Reese (1998) suggested that the error incurred using discrete curves is a second-order effect, taking into account the difficulty of precisely predicting the relevant properties of the soil, especially next to the pile where the soil properties are strongly affected by the pile installation problem.

3.3.1.1 Back-Calculated p - y Curves for Sand, Stiff Clay, and Soft Clay

Figures 3.3 and 3.4 show back-calculated p - y curves for cohesionless and cohesive soils obtained from field tests. The envelope curves can be characterized mainly by their initial stiffness and ultimate resistance, which is mobilized at large displacements. The initial stiffness and ultimate soil resistance increase with depth in a uniform granular soil, since the soil stiffness and confinement increase with depth. The characteristics of the p - y curves depend on soil type, loading condition, and ground water location, since these reflect the nonlinear shearing characteristics of the soil. Figure 3.2 clearly shows that the ultimate lateral soil resistance of a sand under cyclic loading is smaller than that obtained for static loading. This pattern is more clear in stiff clays, as shown in Figure 3.3. However, the difference between sand and stiff clays subjected to cyclic loading is that the ultimate resistance of sands stays constant after a peak value is reached, while the ultimate resistance in stiff clays decreases significantly after the peak value.

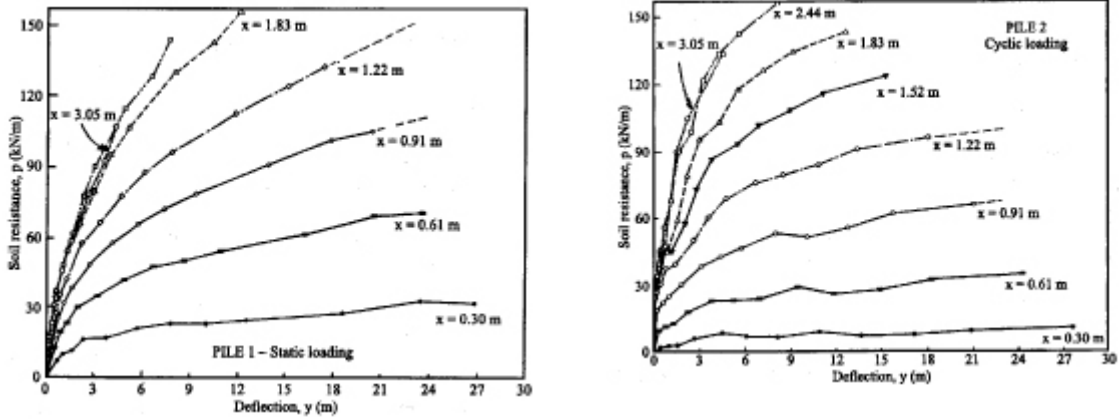


Fig. 3.2 Back-calculated p-y curves for sand from field tests (after Reese et al. 1975).

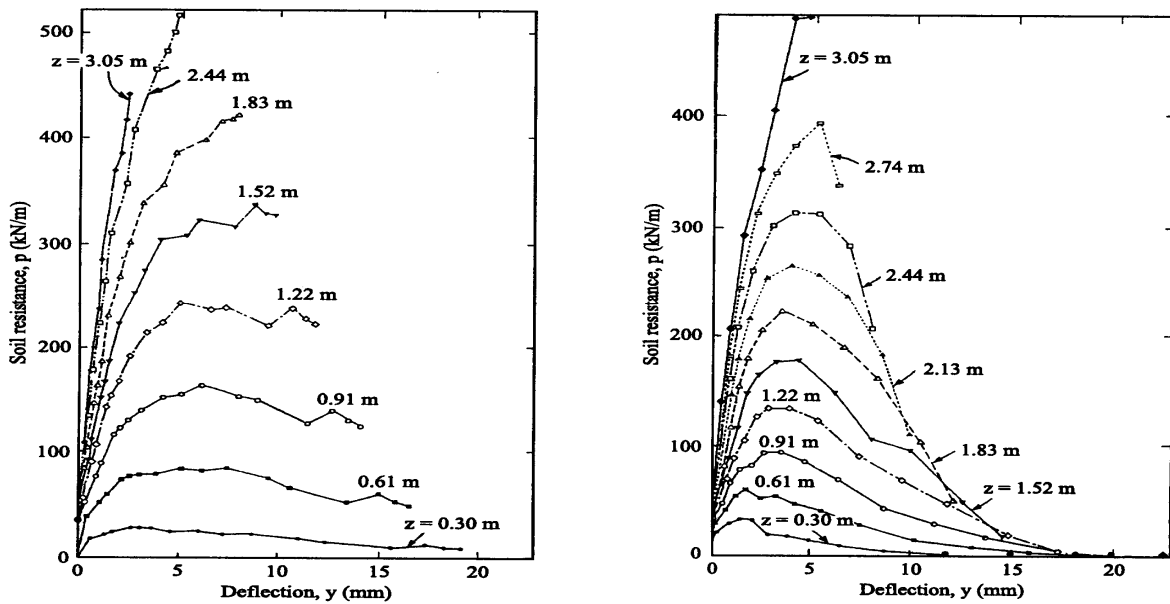


Fig. 3.3 Back-calculated p-y curves for stiff clay from field tests (after Reese et al. 1974).

In soft clays, the soil resistance increases with pile displacement reaching a constant ultimate resistance under static loading, while the ultimate resistance becomes smaller under cyclic loading. An important feature observed in soft clays subjected to cyclic loading is the

formation of gaps between the pile and the soil near the ground surface. Figure 3.4 shows experimental p-y curves for soft clays subjected to cyclic loading.

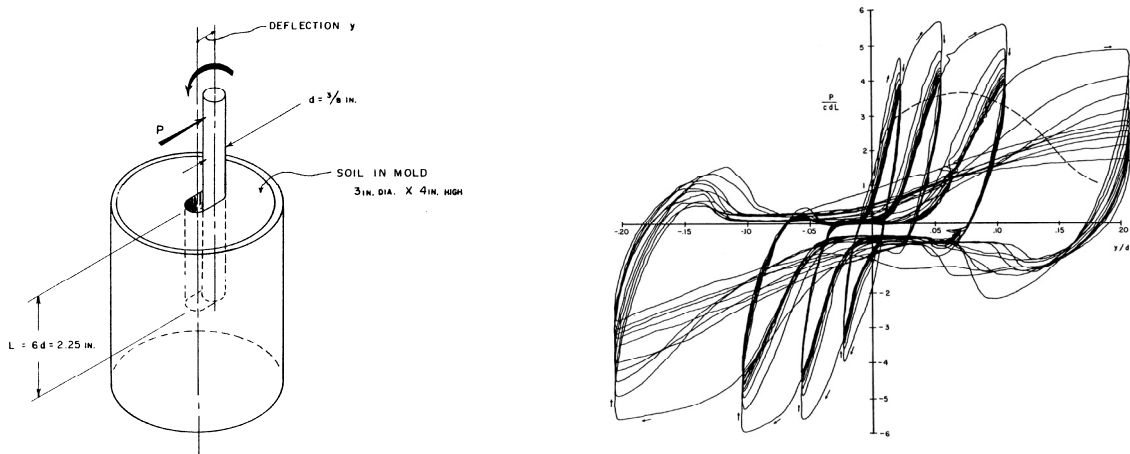


Fig. 3.4 Cyclic response of rigid pile in soft clay (after Matlock 1970).

From experimental observations, Reese, Matlock, and other researchers proposed several p-y curve construction methods for various soil types, ground water conditions, and loading types. The details of these methods are summarized in the following subsections.

3.3.1.2 Initial Stiffness of p-y Curves

The initial stiffness of p-y curves may have little consequence for most pile analysis (Reese and Van Impe (2001)). The reason is that when a pile is subjected to large lateral loading, most of the reaction occurs near the ground surface where the mobilized lateral soil resistance is close to the ultimate resistance; which is mobilized at displacement levels that are beyond the initial p-y curve portion. The cases where the initial p-y curve stiffness can be important is when piles are subjected to vibratory loading or when piles are installed in brittle soils.

The initial stiffness is often defined in terms of indirect parameters. For clays, the displacement at which half of the ultimate soil resistance is mobilized, called y_{50} , is used to define the initial p-y stiffness. y_{50} for clays is usually defined as

$$y_{50} = 2.5\epsilon_{50}D \quad (3.3)$$

where ϵ_{50} represents the strain corresponding to one half of the undrained strength and D is pile diameter. Table 3.1 and 3.2 present typical ϵ_{50} values for normally- and overconsolidated clays, respectively.

For sands, Reese et al. (1974) suggest an initial p-y stiffness equal to k_{py} times depth. Table 3.3 presents typical k_{py} values for sands.

Table 3.1 Representative values of ϵ_{50} for normally consolidated clays—Peck et al. (1974) (after Reese and Van Impe 2001).

clay	average undrained shear strength, (kPa)	ϵ_{50}
soft clay	< 48	0.020
medium clay	48–96	0.010
stiff clay	96–192	0.005

Table 3.2 Representative values of ϵ_{50} for overconsolidated clays (after Reese and Van Impe 2001).

	average undrained shear strength, (kPa)	ϵ_{50}
overconsolidated	50–100	0.007
clay	100–200	0.005
	300–400	0.004

Table 3.3 Representative values of k_{py} for sand (after Reese and Van Impe 2001).

	k_{py} for submerged sand	k_{py} for above GWT
loose sand	5.4 MN/m ³	6.8 MN/m ³
medium sand	16.3 MN/m ³	24.4 MN/m ³
dense sand	34.0 MN/m ³	61.0 MN/m ³

3.3.1.3 Ultimate Resistance of p-y Curves

Ultimate soil resistances are calculated using two simple mechanisms based on limit equilibrium analysis. For near-surface p-y curves, a three-dimensional sliding surface wedge is considered. For deeper p-y curves, a two-dimensional flowing soil failure mode around the pile in a horizontal plane is considered. In both cases, the ultimate resistance is a function of pile diameter, depth (or overburden), and soil strength parameters. Matlock (1970) proposed ultimate resistance expressions for clays. In his analysis Matlock recognized that the ultimate resistance for clays at deeper depths is strongly affected by cohesion and pile diameter and is insensitive to depth. Therefore, the following expressions were proposed to evaluate the ultimate resistance for piles in soft clays at shallow and deeper depths.

$$p_{ult} = \begin{cases} \left[3 + \frac{\gamma'}{c_u z + \frac{J}{b} z} \right] c_u b & \text{for shallow depths} \\ 9c_u b & \text{for deeper depths} \end{cases} \quad (3.4)$$

where γ' is the average effective soil unit weight, c_u is the undrained shear strength of the soil at depth z , b is pile diameter or width, and J is an experimentally determined coefficient (0.5 for soft clay and 0.25 for medium stiff clay).

Similarly, Reese et al. (1974) suggested ultimate resistance expressions for sands. In their analysis, theoretically calculated values (p_s) were factored by experimental coefficients that varied with loading type and depth. The resulting expressions for ultimate resistance are

$$p_{ult} = \begin{cases} A_s p_s & \text{for shallow depths} \\ A_c p_c & \text{for deeper depths} \end{cases} \quad (3.5)$$

where A_s or A_c are experimental factors associated with loading type and depth (Reese et al. 1974). The value of p_s is calculated by

$$p_s = \begin{cases} p_s = \gamma z \left[\frac{K_0 z \tan \phi \sin \beta}{\tan(\beta - \phi) \cos \alpha} + \frac{\tan \phi}{\tan(\beta - \phi)} (b + z \tan \beta \tan \alpha) \right] & \text{for shallow} \\ & \text{depths} \\ p_s = K_a b \gamma z (\tan^8 \beta - 1) + K_0 b \gamma z \tan \phi \tan^4 \beta & \text{for deeper} \\ & \text{depths} \end{cases} \quad (3.6)$$

where $\alpha = \phi/2$; $\beta = 45 + \phi/2$; $K_0 = 0.4$, $K_a = \tan^2(45 - \phi/2)$, b = pile diameter or width, ϕ = soil friction angle at depth z , and γ = soil unit weight.

Recently, Zhang et al. (2005) proposed a method to calculate the ultimate soil resistance for cohesionless soil considering the normal and side resistance that develops around the pile. To evaluate the normal resistance, they suggested a method originally proposed by Fleming et al. (1992) such that $p_u = K_p^2 \gamma z b$. To evaluate the side resistance, an additional term is included. The total ultimate resistance is then expressed as

$$p_u = (\eta K_p^2 \gamma z + \xi K \gamma z \tan \delta) b \quad (3.7)$$

where $\eta = 0.8$ and $\xi = 1.0$ for a circular pile; $\eta = 1.0$ and $\xi = 2.0$ for a square section pile (Briaud and Smith 1983), δ = interface friction angle between pile and soil, and b = pile diameter. Their study compared several small-scale pile tests and centrifuge test results performed by Barton and Finn (1983). Their results showed that Broms's (1964) ultimate resistance expression, as shown

in Figure 3.7, underpredicts the ultimate lateral resistance at all depths, while the method of Reese et al. (1974) underpredicts ultimate lateral resistances at shallower depths, but overpredicts the ultimate lateral resistance at deeper depths. Figure 3.6 compares patterns of several suggested ultimate lateral soil resistance distributions for cohesionless soil.

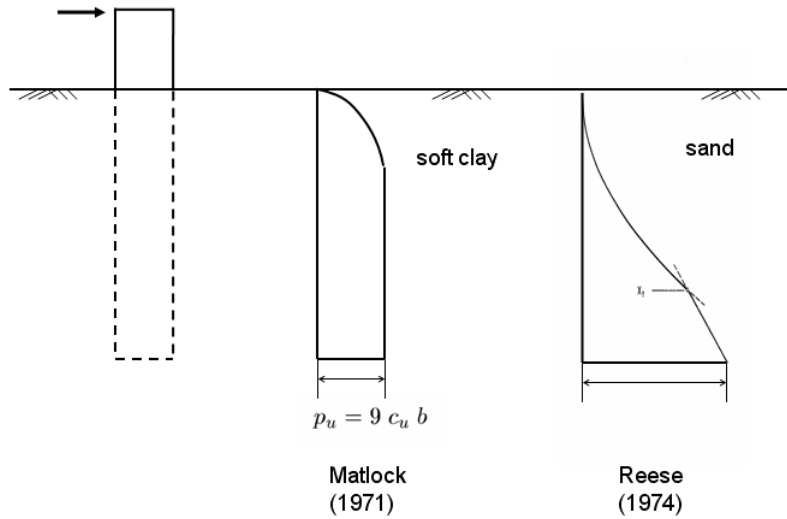


Fig. 3.5 Comparison of ultimate soil resistance of soft clay (Matlock 1971) and sand (Reese et al. 1974).

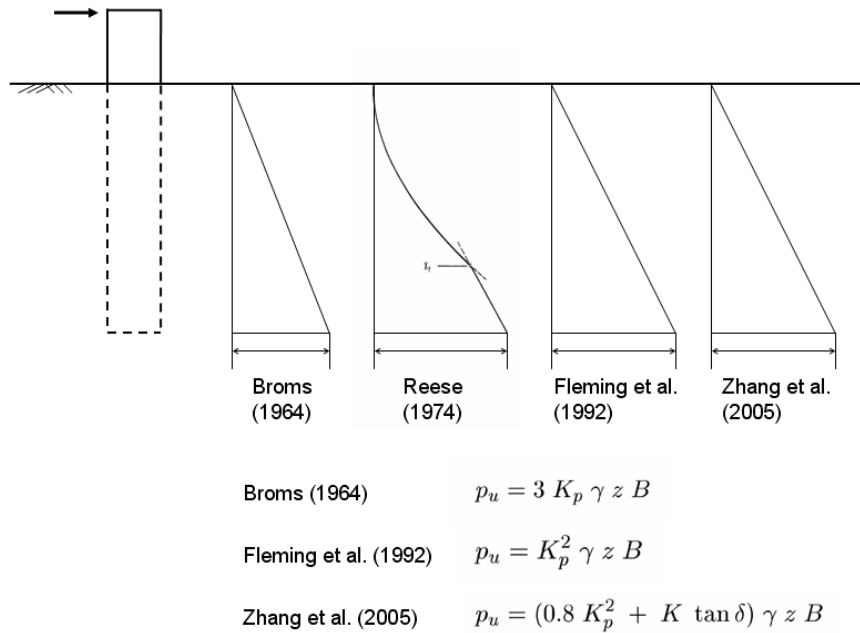


Fig. 3.6 Suggested ultimate soil resistance for cohesionless soil.

3.3.2 p-y Curves for Liquefiable Soil

In the previous subsection, conventional p-y curves were introduced. These curves were developed mainly from experimental tests where the pile head was loaded monotonically or cyclically. Since the applied loading rate was slow in most cases, there was no excess porewater pressure built-up in the saturated soil around the pile. However, when a pile is subjected to earthquake shaking, the soil around the pile may liquefy, if susceptible, and the soil resistance may change due to porewater pressure generation. This is an important aspect, particularly for deep foundations on liquefiable soils. In this section, recent studies on the lateral resistance of piles in liquefiable soil are discussed.

3.3.2.1 Back-Calculated p-y Curves for Piles in Level Ground Liquefiable Soils

When the soil around a pile is liquefied the soil resistance around the pile changes. To better understand these changes several types of dynamic experiments have recently been performed including: (i) centrifuge tests (Dobry et al. 1995; Wilson et al. 2000), (ii) large-scale laminar shear box shaking tests (Tokimatsu et al. 2001), and (iii) full-scale field blasting tests (Rollins et al. 2005; Weaver et al. 2005; Gerber and Rollins (2005).

Among the results obtained from these tests, it is worth examining the p-y curves back-calculated from the centrifuge tests performed by Wilson et al. (2000). Some of these results are shown in Figure 3.7. The figure illustrates observed p-y curve pattern in liquefiable soils. In these tests, different soil densities were used. From these results it was observed that the lateral soil resistance was similar to that observed during undrained tests, showing degradation and hardening of the lateral soil resistance due to porewater pressure generation and dissipation. After liquefaction, denser sands showed larger lateral resistance than loose sands. Medium dense sands showed a progressive softening of lateral resistance with pore pressure increase with number of cycles, especially near the ground surface. The p-y behavior was softest when the pore pressure ratio was high and when the lateral displacements were smaller than those corresponding to past peak values. When dilation occurred at large pile displacements in medium dense to dense sands, the lateral soil resistance against pile increased to a level that was sometimes greater than the ultimate resistance of the non-liquefiable soil. This effect can be correlated to the pore pressure drop associated with dilation under rapid, undrained loading conditions. In addition, the lateral resistance was affected by the amount of pile displacement,

loading rate, and degree of pore pressure dissipation. Similar patterns were observed in other experimental tests.

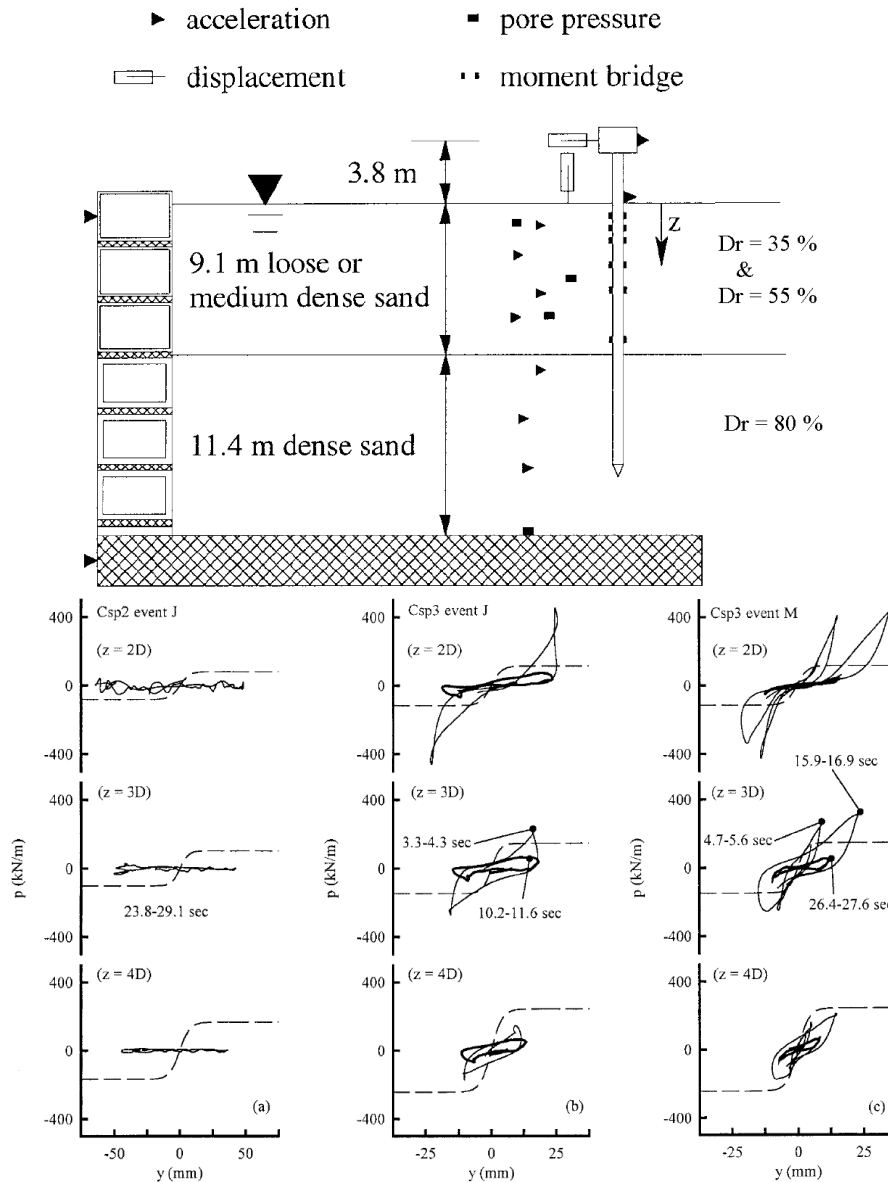


Fig. 3.7 Back-calculated p-y behavior during shaking (after Wilson et al. 2000).

3.3.2.2 Lateral Soil Pressure on Piles due to Lateral Spreading

When a soil in a slope, or at the base of a slope, undergoes liquefaction, the driving shear stresses induced by gravity in the soil deposit may cause permanent strains to accumulate in one preferential direction, and thereby lead to lateral spreading. The accumulated soil deformation

during shaking can induce large amounts of kinematic forces on the pile foundation, which may result in severe damage to foundations and structures such as a bridges or port facilities.

To analyze piles subjected to lateral spreading, the lateral force induced by the liquefied layer must be considered. This can be done assuming a constant pressure distribution independent of the amount of soil displacement, or by using spring forces that depend on imposed soil displacements. In both approaches, the lateral force applied to the pile depends on the liquefied soil properties, distribution of soil displacement, and the velocity of the lateral flow (Wang and Reese (1998)). Among these factors, the strength of the liquefied soil is most important.

To estimate the liquefiable soil resistance, the conventional soil resistance without liquefaction is scaled by a p -multiplier that accounts for a simplified distribution of pore pressure ratio along the pile. p -multipliers for fully liquefied soils vary depending on the test conditions (Dobry et al. 1995; Wilson 1998). For example, the Japan Road Association (JRA 2002) guidelines suggests a 30% of total overburden stress times pile diameter for the lateral pressure imposed by the liquefiable soil with an additional reduction factor associated with the distance from the waterfront.

Another way to estimate the kinematic load on the pile from lateral spreading is to assume that the liquefied sand behaves as an undrained soil with a certain residual shear strength. Among several ways to estimate the residual strength, the in-situ test approach is commonly used. This method is based on correlations between SPT resistance and back-calculated shear strengths from flow slide case histories (Seed 1986; Stark and Mesri 1992; Seed and Harder 1990). Figure 3.8 shows one of these correlations. Unfortunately, this approach includes considerable uncertainties due to the variability of soil and stress conditions in the case histories.

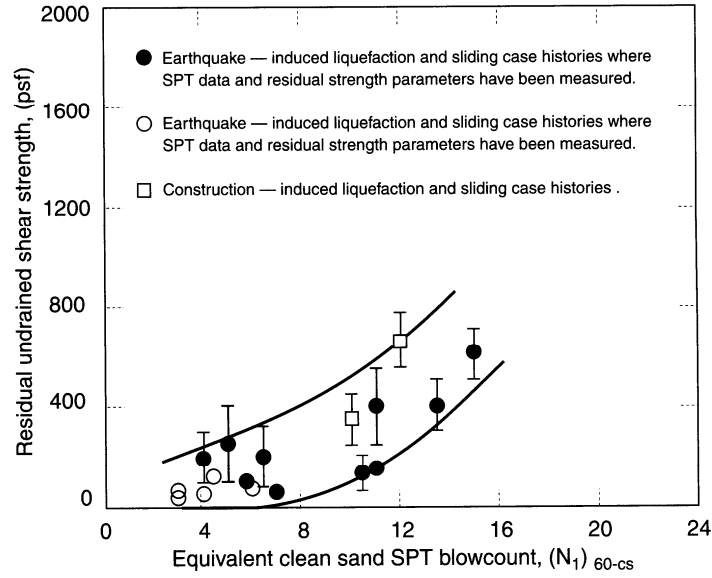


Fig. 3.8 Relationship between residual strength and corrected SPT resistance (Seed and Harder 1990).

As another approach, the use of normalized shear strengths (S_r / σ'_{v0}) is widely accepted and has been shown to have several advantages. However, normalized shear strengths vary considerably for different soils (Kramer 1996).

As an improved in-situ method approach, Kramer (2006) proposed a hybrid residual strength model that accounts for uncertainties using different weights that depends on documentation quality. The probabilistic form of the residual strength in this hybrid model is expressed as

$$S_r(P) = \exp[\ln S_r + \Phi^{-1}(P)\sigma_{\ln S_r}] \quad (3.8)$$

where,

$$\ln S_r = -8.444 + 0.109 N + 5.379 (\sigma'_{v0})^{0.1}$$

$$\sigma_{\ln S_r} = \sqrt{\sigma_m^2 + 0.00073 N^2 COV_N^2 + 4.935 (\sigma'_{v0})^{0.2} COV_{\sigma'_{v0}}^2}$$

$$\sigma_m^2 = 1.627 + 0.00073 N^2 + 0.0194 N - 0.027 N (\sigma'_{v0})^{0.1} - 3.099 (\sigma'_{v0})^{0.1} + 1.621 (\sigma'_{v0})^{0.2}$$

P = the probability of non-exceedance (i.e., the percentile value), σ'_{v0} = vertical effective stress in atm, $N = (N_1)_{60}$, $COV_N = 0.3$, and $COV_{\sigma'_{v0}} = 0.05$.

3.3.2.3 Approximation of Liquefiable p-y Curves

As discussed previously, the lateral resistance of liquefiable soil against piles cannot be simply defined using conventional p-y backbone envelopes. Moreover, the resistance is found to be strongly correlated to the characteristics of the undrained soil behavior; which depends on density, displacement history and displacement level, depth (i.e., confining pressure), and other factors. Several researchers have tried to encapsulate these effects within the pore pressure ratio, r_u , and establish approximate p-y curves based on this parameter; since the pore pressure change and phase transformation effects (contraction and dilation) governs the undrained soil behavior. In this approximation, the lateral resistance is assumed to be inversely proportional to pore pressure ratio (r_u) in a degradation parameter (often also called p-multiplier).

Dobry et al. (1995) used this inverse relationship to capture the response observed in centrifuge pseudo-static tests of single pile embedded in liquefiable leveled ground soil ($D_r \gg 40\%$). Using measured pore pressure ratio distributions with depth to evaluate the degradation of the p-y curves, pile bending moments were predicted reasonably well. Using a similar approach, Wilson (1998) concluded that p-multipliers ranging from 0.1 to 0.2 for $D_r \gg 40\%$ and from 0.25 to 0.35 for $D_r \gg 55\%$ in pseudo-static analysis give reasonable results for representative peak loading cycles on a single pile. In a recent work Brandenberg (2005) recommended more refined p-multiplier values to account for liquefaction effects in pseudo-static analysis for different $(N_1)_{60-cs}$. These values are shown in Table 3.4.

Table 3.4 Recommended p-multipliers for pseudo-static analysis (after Brandenberg 2005).

$(N_1)_{60-cs}$	m_p
< 8	0 to 0.1
8–16	0.1 to 0.2
16–24	0.2 to 0.3
> 24	0.3 to 0.5

Boulanger et al. (2004) performed nonlinear FEM analyses for a centrifuge test for a single pile in liquefiable soil (Wilson 1998). In their finite element model the p-y springs were connected to adjacent soil elements to transfer pore pressure ratio information. The ultimate capacity and tangential stiffness were scaled by a factor of $(1-r_u)$. Their results, particularly those corresponding to the soil profile and superstructure, agreed very well with the experimental results showing reasonably good ability of the model to capture the principal features of the response observed in the centrifuge.

3.4 PILE RESPONSE TO LATERAL LOADS

In the preceding section, characteristics of conventional p-y curves were discussed with emphasis on initial stiffness and ultimate soil resistance. Although Figures 3.5 and 3.6 illustrate the distribution of ultimate lateral resistance with depth, the actual lateral soil resistance may not reach the full ultimate resistance distribution over the length of the pile. In most cases, pile deflection, especially for long flexible piles loaded statically at their heads, is greatest near the ground surface and most of the lateral soil reaction occurs near the surface. Therefore, maximum bending moments usually occur at depths of 1.25D to 3.3D below the ground surface (Chai and Hutchinson 2002).

During earthquakes, piles are subjected to both inertial and kinematic loading. The inertial loading predominantly affects the response of the soil and pile near the ground surface, while the kinematic loading influences the pile response over its lengths depending on the soil

conditions and their earthquake response characteristics (such as lateral resistance degradation due to liquefaction and lateral spreading). This section discusses the response of piles to monotonic and cyclic loads including details on pile response in layered soils with liquefiable soil.

3.4.1 Pile Response due to Static/Cyclic Lateral Load and Load Transmission

When the load applied to a pile head is increased, the load is transmitted to the soil. If the soil resistance near the surface reaches an ultimate state, the deeper soil takes additional loading. This resistance (re-)distribution process is related to pile and soil stiffness and yielding. When the pile stiffness is high relative to the soil, the pile tends to show a smaller curvature and the soil resistance is mobilized to deeper depths. However, once the pile bending moment is close to the yield moment, a plastic hinge can develop and the lateral load transmitted to deeper depths becomes smaller. Since piles usually do not reach the ultimate bending moment at the initial yielding location, and the soil yielding extends progressively downward with increased loads, the plastic hinge location spreads out, rather than remaining concentrated at the initial location (Gerolymos and Gazetas 2005).

3.4.2 Pile Response under Pile Head Load

Using simple ultimate soil resistance diagrams (i.e., constant ultimate resistance with depth in clay and linearly increasing ultimate resistance with depth in sand as shown in Figs. 3.5–3.6), Broms (1964a,b) (1964a) calculated maximum lateral pile head forces and bending moments for different possible failure modes using different pile lengths (short, intermediate, and long), soil types (cohesive and cohesionless), and pile head conditions (free and fixed). In Brom's study, pile length, pile head condition, and soil type give different soil reaction patterns and pile bending moment distributions. For example, short piles mobilize full soil resistance, whereas long piles mobilize ultimate soil resistance only near the ground surface. The bending moment distribution is also affected by pile head fixity.

3.4.3 Pile Response during Lateral Spreading

The pile bending moment distribution mainly depends on the boundary forces that develop along the pile length. During an earthquake, kinematic loads cause large pile bending moments at the interface between soils of different stiffness. In many cases, large pile bending moments and failure have been observed at the interface between these layers. Figure 3.9 shows an example where pile failures occurred at the soil layer interface. Large bending moment concentrations at soil layer interfaces are more obvious when one of the soil layers is liquefied.

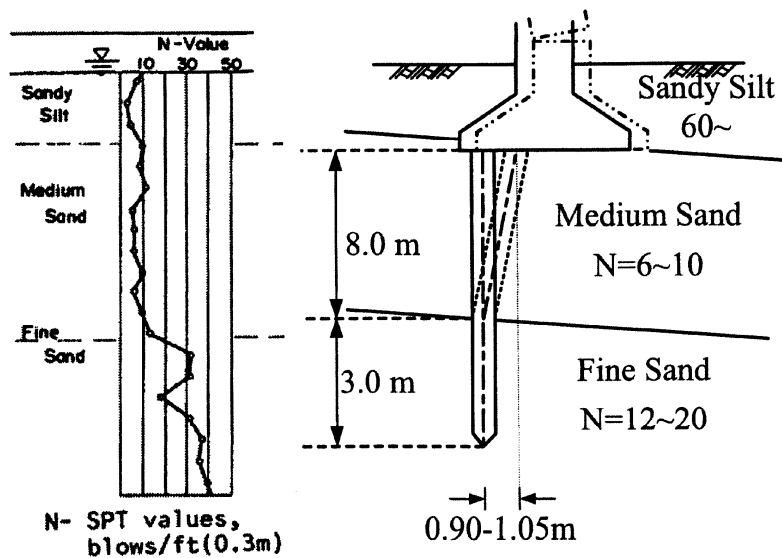


Fig. 3.9 Pile foundation failure of Yachiyo bridge due to kinematic loading (after Hamada 1992).

When a soil over a non-liquefiable soil liquefies, the total lateral soil resistance varies with the degree of liquefaction over the length of the pile. In many cases the underlying non-liquefiable soil may control the pile response due to the rotational restraint associated with its flexural stiffness and embedment length. For this reason, the location of the interface between liquefiable and non-liquefiable layers and the combination of liquefiable and non-liquefiable layers have an important influence on pile response. From centrifuge tests where lateral spreading was considered using different liquefiable layer combinations, Abdoun et al. (2003) observed that maximum bending moments occurred at the interface between the liquefiable and non-liquefiable layers. After the pile bending moment reached a peak value, the moment value decreased with the pile bouncing-back. Abdoun et al. also observed that a floating pile installed

in a non-liquefiable layer over a liquefiable layer had a maximum bending moment at the top of the liquefiable layer since displacements at the upper non-liquefiable soil exceeded that of the liquefied lower layer. In cases where piles were embedded in three layers (non-liquefiable layer over liquefiable layer over a non-liquefiable layer), large maximum bending moments occurred at the layer interfaces (i.e., at the top and bottom of the liquefiable layer) although the larger maximum values occurred at the lower interface. In these cases, it was also observed that the measured bending moment distribution within the liquefied layer was nearly linear showing little contribution to the pile bending moment from the liquefied soil. Another observation was that soil densification due to pile driving resulted in larger bending moments than those in cast-in-place piles due to the fact that the densification increased the initial effective stress, and hence the stiffness of the soil surrounding the pile.

3.5 PILE GROUP RESPONSE TO LATERAL LOADS

Pile groups consist of rows of piles whose heads are connected by a rigid pile cap. The lateral capacity of pile groups depends on the individual pile capacities, pile spacing, pile installation method, pile cap resistance, and other factors.

3.5.1 Group Effect

The efficiency of an individual pile in a pile group (compared to a single isolated pile) depends primarily on pile spacing, alignment, and location within the group. When piles in a group are closely spaced, lateral pile movements affect the stresses in the soil around the adjacent piles. Figure 3.10 shows two possible pile alignments: in-line and side-by-side. In in-line alignments, a front pile (or leading pile) takes more load than the others and the rear pile (trailing pile) mobilizes less soil resistance. This effect is referred to as the shadow effect. In side-by-side alignments, corner piles located at the corner or at the edge of a pile group take a greater share of the load than the interior piles. This is particularly noticeable when piles are closely spaced. This effect is referred to as the edge effect.

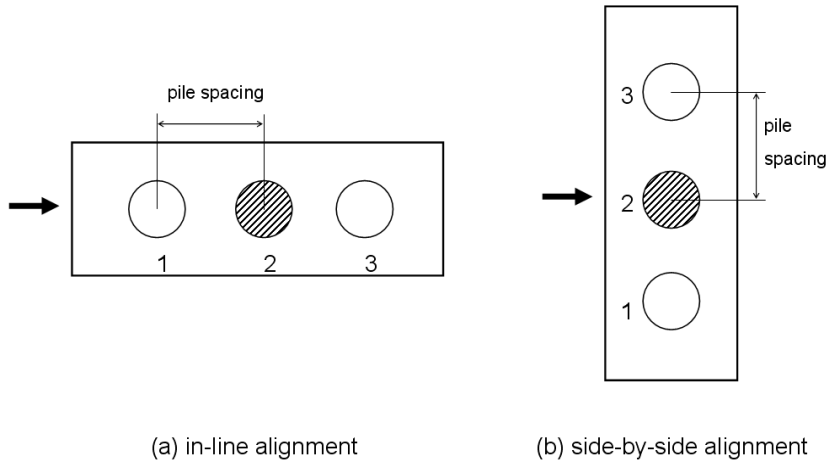
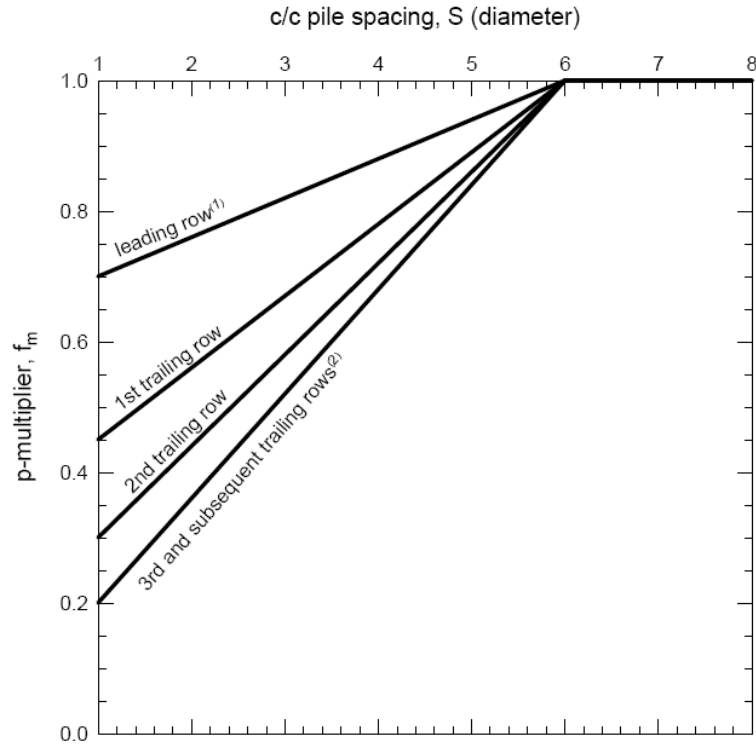


Fig. 3.10 Schematic of pile alignment in group.

To capture the response of piles in a pile group, group efficiency factors are included in the p-y curves using p-multipliers (Brown et al. 1988). To evaluate these p-multipliers several researchers have performed experimental tests on pile groups using different pile group sizes (i.e., number of rows and piles per row), pile spacing, pile cap rotational conditions, and soil type and density. Mokwa (1999) studied pile group behavior and pile cap resistance and completed a comprehensive literature review using 350 journal articles and other publications, including 37 experimental studies (15 full-scale tests, 16 1-g model tests, and 6 centrifuge tests) and approximately 30 analytical studies. Based on these studies, he concluded that pile spacing is the dominant factor affecting pile group response and that group effects are negligible when the center-to-center pile spacing is greater than $6D$ in in-line configurations or greater than $3D$ in the side-by-side configurations. He also concluded that soil type and density does not affect significantly the pile group efficiency, and that efficiency decreases with increasing displacement and becomes constant after a deformation of 5% of pile diameter. He also developed relationships to estimate pile group efficiencies and p-multipliers as a function of pile arrangement and pile spacing. Figure 3.11 shows Mokwa's p-multipliers for leading and trailing rows. Other group efficiency values versus pile spacing for different pile alignments in a pile group can be found in Mokwa (1999).



Notes:

- (1) The term row used in this chart refers to a line of piles oriented perpendicular to the direction of applied load.
- (2) Use the f_m values recommended for the 3rd trailing row for all rows beyond the third trailing row.
- (3) Bending moments and shear forces computed for the corner piles should be adjusted as follows:

<u>side by side spacing</u>	<u>corner pile factor</u>
3D	1.0
2D	1.2
1D	1.6

Fig. 3.11 Design Chart for p-multipliers (after Mokwa 1999).

3.5.2 Pile Cap Resistance

The pile cap in a pile group strongly affects the rotational and lateral capacity of the whole foundation. When a pile cap is subjected to lateral loading, the rotational tendency of the pile cap is restrained by the vertical soil resistance that develops along the pile shafts and at the pile tip. This is schematically shown in Figure 3.12. Mokwa (1999) compared field load test results for a pile group to numerical simulations based on two cases: (1) a fixed-head case (no pile cap rotation) and (2) a free-head case (without any pile cap rotational constraint). Figure 3.13 shows the pile group resistance recorded in the experiment and calculated using these two extreme

numerical cases. It is clear from the figure that the experimental results fit in the middle of the two extreme cases, indicating that the rotational soil resistance due to the pile axial resistance significantly influences the pile group response.

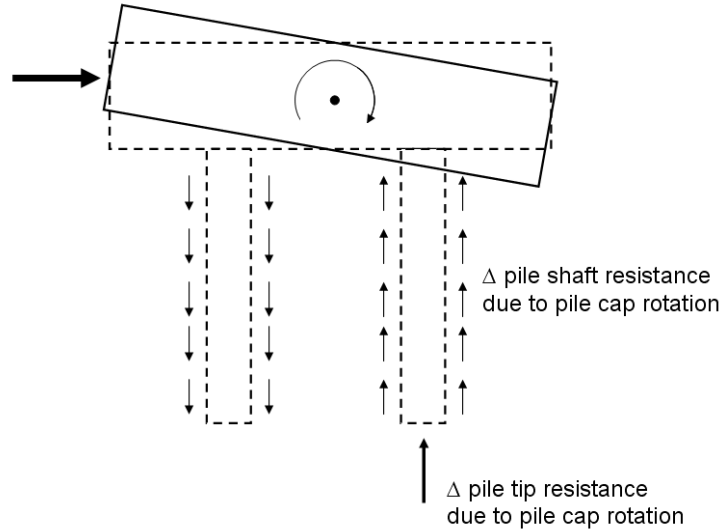
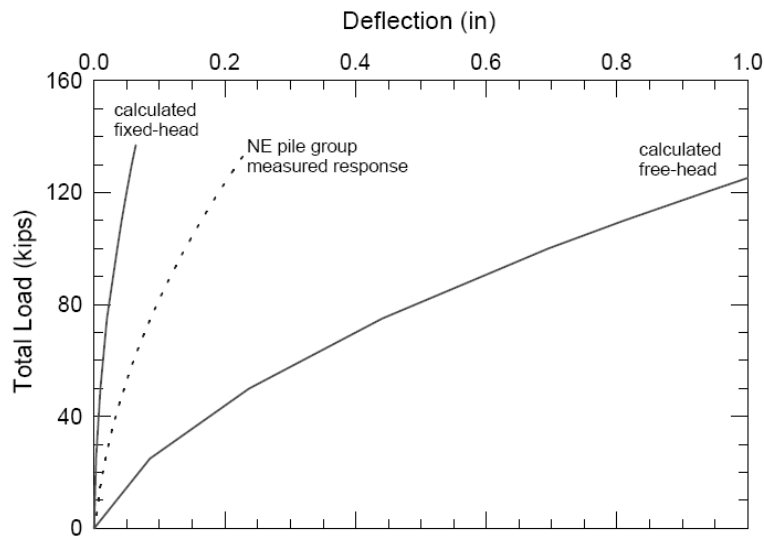


Fig. 3.12 Schematic of rotational soil resistance due to pile cap rotation.



(a) Calculated response for fixed-head and free-head boundary conditions.

Fig. 3.13 Illustration of axial load transfer in a pile (after Vijayvergiya 1997).

Pile caps can also mobilize considerable lateral soil resistance themselves when they are subjected to lateral loading. The lateral resistance of the soil against the pile cap movement depends on the passive earth pressure at the front face of the cap, the sliding resistance on the sides and base, and the active pressure on the back face of the cap. Mokwa (1999) found that the sliding resistance and active forces are negligible, since the values are small compared to the passive resistance and they tend to offset each other.

To calculate the passive earth pressure resistance, several passive earth pressure theories, such as the log spiral, Rankine, and Coulomb theories can be used. Using Rankine's theory, the passive earth pressure at the cap face can be determined by

$$E_p = \frac{1}{2} \gamma H^2 K_p + 2cH \sqrt{K_p} + qHK_p \quad (3.9)$$

where $K_p = \tan^2(45 + \phi/2)$, ϕ = friction angle of soil, c = cohesion of soil, q = surcharge pressure, γ = unit weight of soil, and H = height of pile cap.

For large soil-wall friction angles (ϕ), the log spiral theory gives more accurate results than Rankine's or Coulomb's earth pressure theories. This is due to the fact that: (1) Rankine's theory does not consider wall friction; resulting in underestimated passive earth pressures, especially at high ϕ 's, and (2) K_p values from Coulomb's theory are unconservative and can be very inaccurate when the wall friction angle is greater than about 0.4ϕ (Mokwa 1999). To account for large values of wall friction angle (ϕ), Mokwa (1999) developed a procedure based on the log spiral theory. In his procedure, the soil weight over a log spiral failure surface and the log spiral center location are determined using an iterative technique. With these values the earth pressure forces ($P_{p\phi}$, P_{pc} , and P_{pq}) are calculated to determine the earth pressure coefficients shown in Equation (3.10).

$$E_p = \frac{1}{2} \gamma H^2 K_{p\phi} + 2cH \sqrt{K_{pc}} + qHK_{pq} \quad (3.10)$$

where $K_{p\phi} = \frac{2P_{p\phi}}{\gamma H^2}$, $K_{pc} = \frac{P_{pc}}{2cH}$, and $K_{pq} = \frac{P_{pq}}{qH}$

The resulting passive earth pressure force is determined for a unit length of soil in two dimensions. In a real pile cap, or bulkhead, the passive region is wider than in a two-dimensional model. Therefore, larger passive earth pressures are mobilized. The zone of mobilized soil

resistance depends on the friction angle of the soil and on depth. To include the three-dimensional pile cap effect, Mokwa (1999) performed field load tests on bulkheads and measured the pure pile cap lateral resistance without the lateral resistance of the piles. Mokwa found that using log spiral theory, together with Oveson's (Ovesen 1964) three-dimensional shape factors, accurate results were obtained for both $c-\phi$ natural soils and cohesionless crusher run backfill. Ovesen (1964) introduced a 3-D modifying factor (R) expressed by

$$R = 1 + (K_p - K_a)^{2/3} \left[1.1E^4 + \frac{1.6B}{1 + 5\frac{b}{H}} + \frac{0.4(K_p - K_a)E^3B^2}{1 + 0.05\frac{b}{H}} \right] \quad (3.11)$$

where $B = 1$ for a single pile cap or anchor block, $E = 1 - \frac{H}{z+H}$, and z is embedment depth from the ground surface to the top of the pile cap.

For cohesionless soil, the ultimate earth pressure force, accounting for the 3-D effect, can be expressed by

$$P_{ult.cap} = RE_p b = R(P_{p\phi} + P_{pc} + P_{pq}) b \quad (3.12)$$

where R is Ovesen's 3-D modifying factor calculated from Equation (3.11), E_p is the 2-D passive earth pressure obtained using Equation (3.10), and b is pile cap width.

For cohesive soils ($\phi = 0$), Mokwa (1999) suggested the so-called $\phi=0$ sliding wedge method to calculate passive earth pressure. The method follows Reese's sliding surface wedge approach for a laterally loaded pile and is based on full-scale test results. Equation (3.13) shows a semi-empirical equation for the ultimate passive earth pressure for cohesive soils

$$P_{ult.cap} = \frac{cbH}{2} \left(4 + \frac{\gamma H}{c} + \frac{0.25H}{b} + 2\alpha \right) \quad (3.13)$$

where α is a factor that accounts for adhesion between the cohesive soil and the wall. Table 3.5 shows typical values for α . Since the three-dimensional and shape effects are implicitly included in the experimental tests, no additional modification factors are needed.

Table 3.5 Typical values of soil adhesion factor, α (after NAVFAC 1982).

interface soil	soil cohesion, c (psf)	adhesion factor, α
Very soft cohesive soil	0 to 250	1.0
Soft cohesive soil	250 to 500	1.0
Medium stiff cohesive soil	50 to 1000	1.0 to 0.75
Stiff cohesive soil	1000 to 2000	0.75 to 0.5
Very stiff cohesive soil	2000 to 4000	0.5 to 0.3

3.5.3 Response of Pile Groups Subjected to Earthquake Loading

The dynamic response of pile groups is complicated by the presence of the pile cap. When the soil is liquefied, the soil-pile-structure interaction becomes even more complicated.

Curras et al. (2001) performed centrifuge tests on a superstructure supported by a pile group founded in an upper clay layer underlain by dense sand. Using p-y, t-z, and q-z interface springs and conventional group efficiency factors for pile groups, good predictions were obtained. In their study, it was observed that higher nonlinear response due to soil-pile group interaction caused the translational and rotational stiffness to decrease and led to longer first modal periods.

Several researchers have performed centrifuge tests (Abdoun et al. 2003; Brandenberg et al. 2005), large shaking table tests (Suzuki et al. 2006; He et al. 2006), and full-scale field blasting tests (Juirnarongrit and Ashford 2004; Kawamata et al. 2006) to investigate pile group response due to lateral spreading.

From centrifuge tests on two pile groups (2.5D and 4D pile spacing) subjected to lateral spreading, Abdoun et al. (2003) found that the soil between cast-in-place 4D spacing piles was liquefied, but the soil between driven 2.5D spacing piles was not fully liquefied ($r_u = 0.8$). They also observed that the front and rear piles had similar maximum bending moments. The maximum bending moment values were much smaller than those measured in single piles due to the frame effect associated with axial forces of individual piles.

Kawamata et al. (2006) performed numerical analysis on pile groups subjected to lateral spreading induced by blasting using simplified 1-D and 2-D pile models. The 1-D pile model consisted of a single pile with an equivalent stiffness and p-y springs. The 2-D pile models

represented a pile group with two rows of equivalent piles. Using the 2-D simplified model, the rotational resistance of the pile group was included. In their analysis, conventional p-y springs with p-multipliers were used. The recorded ground deformation was applied to the p-y springs and it was assumed that the p-y springs in liquefiable layer had no stiffness. The 2-D simulations were in good agreement with the experimental results.

3.6 AXIALLY LOADED SINGLE PILE

The behavior of an axially loaded pile relies on the skin resistance of the pile (Q_s) and the pile tip (point) resistance (Q_p). The total axial resistance of a pile (Q_t) is simply expressed by

$$Q_t = Q_s + Q_p \quad (3.14)$$

The axial load-transfer mechanism is complicated due to several reasons: (1) the maximum values of Q_s and Q_p do not occur simultaneously; (2) the induced elastic displacements at different depths along the pile vary and the skin resistance versus displacement relationship is nonlinear; and (3) the pile tip resistance affects the overall distribution of skin resistance. Figure 3.14 illustrates a typical load transfer mechanism in a single pile.

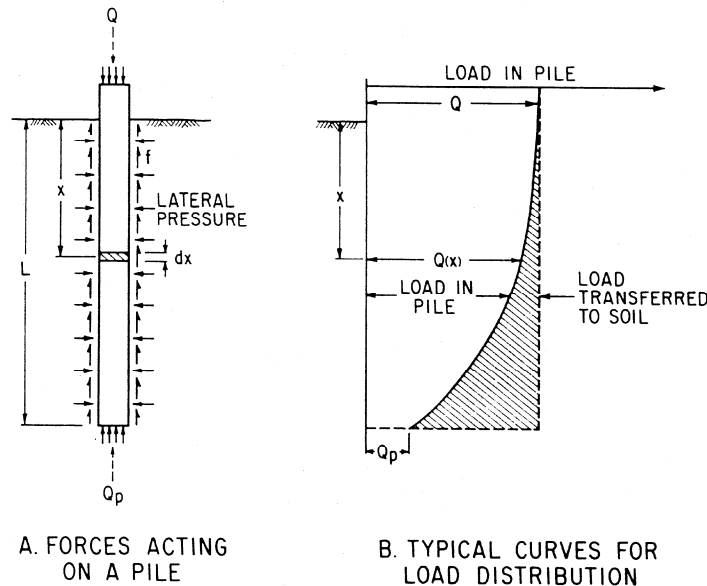


Fig. 3.14 Illustration of axial load transfer mechanism in a pile (after Vijayvergiya 1997).

The nature of the load transfer mechanism is different depending on soil type. In clays, the total resistance of the pile generally reaches a maximum value after some pile movement and then drops gradually to a residual value. In contrast, in sands the total resistance continues to increase at a decreased rate or tends to reach a maximum value. This typical behavior between mobilized total resistance and movement of pile top is shown in Figure 3.15. As shown in the figure, the frictional resistance in clays increases rapidly and reaches a maximum value at a small displacement and then decreases gradually and reaches a residual value. However, the point resistance in clays continues to increase and reach a maximum value, commonly obtained from end bearing capacity theory at a relatively larger displacement. The displacement at which the maximum resistance is obtained is referred to as the critical displacement (or movement). On the other hand, the frictional resistance in sands remains almost constant after reaching a peak value. The point resistance for sands continues to increase gradually.

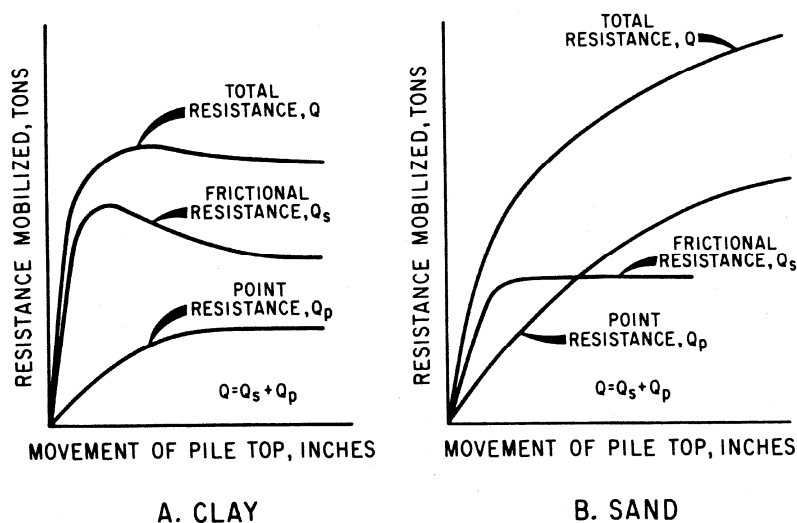


Fig. 3.15 Typical load-movement characteristics of an axially loaded pile (after Vijayvergiya 1997).

In practice, the skin resistance and the point resistance are modeled by t - z curves and q - z curves which are similar to the p - y curves used for lateral soil resistance. Many authors—for example, Coyle and Sulaiman (1967), Vijayvergiya (1997), Parker and Reese (1969), Mosher (1984), and O'Neill and Reese (1999) have investigated field and lab tests and suggested methods or formulas to develop these curves.

3.6.1 Ultimate Skin Resistance (t_{ult}) and Ultimate Point Resistance (q_{ult}) for Sands

Vijayvergiya (1997) proposed a relationship for skin and point resistance for driven piles based on his review of the literature and his experience. The mobilized unit friction resistance for any movement of a pile is expressed in Equation (3.15). The relationship can be used for clays and sands.

$$f = f_{max} \left(2 \sqrt{\frac{z}{z_c}} - \frac{z}{z_c} \right) \quad (3.15)$$

where f = unit friction mobilized along a pile segment at a displacement (z), f_{max} = maximum unit friction, and z_c = critical displacement corresponding to q_{max} . The value of f_{max} is obtained using Equation (3.16).

$$f_{max} = K \sigma_v \tan \delta \quad (3.16)$$

where K = coefficient of lateral earth pressure, σ_v = effective vertical stress, and δ = angle of friction between soil and pile surface. The value of δ is usually approximated by $\delta = \phi - 5$ in degrees. The value of K for medium dense to dense sand ranges from 0.8 for tension to 1.25 for compression, but the value of K for loose sand may be lower and close to K_a , the coefficient of active lateral earth pressure. Table 3.6 gives API (1993)'s recommendations for the value of δ and limiting values for f_{max} . The value of z_c , where f_{max} is mobilized, ranges from 0.2 to 0.3 in. in both clays and sands. Equation (3.16) is plotted in Figure 3.16.

Table 3.6 Recommended parameters for cohesionless siliceous soil (after API 1993).

soil type	δ (degree)	f_{max} (kPa)	N_q in Eq. Error! Reference source not found.	q_{max} (kPa)
Clean Sand	30	95.8	40	9580
Silty Sand	25	81.4	20	4790
Sandy Silt	20	67.1	12	2870
Silt	15	47.9	8	1920

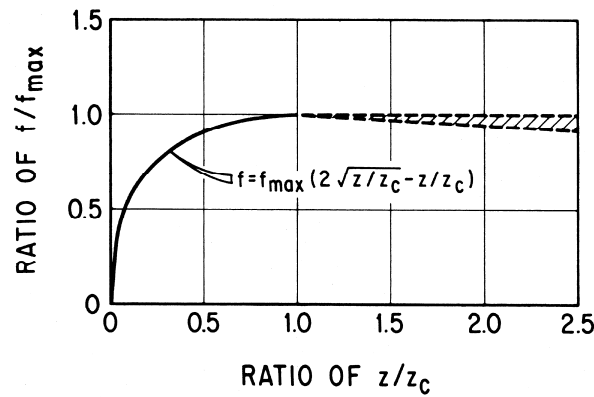


Fig. 3.16 Normalized t-z (or f-z) curve for clay and sand (after Vijayvergiya 1997).

The mobilized tip resistance for any tip movement, z , can be obtained using the following empirical relationship.

$$q = \sqrt[3]{\frac{z}{z_c}} q_{max} \quad (3.17)$$

where q = tip resistance mobilized at any value of $z < z_c$, q_{max} = maximum tip resistance, and z_c = critical displacement corresponding to q_{max} . The value of q_{max} is determined using Equation (3.18).

$$q_{max} = N_q \sigma_v \quad (3.18)$$

where N_q = bearing capacity factor, and σ_v = effective vertical stress at the base of the pile. The value of N_q depends on the angle of internal friction of the granular soil. API recommendations of N_q for driven piles in medium dense to dense sand is given in Table 3.6. Vesic (1970) and Kerisel (1964) suggested that the value of q_{max} increases linearly to a limited depth. Beyond certain depths, the values should be limited. Limiting values are also given in Table 3.6. The critical displacement z_c is defined as a vertical displacement at which the maximum unit point bearing resistance of the pile tip q_{max} is mobilized. The value of z_c is approximated to be 0.03D to 0.09D for clays and sands (or 0.04 D for clay to 0.06 D for sand); where D represents pile diameter. A normalized q-z curve is illustrated in Figure 3.17.

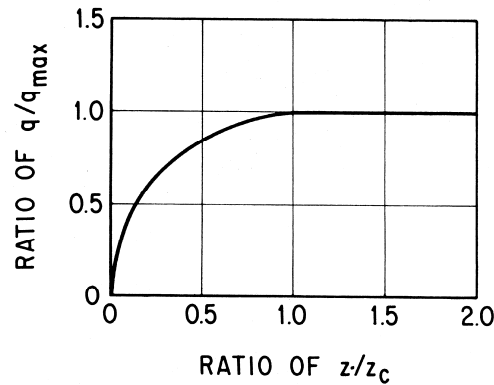


Fig. 3.17 Normalized q-z curve for sand and clay (after Vijayvergiya 1997).

Mosher (1984) proposed another method to evaluate skin resistance and point resistance. In his method, the skin resistance f is computed using Equation (3.19) using f_{max} obtained from Castello (1980)'s charts. The tip resistance is calculated using Equation (3.20) which takes into consideration density and assumes that q_{max} occurs at 0.25 in.

$$f = \frac{z}{\frac{1}{E_f} + \frac{1}{f_{max}}(z)} \quad (3.19)$$

$$q = \left(\frac{z}{z_c} \right)^m q_{max} \quad (3.20)$$

Here, the value of m is $1/2$ for loose sand, $1/3$ for medium sand, and $1/4$ for medium dense sand. The value of q_{max} is determined from Castello (1980)'s curves. O'Neill and Reese (1999) provided methods for computing the nominal axial resistance for drilled shafts considering various soil types, drainage conditions, and loading directions.

3.7 SPSI AND STRUCTURAL STIFFNESS

The interaction between piles and the surrounding soil also affects the overall stiffness of a soil-structure system. As such, it can affect the dynamic response of that system. This section describes SPSI effects on the superstructure response.

3.7.1 SPSI Effect on Structural Response

In an ideal case where a structural column base is fixed, which could occur when the column is socketed into hardrock, the column stiffness can be calculated using well-known equations, as shown in Figure 3.18. However, for the column case of bridges founded on soils, the column base conditions are not fixed. During an earthquake, the base of a structure supported by a pile or pile group system undergoes translational and rotational movements. The actual stiffness of the columns vary due to changes in structural boundary conditions. The local soil deformation around the pile near the ground surface and the rocking behavior causes energy dissipation and stiffness decrease resulting in longer structural natural periods. The frame effect in a pile group provides rotational resistance.

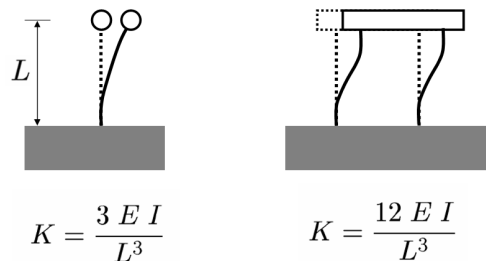


Fig. 3.18 Lateral stiffness of column with and without rotational restraint at top.

Since SPSI increases the fundamental period of the structure, the prevailing structural view is that this effect is beneficial (i.e., longer periods frequently exceed the critical period in a design spectrum). However, this beneficial effect is true only when the response spectrum of an

earthquake motion is consistent with the design spectrum. When the input motion has large components at frequencies contents that correspond to the SPSI-associated natural periods, and out of the design spectrum critical period, the structure may undergo severe damage. These effects have been observed in many case histories (Gazetas and Mylonakis 1998).

3.7.2 Other Factors That Influence Structural Response

As explained above, the structure and pile response is affected by pile section stiffness, and other geometric characteristics, such as, clear height above the ground surface, pile head rotational constraint, pile embedment length, and degree of rocking.

When the clear height above the ground surface is long, the maximum bending moment occurs near the ground surface. In a structure whose supporting columns have different clear heights, the short column tends to show relatively larger lateral demand due to its larger stiffness.

Pile embedment is another influencing factor. When the pile embedment is long enough and the induced deformations and bending moments are confined to the upper part of the pile, the piles are regarded as “flexible,” since the overall length of the pile does not significantly affect the response of the pile, (Randolph 1981). Using elastic beam theory and considering elastic springs with uniform or linearly increasing modulus to represent the soil, a critical length (R_c and R_s) beyond which the pile length no longer significantly affects the response under lateral loading is calculated by

$$l_c \approx 4 \cdot \sqrt[4]{EI/k_h} \quad (3.21)$$

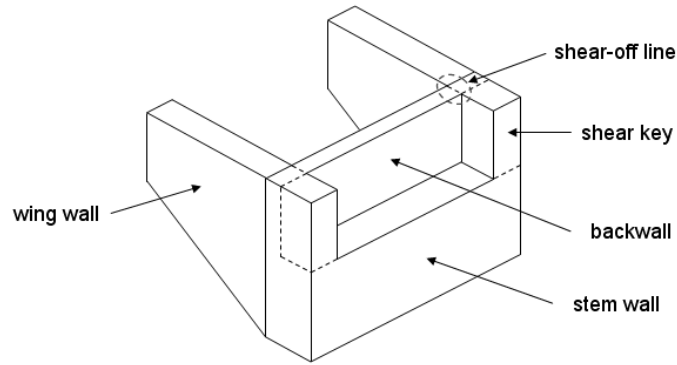
where E and I are the Young’s modulus and the pile cross section moment of inertia, respectively, and k_h is the constant horizontal subgrade reaction modulus of the soil and n_h is the rate of increase of horizontal subgrade reaction modulus.

3.8 SOIL-ABUTMENT-BRIDGE INTERACTION

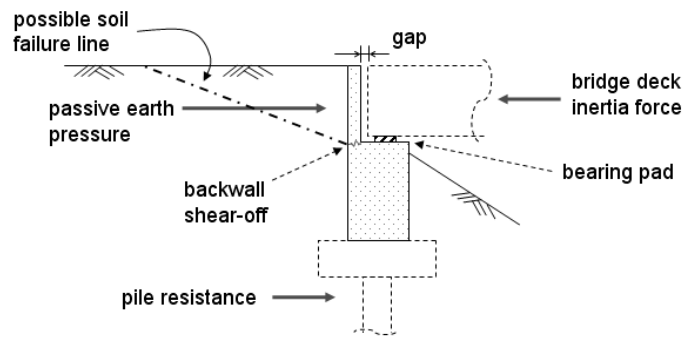
Bridge abutments can significantly affect the response of a bridge deck by providing longitudinal and transverse resistance and impeding lateral bridge displacements. In this review, the transverse abutment response is not considered. The longitudinal abutment response depends on abutment type, and backfill soil characteristics, and abutment foundation. Typical bridge

abutment types include diaphragm abutments, seat abutments, and cast-in-drilled-hole (CIDH) shaft-controlled abutments. To be consistent with current abutment design practice (Caltrans 2004) at the California Department of Transportation (Caltrans), this review focuses only on seat abutments.

Figure 3.19 shows a schematic drawing of a seat-type abutment and bridge deck–abutment–soil interaction. Seat-type abutments consist of a backwall on a stem wall and wing walls. The structure can be supported by pile foundations or shallow foundations. The bridge deck is seated on bearing pads on top of the stem wall and is separated horizontally from the backwall to provide an initial gap. The bridge deck inertial force is then transmitted through the bearing pad friction to the stem wall until the bridge deck reaches the backwall. To protect the piles from highly nonlinear response or severe damage, the backwall and shear keys are often designed to shear off in such a way it is easy to retrofit them after an earthquake. When the deck inertial force increases and the deck comes into contact with the backwall, the lateral resistance derives from the soil resistance on the backwall plus the stem wall and pile. Once the backwall is sheared off, the lateral resistance mainly comes from the mobilized passive earth pressure in the embankment backfill above the level of the backwall failure.



(a) seat abutment structure components



(b) bridge deck-abutment-soil

Fig. 3.19 Schematic of seat-type abutment structural components and bridge deck-abutment-soil interaction.

This mechanism is quite complicated and difficult to simulate. Therefore, the abutment reaction is often simplified as a 1-D load-displacement spring that captures the overall interaction between the bridge deck and abutment system including backfill soil and gap. For the abutment stiffness and capacity, Caltrans uses empirical relationships developed from full-scale abutment tests conducted at UC Davis (Maroney 1995). The initial abutment stiffness, including pile, can be expressed by

$$K_{abut} = k_i w \left(\frac{h_{abut}}{5.5 \text{ ft}} \right) \quad (3.22)$$

where k_i is 20.0 k/in /ft, w is the width of the backwall (ft), and h_{abut} is the height of the backwall in feet. The ultimate abutment capacity due to the backfill soil can be expressed as

$$P_{abut} = A_e \times (5.0 \text{ksf}) \times \left(\frac{h_{abut}}{5.5 \text{ft}} \right) \quad (3.23)$$

where A_e = the effective abutment area in ft^2 . The coefficient (5.0 ksf) is intended to account for the static shear strength of a typical embankment material. Using the initial stiffness and ultimate capacity, a 1-D load-displacement curve can be approximated using a simple curve as shown in Figure 3.20.

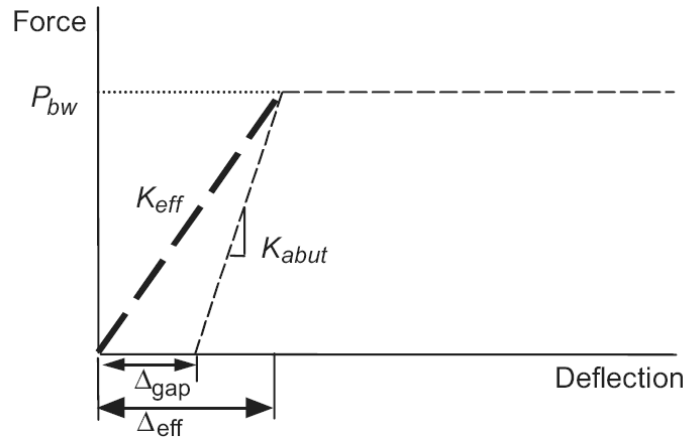


Fig. 3.20 Simplified abutment load-deflection characteristic using initial stiffness and ultimate resistance in Caltrans's guideline (after SDC 2004).

3.9 SUMMARY

This chapter reviewed soil-structure interaction effects in bridge components with a focus on the interface spring characteristics of piles and pile groups in various soil and loading conditions, such as sands, clays, and liquefiable soils subjected to static and dynamic loading. The soil-pile system response subjected to lateral spreading and factors that can influence the dynamic response characteristics of pile-supported structures were reviewed. Finally, the soil-abutment interaction was briefly discussed.

4 Characteristics of Testbed Highway Bridge

4.1 INTRODUCTION

For reliable estimation of bridge performance, especially when subjected to liquefaction and lateral spreading, appropriate modeling of soil-structure interaction and understanding of the global bridge behavior are essential. In practice, soil and foundation systems are often approximated using very simple foundation springs or unrealistic lateral spreading mechanisms that may not represent all important aspects of the global system behavior. In this context, a detailed bridge model in liquefiable soils was developed, putting emphasis on an accurate modeling of both the structural and soil behavior including various SPSI modeling strategies for several bridge system components such as pile, pile cap, and abutment wall structure. This model was used to apply the PEER Performance-Based Earthquake engineering (PBEE) framework described in Chapter 2.

4.2 TESTBED BRIDGE SYSTEM

This study considered a typical Caltrans highway bridge underlain by liquefiable soils susceptible to lateral spreading. The superstructure of the five-span bridge is identical to that of Stojadinović and Mackie (2007) who studied its performance assuming fixed-base conditions. In this project, the bridge is supported on pile foundations that extend through a profile with loose, saturated sandy soils that are susceptible to liquefaction and lateral spreading. A schematic layout of the bridge is shown in Figure 4.1.

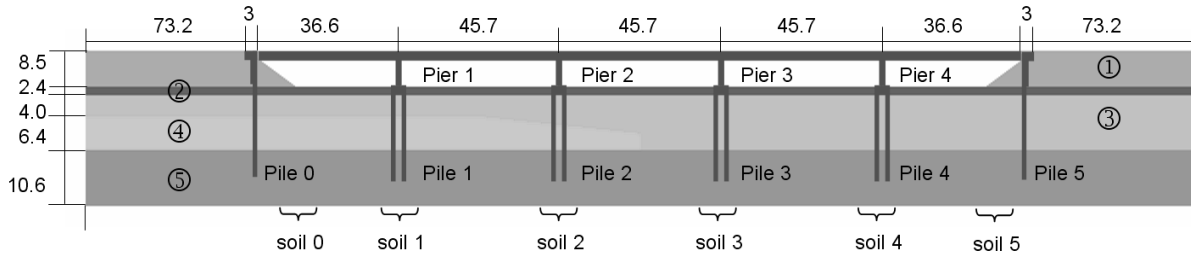


Fig. 4.1 Testbed bridge configuration (dimensions in meters).

4.2.1 Soil Conditions

The soil profile was designed to be representative of a bridge site across a river or estuary. The profile was specified to have somewhat different soil conditions beneath the left and right abutments to enhance the degree of soil-foundation-structure interaction that would take place. The properties of the loose, saturated sands were specified so that liquefaction would be expected to occur but flow sliding would not.

The soil below the left embankment consists of a medium stiff clay crust underlain by a thin, loose to medium dense sand, a layer of stiff clay, and a dense sand layer underlain by rock. The soil beneath the right embankment consists of the same clay crust underlain by a thicker layer of the loose sand, followed by a dense sand layer underlain by rock. The lower clay layer below the left abutment becomes thinner toward the center of the bridge and does not exist below the right embankment. The embankments are 8.53 m (28 ft) in height and have 2:1 slopes. The groundwater table is located at the bottom of the surface clay layer. The properties of the loose and medium sand layers across the bridge were aimed to induce liquefaction under moderate ground shaking so that lateral spreading, especially in the vicinity of the right abutment, triggered broad bridge damage. Soil types and properties are shown in Table 4.1. To define the model soil properties, the soil layers including embankment, sand and clay layers were divided into 49 sublayers as schematically shown in Figure 4.2. In Table 4.2, corrected standard penetration test (SPT) blow counts ($N_{1,60}$) are shown for the sand layer below the left and right embankments together with the corresponding sublayer number. SPT profiles at both locations are illustrated in Figure 4.3. The clay below the embankments were set to have higher strength, due to higher consolidation stresses, than the clay located in the center bridge area. The variation of undrained shear strength of the clay layer is shown in Figure 4.4. These variable soil

conditions along the bridge length contributed to the generation of incoherent motions at each bridge pier.

Table 4.1 Soil types and properties.

Soil layer number	Soil type	Unit weight (kN/m^3)	Strength parameters
1	Dense sand	21.2	$\phi = 45^\circ$
2	Medium stiff clay	17.3	$c = 36 \sim 58$ kPa
3	loose sand	18.0 ~ 20.2	$\phi = 33^\circ \sim 36^\circ$
4	Medium stiff clay	17.3	$c = 40 \sim 58$ kPa
5	Dense sand	21.2	$\phi = 40^\circ$

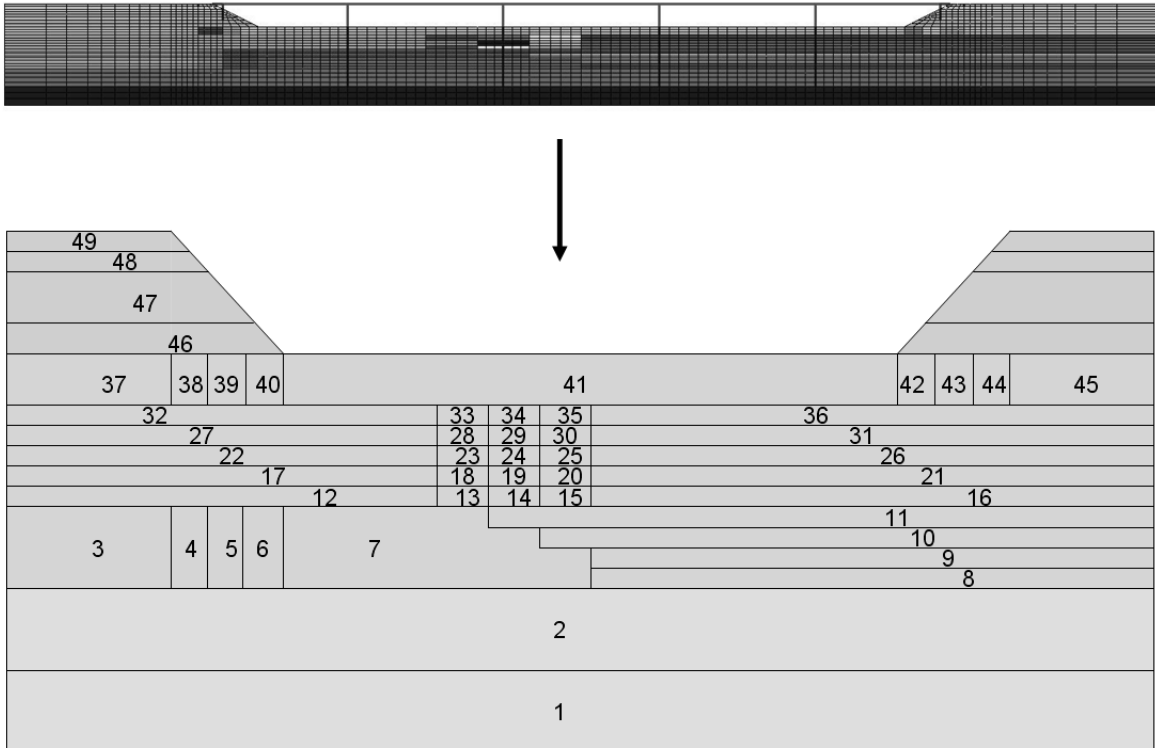


Fig. 4.2 Layer definition and identification.

Table 4.2 SPT profiles below embankments.

below left embankment			below right embankment		
layer number	depth (m)	$N_{1,60}$	layer number	depth (m)	$N_{1,60}$
32	2.83	15	36	2.83	13
27	3.51	19	31	3.51	13
22	4.26	27	26	4.26	16
17	5.04	32	21	5.04	16
12	5.91	22	16	5.91	16
			11	7.08	18
			10	8.40	22
			9	9.75	25
			8	11.25	28

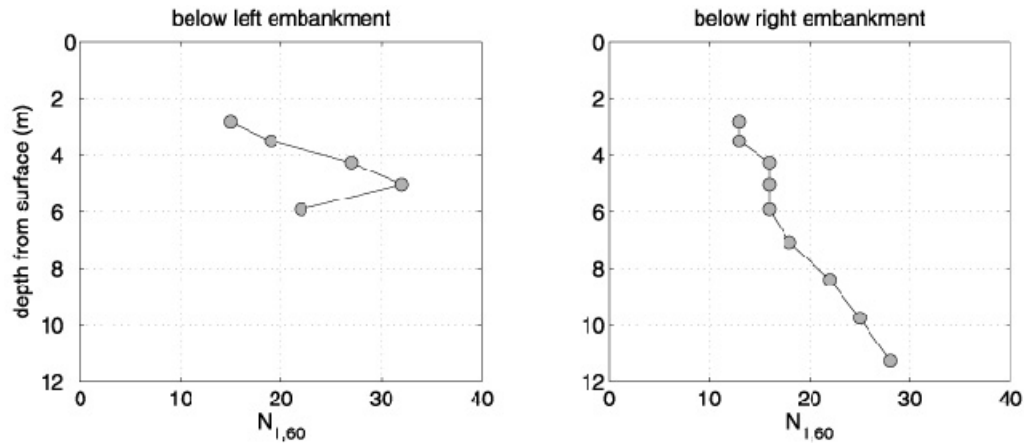


Fig. 4.2 SPT profiles of loose sand layer below both embankments.

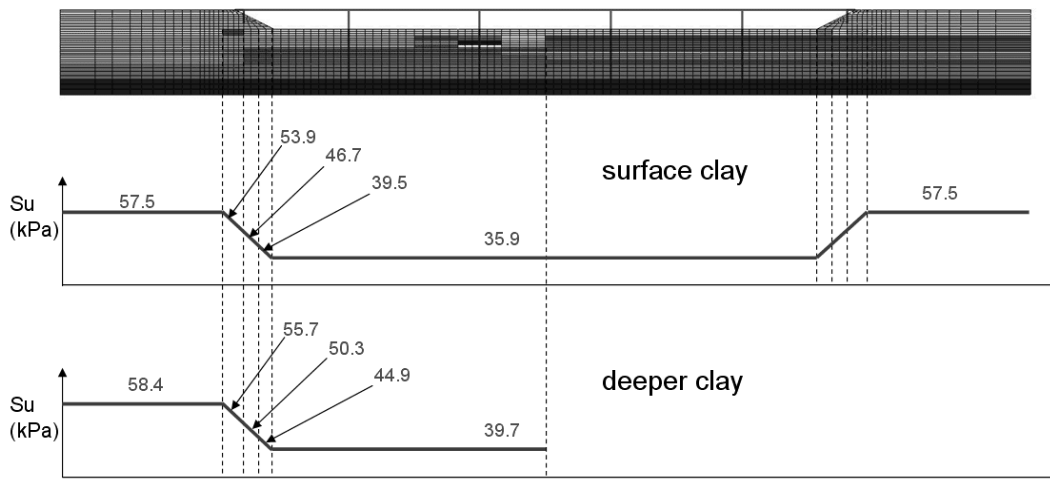


Fig. 4.3 Variation of undrained shear strength of clay layer across bridge.

4.2.2 Bridge and Abutments

The configuration of the target bridge structure and abutments are shown in Figure 4.5. The bridge consists of a five-span reinforced concrete structure with a post-tensioned reinforced concrete box girder deck section and monolithic piers. The three middle spans are 45.7 m (150 ft) long and the two end spans are 36.6 m (120 ft) long. The deck is 1.83 m (6 ft) thick and the four piers are 6.71 m (22 ft) long. The pier columns are 1.2 m (4 ft) in diameter with a 2% longitudinal steel reinforcing ratio. The deck forces are transmitted through elastomeric bearing pads to seat wall abutments, and subsequently to piles and the backfill. The bearing pads were assumed to be 51 cm^2 (8 in^2) and 5 cm (2 in.) thick and to fail in shear before sliding with 15 cm (4 in.) displacement. Expansion joints between the deck and abutment walls were set to 10 cm (4 in.) initial gaps. The backwalls were designed to shear off when subjected to large longitudinal bridge forces based on Caltrans Seismic Design Criteria (SDC) (Caltrans 2004). The details of the bridge structure design are presented by Ketchum et al. (2004), and the OpenSees structure modeling is described in more detail by Mackie and Stojadinović (2003) and Mackie et al. (2004).

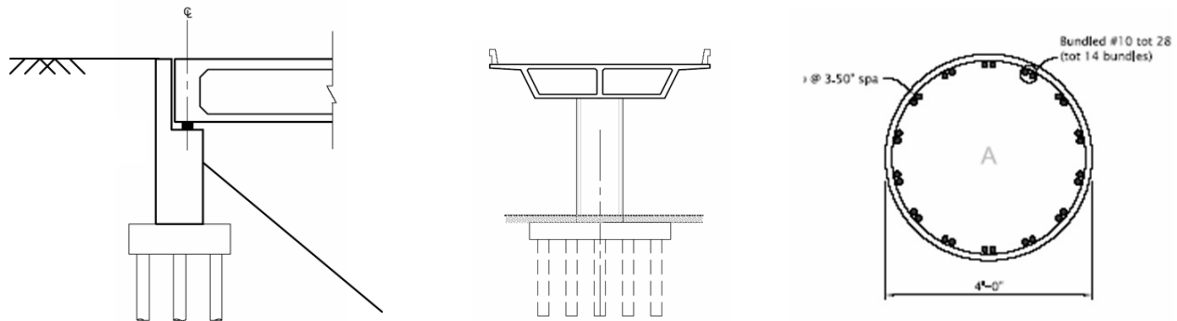


Fig. 4.4 Structure configuration.

4.2.3 Pile Foundations

The bridge piers are supported by pile groups (3 by 2, center-to-center spacing = 1.83 m (6 ft)). The individual piles are open-ended steel pipe piles (diameter = 0.61 m (2 ft), wall thickness = 0.0127 m (0.5 in.), and yield stress = 413,700 kPa (60 ksi)). The same pile type was used for the abutment foundations (6 by 1, center-to-center spacing = 2.44 m (8 ft)). The details of the pile design are presented by Ledezma and Bray (2006a) and Ledezma and Bray (2006b). The bridge

piers and pile groups are labeled from the left abutment to the right as Pier 1, Pier 2, Pier 3, Pier 4, and Pile 1, Pile 2, Pile 3, Pile 4, respectively. The abutment pile groups in the left and right slopes are labeled as Pile 0 and Pile 5. The abutment piles were assumed to be installed to the same depth as the other bridge piles.

4.3 SUMMARY

A testbed bridge and soil profile were selected for use in illustrating application of the PEER PBEE methodology to a realistically complex problem. The bridge structure was designed by a structural consulting firm with extensive experience in the design of highway bridges for the California Department of Transportation. The characteristics of the soil profile were selected to produce liquefaction and lateral spreading beneath the abutments under moderate to strong shaking. The potentially liquefiable soils were thicker under one abutment than the other, and a layer of clay existed beneath one side of the bridge but not the other. The purpose of the variable soil conditions was to induce permanent soil deformations in the vicinities of the abutments under strong shaking so that significant kinematic and inertial interaction was induced in the bridge and its foundations.

5 OpenSees Model of Testbed Highway Bridge

5.1 INTRODUCTION

This chapter describes the numerical model created in OpenSees for the target bridge system. The model of the bridge structure itself, i.e., the above-ground portions of the bridge, was developed by Mackie and Stojadinović (2003) and provided by Kevin Mackie. This model was “connected” to a detailed model of the soils, foundations, and abutments that was developed and validated as part of this research.

5.2 SOIL CONDITIONS

Using the target soil profiles and foundation design described in Chapter 4, the soil-foundation system was modeled in OpenSees. The pressure-dependent multi-yield (PDMY) elasto-plastic material model developed by Yang et al. (2003) was used to model sandy soils. To account for saturated conditions, the PDMY material was coupled with a fluid solid porous material (FSPM) model. This material imposes an incompressibility condition that allows the generation of pore pressures. For the clay, the pressure-independent multi-yield (PIMY) material model was used. To capture these soil conditions in OpenSees, the system of 49 sub-soil layers shown in Figure 4.2 was used. The soil parameters used in this study were based on recommendations provided by Yang and Elgamal (<http://cyclic.ucsd.edu/opensees/>) for typical soil conditions. Relative densities (D_r) for the sandy soils were determined based on the $N_{1,60}$ values selected for the target bridge soil conditions and Equation (5.1).

$$N_{1,60} = 60(D_r)^2 \quad (5.1)$$

Then, using the recommended values, the 16 material parameters required for the PDMY model for each sublayer were obtained by interpolation of relative densities. The interpolation was performed in the 40% to 75% relative density range, where the model parameters show a linear relationship with relative density. Figure 5.1 shows the interpolated parameter values. The PIMY material parameters for clay were interpolated in the same way using the selected undrained shear strength values. The soil parameter values for 49 sublayers of sand and clay are tabulated with layer number in Tables 5.1 and 5.2. A total of 3874 quadrilateral finite elements and 4050 nodes were used to represent the soil domain.

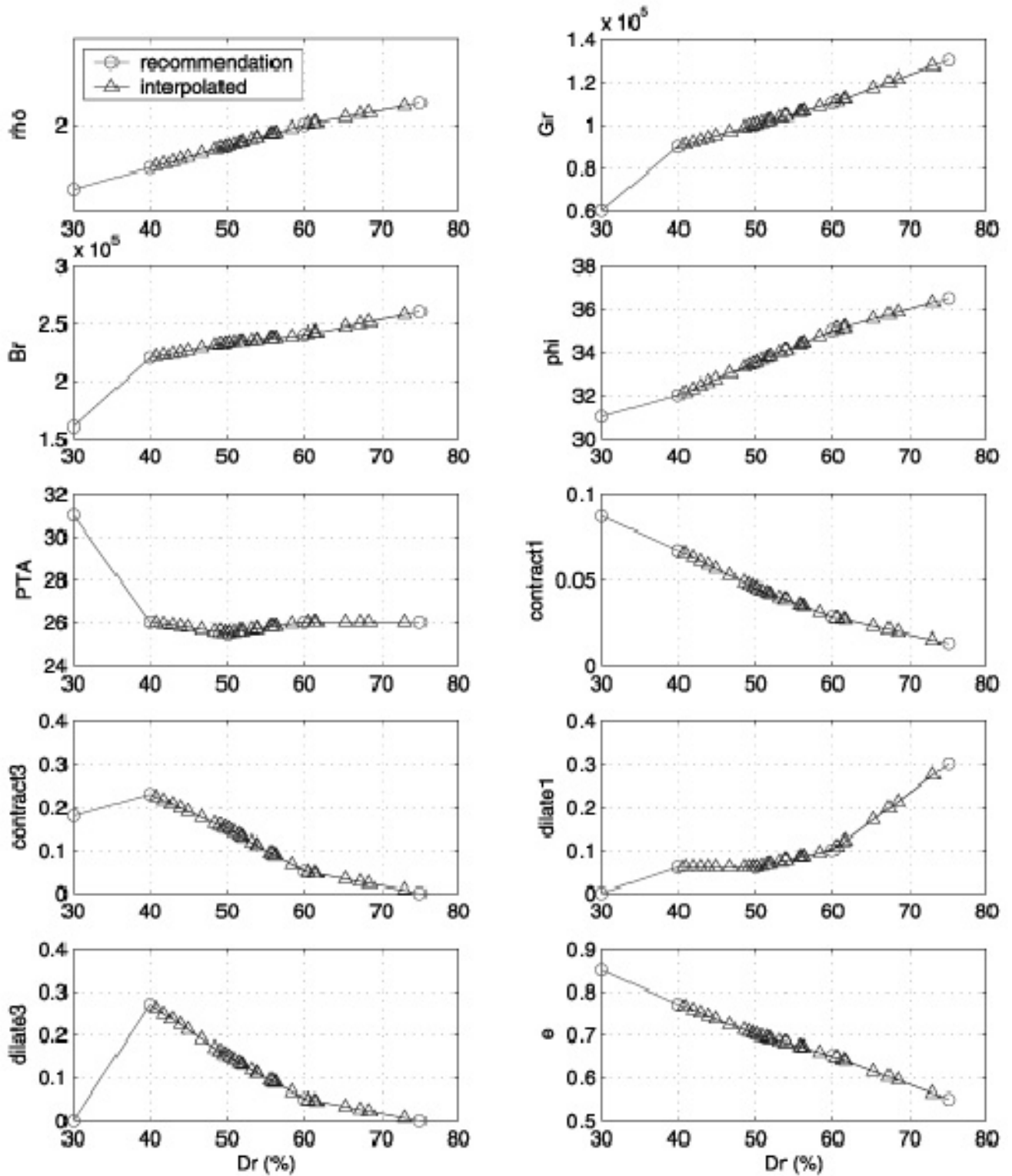


Fig. 5.1 Recommended loose sand material parameters in OpenSees and interpolations.

Table 5.1 Summary of PIMY material parameter values used for cohesive soil.

soil	layer number	Su (kPa)	rho (Mg/m ³)	Gr (kPa)	Br (kPa)
deep clay	3	58.4	1.669	110684	553421
	4	55.7	1.648	104289	521447
	5	50.29	1.605	91476	457381
	6	44.89	1.562	78687	393434
	7	39.7	1.521	66395	331973
surface clay	37	57.5	1.662	108553	542763
	38	53.9	1.633	100026	500131
	39	46.7	1.577	82974	414868
	40	39.5	1.520	65921	329605
	41	35.9	1.488	57279	286394
	42	39.5	1.520	65921	329605
	43	46.7	1.577	82974	414868
	44	53.9	1.633	100026	500131
45	57.5	1.662	108553	542763	

Table 5.2 Summary of PDMY material parameter values used for granular soils.

soil	layer number	$N_{1,60}$	Dr (%)	rho (Mg/m ³)	Gr (kPa)	Br (kPa)	phi (°)	PTA (°)	cnt1	cnt3	dil1	die3	e	
dense sand	1	40.0	99.0	2.292	159760	283040	39.9	26.0	0.002	0.000	0.617	0.000	0.406	
	2	40.0	95.0	2.260	154800	279200	39.3	26.0	0.004	0.000	0.564	0.000	0.430	
loose sand	8	28.0	68.3	2.055	121084	251084	35.8	26.0	0.020	0.022	0.211	0.022	0.595	
	9	25.0	64.5	2.030	116066	246066	35.5	26.0	0.023	0.035	0.161	0.035	0.620	
	10	22.0	60.6	2.004	110737	240737	35.1	26.0	0.027	0.048	0.107	0.048	0.646	
	11	18.0	54.8	1.948	104772	236341	34.2	25.7	0.037	0.102	0.079	0.102	0.676	
	12	22.0	60.6	2.004	110737	240737	35.1	26.0	0.027	0.048	0.107	0.048	0.646	
	13	20.5	58.5	1.985	108452	238917	34.8	25.9	0.031	0.065	0.094	0.065	0.658	
	14	19.0	56.3	1.963	106273	237391	34.4	25.8	0.034	0.087	0.085	0.087	0.669	
	15	17.5	54.0	1.940	104006	235804	34.1	25.7	0.038	0.110	0.076	0.110	0.680	
	16	16.0	51.6	1.916	101640	234148	33.7	25.6	0.042	0.134	0.067	0.134	0.692	
	17	32.0	73.0	2.087	127373	257373	36.3	26.0	0.015	0.007	0.274	0.007	0.563	
	18	28.0	68.3	2.055	121084	251084	35.8	26.0	0.020	0.022	0.211	0.022	0.595	
	19	24.0	63.2	2.022	114327	244327	35.3	26.0	0.025	0.039	0.143	0.039	0.628	
	20	20.0	57.7	1.977	107735	238415	34.7	25.9	0.032	0.073	0.091	0.073	0.661	
	21	16.0	51.6	1.916	101640	234148	33.7	25.6	0.042	0.134	0.067	0.134	0.692	
	22	27.0	67.1	2.047	119443	249443	35.7	26.0	0.021	0.026	0.194	0.026	0.603	
	23	24.0	63.2	2.022	114327	244327	35.3	26.0	0.025	0.039	0.143	0.039	0.628	
	24	21.5	59.9	1.999	109861	239903	35.0	26.0	0.028	0.051	0.099	0.051	0.651	
	25	19.0	56.3	1.963	106273	237391	34.4	25.8	0.034	0.087	0.085	0.087	0.669	
	26	16.0	51.6	1.916	101640	234148	33.7	25.6	0.042	0.134	0.067	0.134	0.692	
	27	19.0	56.3	1.963	106273	237391	34.4	25.8	0.034	0.087	0.085	0.087	0.669	
	28	17.5	54.0	1.940	104006	235804	34.1	25.7	0.038	0.110	0.076	0.110	0.680	
	29	16.0	51.6	1.916	101640	234148	33.7	25.6	0.042	0.134	0.067	0.134	0.692	
	30	14.5	49.2	1.892	99160	231907	33.4	25.5	0.047	0.157	0.060	0.160	0.706	
	31	13.0	46.5	1.865	96547	228512	33.0	25.7	0.053	0.178	0.060	0.191	0.724	
	32	15.0	50.0	1.900	100000	233000	33.5	25.5	0.045	0.150	0.060	0.150	0.700	
	33	14.5	49.2	1.892	99160	231907	33.4	25.5	0.047	0.157	0.060	0.160	0.706	
	34	14.0	48.3	1.883	98305	230796	33.2	25.6	0.049	0.164	0.060	0.170	0.712	
	35	13.5	47.4	1.874	97434	229664	33.1	25.6	0.051	0.171	0.060	0.181	0.718	
	36	13.0	46.5	1.865	96547	228512	33.0	25.7	0.053	0.178	0.060	0.191	0.724	
	embankment	46	40.0	95.0	2.260	154800	279200	39.3	26.0	0.004	0.000	0.564	0.000	0.430
		47	40.0	95.0	2.260	154800	279200	39.3	26.0	0.004	0.000	0.564	0.000	0.430
		48	40.0	95.0	2.260	154800	279200	39.3	26.0	0.004	0.000	0.564	0.000	0.430
		49	40.0	95.0	2.260	154800	279200	39.3	26.0	0.004	0.000	0.564	0.000	0.430

The embankment side soil was extended 73.2 m (240 ft) outward from the slope crest. The outer-most soil column elements were modified to generate a free-field response by increasing their out-of-plane thicknesses and constraining the outer-most soil column element nodes at the same elevation to have the same horizontal movement.

5.3 BRIDGE STRUCTURE

The OpenSees bridge structure model used in this study was originally developed and used for a PBEE investigation of a bridge on very competent (stiff and strong enough that negligible nonlinear soil response was observed) soil by Mackie and Stojadinović (2003). The original model used simple foundation springs at the bottom of the piers and abutment springs at the bridge deck-end to model soil compliance. To couple the bridge structure model with the soil-foundation model developed for this investigation, the simple foundation springs used by Mackie and Stojadinović (2003) were removed and the pier columns were connected to pile groups. The abutment springs were also separated into bearing pad springs and passive earth pressure springs.

5.4 PILE FOUNDATIONS

To model soil-structure interaction, several types of interface springs were used as shown in Figure 5.2. The parameters assigned to these interface elements reflect the complicated ground conditions and foundation types; i.e., different soil conditions and types, ground water conditions, pile group effects, and passive earth pressures in pile caps and abutments.

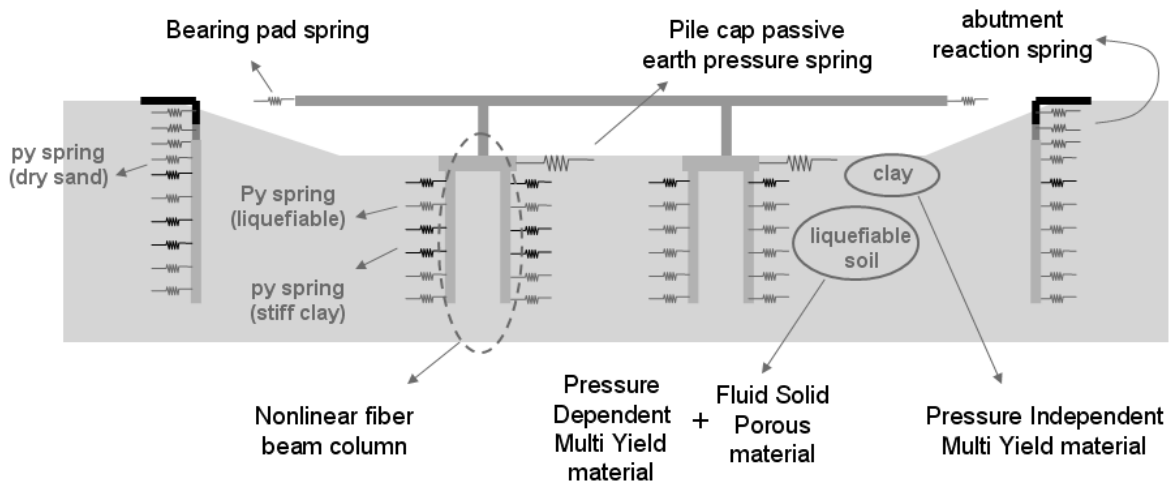


Fig. 5.2 Modeling of soil-structure interaction in OpenSees.

The 3 x 2 pile groups that support the piers were simplified for two-dimensional analysis using an equivalent 1 x 2 pile group model; the three piles in each out-of-plane row were combined to produce an equivalent single pile. In OpenSees, these equivalent piles were generated by patching three individual pile sections without changing the diameter or pile wall thickness. Each pile section was modeled using nonlinear fiber beam elements.

5.4.1 Pile p-y Springs

The p-y springs in the liquefiable soils were modeled using the pyLiq1 model (Boulanger et al. 2004) available in OpenSees. The pyLiq1 material was coupled with adjacent soil elements that provided porewater pressure ratio information; spring resistance forces based on API (1993) criteria were factored by the porewater pressure ratio to approximate the effect of liquefaction on soil-pile-structure interaction. The residual strengths after liquefaction were calculated based on correlations to $N_{1,60}$ as proposed by Kramer (2006) (Eq. 3.8). Figures 5.3 and 5.4 show p-y spring parameter profiles for the six piles across the bridge (i.e., plots of ultimate lateral resistance, residual ultimate resistance ratio of liquefied soil, and y_{50}). These values correspond to individual springs in a single pile before group effects are considered. Residual ultimate lateral resistances ($p_{ult,res}$) for the case in which all soils were fully liquefied were obtained using each soil's residual strength. Ratios of $p_{ult,res}$ to p_{ult} , here referred to as residual ultimate resistance ratio, are shown in Figures 5.3a,b. The y_{50} values shown in Figure 5.4 represent the displacement that corresponds to resistances of 50% of p_{ult} . These values were calculated by solving Equation (5.2) for y using a 50% p_{ult} :

$$p = p_{ult} \tanh\left(\frac{kz}{p_{ult}} y\right) \quad (5.2)$$

where z is depth, and k is a coefficient that can be determined from API (1993) charts based on density (or friction angle) and ground water condition.

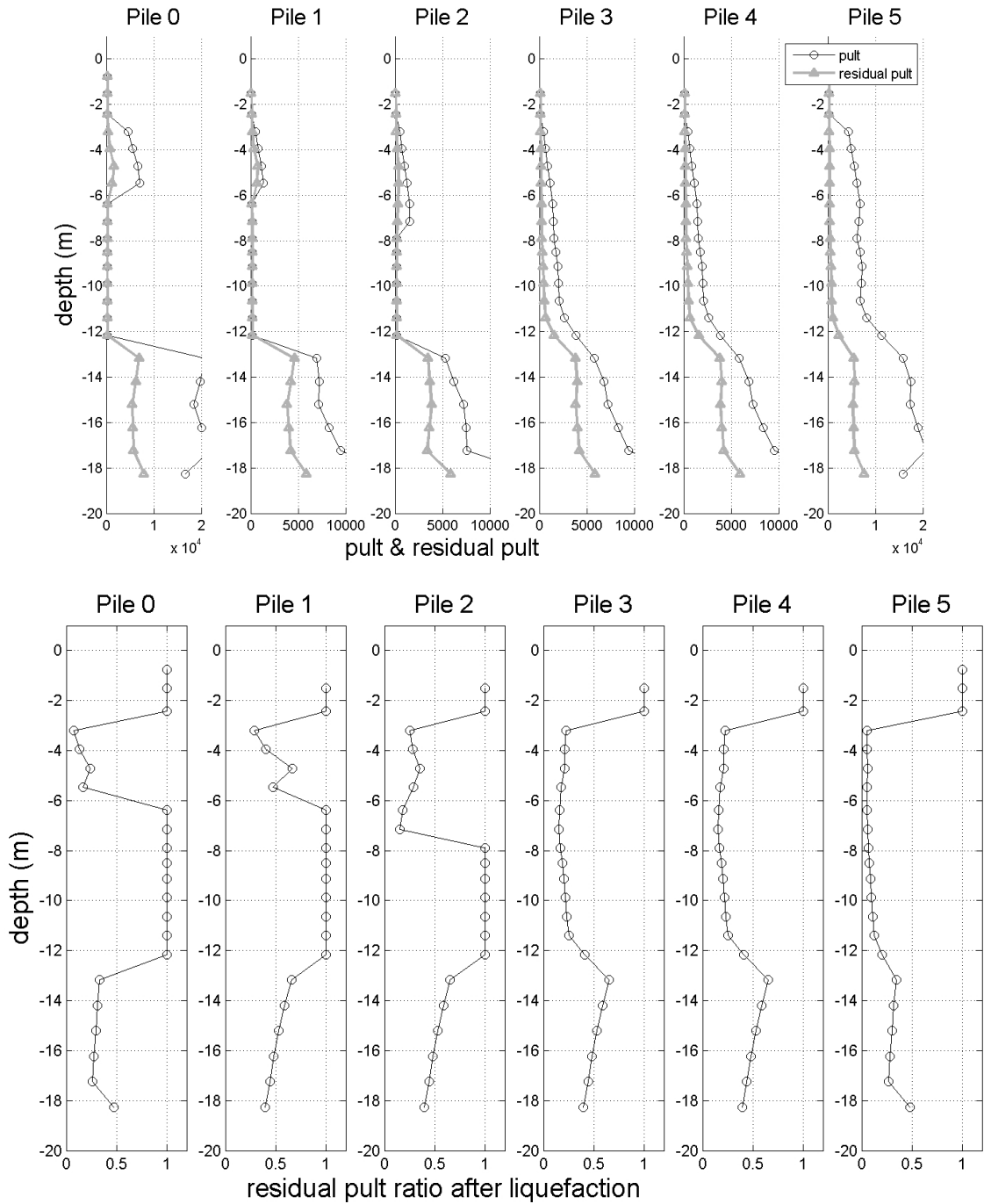


Fig. 5.3 p-y spring parameters: ultimate lateral resistance (p_{ult}).

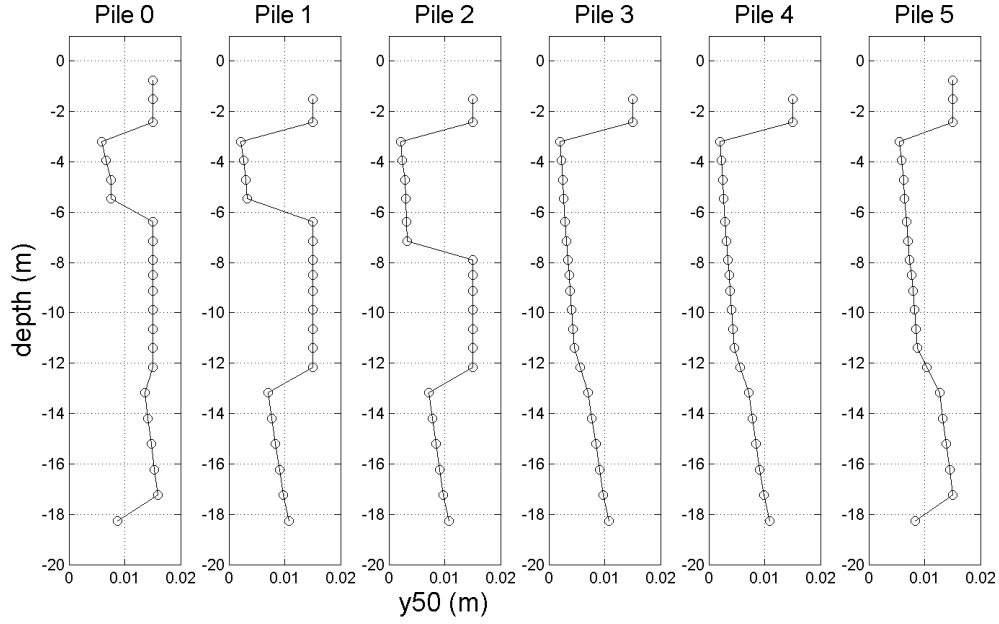


Fig. 5.4 p-y spring parameters: y_{50}

To account for pile group effects, the strength spring parameters were factored using group efficiency factors, G_e , defined as the ratio of the average lateral capacity per pile in a group to the lateral capacity of a single pile. The group efficiency factor can also be expressed using Equation (5.3) as an average for the p-multipliers for each individual pile (i.e., the sum of the p-multipliers for all individual piles divided by pile number)

$$G_r = \sum_{i=1}^N \frac{f_{m_i}}{N} \quad (5.3)$$

where N is the number of piles and f_m is an empirical reduction factor (i.e., p-multiplier) to adjust p-y curves for pile arrangement and pile spacing. To obtain the group efficiency factors for the 3×2 pile groups in the target bridge, the p-multipliers for the leading and trailing piles were determined as 0.82 and 0.76 according to Figure 5.5. For the leading and trailing rows of piles in the out-of-plane direction, the p-multiplier values were set to 1.0, since the group effect can be ignored when the side-by-side pile spacing is greater or equal than $3D$. The resulting group efficiency factor for each pile group was 0.79. The capacity of each pile in the simplified 1×2 pile group was calculated as $3 \times$ group efficiency factor \times the capacity of a single pile. For

the 1×6 pile groups under the abutments, no group effects were considered, since they have a single row of piles and the side-by-side pile spacing (4D) is greater than 3D. The skin resistance and pile tip resistance was modeled using t-z and q-z springs. These springs were assumed to have no group effects.

5.4.2 Pile Cap Passive Earth Pressure Springs

To capture the response of the pile caps, three passive earth pressure springs were used at the top, middle, and bottom of the cap. The clay passive earth pressure envelope of the pile cap was determined using the $\phi = 0$ sliding wedge method (Eq. 3.13) suggested by Mokwa (1999). It was assumed that the bridge longitudinal and transverse pile cap lengths were 3.6 m (12 ft) and 5.4 m (18 ft), respectively, and that the pile cap height was 1.5 m (5 ft). An adhesion factor (α) of 0.75 was used in the method for the medium stiff clay.

5.5 ABUTMENT INTERFACE SPRINGS

The height of the backwall (break-off wall) was 1.8 m (6ft) and its width was 13.7 m (45 ft). The interaction between the bridge deck and abutment was decomposed into two interaction components. A schematic of the bridge deck-abutment interaction and its modeling are shown in Figures 3.18 and 5.15. The first component combined the bearing pad resistance and backwall resistance in a single spring model. This spring force was transferred to the stem wall and abutment pile foundation. The stem wall was connected to the soil without interface assuming its relative displacement was small. The second component included the expansion joint gap and backwall lateral soil resistance. In this case the force-displacement envelope was obtained by combining a gap spring and a soil spring whose parameters were obtained based on Caltrans's Seismic Design Criteria (Caltrans 2004). For the selected abutments, the initial stiffness and ultimate resistance used were 164,300 kN/m/m (20 kips/in/ft) and 6,258kN (1290 kips), respectively.

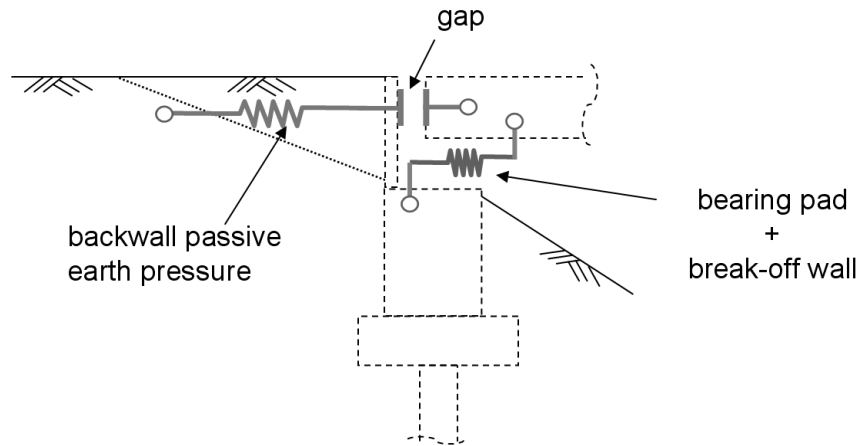


Fig. 5.5 Modeling of bridge deck-abutment–soil interaction in OpenSees.

5.6 SUMMARY

A finite element model of the soil-foundation-bridge system was developed using the computer program, OpenSees. The model used two primary soil constitutive models—one for primarily cohesive soils and the other for primarily frictional soils—calibrated for consistency with the site conditions. The model for the bridge structure was developed and tested by others for fixed-base support conditions. That model was supported on pile groups for the analyses described in this report. The piles were designed according to Caltrans criteria and modeled using nonlinear fiber elements. Pile-soil interaction was modeled using p-y, t-z, and q-z curves. Finally, the abutments were modeled with bearing pads and a breakable backwall to limit thrust forces in the bridge deck.

6 Response of Testbed Highway Bridge

6.1 INTRODUCTION

The OpenSees model described in the previous chapter was used to estimate a variety of engineering demand parameters (*EDPs*) under different levels of seismic loading. The main purpose of these analyses was to evaluate the *EDP-IM* relationship, i.e., to characterize the distribution of *EDP|IM*. This chapter describes the results of a series of validation exercises using two specific ground motions.

6.2 MODEL VALIDATION ANALYSES

Before using the PEER PBEE methodology, it was considered important to examine the global and local response of the bridge model under typical earthquake excitations to validate the general and specific aspects of its performance. This section presents details of the global and local seismic bridge response characteristics for a moderate intensity motion (Northridge 1994 at Century City LACC North, CMG Station 24389, $a_{\max} = 0.25$ g) and a stronger motion (Erzincan, Turkey, 1992, $a_{\max} = 0.70$ g). In this study, the soil lateral spreading response and its effect on the global bridge behavior was first investigated. Then, the local response of the bridge structure, abutment, piles, and interface springs was addressed.

6.2.1 Soil Response

The global bridge response was complicated by the interaction between the bridge system components, i.e., bridge, free-field, and sloping soil, and abutment structure. Lateral spreading can induce significant demands on the bridge and pile structures in addition to those observed by

Mackie and Stojadinović (2007) in their analyses. In addition, the presence of clay layers can complicate the soil displacement profile due to the possibility of shearing at the clay-sand layer boundaries. Figures 6.1(a) and 6.2(a) present permanent displacement patterns of the bridge system for the Northridge and Erzincan motions. These figures show that larger lateral deformation occurred in the vicinity of the right abutment than the left abutment, as was expected due to the greater thickness of liquefiable soils in that area. The deformed meshes show that the shearing deformations beneath the left abutment, induced by the stronger motion (Erzincan, Turkey, 1992, $a_{\max} = 0.70$ g), occurred at a greater depth than that produced by the moderate motion (Northridge 1994, $a_{\max} = 0.25$ g). This observation is more clearly illustrated in Figures 6.3 and 6.4 where the time variation of the estimated horizontal shear strain distributions with depth below the left and right abutments is presented for both motions. For the moderate shaking event, the large shear strains below the left embankment were concentrated at the top of the loose sand layer due to liquefaction of the sand layer. For the strong shaking, large shear strains below the left abutment developed at and just above the interface between the clay layer and dense sand layer. Below the right abutment, shear strains were distributed more evenly over the thickness of the loose sand layer for both motions.

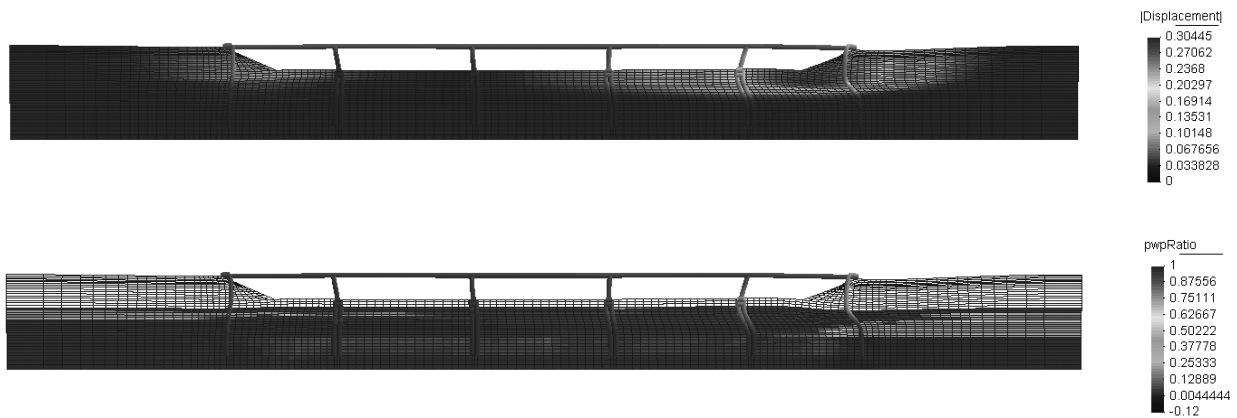


Fig. 6.1 Horizontal and vertical displacements of bridge and pore pressure ratio in soil following earthquake—Northridge motion. Displacements magnified by factor of 20.

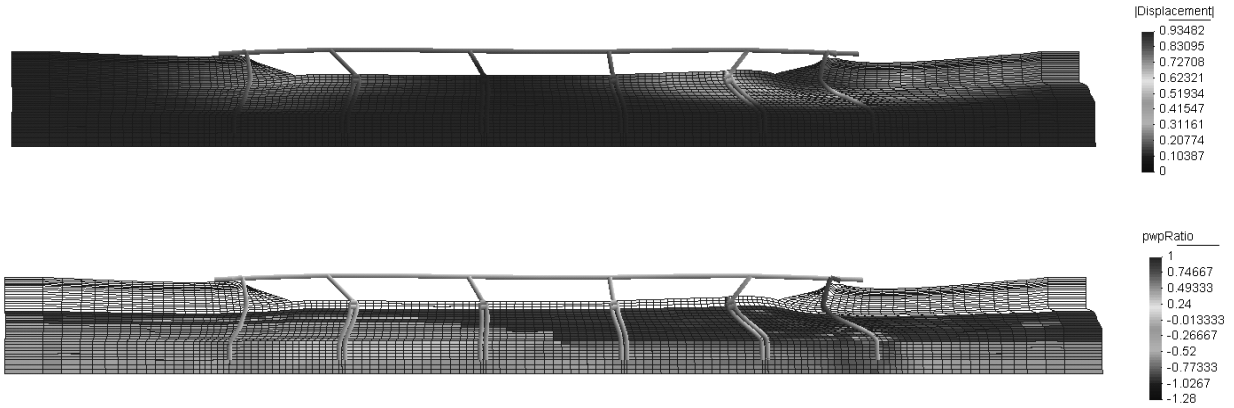


Fig. 6.2 Horizontal and vertical displacements of bridge and pore pressure ratio in soil following earthquake—Erzincan motion. Displacements magnified by factor of 20.

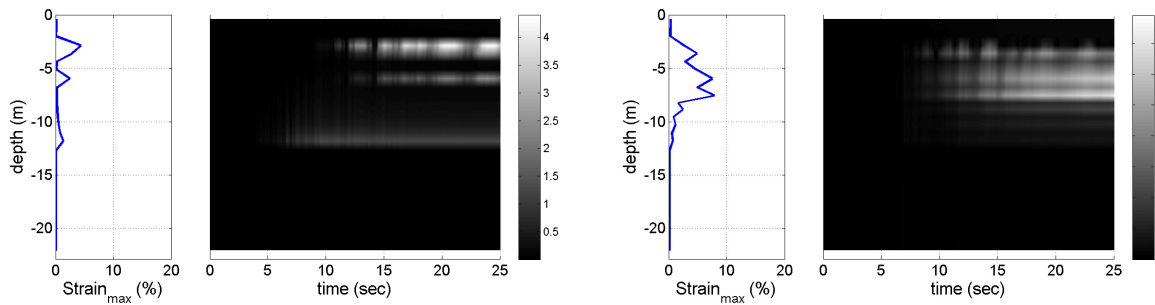


Fig. 6.3 Variation of shear strain with time and depth: (a) below left abutment, and (b) below right abutment—Northridge motion

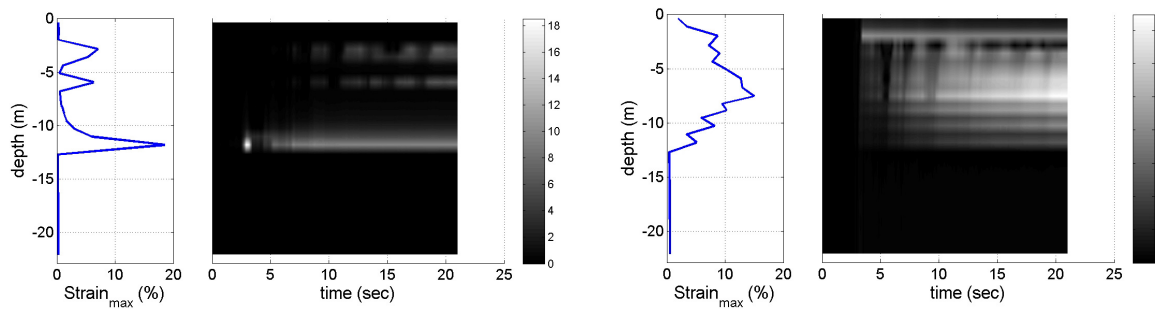


Fig. 6.4 Variation of shear strain with time and depth: (a) below left abutment, and (b) below right abutment—Erzincan motion.

To show the degree of liquefaction in the soil beneath the right abutment, pore pressure ratios measured at several soil locations are shown in Figure 6.5(a). The pore pressure ratio time histories in the loose sand below the right abutment are shown in Figure 6.5(b) for the moderate shaking level. The figure shows that the upper layer of the loose sand was fully liquefied across the right side of the bridge. However, the bottom layer of the loose sand below the embankment had pore pressure ratios less than 1.0; the soil at this location was slightly denser and had higher initial effective stress than the soils that were not beneath the embankment. Figure 6.6 shows the time variation of pore pressure ratio with depth below the right abutment for the Northridge motion illustrating different degrees of pore pressure generation with time.

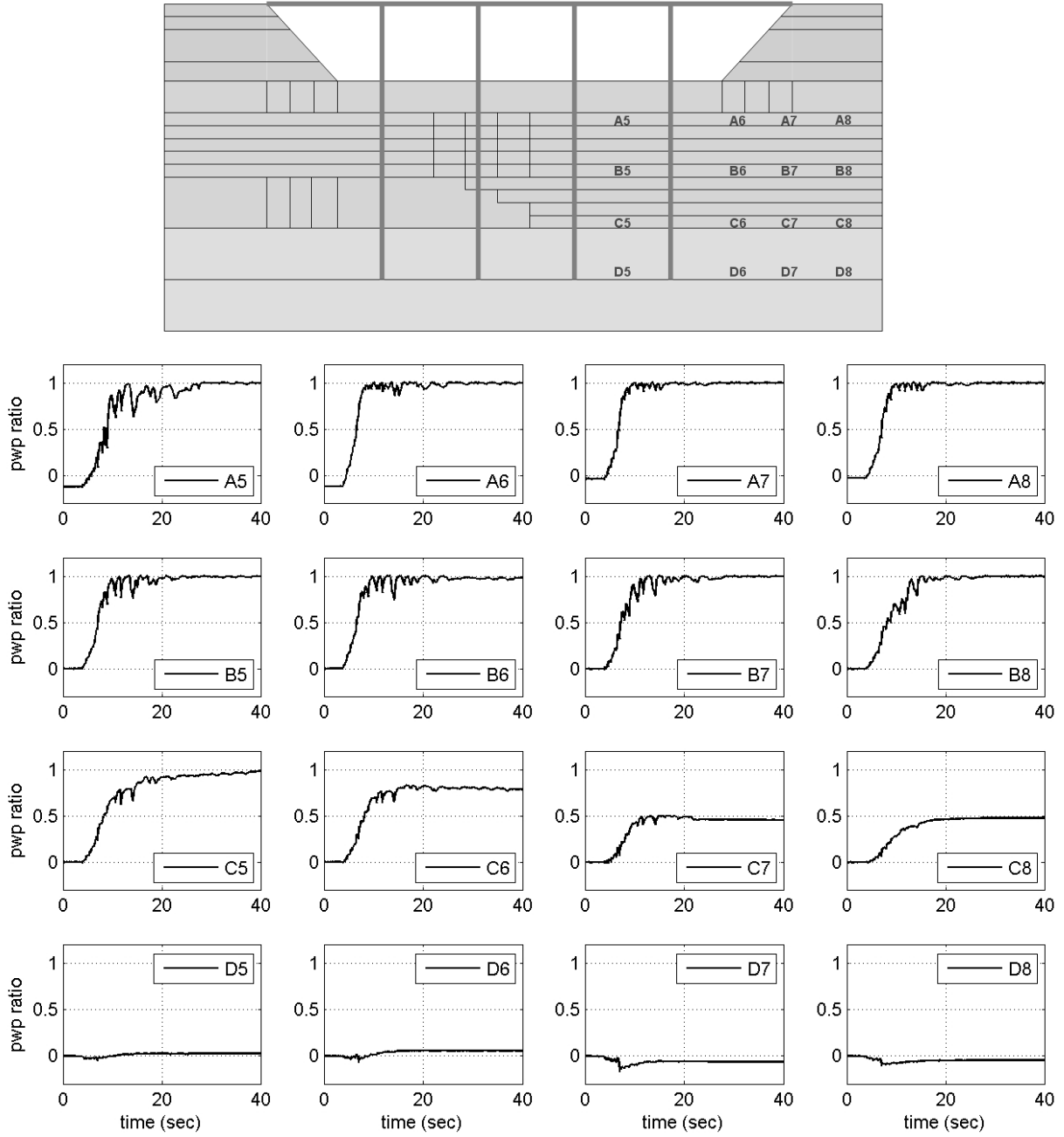


Fig. 6.5 Pore pressure ratio time histories in liquefiable soil.

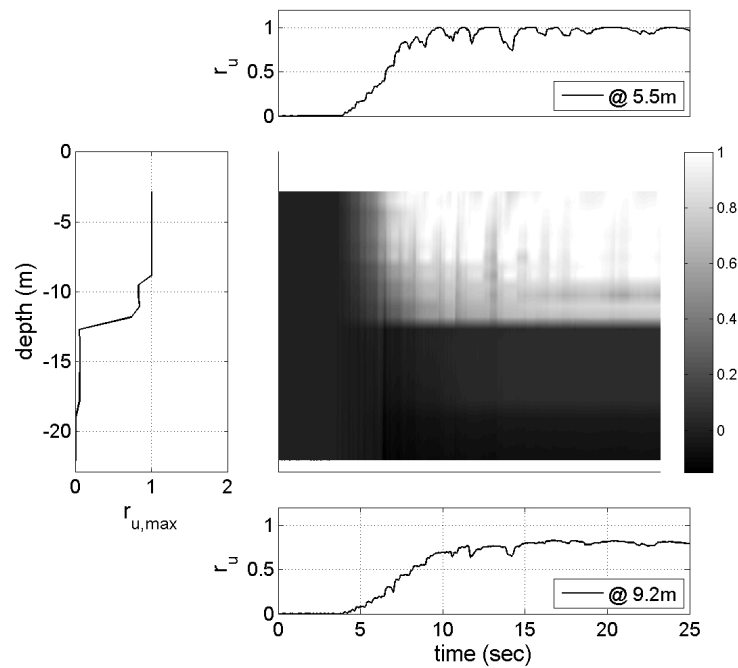


Fig. 6.6 Spatial and temporal variation of pore pressure profile below right abutment in liquefiable soil—Northridge motion.

6.2.2 Pinning Effect and Soil Element Out-of-Plane Thickness

Embankment slope deformation can be affected by the presence of pile foundations which resist soil deformation. This effect is often referred to as the pile pinning effect. Due to the presence of pile foundations, actual lateral and vertical displacements can be smaller than the displacements that would occur in the free-field case. This problem can be approximately simulated in a 2-D plane strain model by adjusting the soil element out-of-plane thickness. If the soil element out-of-plane thickness is very small, the piles will severely restrain the soil and the slope displacements would be underestimated. If the thickness is very large, the slope displacements would be close to the free-field displacements (i.e., those of a slope without pile foundations). To understand the effects of out-of-plane thickness on slope deformation and pile cap movement for this bridge system, simulations with several thicknesses were performed. Figure 6.7 shows that the use of a thickness smaller than 5 m gave very small soil displacement relative to the other cases. When the thickness was greater than 75 m, the displacements converged to a limiting

value beyond which they were insensitive to the out-of-plane thickness. This pattern was also observed in the pile cap lateral displacement near the slope.

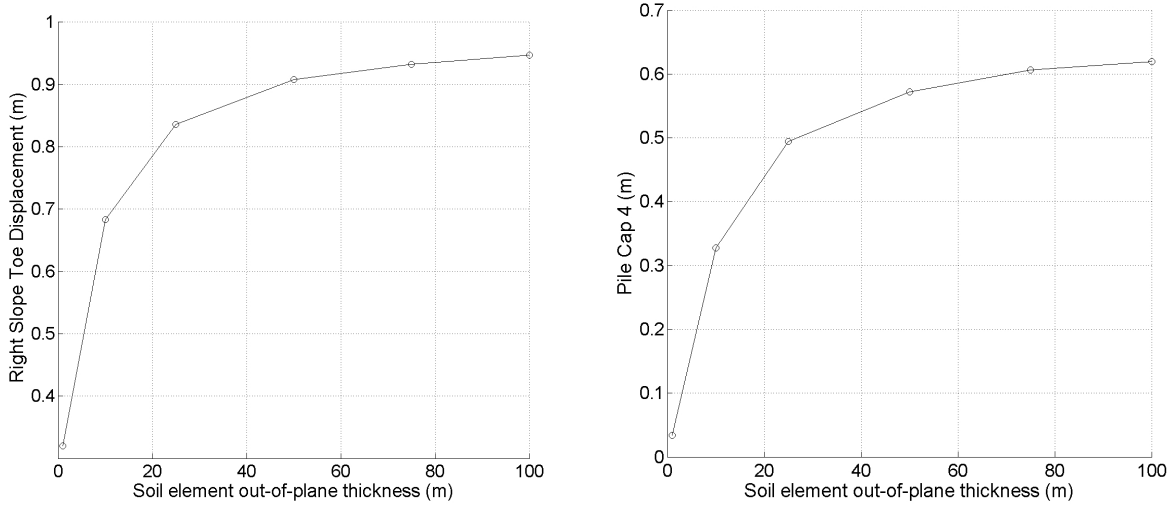


Fig. 6.7 Effect of soil element out-of-plane thickness on slope toe and pile cap lateral displacement—Erzincan motion.

An appropriate thickness can be determined considering several factors that contribute to the pinning effect such as ground motion intensity, 3-D embankment configuration and deformation pattern, actual demand on adjacent structures, and the tributary width of the embankment. First, the pinning effect can be slightly different when different intensities of motions are used. Second, even though the two-dimensional model is affected only by longitudinal shaking, an actual slope may deform in the longitudinal and transverse directions; as schematically shown in Figure 6.8, resulting in larger displacements than would be simulated in a 2-D FEM analysis. Third, structural demands due to possibly larger ground deformation can be reduced by the nonlinear behavior of the interface springs, (e.g., a simulation where the pile cap passive earth pressure springs reach ultimate resistance after which it shows a constant resistance with continued soil displacement). Finally, the tributary width of the embankment may strongly affect the system response and should be taken into consideration. In the case under consideration, the width of the pile foundation at the abutment is about 30 m, which is similar to the tributary width based on the trapezoidal shape of sloping embankment (Boulanger et al.

2005). For these reasons, a 50 m soil element out-of-plane thickness was chosen for the analysis. For improved estimation of out-of-plane thickness effects, 3-D model studies are required.

This is certainly a limitation of two-dimensional analysis (performed in this study). However, two-dimensional analysis brings the possibility to evaluate the response of the complete structure in a logical way, while keeping the computational time at reasonable levels.

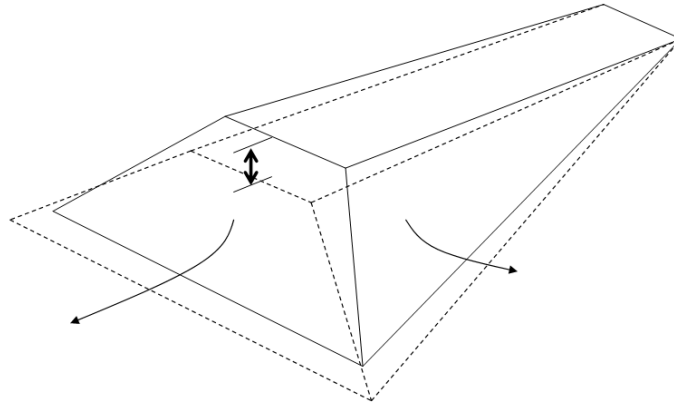


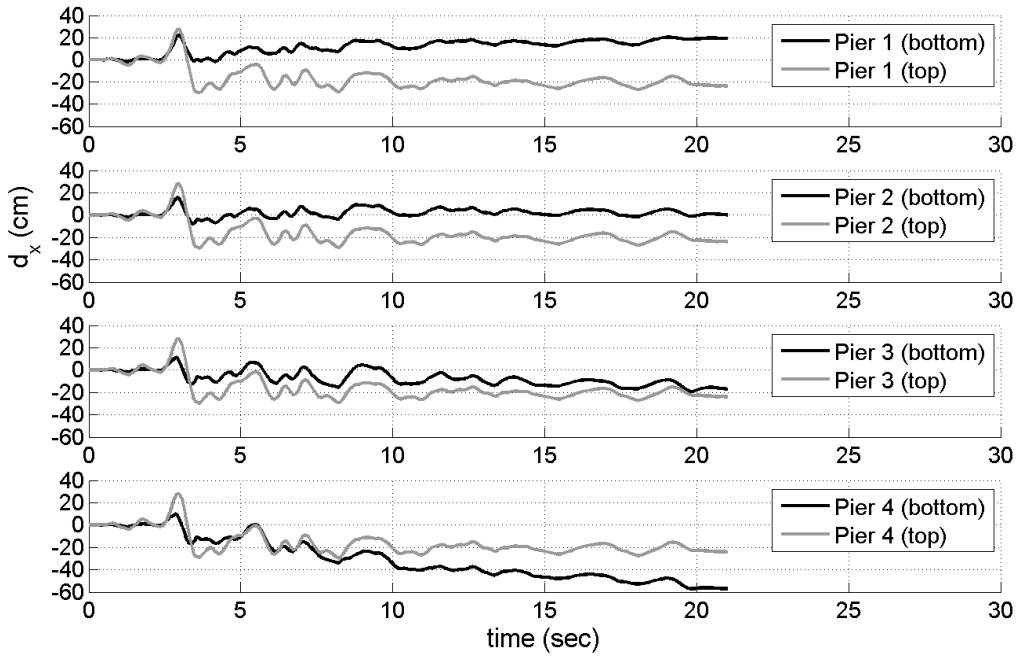
Fig. 6.8 Schematic drawing of 3-D embankment deformation.

6.2.3 Global Behavior of Bridge System

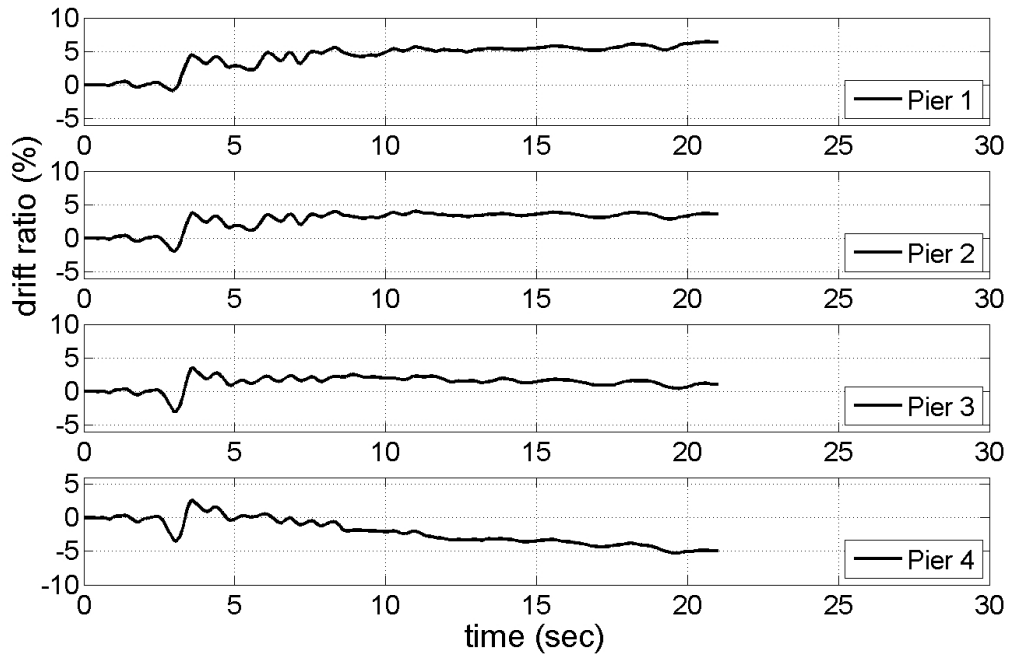
The numerical simulations showed that the expansion joints between the bridge deck and abutment backwalls close when lateral spreading occurred. Since the amount of lateral spreading beneath the right abutment was considerably larger than that beneath the left abutment, the entire bridge deck tended to be pushed to the left. At the same time, lateral spreading also pushed the pile cap of Pier 4 to the left resulting in relatively small drift in that column. On the other hand, Pier 1 was subjected to large column drift because the bridge deck moved the upper end of the column to the left while lateral spreading moved the pile cap at the base of the column to the right. This global bridge behavior, which would likely not be anticipated by typical analyses that model only individual parts of the bridge, greatly affected the demands on many local components of the bridge. The details of the local response of bridge piers, abutments, and piles are discussed in the following sections.

6.2.4 Bridge Pier Response

The bridge pier response was investigated using the displacements of the bridge deck and pile cap. Figure 6.9(b) shows drift ratios associated with the difference in displacement between the tops and bottoms of piers. The bottoms of the four piers (pile caps) moved toward the center of the bridge by amounts that varied due to different levels of lateral spreading. As shown in Figure 6.9(a), Pier 1 base residual lateral displacement was about 20 cm after shaking and Pier 4 base residual lateral displacement was about 60 cm. In the meantime, the tops of all piers moved to the left as the larger lateral spreading beneath the right abutment pushed the entire bridge deck to the left. This bridge deck movement increased Pier 1 drift and decreased Pier 4 drift. Due to this global response, similar drift ratios were observed in Pier 1 and Pier 4 for this particular motion even though the base residual lateral displacement of Pier 4 was much greater than that of Pier 1. These analyses demonstrated that lateral spreading in an abutment slope can affect the column drift in the other side of bridge.



(a)



(b)

Fig. 6.9 (a) Displacement of each bridge column at top and bottom and (b) drift ratios (column height = 6.7 m)—Erzincan motion.

Actual input motions at the bottom of each bridge pier are presented in Figure 6.10 in terms of acceleration time histories and acceleration response spectra. Due to non-uniform soil conditions (i.e., different soil profiles below the left and right abutments) and liquefaction-induced lateral spreading, the bottom of each pier was subjected to different acceleration time histories and peak accelerations.

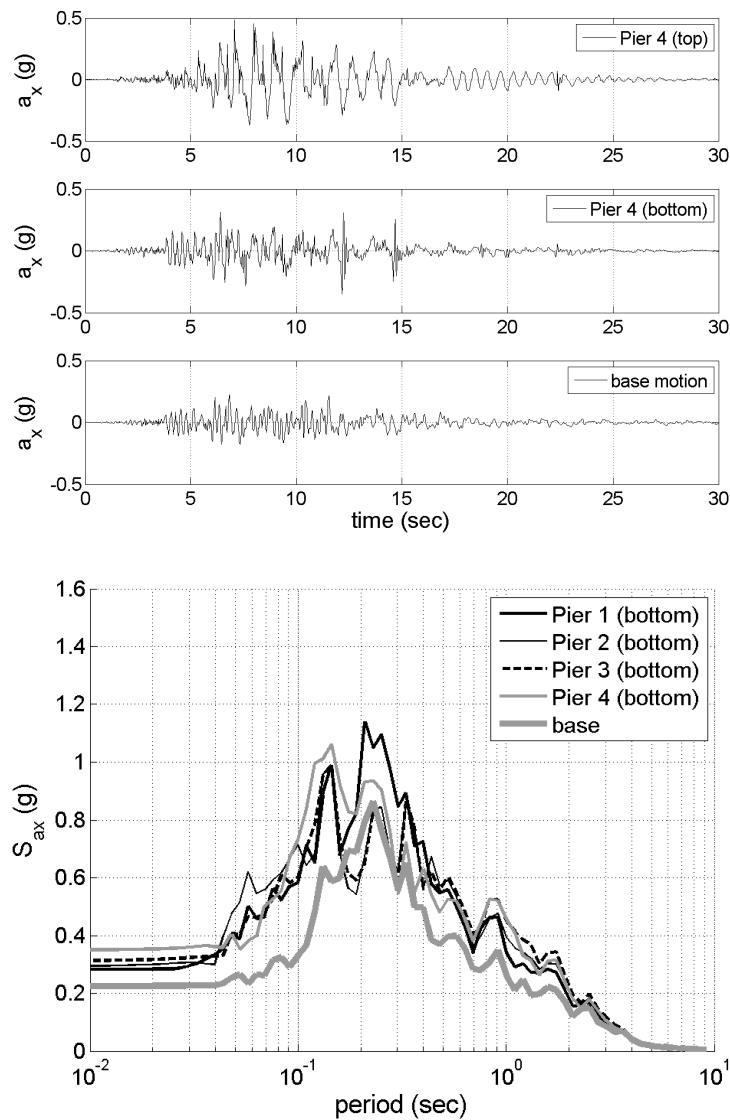


Fig. 6.10 Acceleration time histories and response spectra at soil base and pile cap—Northridge motion.

The horizontal slope movements significantly influenced the pile and pier bending moments. In particular, the bending moments in Pier 4 appear to be closely correlated to horizontal slope movements. For small to moderate shaking events, the maximum bending moments at each bridge pier were greater than the residual bending moments after shaking, indicating that inertial forces controlled the maximum bending moments. For strong shaking events, however, the residual bending moment at each bridge pier or deck was greater than the transient maximum bending moment, indicating that the kinematic forces associated with lateral spreading controlled the maximum bending moment.

6.2.5 Abutment Response

The bridge deck and abutment structure interaction was investigated by looking at relative displacements between the bridge deck and abutment and interaction forces in the bearing pad, break-off wall, and backfill. Figure 6.11 shows the horizontal and vertical positions of the bridge deck and abutment during shaking. Each abutment was set to have 10 cm initial expansion joint gaps. The abutments (black line in the figure) moved toward the center of the bridge with increasing vertical displacement. For the Northridge motion, the expansion joint gap was closed at the end of shaking, but the backwall did not break. For the stronger Erzincan motion, the left abutment showed about 25 cm permanent lateral movement, while the right abutment showed approximately 90 cm permanent lateral movement with slightly more vertical displacement. Figure 6.11(b) shows that for the strong shaking, and due to the large ground deformation in the right abutment, the bridge deck moved to the left until it contacted the left abutment. As a result, abutment-abutment interaction occurred through the bridge deck. Moreover, the relative position of the deck-end and backwall, which defines the initial gap, indicates shearing failure of the back wall and bridge deck penetration into the backfill soil. At the end of the shaking, the permanent penetration of the left and right bridge-deck-ends into the soil were around 30 cm and 60 cm, respectively.

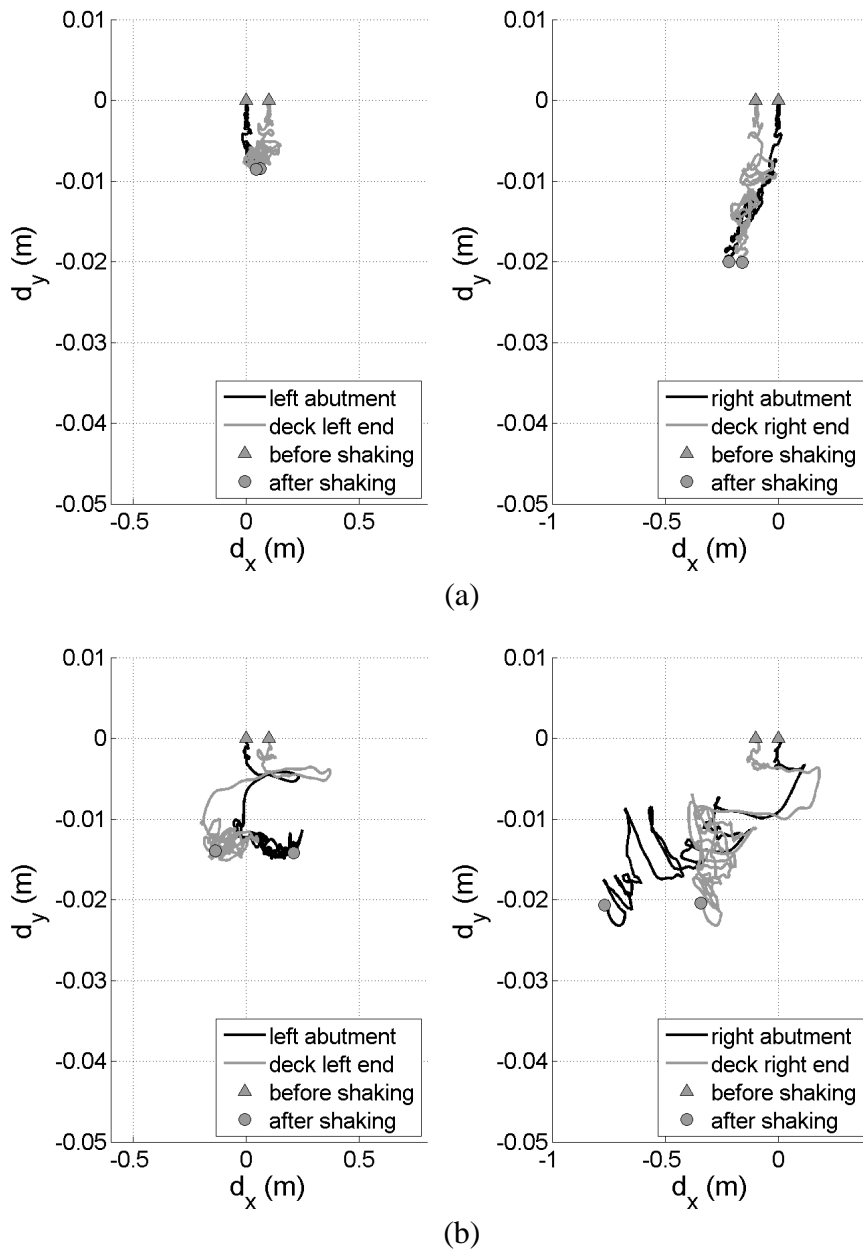


Fig. 6.11 Abutment and bridge deck movements, (a) Northridge, California, 1994, $a_{\max}=0.25$ g, (b) Erzincan, Turkey 1992, $a_{\max}=0.70$ g.

The bridge deck and abutment interaction is illustrated in Figure 6.12 in terms of spring force-displacements for a strong shaking event. Figures 6.12(a) and (b) show lateral resistance in the bearing pad and backwall. After 10 cm of displacement, where bearing pad resistance develops, large lateral resistance was mobilized in the break-off wall. This wall resistance disappeared after the wall ultimate resistance was reached. This interaction force was then transferred to the stem wall of the abutment. Figures 6.12(c) and (d) show that the passive earth pressure resistance in the backfill soil mobilized after reaching the maximum capacity of the break-off wall. Figures 6.12(e) and (f) show the total lateral resistance transmitted from the abutment system to the bridge deck.

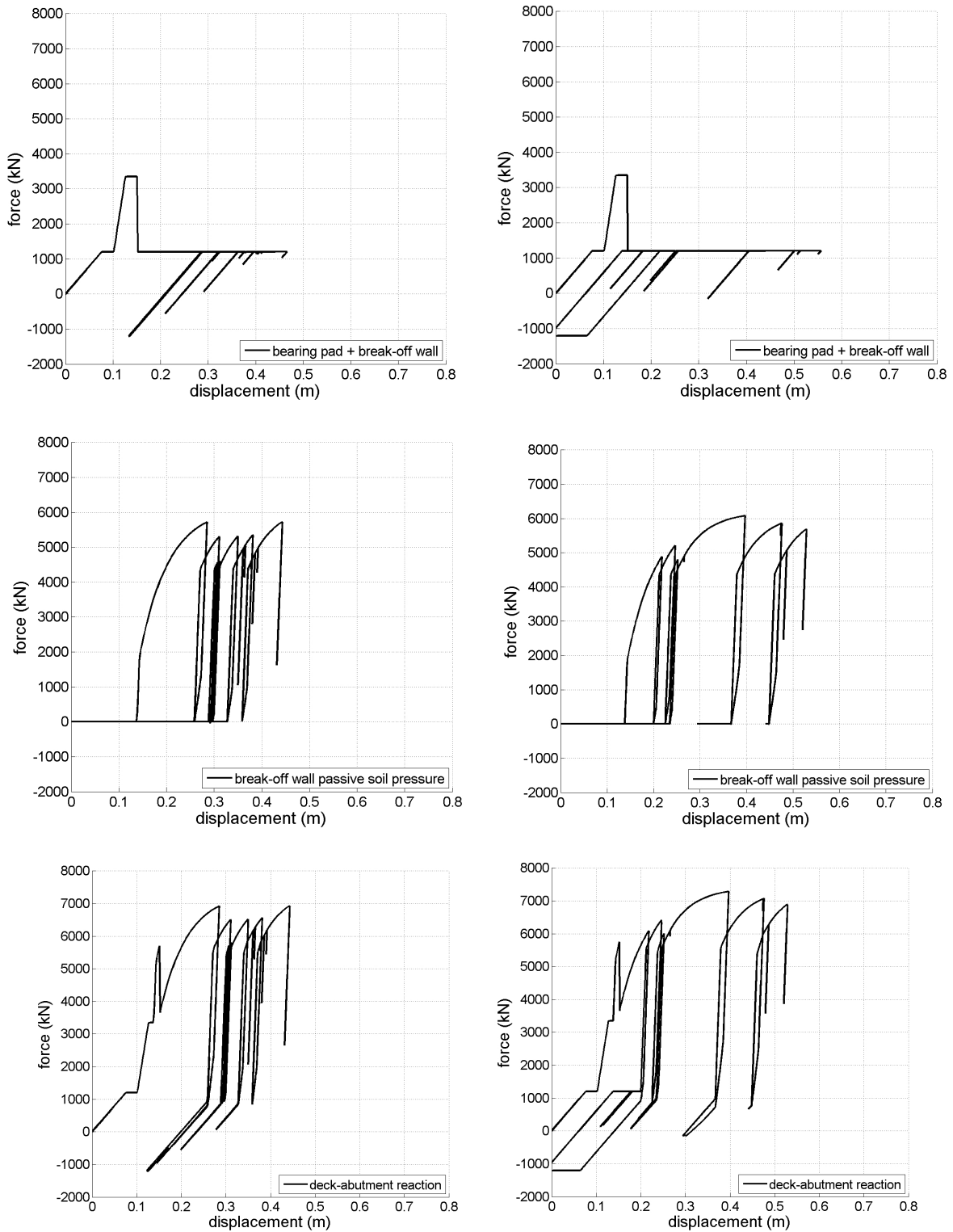


Fig. 6.12 Bridge deck and abutment interaction force-displacement—Erzincan motion.

6.2.6 Pile and p-y Spring Response

Figure 6.13 shows residual pile bending moments after shaking and the distribution of kinematic lateral force on the soil due to lateral spreading for the Erzincan motion. The maximum residual bending moments occurred at the interface between the loose and dense sand (around 12 m depth) in all piles. Since most of the loose sand layer was liquefied and the lateral soil resistance of the clay layer was relatively small, the overall mobilized soil resistance was small except for the non-liquefied soil at 5 m depth near Pile 1 and the dense sand layer below 12 m depth. The kinematic p - y spring force between 2 m to 6 m in Pile 4 reached the ultimate residual lateral soil resistance corresponding to the fully liquefied soil. In Figure 6.14, the p - y spring response time history of Pile 4 at 5.5 m is plotted together with the corresponding pore pressure ratio (r_u) time history of an adjacent soil element. The API-based soil resistance time history mobilized by the same displacement is also presented in the figure. After 5 seconds, when the soil liquefied (i.e., $r_u = 1$), the lateral soil resistance reached an ultimate residual lateral resistance. The figure shows the clear effect of liquefaction on lateral soil resistance by comparison with a possible API-based resistance. The liquefaction effect is also observed in Figure 6.15 which shows p - y curves for Pile 3 and Pile 4 at two locations in the liquefiable layer. Finally, Figure 6.16 shows pile cap lateral passive earth pressure spring force-displacement curves for four pile caps during the strong motion. The Pile cap 4 interface spring reached ultimate resistance with lateral-spreading-induced large soil displacements.

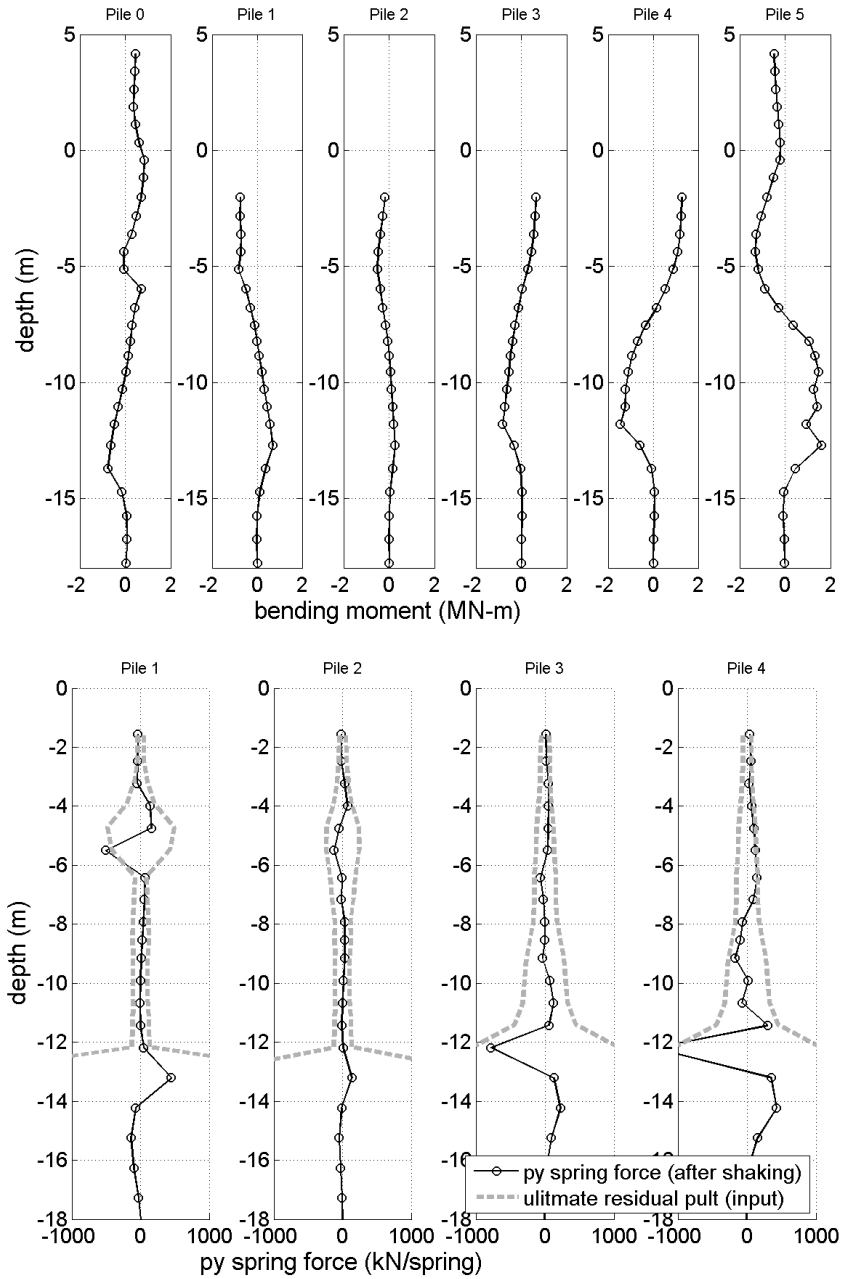


Fig. 6.13 Residual pile bending moments and lateral soil resistance during earthquake—Erzincan motion.

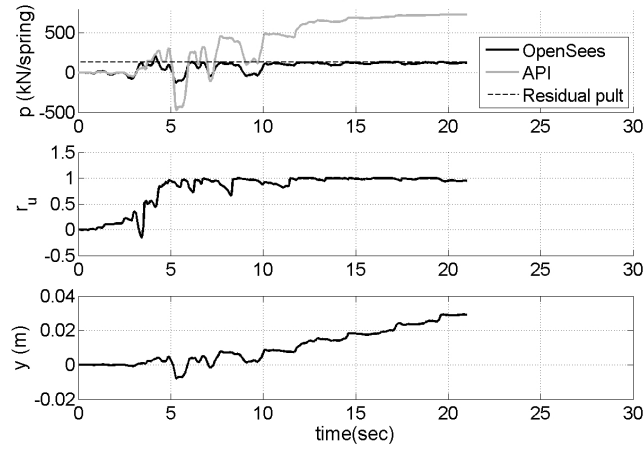


Fig. 6.14 p-y time histories during earthquake excitation—Erzincan motion.

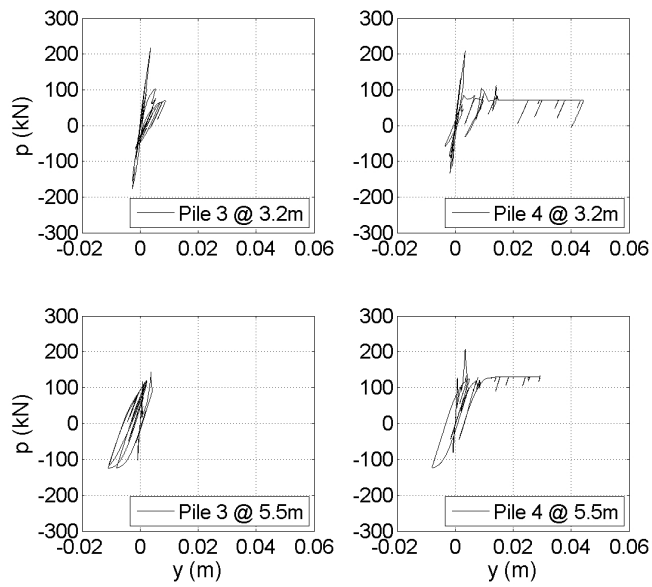


Fig. 6.15 p-y curves during earthquake excitation—Erzincan motion.

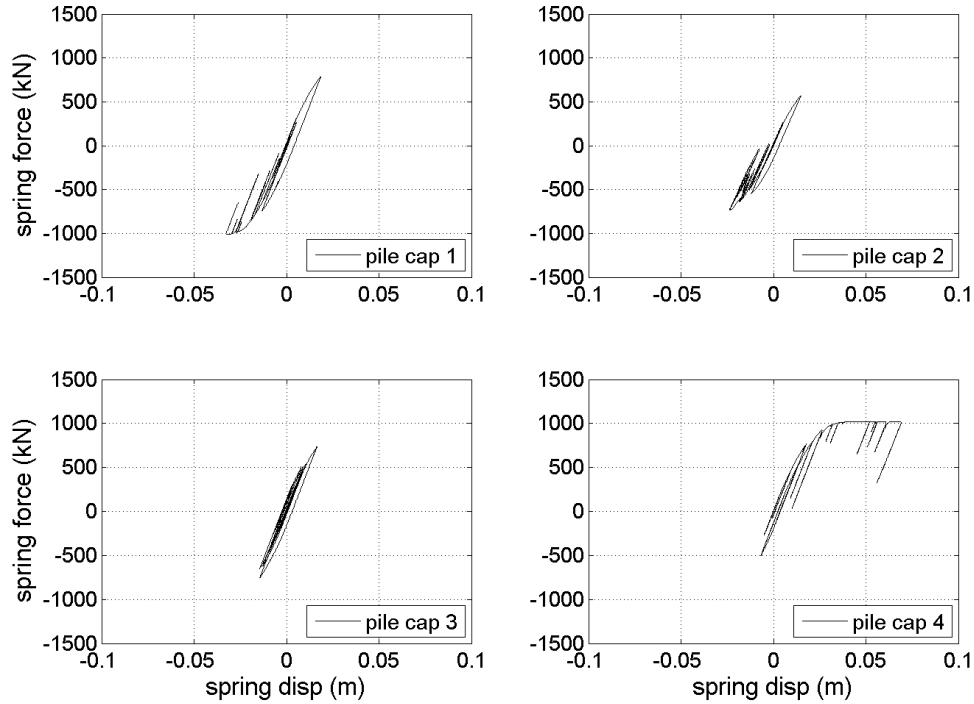


Fig. 6.16 Pile cap resistance curves—Erzincan motion.

6.3 SUMMARY OF RESPONSE IN VALIDATION EXERCISES

The complete model including pile foundations embedded in realistic soil conditions and abutment structures was developed and coupled to a bridge structure model (Mackie and Stojadinović 2003). Appropriate modeling of soil-pile-structure interaction and soil-abutment-bridge interaction under lateral spreading soil conditions allowed the model to capture realistic force boundary conditions at the pier base and bridge deck ends. Using the coupled model, the global behavior of the bridge system could be better understood and important bridge performance variables could be identified. This study showed that the global response of a soil-foundation-bridge system was quite complex, particularly due to the presence of the soft and/or liquefiable soils. The use of OpenSees simulations provided improved understanding of the global response, and allowed identification of damage mechanisms that would not be captured by simplified analyses commonly used in contemporary practice.

One of the important components of the global bridge response was the abutment-to-abutment interaction caused by different levels of lateral spreading beneath the two approach embankments and the resulting effect on the bridge pier drift. Since the amount of the right

abutment lateral spreading in the simulation was considerably greater than that in the left abutment, the entire bridge deck moved toward the left. At the same time, lateral spreading also pushed the pile cap of the pier near the right slope to the left, so the drift of that column became smaller. On the other hand, the pier near the left slope was subjected to large column drift because the bridge deck moved to the left and the pile cap at the bottom of the column moved to the right due to lateral spreading. This type of response can be obtained only using models that consider the entire soil-foundation-structure system.

The bridge pier response was investigated with respect to displacement at the top and bottom of the piers and it was found that drifts at all piers were strongly affected by lateral spreading. The relative position between bridge deck and abutment during the shaking, and corresponding interaction forces, were described to show abutment-bridge-soil interaction.

7 Estimation of *EDP-IM* Relationships for Testbed Highway Bridge

7.1 INTRODUCTION

The OpenSees model validated in the previous chapter was used to estimate a variety of engineering demand parameters (*EDPs*) under different levels of seismic loading. The main purpose of these analyses was to evaluate the *EDP-IM* relationship, i.e., to characterize the distribution of *EDP|IM*. This chapter describes the results of the “production” analyses using a series of 40 ground motions scaled to be representative of four different hazard levels.

7.2 ANALYSES FOR *EDP|IM* EVALUATION

Estimation of the seismic performance of bridges is an important part of evaluating the potential costs of earthquake damage and identification of appropriate retrofit strategies. This section describes the results of analyses performed for the purpose of characterizing the response of the soil-foundation-structure system, i.e., of *EDP|IM*, at different hazard levels. These results represent an integral component of the PEER PBEE framework.

For the PBEE analyses performed in this study, ground motions corresponding to four hazard levels were used in OpenSees simulations with the bridge system model validated in Section 6.2. Measures of structural and geotechnical response relevant to bridge damage were identified. Using OpenSees results, record-to-record uncertainties were estimated, and the relative efficiencies of several *IMs* were investigated to reduce the response model uncertainties. In addition to record-to-record uncertainty, model parameter uncertainty and spatial variability effects were investigated. To demonstrate the effects of parametric uncertainty, significant parameters were first identified by creating tornado diagrams. Response uncertainties were also estimated using FOSM analyses. To assess the effects of spatial variability, Gaussian stochastic fields were generated for the liquefiable and clay soil layers.

7.2.1 Input Motions and Intensity Measures

To apply the PEER PBEE methodology, four sets of input motions corresponding to return periods of 15, 72, 475, and 2475 years (i.e., 97 %, 50 %, 10 %, and 2 % in 50 years) at the site of an I-880 bridge study (Somerville 2000) were used as input to the bridge model. The near-fault ground motions used in the I-880 study are different from ordinary ground motions, since they are often dominated by strong, long-period pulses, which result from rupture directivity effects. The details of the characteristics of the selected near-fault ground motions are described by Somerville (2000). Figure 7.1 shows acceleration and displacement time histories for one of these motions with a return period of 275 years. In the simulations performed in this study, the bridge was assumed to be subjected to fault-normal motions.

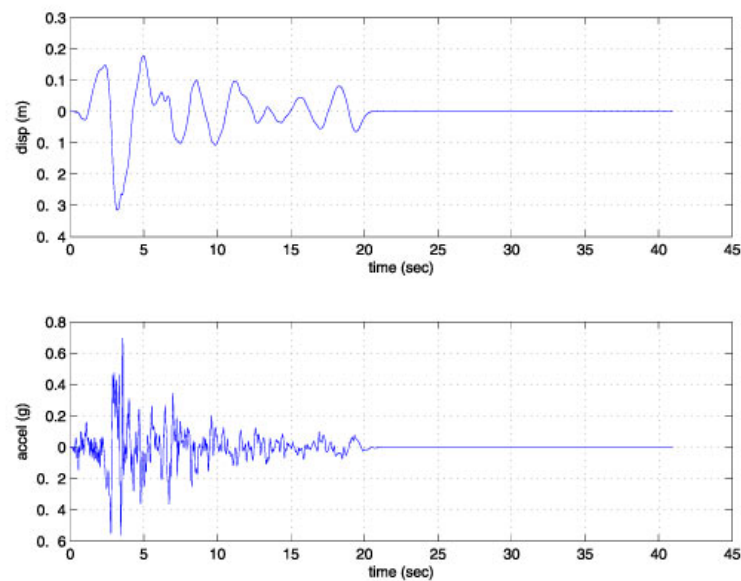


Fig. 7.1 Example of input motion used in comprehensive bridge study—Erzincan motion.

Somerville (2000) provided soft rock uniform hazard spectra for three hazard levels (50%, 10%, and 2% in 50 years) for the I-880 site. The modal magnitudes for these three hazards were obtained from deaggregation data as 6.6, 6.8, and 7.0, respectively. The corresponding target peak acceleration values were 0.453 g, 0.871 g, and 1.228 g, respectively. In this study, to minimize dispersion in the *EDP* versus *IM* relationships, particularly for the case where lateral spreading affects the bridge response, motions for each hazard level were scaled to a constant value of a target magnitude-corrected PGA (PGA_M), expressed as

$$PGA_M = \frac{PGA}{MSF} \quad (7.1)$$

where PGA is the mean PGA for the hazard level of interest and MSF is the magnitude scaling factor corresponding to the modal magnitude for that hazard level. Magnitude scaling factors can be calculated using NCEER's recommendations as

$$MSF = \begin{cases} \left(\frac{7.5}{M_w}\right)^{2.95} & M_w \geq 7.5 \\ \left(\frac{7.5}{M_w}\right)^{2.56} & M_w < 7.5 \end{cases} \quad (7.2)$$

where M_w is modal magnitude. Using the target modal magnitudes and their corresponding MSF values, PGA_M values were computed for each hazard level (Table 7.1). To include a hazard level that did not cause widespread liquefaction, the motions used for 50% in 50 years were scaled for a target magnitude-corrected peak acceleration of 0.094 g, which corresponds approximately to a 97% in 50 years hazard.

Table 7.1 Magnitude-corrected PGA.

Hazard Level	a_{max} (g)	modal magnitude	MSF	PGA_M
50 % in 50 years	0.453	6.6	1.516	0.299
10 % in 50 years	0.871	6.8	1.335	0.652
2 % in 50 years	1.228	7.0	1.226	1.002

Ten motions were selected for each hazard level. Individual motions were scaled to have the target magnitude-corrected peak acceleration in each hazard. The values are presented in the 7th column (i.e., PGA_M) in Table 7.2.

Since the scaled motions were based on rock outcrop conditions, the motions were corrected using the computer program ProShake to remove free surface effects prior to their use as rigid base input motions in OpenSees. Information for the 40 motions is summarized in Table 7.2. Figure 7.2 shows the range of PGAs for each hazard level and the corresponding PGA hazard curve.

Table 7.2 I-880 Input motion characteristics (four hazards).

hazard level	Record (station)	File	Earthquake	Magnitude	MSF	PGA_M	dt	PGA	duration
return period 72 yrs target PGA_M = 0.299g	Coyote Lake Dam abutment	A01	Coyote Lake	5.7	2.247	0.672	0.005	0.574	40.96
	Gilroy #6	A02	(6/8/1979)	6.0	1.931	0.578	0.005	0.610	40.96
	Temblor	A03	Parkfield				0.010	0.469	40.96
	Array #5	A04	(6/27/1966)				0.010	0.470	81.92
	Array #8	A05					0.010	0.394	40.96
	Fagundes Ranch	A06	Livermore	5.5	2.497	0.747	0.005	0.606	20.48
	Morgan	A07	(6/27/1980)				0.005	0.483	40.96
	Territory Park	A08	Morgan Hill	6.2	1.753	0.524	0.005	0.423	40.96
	Coyote Lake Dam abutment						0.005	0.435	40.96
	Anderson Dam						0.005	0.435	40.96
DS	A09	(4/24/1984)				0.005	0.435	40.96	
Halls Valley	A10					0.005	0.464	40.96	
return period 475 yrs target PGA_M = 0.652g	Los Gatos Presentation Ctr	B01	Loma Prieta	7.0	1.226	0.799	0.005	0.687	40.96
	Saratoga	B02	(10/17/1989)				0.005	0.728	40.96
	Aloha Avenue	B03					0.005	0.709	40.96
	Corralitos						0.005	0.699	40.96
	Gavilan	B04					0.005	0.699	40.96
	College	B05					0.005	0.691	40.96
	Gilroy Historic						0.020	0.759	40.96
	Lexington	B06					0.020	0.759	40.96
	Dam abutment	B07	Kobe, Japan (1/17/1995)	6.9	1.279	0.834	0.020	0.781	81.92
	Kobe JMA								
	B08	Tottori, Japan	6.6	1.458	0.951	0.010	0.622	40.96	
	B09	(10/6/2000)				0.005	0.897	81.92	
	B10	Erzincan	6.7	1.395	0.909	0.005	0.696	40.96	
			(3/13/1992)						
return period 2475 yrs target PGA_M = 1.002g	Los Gatos Presentation Ctr	C01	Loma Prieta	7.0	1.226	1.228	0.005	1.101	40.96
	Saratoga	C02	(10/17/1989)				0.005	1.141	40.96
	Aloha Avenue	C03					0.005	1.078	40.96
	Corralitos						0.005	1.055	40.96
	Gavilan	C04					0.005	1.055	40.96
	College	C05					0.005	1.063	40.96
	Gilroy Historic						0.020	1.191	40.96
	Lexington	C06					0.020	1.191	40.96
	Dam abutment	C07	Kobe, Japan (1/17/1995)	6.9	1.279	1.282	0.020	1.221	81.92
	Kobe JMA								
	C08	Tottori, Japan	6.6	1.458	1.461	0.010	1.092	40.96	
	C09	(10/6/2000)				0.005	1.399	81.92	
	C10	Erzincan, Turkey	6.7	1.395	1.398	0.005	1.107	40.96	
			(3/13/1992)						
return period 15 yrs target PGA_M = 0.094g	Coyote Lake Dam abutment	D01	Coyote Lake	5.7	2.247	0.211	0.005	0.168	40.96
	Gilroy #6	D02	(6/8/1979)	6.0	1.931	0.182	0.005	0.167	40.96
	Temblor	D03	Parkfield				0.010	0.157	40.96
	Array #5	D04	(6/27/1966)				0.010	0.137	81.92
	Array #8	D05					0.010	0.119	40.96
	Fagundes Ranch	D06	Livermore	5.5	2.497	0.235	0.005	0.189	20.48
	Morgan	D07	(6/27/1980)				0.005	0.148	40.96
	Territory Park	D08	Morgan Hill	6.2	1.753	0.165	0.005	0.122	40.96
	Coyote Lake Dam abutment						0.005	0.126	40.96
	Anderson Dam						0.005	0.126	40.96
DS	D09	(4/24/1984)				0.005	0.126	40.96	
Halls Valley	D10					0.005	0.124	40.96	

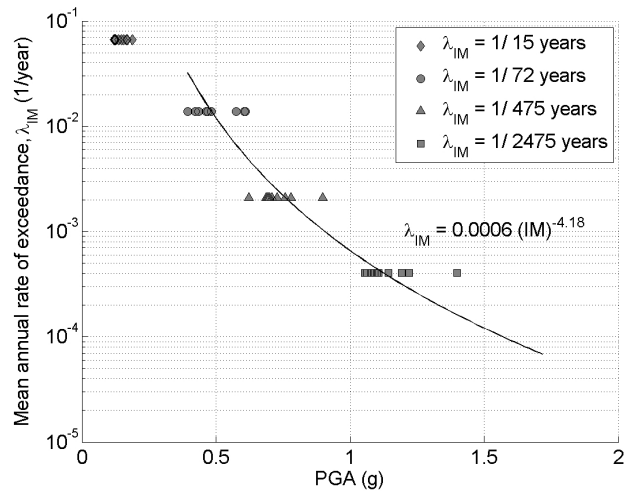


Fig. 7.2 PGA hazard curve.

The uncertainties in the estimated *EDP* versus *IM* relationships are different for different *EDPs* and *IMs*. An efficient *IM* is one for which an *EDP* of interest is closely related, i.e., one for which a plot of *EDP* versus *IM* exhibits little scatter. The use of efficient *IMs* leads to more accurate and less conservative performance estimation in PBEE evaluation procedures. For example, to capture the inertial structural response, the first-mode spectral acceleration and the Cordova (2000) predictor (Table 7.3) are generally recognized as efficient *IMs*. For a situation influenced by the occurrence of liquefaction, however, the response should be more closely related to an *IM* that reflects the liquefaction response, e.g., PGA, I_a , or CAV_5 . For example, Kramer and Mitchell (2006) have shown that excess pore pressure generation in potentially liquefiable soils is considerably more closely related to CAV_5 than to other intensity measures. To account for this effect, in this study several *IMs* (Table 6.3) were considered for the prediction of *EDPs*.

Table 7.3 Intensity measures.

IM name	Definition	Units
Peak ground acceleration	$PGA = \max a(t) $	g
Peak ground velocity	$PGV = \max v(t) $	m/s
Arias intensity	$I_a = \frac{\pi}{2g} \int_0^{T_d} [a(t)]^2 dt$	cm/s
Cumulative absolute velocity	$CAV_5 = \int_0^{T_d} \langle \chi \rangle a(t) dt$ where T_d = earthquake duration $\langle \chi \rangle = 0$, if $ a(t) < 5 \text{ cm/s}^2$ $\langle \chi \rangle = 1$, if $ a(t) \geq 5 \text{ cm/s}^2$	cm/s
Spectral acceleration	$Sa(T_1) = Sa(T_1)$	g
Cordova predictor	$Sa^*(T_1) = Sa(T_1) \sqrt{\frac{Sa(2T_1)}{Sa(T_1)}}$	g

An *IM* hazard curve is usually obtained from a probabilistic seismic hazard analysis (PSHA). Since *IM* hazard curves can often be approximated by power laws over certain hazard ranges, the hazard curve can be expressed as

$$\lambda_{IM} = k_0 (IM)^{-k} \quad (7.3)$$

where the two unknown coefficients, k_0 and k , can be obtained solving Equation (6.3) after substituting values for two hazard levels, e.g., (IM_1, λ_1) and (IM_2, λ_2) . In this research, a hazard curve was available (from the I-880 study) for PGA. The mean annual rates of exceedance for other *IMs* should be obtained from PSHAs performed using attenuation relationships corresponding to each *IM*. As an approximate estimation of each *IM* hazard curve, the *IM* value of each individual motion was calculated based on the definitions shown in Table 6.4 considering the same mean annual rate of exceedance obtained for PGA. The generated *IM* hazard curves for different *IMs* are shown in Figure 7.3. The figure shows a large scatter for some *IMs*. Therefore, if a set of motions obtained from a PSHA analysis for a particular *IM* is used for other *IM* hazard curve construction, the *IM* hazard curve should be used with care. The power law coefficients for each *IM* hazard curves are summarized in Table 7.4.

Table 7.4 IM hazard curve coefficients for I-880 input motions.

IM	coefficient k_0	coefficient k
Peak ground acceleration (PGA)	6.578e-04	-4.1808
Peak ground velocity (PGV)	1.520e-03	-2.4645
Arias Intensity (I_a)	1.586e+01	-1.4230
Cumulative absolute velocity (CAV_5)	7.881e+04	-2.3859
Spectral acceleration ($Sa(T=0.5 \text{ sec})$)	9.455e-03	-3.5338
Spectral acceleration ($Sa(T=1.0 \text{ sec})$)	1.675e-03	-2.0630
Cordova predictor (Cordova($T=0.5 \text{ sec}$))	2.799e-03	-2.6514

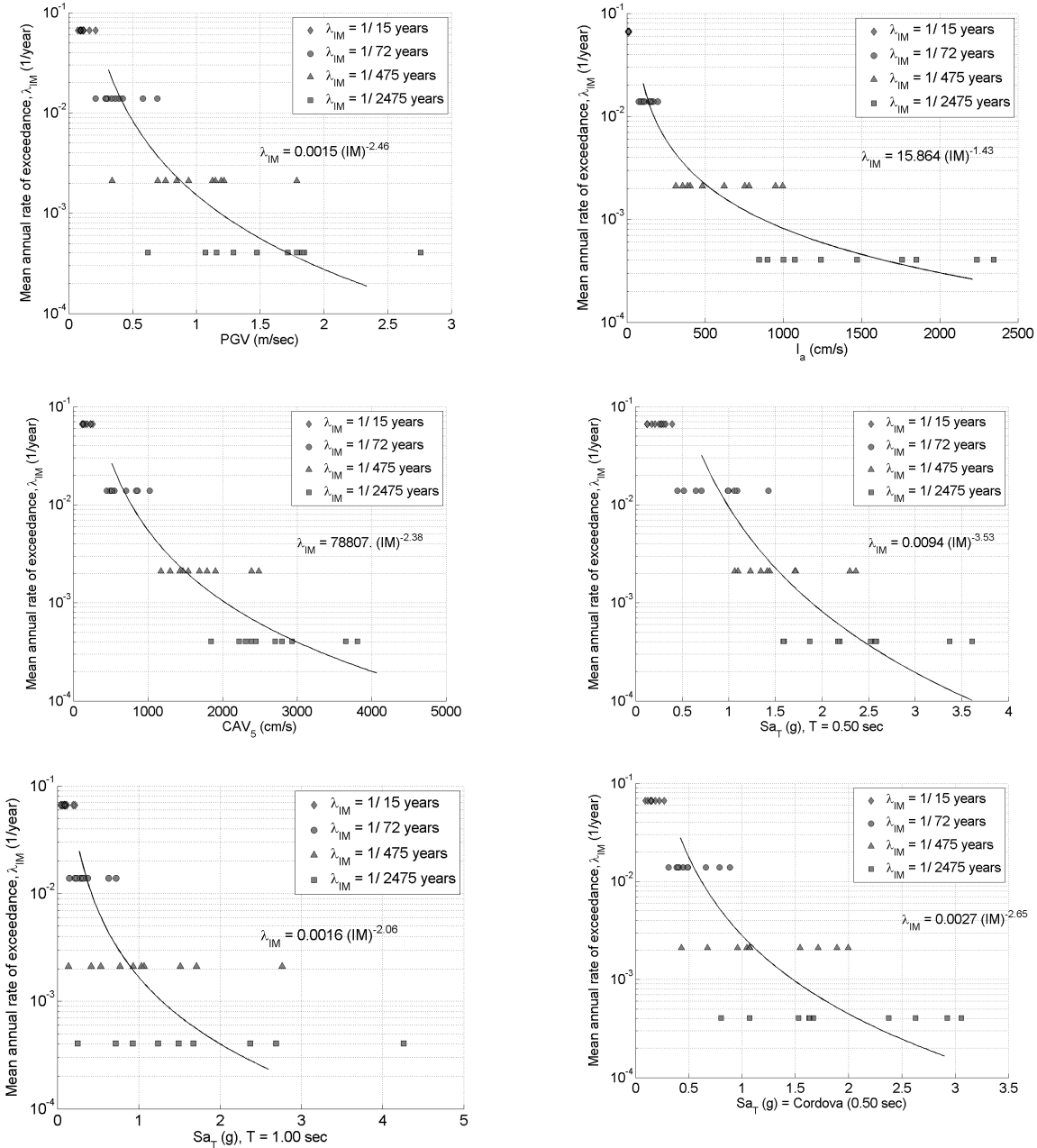


Fig. 7.3 Implied hazard curves for different IMs.

7.2.2 EDPs of Bridge System

By examining the bridge behavior from multiple numerical analyses, important *EDPs* (such as maximum and residual values of bridge pier drift, horizontal slope movement, embankment settlement, relative displacement between bridge deck and abutment approach, pile cap movement, and pile curvature) were identified. A list of possible *EDPs* for the bridge system is shown in Table 7.5.

Table 7.5 EDP list.

<i>EDP</i> group	<i>EDP</i> description	<i>EDP</i> symbol	Definition
column	drift ratio	$C1_{[drift,max]}$ $C2_{[drift,max]}$ $C3_{[drift,max]}$ $C4_{[drift,max]}$	maximum drift ratio = maximum drift/column height
pile cap	pile cap drift (displacement)	$P0_{[drift,res]}$ $P1_{[drift,res]}$ $P2_{[drift,res]}$ $P3_{[drift,res]}$ $P4_{[drift,res]}$ $P5_{[drift,res]}$	permanent lateral displacement of pile cap
abutment expansion joint	gap between deck and abutment	$EJ1_{[gap,res]}$ $EJ2_{[gap,res]}$	relative distance between deck end and break-off wall
abutment backwall	backwall displacement	$BW1_{[dx,max]}$ $BW2_{[dx,max]}$	break-off wall displacement = disp. of bearing pad spring - initial gap
abutment approach	bridge approach vert. off-set	$BA1_{[dy,res]}$ $BA2_{[dy,res]}$	relative vertical displacement between abutment top and adjacent backfill soil
bearing pad	bearing pad displacement	$BP1_{[dx,max]}$ $BP2_{[dx,max]}$	maximum relative lateral displacement between deck and stem wall
embankment slope	lateral disp. settlement	$E1_{[dx,res]}$ $E2_{[dx,res]}$ $E1_{[dy,res]}$ $E2_{[dy,res]}$	average lateral displacement of slope top and toe average vertical displacement of slope top and toe

The list divides *EDPs* into several groups that can be associated with structural and geotechnical damage and cost estimation. The structural *EDP* groups include column drift, expansion joint displacement, bridge approach vertical off-set, break-off wall displacement, and bearing pad shear strain. The structural *EDPs* were selected to be consistent with the *EDP* groups used by Mackie et al. (2004), who performed similar analyses using the same bridge model on competent soil. Abutment slope deformation and pile cap displacement were included as new geotechnical *EDP* groups. Even though the actual damage to a pile is most closely related to pile bending moment or curvature, these *EDPs* may not be practical for estimation of damage, since

they cannot be easily observed following an earthquake. In an attempt to extract bending moment and curvature information, the correlation between pile cap displacement and pile curvature was investigated. Figure 3.4 shows that the residual pile cap displacement after shaking and maximum pile curvature were reasonably well correlated, especially for large pile cap displacements.

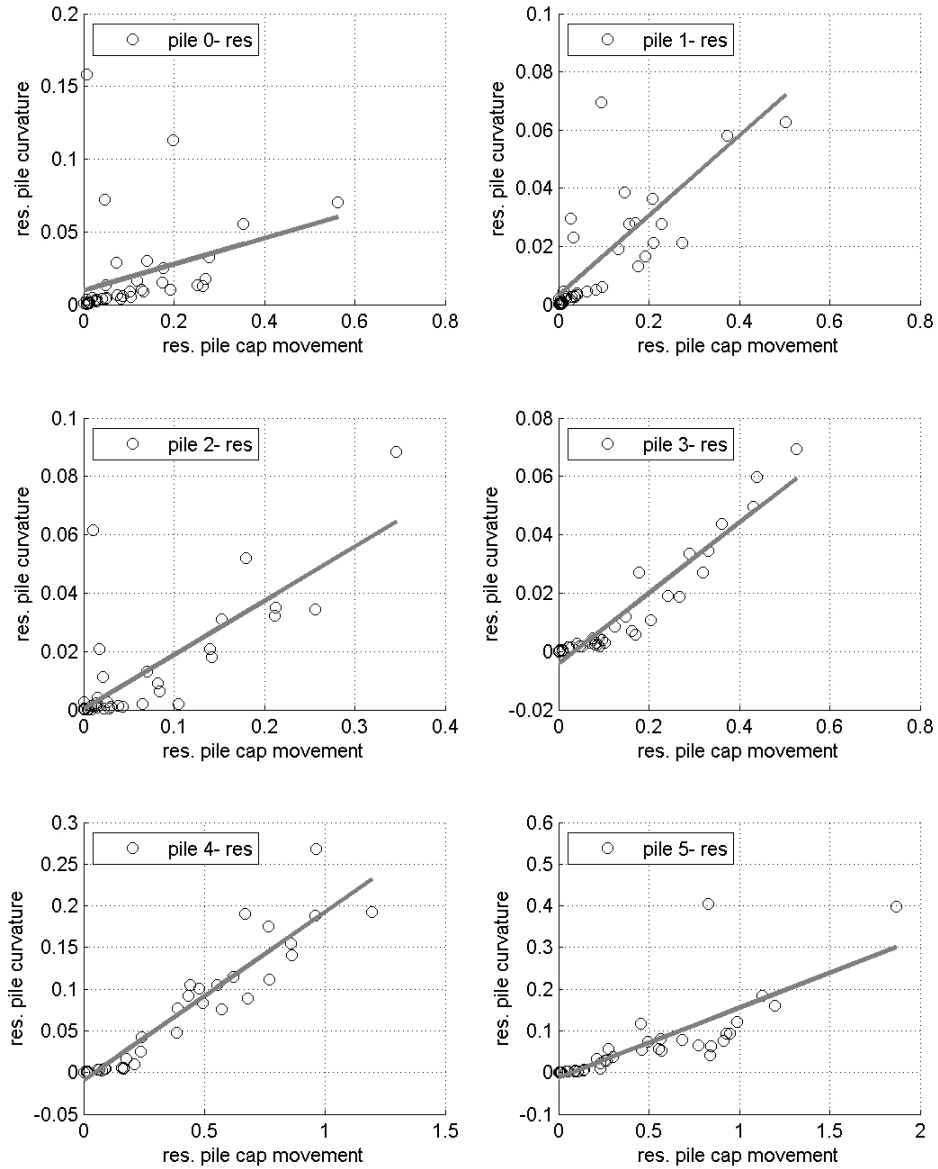


Fig. 7.4 Correlation between lateral pile cap displacement and curvature from simulations for Northridge 1994, 0.2557 g; unit of curvature = 1/m.

7.2.3 Uncertainties in Inputs to Response Analyses

There are several sources of uncertainty in *EDP* estimation as illustrated in Figure 7.5. One of the major sources of uncertainty is the record-to-record uncertainty that originates from the different characteristics of the scaled input motions. The response of any structural or geotechnical system response is affected by ground motion characteristics such as amplitude, frequency content, and duration. For example, two motions that have the same peak acceleration could result in significantly different responses if they have different frequency contents and durations. Estimation of performance uncertainty, therefore, requires the use of multiple motions that reflect a range of earthquake source and path characteristics similar to those affecting the site of interest. In such situations involving multiple simulations, it is important to identify efficient *IMs* to reduce the uncertainty in the response (less dispersion in *EDP-IM* relationship) as well as to reduce the number of simulations required to achieve a given level of confidence in the *EDP-IM* relationship.

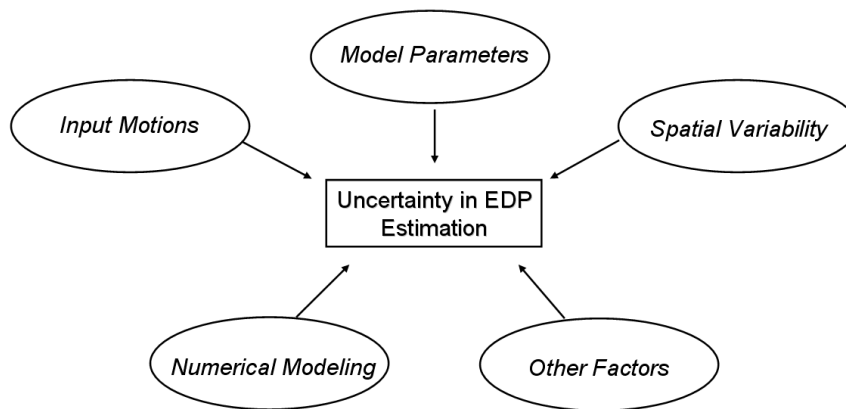


Fig. 7.5 Components of total uncertainty in *EDP* estimation.

The second source of uncertainty is the parametric uncertainty that results from inherent material property uncertainties. This uncertainty is comprised of aleatory uncertainty, which represents the natural randomness of a property, and epistemic uncertainty, which results from the lack of information or knowledge and shortcomings in measurements and calculations.

Another factor in the description of aleatory uncertainty originates from spatial variability. Soil physical properties vary from place to place within a soil deposit due to

depositional factors such as sedimentation, erosion, transportation, and weathering processes and loading history. Epistemic uncertainty can be reduced with the acquisition of new information or knowledge, but aleatory uncertainty cannot.

A final source of uncertainty originates from the numerical modeling. Since the OpenSees bridge model uses model components where assumptions, approximations and simplifications are made, especially for a complete bridge including several interacting components, the simulated response cannot be free from model uncertainty even though the uncertainty can be reduced using advanced and verified analysis methods and tools that can handle the simulation properly.

In this study, aleatory and epistemic uncertainties were included in the *EDP* estimation procedure. To estimate the record-to-record uncertainty, motions for four hazards levels were used in the simulations. To estimate parametric uncertainty, 16 model parameters were varied and results from the simulations were used in first-order second-moment(FOSM) analysis. To model spatial variability effects, stochastic fields were generated using Gaussian random fields. The numerical modeling uncertainty was not explicitly evaluated in this study.

7.2.4 Record-to-Record Uncertainty

Using simulation results for all four hazard levels, several *EDP-IM* relationships and uncertainty parameters were obtained for different *IMs* using a cloud analysis approach. From the *EDP-IM* relationships linear regressions in log-log space were obtained to estimate record-to-record uncertainties assuming a constant lognormal probability distribution of *EDP* conditional upon *IM*.

Based on these results, efficient *IMs* were identified for different *EDPs*. For example, Figure 7.6 shows residual settlements in the right abutment slope as a function of six different *IMs*. The figure also shows the standard deviation of $\ln EDP$ residual and median relationship with median \pm standard deviation lines. Figure 7.7 shows the same information for maximum drift ratio in Pier 4. For the right abutment settlement, CAV_5 appears to be the most efficient *IM* (least dispersion in *EDP-IM*) among the *IMs* considered in Table 7.3. For the Pier 4 drift ratio, the Cordova parameter at the fundamental structural period appears to be the most efficient *IM*. Figure 7.8 compares the efficiency of *IMs* for the two *EDPs*. These results show that the most efficient *IMs* depend on the *EDP* being considered.

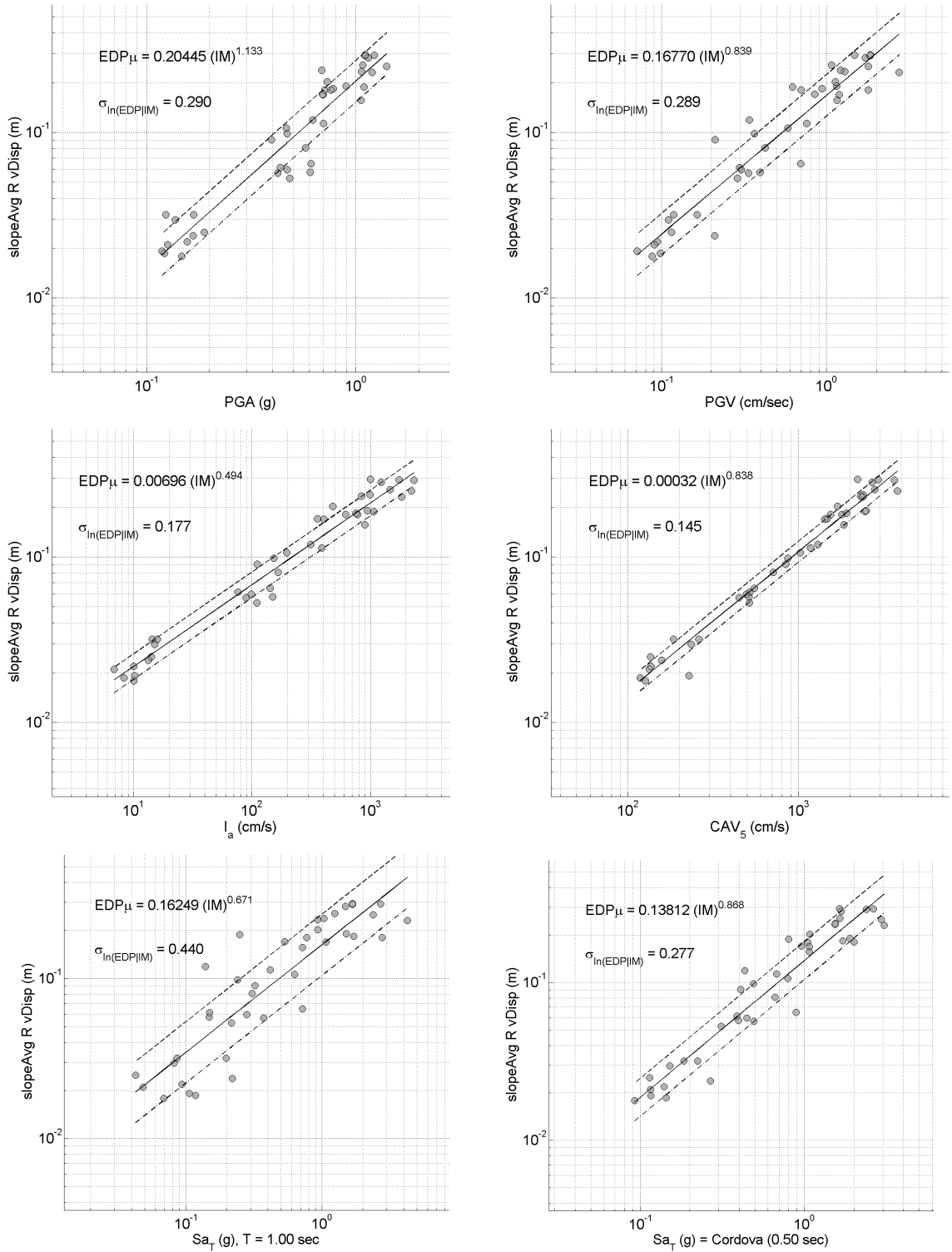


Fig. 7.6 EDP-IM relationships for right abutment slope residual vertical settlement.

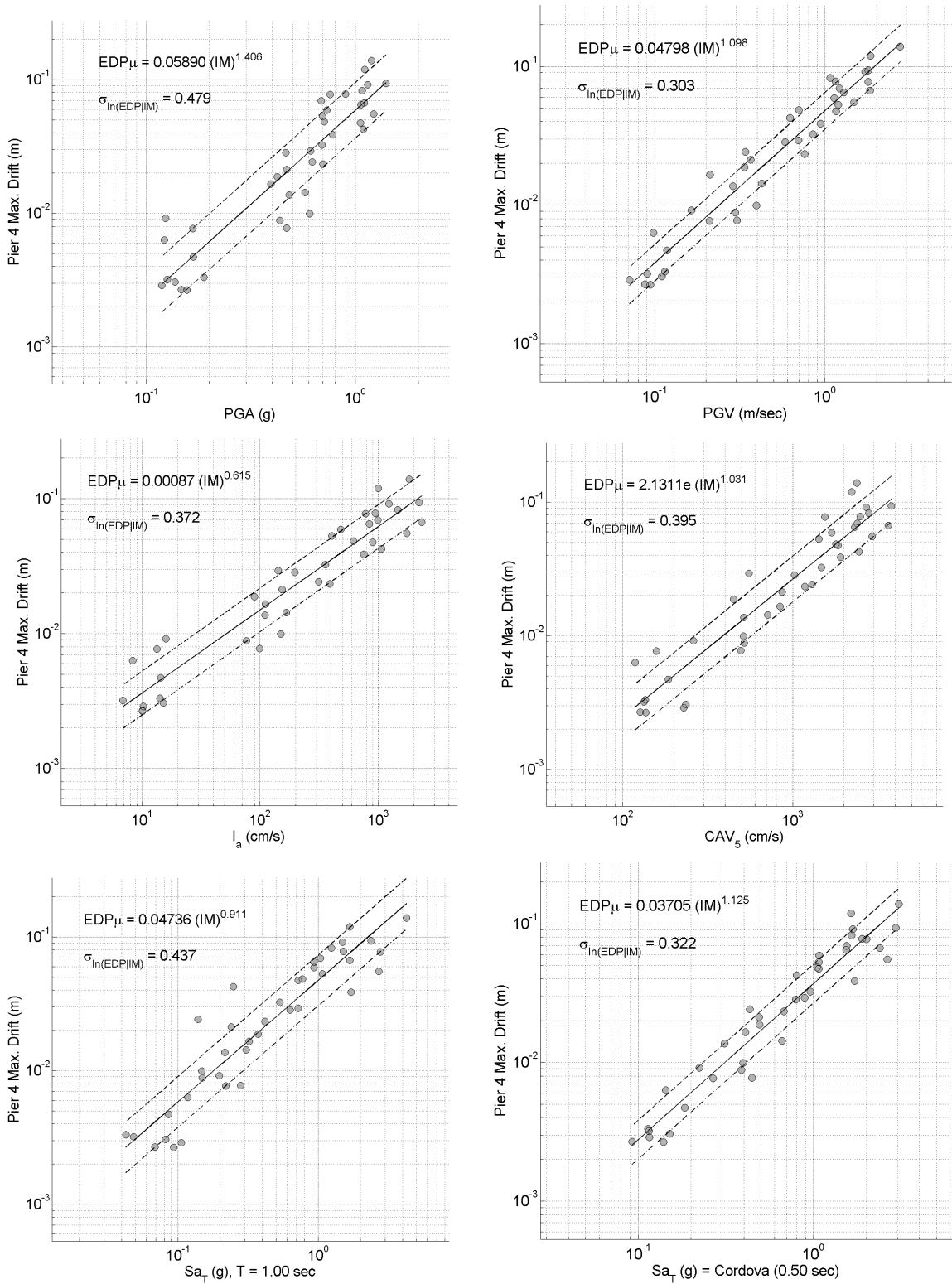


Fig. 7.7 EDP-IM relationships for Pier 4 maximum drift.

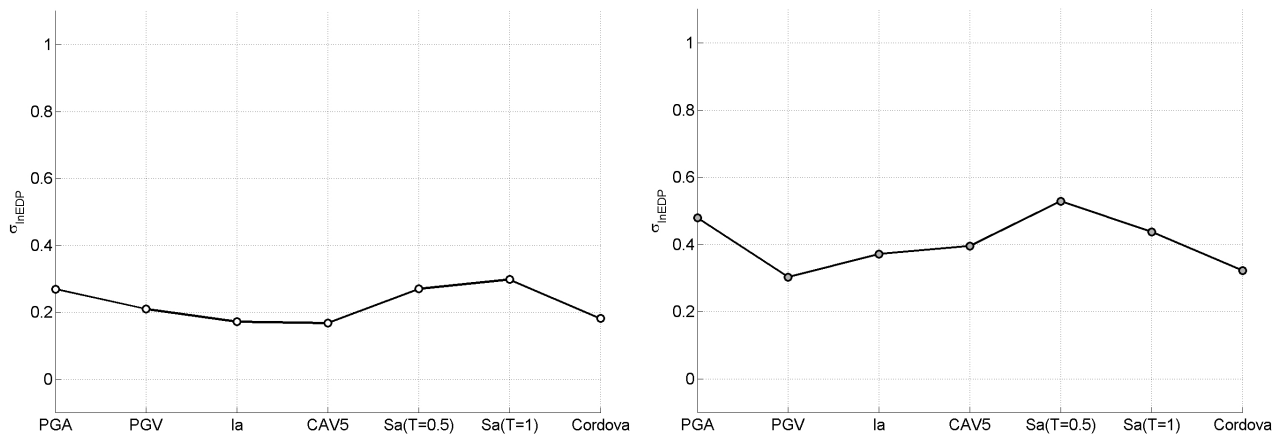


Fig. 7.8 Relative efficiencies of different IMs.

Using *EDP-IM* results, record-to-record uncertainties and median *EDP-IM* relationships were obtained for several *EDP* groups. The results are summarized in Table 7.6 where the corresponding efficient *IMs* are indicated. This summary table shows that CAV_5 is one of the most efficient *IMs* for the *EDPs* affected by lateral spreading such as slope deformation, abutment expansion joint movement, and pile cap lateral movement near slopes, while spectral acceleration or PGV is more efficient for structural related *EDPs* such as bridge pier drift ratio. Overall, residual *EDPs* obtained at the end of shaking showed higher uncertainty than maximum *EDPs*. Pile cap displacements also showed higher uncertainty than bridge pier drifts.

Table 7.6 Summary of *EDP* median coefficients and record-to-record uncertainty for power-law median response model, $EDP = a IM^b$.

<i>EDP</i> group	<i>EDP</i> description	<i>EDP</i> symbol	efficient <i>IM</i>	<i>EDP</i> median coef. (a,b)	$\sigma_{\ln EDP/IM}$
column	drift ratio	$C1_{[drift,max]}$	Cordova(T=0.5)	3.520e-2, 1.0318	0.327
		$C2_{[drift,max]}$	<i>PGV</i>	3.080e-2, 0.9867	0.401
		$C3_{[drift,max]}$	Sa(T=1.0)	3.194e-2, 0.9230	0.432
		$C4_{[drift,max]}$	<i>PGV</i>	4.799e-2, 1.0983	0.304
pile cap	pile cap drift (displacement)	$P0_{[drift,res]}$	CAV_5	5.567e-5, 0.9996	1.275
		$P1_{[drift,res]}$	I_a	9.908e-4, 0.6818	1.026
		$P2_{[drift,res]}$	Sa(T=0.5)	1.930e-2, 1.6540	1.266
		$P3_{[drift,res]}$	CAV_5	7.943e-7, 1.6357	0.673
		$P4_{[drift,res]}$	I_a	2.526e-4, 1.1586	0.761
		$P5_{[drift,res]}$	CAV_5	2.464e-6, 1.6554	0.687
abutment exp. joint	gap between deck and abutment	$EJ1_{[gap,max]}$	Sa(T=1.0)	7.475e-2, 0.7899	0.737
		$EJ2_{[gap,max]}$	Sa(T=1.0)	6.153e-2, 0.6047	0.715
abutment backwall	backwall displacement	$BW1_{[dx,max]}$	<i>PGV</i>	3.899e-1, 0.4383	0.197
		$BW2_{[dx,max]}$	<i>PGV</i>	5.205e-1, 0.5915	0.195
abutment approach	bridge approach vert. off-set	$BA1_{[dy,max]}$	CAV_5	5.373e-4, 0.6521	1.173
		$BA2_{[dy,max]}$	CAV_5	2.259e-4, 0.8635	0.176
bearing pad	bearing pad displacement	$BP1_{[dx,max]}$	<i>PGV</i>	2.874e-1, 0.8228	0.340
		$BP2_{[dx,max]}$	<i>PGV</i>	3.683e-1, 0.9540	0.288
embankment slope	lateral disp. settlement	$E1_{[dx,res]}$	CAV_5	1.915e-4, 0.8484	0.874
		$E1_{[dy,res]}$	CAV_5	6.488e-4, 1.6115	0.601
		$E2_{[dx,res]}$	CAV_5	3.480e-6, 0.6601	0.168
		$E2_{[dy,res]}$	CAV_5	3.279e-4, 0.8396	0.142

7.2.5 Model Parameter Uncertainty

As mentioned before, an important source of uncertainty in the bridge response results from uncertainties in the evaluation of material input parameters. The main material properties used in these analyses, such as soil shear modulus, density, friction angle, and undrained shear strength, have uncertainties that originate from several sources including: (1) spatial variation of soil deposit and testing error due to randomness of test sample or location (e.g., an erratic boulder) and (2) measurement procedures and statistical error due to insufficient data. The first source is categorized as aleatory uncertainty associated with the natural randomness of the property. The second source is categorized as epistemic uncertainty related to the lack of information and shortcomings in measurement and calculation.

In this study, a list of material model parameters was considered to evaluate this uncertainty. Input parameter uncertainties were estimated based on data found in a literature review and on judgment. Using the values of the mean \pm one-half standard deviation for each

input parameter, a sensitivity study was performed, and tornado diagrams were generated to identify the most influential parameters. Following that, First-order second-moment (FOSM) analyses were conducted to estimate the parametric uncertainty of the bridge system for different *EDPs*.

7.2.5.1 List of Model Parameters

Several bridge model input parameters were considered to estimate the parametric uncertainty. Shear modulus, friction angle, and undrained shear strength were considered for all soils. To evaluate the liquefaction sensitivity, a parameter that controlled pore pressure generation in the PDMY material, was also considered. For the various types of interface springs, initial stiffness and ultimate resistance were considered including the abutment backwall break-off capacity and bearing pad stiffness. Table 7.7 summarizes the selected parameters and their coefficients of variance (COV). Jones et al. (2002) compiled COV values for several soil properties measured from laboratory and field tests based on studies by Harr (1987), Kulhawy (1992), Lacasse and Nadim (1996), Phoon and Kulhawy (1999), and Duncan (2000).

Table 7.7 Input parameter uncertainties.

Parameters	COV	Related materials or models	Comments
Shear modulus, G	0.4	embankment, clay, loose sand	
undrained shear strength, c	0.3	upper and lower clay layer	geotechnical
friction angle, ϕ	0.1	embankment, loose sand	
contraction parameter, contract1	0.2	loose sand	constitutive
py spring (stiffness, K_1)	0.4	pile, pile cap, abutment wall	interaction
py spring (pult): clay	0.3	pile, pile cap	spring
py spring (pult): sand	0.1	pile, pile cap	
abutment earth spring (stiffness, K_2)	0.4	abutment wall	
break-off wall capacity	0.1	break-off wall in abutment	structural
bearing pad (stiffness, K_3)	0.05	bearing pad	
Shear wave velocity, V_s	0.2		indirect
SPT resistance	0.3		parameters
density	0.08		

7.2.5.2 Tornado Diagrams

The input parameters expected to strongly influence the bridge behavior can be identified from sensitivity studies using tornado diagrams. The parameter values described in Tables 5.1 and 5.2 for the target bridge model represent the mean values used here as base parameters. These input

values were also used in the simulations performed to evaluate record-to-record uncertainty. To account for the effect of parameter uncertainty on the bridge response, each input parameter, X , was permuted upward and downward by $0.5\sigma_X$, while the other parameters were kept constant (i.e., at their mean values). These simulations gave three responses, $g(X_{\mu-\sigma/2})$, $g(X_\mu)$, and $g(X_{\mu+\sigma/2})$. The results of a tornado diagram analysis are presented graphically from top to bottom in order of decreasing relative swing, which is calculated as the absolute value of the difference in two outputs, $g(X_{\mu-\sigma/2})$ and $g(X_{\mu+\sigma/2})$ divided by $g(X_\mu)$. Even though the motion dependency was considered in the record-to-record uncertainty, a couple of motions were used for additional simulations to account for the effect of motion characteristics on the input parameter sensitivities. The motions selected were those closest to the average response spectrum for each hazard level. Additionally, the Northridge motion described in Section 6.2 was considered as a non-near-fault motion and used with its PGA scaled to different values.

Figure 7.9 shows tornado diagrams for the horizontal slope displacements and pile curvatures for the Temblor 1966 motion at Parkfield ($a_{max} = 0.47$ g, $T_R = 72$ years). The horizontal axis represents normalized maximum $EDP(g(X_{\mu-\sigma/2})/g(X_\mu))$ and $EDP(g(X_{\mu+\sigma/2})/g(X_\mu))$. The vertical axis represents the parameters ordered by swing. Figures 7.9(a) and (b) show that the horizontal slope displacement in the left abutment is sensitive to the variation of the undrained shear strength of the clay, while the horizontal slope displacement in the right abutment is sensitive to the friction angle, clay undrained shear strength, and sand soil contraction parameter. Figures 7.9(c) and (d) show that the clay undrained shear strength controls the maximum curvatures of Pile 1 near the left slope, while the maximum curvature of Pile 4 near the right slope is sensitive to sand friction angle, clay undrained shear strength, and ultimate resistance of pile cap. Overall, the clay undrained shear strength is one of the controlling parameters for most of the piles that extend through the clay. This was attributed to the large shear strains concentrated in the clay soil interface, resulting in large pile curvatures. In addition, the drift of Pier 1 near the left abutment is sensitive to the clay undrained shear strength and the loose sand friction angle. The drift of Pier 4 next to the right abutment slope is similarly sensitive to several parameters such as the shear modulus of the embankment soil and clay and the ultimate resistance of the pile cap.

Tornado diagrams are helpful in identifying the input parameters that most strongly affect bridge response. The friction angle of the loose sand and undrained shear strength of the clay were found to strongly affect the bridge responses associated with lateral spreading and slope displacement. The secondary influencing parameters were soil shear modulus and pile/pile cap interface spring parameters.

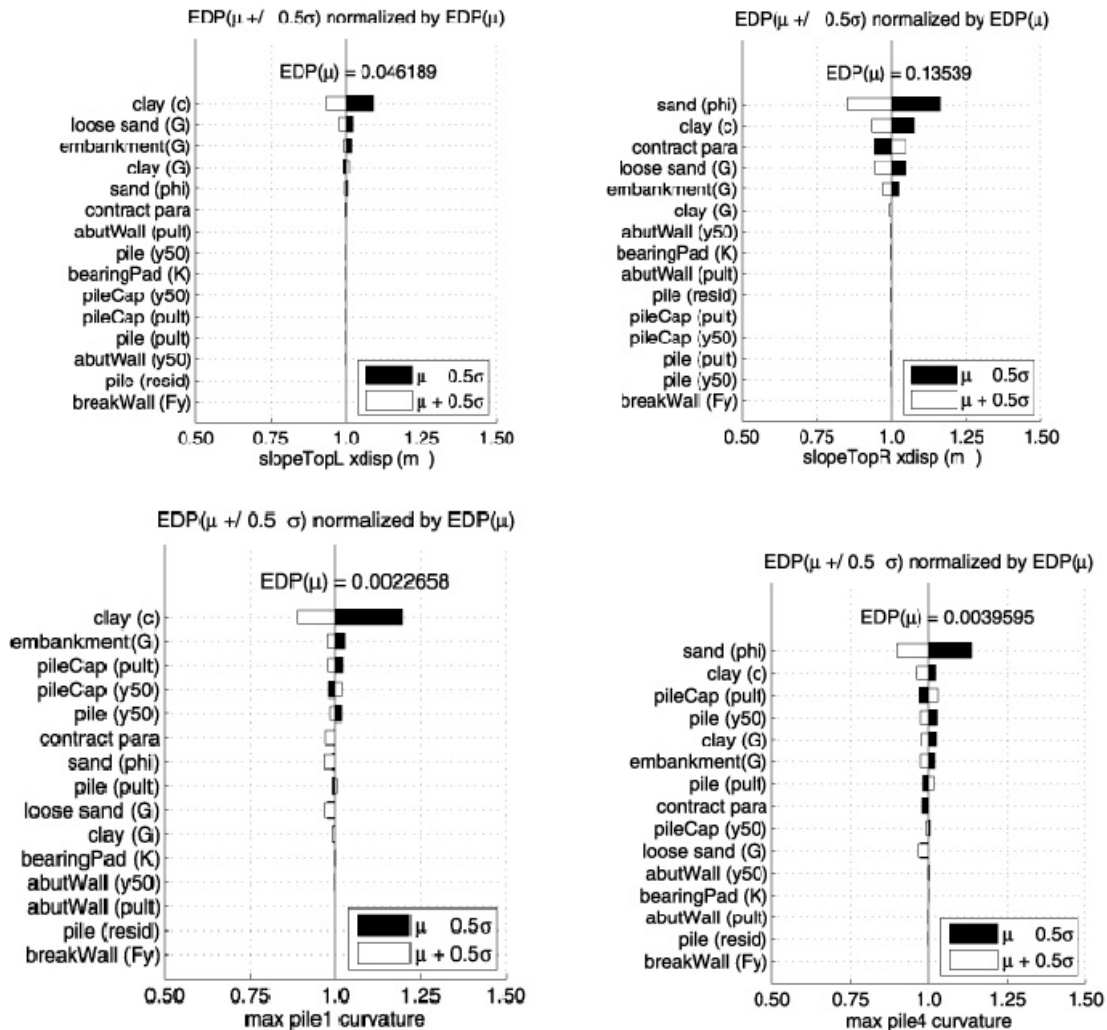


Fig. 7.9 Tornado diagrams for four maximum EDPs: Temblor 1966 motion at Parkfield ($a_{max} = 0.47 g$).

7.2.5.3 First-Order Second-Moment (FOSM) Analysis

Tornado diagrams provide insight into the response sensitivity to variation of individual parameters but do not provide quantitative estimates of uncertainty caused by parameter

variation. To estimate the effect of parametric uncertainties, First-order second-moment (FOSM) analyses were used. The second moment represents the second central moment for a random variable, X. The FOSM method allows estimation of the first two moments (mean value and variance) of some dependent variable given the first two moments (mean values and covariances) of the variables that control the dependent variable. The FOSM method can be easily derived, letting

$$Y=g(X_1,X_2,\dots,X_N) \quad (7.2)$$

where Y is the output response variable and X_i are the input parameters (for $i = 1$ to N). This relationship can be expanded using a Taylor series of the form

$$Y \approx g(\mu_{X_1}, \mu_{X_2}, \dots, \mu_{X_N}) + \frac{1}{1!} \sum_{i=1}^N (X_i - \mu_{X_i}) \frac{\partial g}{\partial X_i} + \frac{1}{2!} \sum_{i=1}^N \sum_{j=1}^N (X_i - \mu_{X_i})(X_j - \mu_{X_j}) \frac{\partial^2 g}{\partial X_i \partial X_j} + \dots \quad (7.3)$$

where μ_{X_i} is the mean value of the i th input parameter. Considering only the first-order terms, the series can be approximated as

$$Y \approx g(\mu_{X_1}, \mu_{X_2}, \dots, \mu_{X_N}) + \sum_{i=1}^N (X_i - \mu_{X_i}) \frac{\partial g}{\partial X_i} \quad (7.4)$$

where the value of $g(\mu_{X_1}, \mu_{X_2}, \dots, \mu_{X_N})$ is the mean response μ_Y . The mean response is obtained from the simulation where all the input parameters are set to the mean (base) values. The variance of the output variable can be expressed as

$$\sigma_Y^2 \approx \sum_{i=1}^N \sum_{j=1}^N \text{cov}(X_i, X_j) \frac{\partial g}{\partial X_i} \frac{\partial g}{\partial X_j} \quad (7.5)$$

where $\text{cov}(X_i, X_j)$ is the covariance of X_i and X_j which can be expressed as

$$\text{cov}(X_i, X_j) = \rho_{X_i, X_j} \sigma_{X_i} \sigma_{X_j} \quad (7.6)$$

and ρ_{X_i, X_j} is the correlation coefficient, which varies from -1 to 1. Since the covariance of a variable with itself is the variance of that variable, Equation (7.8) can be expressed as

$$\sigma_{Y \approx}^2 = \sum_{i=1}^N \sigma_{X_i}^2 \left(\frac{\partial g}{\partial X_i} \right)^2 + \sum_{i=1}^N \sum_{j \neq i}^N \rho_{X_i X_j} \sigma_{X_i} \sigma_{X_j} \frac{\partial g}{\partial X_i} \frac{\partial g}{\partial X_j} \quad (7.7)$$

In this work gradients were approximated numerically by central differences over a range of $\mu_{X_i} - \sigma_{X_i} / 2$ to $\mu_{X_i} + \sigma_{X_i} / 2$ for each variable; the values of the correlation coefficients ($\rho_{X_i X_j}$) between input parameters were approximated as shown in Table 7.8. These values were determined approximately considering possible correlations with judgment. Most of the correlation coefficients between soil and structural parameters were set to zero.

Table 7.8 Correlation coefficients for uncertain input parameters.

		x1	x2	x3	x4	x5	x6	x7	x8	x9	x10	x11	x12	x13	x14	x15
x1	embank(G)	1.0														
x2	clay(G)	0.0	1.0													
x3	sand(G)	0.0	0.0	1.0												
x4	clay(c)	0.0	0.6	0.0	1.0											
x5	sand(ρ)	0.5	0.0	0.6	0.0	1.0										
x6	cntr1	0.0	0.0	0.5	0.0	0.9	1.0									
x7	pile(p_{ult})	0.4	0.4	0.4	0.9	0.9	0.7	1.0								
x8	pile(y_{50})	0.4	0.4	0.4	0.8	0.9	0.7	0.7	1.0							
x9	pile(p_{res})	0.0	0.0	0.3	0.0	0.7	0.8	0.8	0.3	1.0						
x10	pCap(p_{ult})	0.0	0.7	0.0	0.9	0.0	0.0	0.0	0.0	0.0	1.0					
x11	pCap(y_{50})	0.0	0.9	0.0	0.8	0.0	0.0	0.0	0.0	0.0	0.5	1.0				
x12	abutW(p_{ult})	0.7	0.0	0.0	0.0	0.8	0.0	0.0	0.0	0.0	0.0	0.0	1.0			
x13	abutW(y_{50})	0.9	0.0	0.0	0.0	0.8	0.0	0.0	0.0	0.0	0.0	0.0	0.5	1.0		
x14	breakW(F_y)	0.0	0.0	0.0	0.0	0.0	0.0	0.0	0.0	0.0	0.0	0.0	0.0	0.0	1.0	
x15	bPad(K)	0.0	0.0	0.0	0.0	0.0	0.0	0.0	0.0	0.0	0.0	0.0	0.0	0.0	0.0	1.0

EDP uncertainties were obtained based on Equation (6.10) using simulation results using four input motions. The estimated uncertainties for each *EDP* are presented in Table 7.9.

Table 7.9 Summary of parametric uncertainty.

EDP symbol	$\sigma_{\ln(\text{EDP} \text{IM})}$				$\sigma_{\ln(\text{EDP} \text{IM})}$ average
	Northridge (0.1g)	Northridge (0.25g)	A03 (0.46g)	B10 (0.70g)	
$C1_{[\text{drift,max}]}$	0.018	0.040	0.401	0.075	0.134
$C2_{[\text{drift,max}]}$	0.023	0.025	0.024	0.044	0.031
$C3_{[\text{drift,max}]}$	0.013	0.042	0.029	0.042	0.031
$C4_{[\text{drift,max}]}$	0.008	0.052	0.042	0.076	0.045
$P0_{[\text{drift,res}]}$	0.062	0.064	0.090	0.056	0.068
$P1_{[\text{drift,res}]}$	0.118	0.344	0.588	0.082	0.283
$P2_{[\text{drift,res}]}$	0.784	0.060	0.041	0.653	0.384
$P3_{[\text{drift,res}]}$	0.288	0.051	0.042	0.095	0.119
$P4_{[\text{drift,res}]}$	0.219	0.035	0.029	0.065	0.087
$P5_{[\text{drift,res}]}$	0.236	0.086	0.047	0.049	0.105
$EJ1_{[\text{gap,max}]}$	0.346	0.031	0.070	0.074	0.130
$EJ2_{[\text{gap,max}]}$	0.695	0.121	0.075	0.100	0.248
$BW1_{[\text{dx,max}]}$	0.016	0.027	0.022	0.051	0.029
$BW2_{[\text{dx,max}]}$	0.010	0.012	0.018	0.056	0.024
$BA1_{[\text{dy,max}]}$	0.020	0.039	0.025	0.055	0.035
$BA2_{[\text{dy,max}]}$	0.040	0.066	0.043	0.084	0.058
$BP1_{[\text{dx,max}]}$	0.346	0.031	0.070	0.074	0.130
$BP2_{[\text{dx,max}]}$	0.695	0.121	0.075	0.100	0.248
$E1_{[\text{dx,res}]}$	0.059	0.067	0.081	0.054	0.065
$E2_{[\text{dx,res}]}$	0.019	0.034	0.022	0.049	0.031
$E1_{[\text{dy,res}]}$	0.227	0.080	0.047	0.048	0.101
$E2_{[\text{dy,res}]}$	0.035	0.063	0.039	0.080	0.054

7.2.6 Spatial Variability Effects

To investigate the spatial variability uncertainty, Gaussian stochastic random fields were generated for the clay and liquefiable soil layers by randomizing the assigned soil strength parameter over the soil layers with a certain spatial correlation. This section briefly describes the method used to develop the stochastic fields and presents the estimated bridge response uncertainty values due to spatial variability. For this purpose 10 random field simulations were performed for several earthquake motions.

7.2.6.1 Spatial Variability within Homogeneous Soil Deposits

The physical properties of soils vary from place to place within a soil deposit due to varying geologic formation and loading histories such as sedimentation, erosion, transportation, and weathering processes. This spatial variability in the soil properties cannot be simply described by

a mean and variance, since the estimation of the two statistic values does not account for the spatial variation of the soil property data in the soil profile.

Spatial variability is often modeled using two separated components: a known deterministic trend and a residual variability about the trend. These components are illustrated in Figure 6.26.

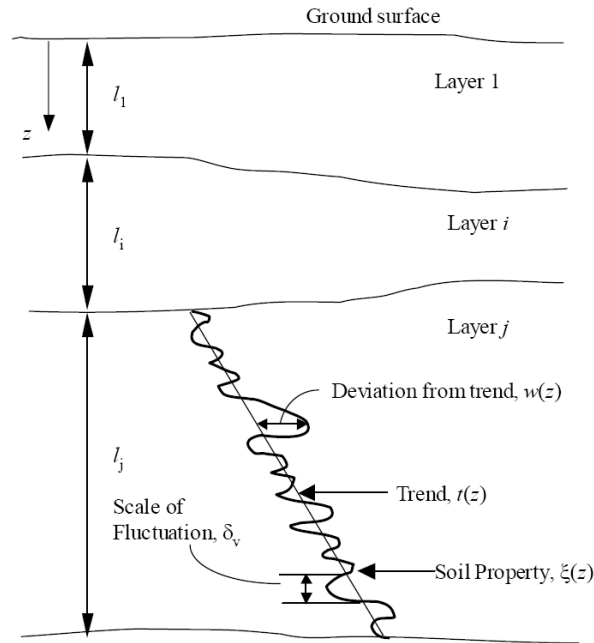


Fig. 7.10 Inherent soil variability (after Phoon and Kulhawy 1999).

The simplified spatial variability (Phoon and Kulhawy 1999) can be expressed as

$$\xi(z) = t(z) + w(z) \quad (7.8)$$

where $\xi(z)$ = soil property at location z , $t(z)$ = deterministic trend at z , and $w(z)$ = residual variation. The trend is a smooth deterministic function that can be obtained from a regression analysis of measured data. The residuals are characterized statistically as random variables, usually with zero mean and non-zero variance. The pattern of the residuals depends on the local spatial variability of a property. The residual about a trend does not change erratically in a probabilistically independent way. Rather, similar property values (positive or negative residuals around a trend) are more likely for closely spaced points than for points at large distances as shown in Figure 6.27. This spatial distribution can be described by a spatial correlation, referred to as autocorrelation, which represents the correlation of an individual variable with itself over

space. This degree of association can be characterized by a correlation coefficient that varies with separation distance.

7.2.6.2 Generation of Gaussian Random Fields

As described earlier, the stochastic random field for a soil property consists of a trend (or mean) field and a residual field.

$$F_{stochastic} = F_{trend} + F_{residual} \quad (7.9)$$

The trend field represents the deterministic mean field shown in Tables 5.1 and 5.2. To obtain the residual field, a Gaussian random field was generated using the generation algorithm proposed by Yamazaki and Shinozuka (1988).

In the Gaussian field generation used in this study, the standard deviation of spectral density function was set to 1.0 and the correlation decay coefficients were set to 1.0. The wave number increment (Δk_x) in the x-direction was determined considering the ratio of the length and height of the space. Several samples of the generated Gaussian field are shown in Figure 7.11.

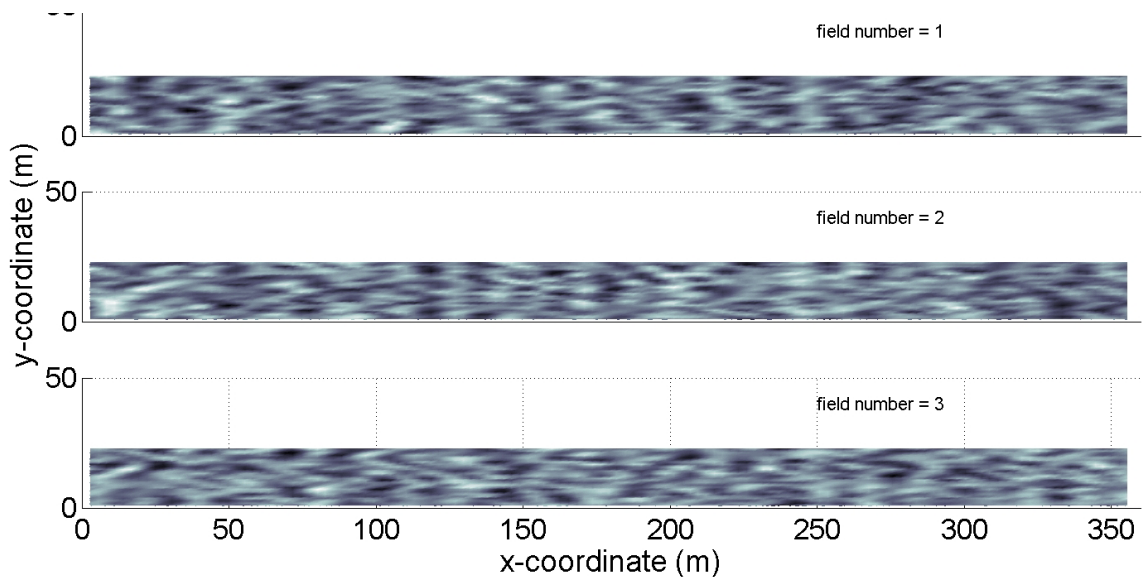


Fig. 7.11 Example of generated Gaussian fields.

In the numerical simulation, since individual soil elements had different soil properties, the stochastic random field was expressed in matrix form as

$$F_{stochastic}(i, j) = F_{mean}(i, j) + F_{residual}(i, j) = F_{mean}(i, j) + F_{mean}(i, j)F_{Gaussian}(i, j) \quad (7.10)$$

where i and j represent the element position in the horizontal and vertical directions. $F_{stochastic}$ is a matrix of stochastic random fields for a soil property, F_{mean} is a matrix of deterministic mean fields, COV is the coefficient of variance of the considered soil property, and $F_{Gaussian}$ represents the residual Gaussian field in matrix form. The dimension of the generated field matrix was the same as that of the soil mesh used in the numerical simulations. That is, the rectangular soil domain that includes loose sand and clay layers below the ground surface and above the dense sand layer (i.e., layer 2, 3, and 4 in Fig. 4.1). The generated Gaussian field could not be directly used in the simulation, since values in the field were calculated for uniform incremental positions in the horizontal and vertical direction, whereas the soil mesh in the OpenSees model did not have uniform element size. Therefore, the values obtained using Yamazaki and Shinozuka (1988)'s method were interpolated according to the soil element center locations. The steps in the random field generation procedure for the bridge analyses were as follows:

1. Generate mean field using mean target soil properties
2. Generate Gaussian random (autocorrelated) fields for ϕ and c in the loose sand and clay layers with mean = 0.0 and $\sigma = 1.0$: Yamazaki and Shinozuka (1988)
3. Normalize the Gaussian field by its maximum value
4. Interpolate the Gaussian field to the FEM mesh
5. Determine COV values for ϕ and c
6. Combine the mean field and Gaussian field to obtain a stochastic field using Equation (7.12).

To illustrate the difference between deterministic and stochastic fields, a stochastic field friction angle was considered for the loose sand layer. Figure 6.28 illustrates the mean, Gaussian, and total friction angle parameter fields.

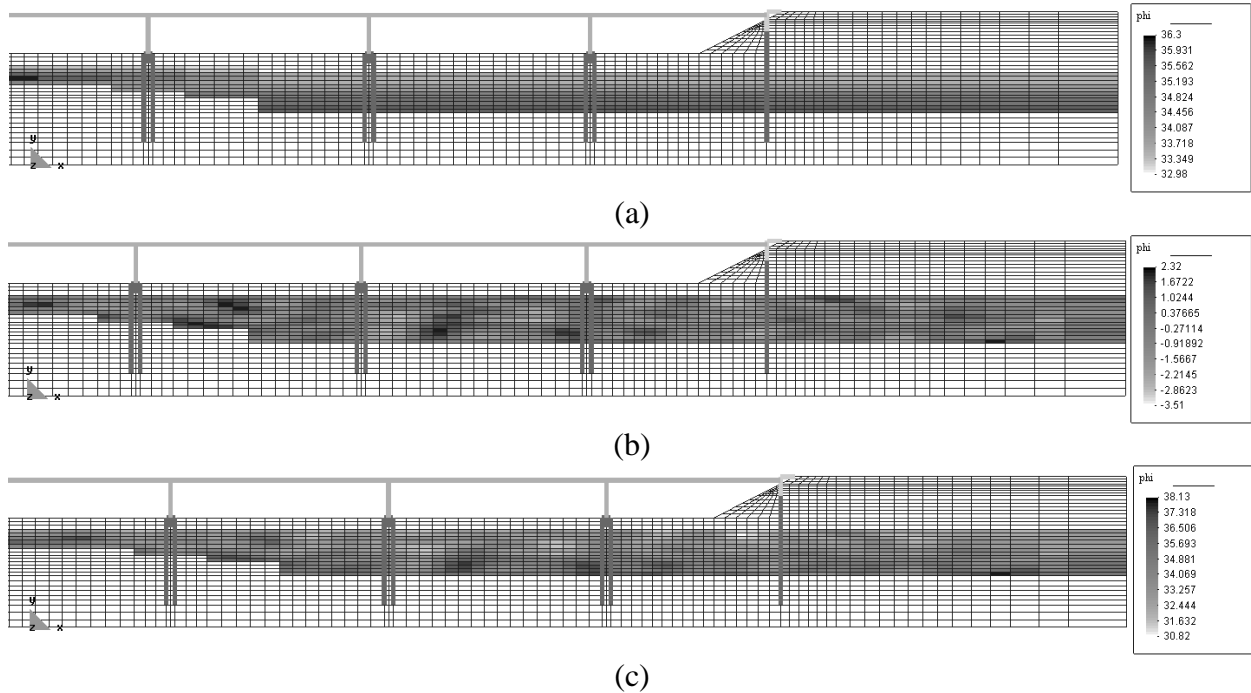


Fig. 7.12 Development of random field for friction angle in loose, saturated sand layer; (a) mean friction angle, (b) residual friction angle, and (c) total friction angle.

7.2.6.3 Effects of Spatial Variability

To evaluate the effects of spatial variability, 10 random fields were generated and analyzed. *COV* values of 0.1 and 0.3 were assumed for the loose sand friction angle and undrained shear strength of clay, respectively. When only loose sand was considered in the Gaussian field, the clay layer was assigned its mean property values. Similarly, when only the clay soil was considered in the random field generation, the sand soil elements were assigned their corresponding mean friction angles. Using several motions corresponding to different hazard levels, the response of the bridge model based on 10 stochastic fields was obtained and the resulting spatial variability uncertainties were investigated for three cases: (1) loose sand and clay, (2) only loose sand, and (3) only clay. Since there was some variation in the spatial uncertainty values due to the effect of different input motions, the uncertainty values were averaged. The results are summarized in Tables 7.10–7.12. Overall, the estimated uncertainties that originated from considering spatial variability of strength parameters in the loose sand and clay soil were quite small compared to record-to-record uncertainty and parametric uncertainty.

Table 7.10 Summary of spatial variability uncertainty (loose sand plus clay).

EDP symbol	Northridge (0.1g)	Northridge (0.25g)	A03 (0.46g)	B10 (0.70g)	average
$C1_{[drift,max]}$	0.008	0.096	0.020	0.066	0.048
$C2_{[drift,max]}$	0.004	0.118	0.018	0.035	0.044
$C3_{[drift,max]}$	0.005	0.012	0.009	0.048	0.018
$C4_{[drift,max]}$	0.004	0.071	0.053	0.072	0.050
$P0_{[drift,res]}$	0.053	0.059	0.052	0.085	0.062
$P1_{[drift,res]}$	0.209	0.189	0.094	0.073	0.141
$P2_{[drift,res]}$	0.108	0.188	0.067	0.488	0.213
$P3_{[drift,res]}$	0.102	0.108	0.048	0.089	0.087
$P4_{[drift,res]}$	0.098	0.075	0.049	0.032	0.064
$P5_{[drift,res]}$	0.080	0.062	0.039	0.044	0.056
$EJ1_{[gap,max]}$	0.016	0.018	0.027	0.070	0.033
$EJ2_{[gap,max]}$	0.004	0.004	0.008	0.008	0.006
$BW1_{[dx,max]}$	0.002	0.005	0.005	0.019	0.008
$BW2_{[dx,max]}$	0.001	0.001	0.002	0.001	0.001
$BA1_{[dy,max]}$	0.009	0.029	0.010	0.096	0.036
$BA2_{[dy,max]}$	0.024	0.041	0.027	0.055	0.037
$BP1_{[dx,max]}$	0.012	0.079	0.016	0.040	0.037
$BP2_{[dx,max]}$	0.004	0.071	0.018	0.050	0.036
$E1_{[dx,res]}$	0.043	0.058	0.044	0.080	0.057
$E2_{[dx,res]}$	0.010	0.025	0.006	0.088	0.032
$E1_{[dy,res]}$	0.067	0.062	0.038	0.040	0.051
$E2_{[dy,res]}$	0.019	0.045	0.029	0.053	0.036

Table 7.11 Summary of spatial variability uncertainty (loose sand).

EDP symbol	Northridge (0.1g)	Northridge (0.25g)	A03 (0.46g)	B10 (0.70g)	average
$C1_{[drift,max]}$	0.003	0.019	0.015	0.026	0.016
$C2_{[drift,max]}$	0.002	0.013	0.014	0.019	0.012
$C3_{[drift,max]}$	0.003	0.008	0.007	0.011	0.007
$C4_{[drift,max]}$	0.002	0.056	0.054	0.057	0.042
$P0_{[drift,res]}$	0.005	0.040	0.027	0.044	0.029
$P1_{[drift,res]}$	0.123	0.070	0.081	0.036	0.077
$P2_{[drift,res]}$	0.095	0.083	0.058	0.233	0.117
$P3_{[drift,res]}$	0.094	0.045	0.042	0.075	0.064
$P4_{[drift,res]}$	0.089	0.049	0.046	0.036	0.055
$P5_{[drift,res]}$	0.076	0.056	0.043	0.019	0.048
$EJ1_{[gap,max]}$	0.003	0.004	0.030	0.002	0.010
$EJ2_{[gap,max]}$	0.001	0.002	0.005	0.002	0.002
$BW1_{[dx,max]}$	0.000	0.001	0.005	0.001	0.002
$BW2_{[dx,max]}$	0.000	0.000	0.001	0.000	0.000
$BA1_{[dy,max]}$	0.002	0.029	0.005	0.040	0.019
$BA2_{[dy,max]}$	0.023	0.035	0.029	0.046	0.033
$BP1_{[dx,max]}$	0.002	0.034	0.018	0.029	0.021
$BP2_{[dx,max]}$	0.001	0.064	0.022	0.023	0.028
$E1_{[dx,res]}$	0.005	0.037	0.024	0.041	0.027
$E2_{[dx,res]}$	0.002	0.024	0.004	0.031	0.015
$E1_{[dy,res]}$	0.063	0.055	0.041	0.019	0.045
$E2_{[dy,res]}$	0.017	0.038	0.030	0.045	0.033

Table 7.12 Summary of spatial variability uncertainty (clay).

EDP symbol	Northridge (0.1g)	Northridge (0.25g)	A03 (0.46g)	B10 (0.70g)	average
$C1_{[drift,max]}$	0.008	0.025	0.019	0.221	0.068
$C2_{[drift,max]}$	0.003	0.006	0.017	0.299	0.081
$C3_{[drift,max]}$	0.003	0.006	0.008	0.071	0.047
$C4_{[drift,max]}$	0.003	0.020	0.060	0.205	0.072
$P0_{[drift,res]}$	0.051	0.071	0.036	0.063	0.055
$P1_{[drift,res]}$	0.130	0.106	0.078	0.065	0.095
$P2_{[drift,res]}$	0.023	0.101	0.046	0.637	0.202
$P3_{[drift,res]}$	0.018	0.051	0.026	0.159	0.063
$P4_{[drift,res]}$	0.018	0.022	0.047	0.041	0.032
$P5_{[drift,res]}$	0.017	0.034	0.013	0.050	0.028
$EJ1_{[gap,max]}$	0.014	0.015	0.028	0.069	0.032
$EJ2_{[gap,max]}$	0.003	0.004	0.007	0.007	0.005
$BW1_{[dx,max]}$	0.002	0.004	0.005	0.018	0.007
$BW2_{[dx,max]}$	0.000	0.001	0.001	0.001	0.001
$BA1_{[dy,max]}$	0.009	0.023	0.009	0.098	0.035
$BA2_{[dy,max]}$	0.006	0.018	0.006	0.029	0.015
$BP1_{[dx,max]}$	0.012	0.036	0.010	0.219	0.069
$BP2_{[dx,max]}$	0.003	0.042	0.005	0.199	0.062
$E1_{[dx,res]}$	0.042	0.069	0.030	0.060	0.050
$E2_{[dx,res]}$	0.010	0.018	0.006	0.090	0.031
$E1_{[dy,res]}$	0.015	0.032	0.012	0.044	0.026
$E2_{[dy,res]}$	0.005	0.014	0.007	0.025	0.013

7.2.6.4 Relative Contributions to Total Uncertainty

The preceding analyses were performed to investigate the effects of record-to-record variability, parametric uncertainty, and spatial variability on uncertainty in system response. The analyses showed that record-to-record variability contributed much more strongly to overall *EDP* uncertainty than did parametric uncertainty; the effects of spatial variability were observed to be small.

7.2.7 Results of Analyses with Ground Motion Database

Following the investigation of the relative effects of record-to-record variability and parametric uncertainty, analyses were performed with the database of 40 hazard-consistent ground motions. Because record-to-record variability was shown to have much more effect on *EDP* uncertainty than parametric uncertainty, these analyses were performed using mean values of the soil and structural parameters. The analyses produced voluminous amounts of data, which were

cataloged, analyzed, and summarized in the form of relatively simple *EDP-IM* relationships. In the following sections, examples of the results of these analyses are presented for a few geotechnically related *EDPs*; then, the results for all *EDPs* are presented in terms of the simplified *EDP-IM* model parameters.

7.2.7.1 Lateral Soil Deformations

An important effect of the presence of the loose, saturated sand layer is the development of permanent soil deformations due to lateral spreading. Figure 7.13 illustrates profiles of permanent lateral deformation within the soil below the embankments (Soil 0 and Soil 5) and at the locations of each bridge pier (Soil 1–Soil 4) for ground shaking consistent with all four hazard levels. The recorded permanent deformations can be seen to vary significantly for each hazard level due to record-to-record variability. The average permanent deformations can be seen to increase with increasing return period; for stronger shaking (longer return periods), significant permanent deformations can be seen to develop in the clay crust that overlies the loose, saturated sand layer.

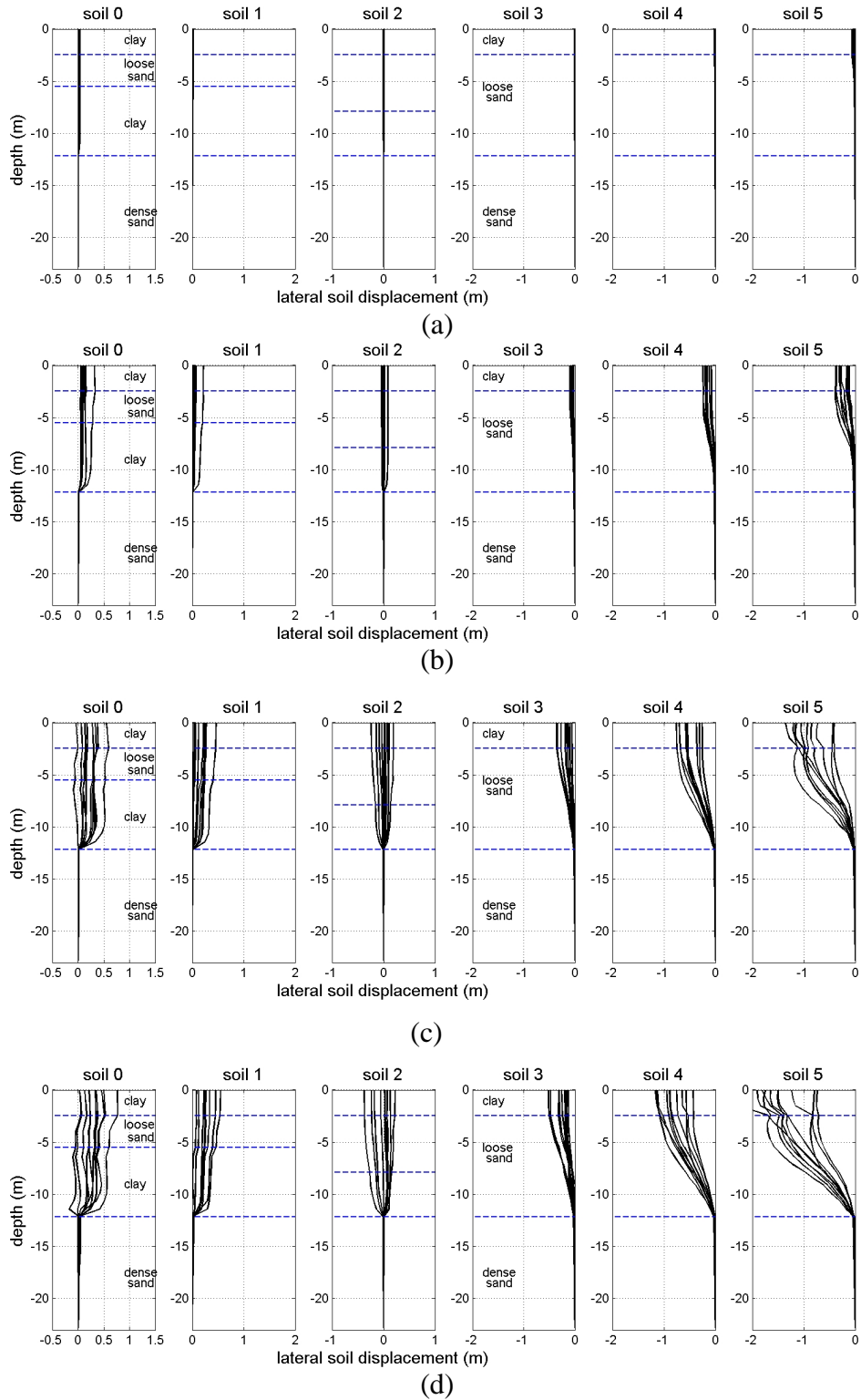


Fig. 7.13 Variation of horizontal subsurface displacements for ground motions with (a) 15-yr return period, (b) 72-yr return period, (c) 475-yr return period, and (d) 2475-yr return period.

Lateral spreading can also be seen to generally be greater below the right abutment (Soil 5) than the left abutment (Soil 0), thereby implying that damage to the bridge would be larger on the right side than on the left. An evaluation of the drift demands on the bridge columns, however, shows that the global interaction between the bridge, its foundations, and the soil serves to shift the bridge deck to the left for some ground motions. As a result, the difference between the displacements of the upper and lower ends of the bridge piers, as shown in Figure 7.14, are actually greater on the left side of the bridge (Pier 1) than on the right. (Pier 4). While not observed for all motions, this aspect of potential system behavior represents a significant potential mode of deformation that should be considered in design.

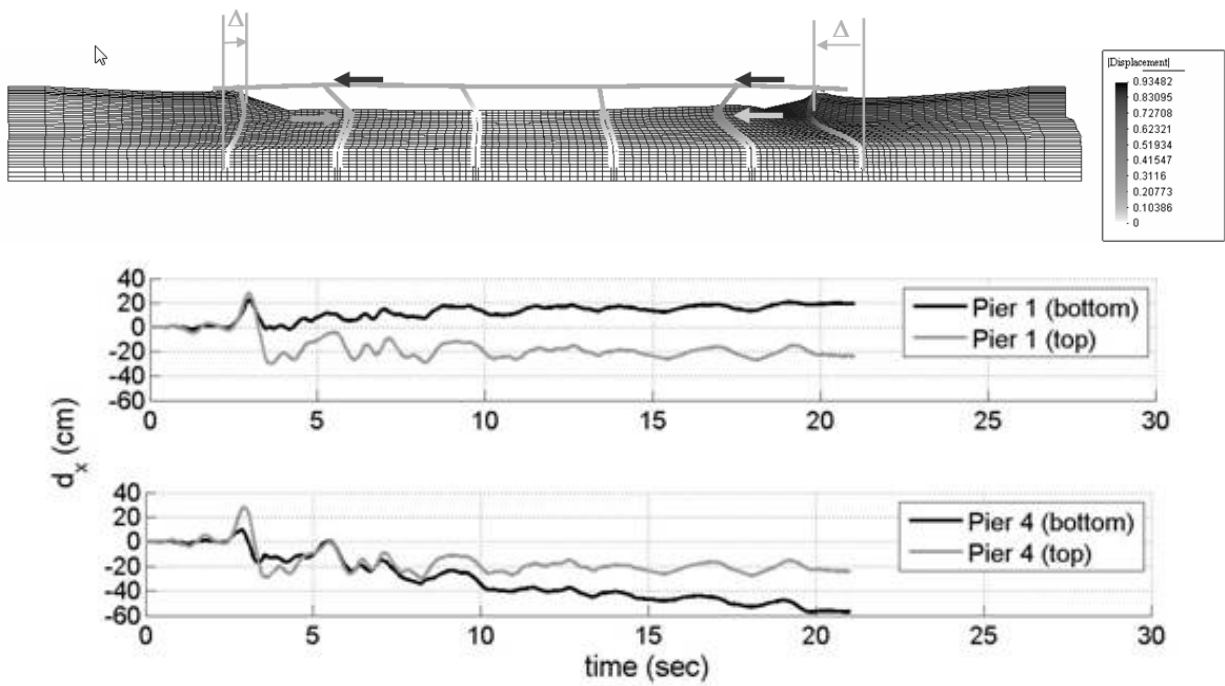


Fig. 7.14 Horizontal displacements at tops and bottoms of Piers 1 and 4. Note that absolute displacement of Pier 4 (bottom) is larger than that of Pier 1, but difference between top and bottom displacements is larger at Pier 1 than Pier 4.

The OpenSees analyses were also able to compute parameters such as the development of gaps at the abutments. Figure 7.15 shows how the sizes of horizontal gaps in the expansion joints at the left and right abutments of the bridge vary with peak ground velocity. The ability of OpenSees to handle soil-pile-structure interaction allows estimation of the lateral displacements of the pile caps supporting the abutments and each of the interior bridge piers (Fig. 7.16); it should be noted that these displacements reflect the lateral spreading that occurs at different pier locations, the interaction of the laterally spreading soil and overlying crust with the piles and pile caps, and the global deformations of the bridge itself.

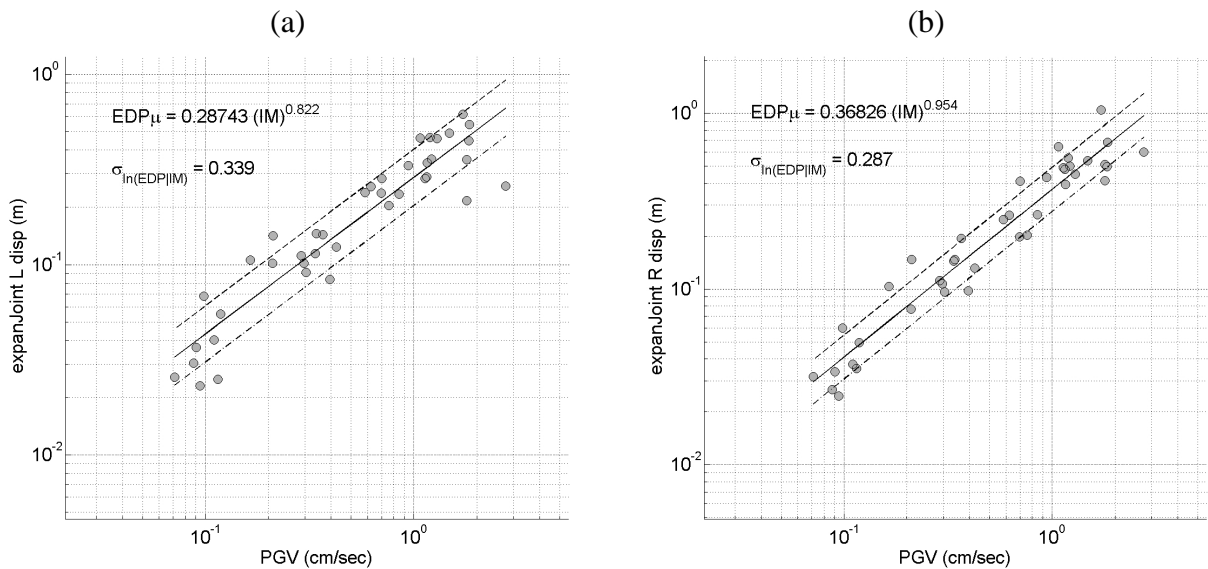


Fig. 7.15 Relationship between PGV and (a) expansion joint displacement at left abutment, (b) expansion joint displacement at right abutment.

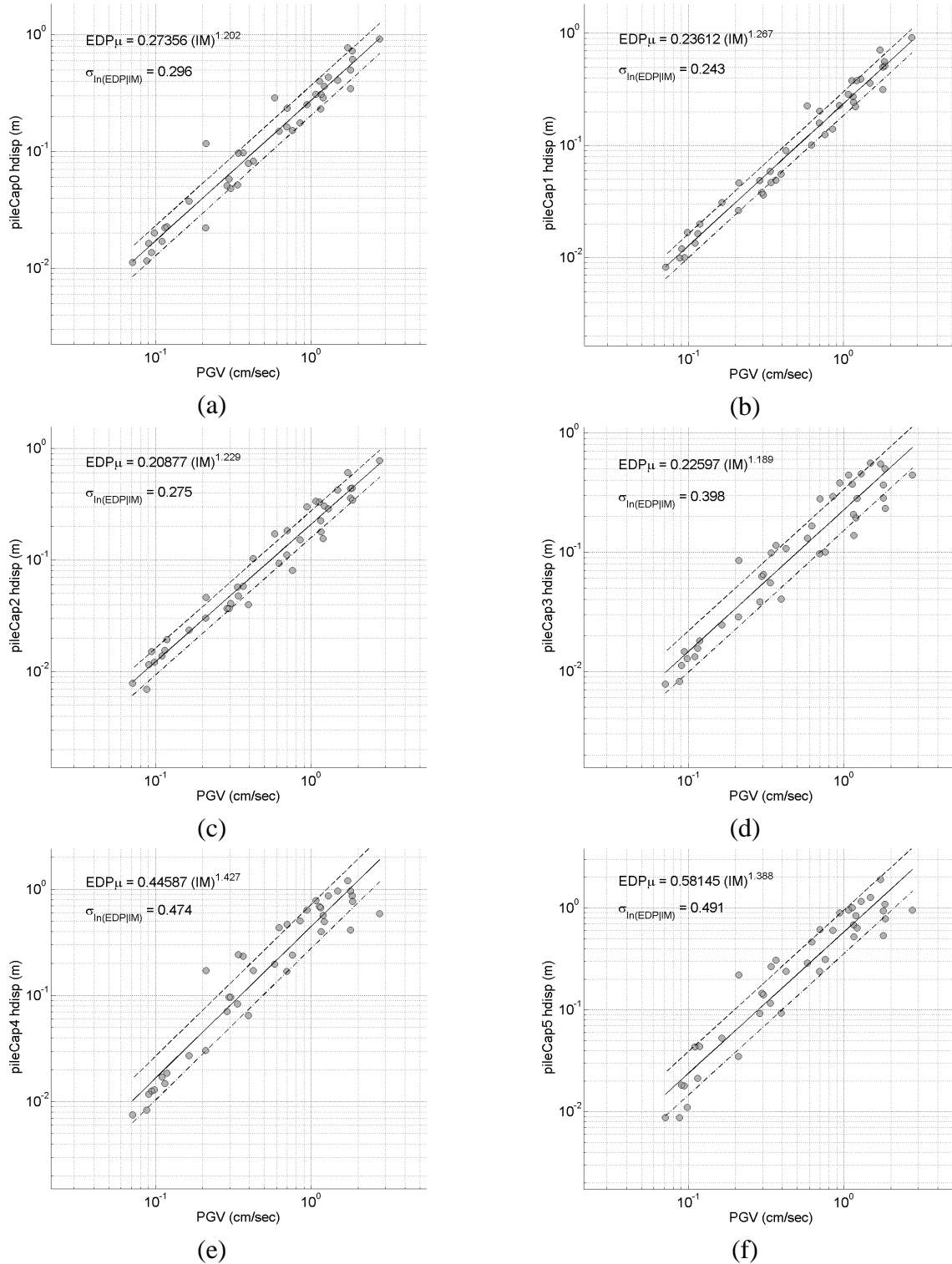


Fig. 7.16 Relationship between PGV and pile cap horizontal displacement for (a) Pier 0 (left abutment), (b) Pier 1, (c) Pier 2, (d) Pier 3, (e) Pier 4, and (f) Pier 5 (right abutment).

7.2.7.2 Vertical Soil Deformations

The OpenSees analyses also provide the ability to predict vertical soil deformations, such as those that could result from differential settlement between the pile-supported bridge and the bridge approach embankments. Figure 7.17 shows the relative vertical displacements at the left and right abutments; the vertical displacements can be seen to be higher at the right abutment than the left, as would be expected due to the greater thickness of looser soils on the right and the greater level of permanent lateral displacements beneath the right abutment.

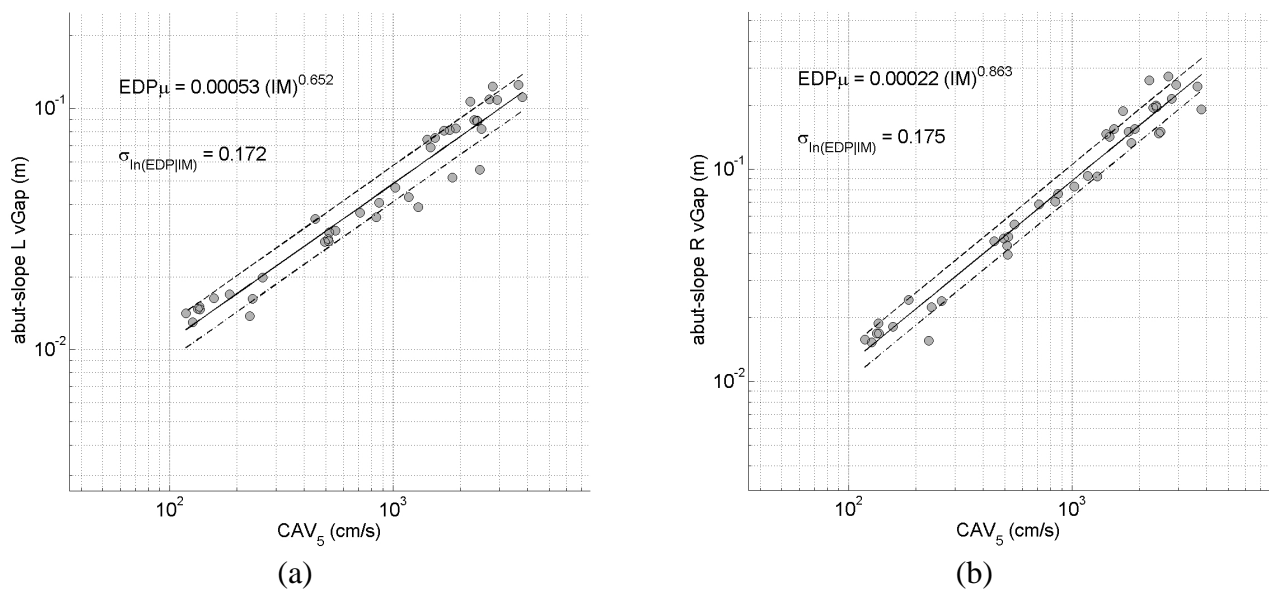


Fig. 7.17 Relationship between CAV_5 and (a) vertical gap at left abutment, and (b) vertical gap at right abutment.

7.2.7.3 Structural Response

An important benefit of the type of detailed soil-foundation-structure modeling utilized in this study is the ability to directly compute estimated structural response. The use of OpenSees provides a particularly beneficial opportunity to investigate the effects of lateral spreading deformations on all significant aspects of structural response.

Figure 7.18 shows the variation of interior pier drift with PGV for the 40 input motions. The curves indicate (by virtue of exponents close to unity) nearly linear relationships between drift and PGV, but the scatter in the response varies significantly from one pier to another. Figure 7.19 shows the median *EDP-IM* relationships plotted on arithmetic axes. The drift in the two outer piers is greater than in the interior piers for the same level of peak velocity.

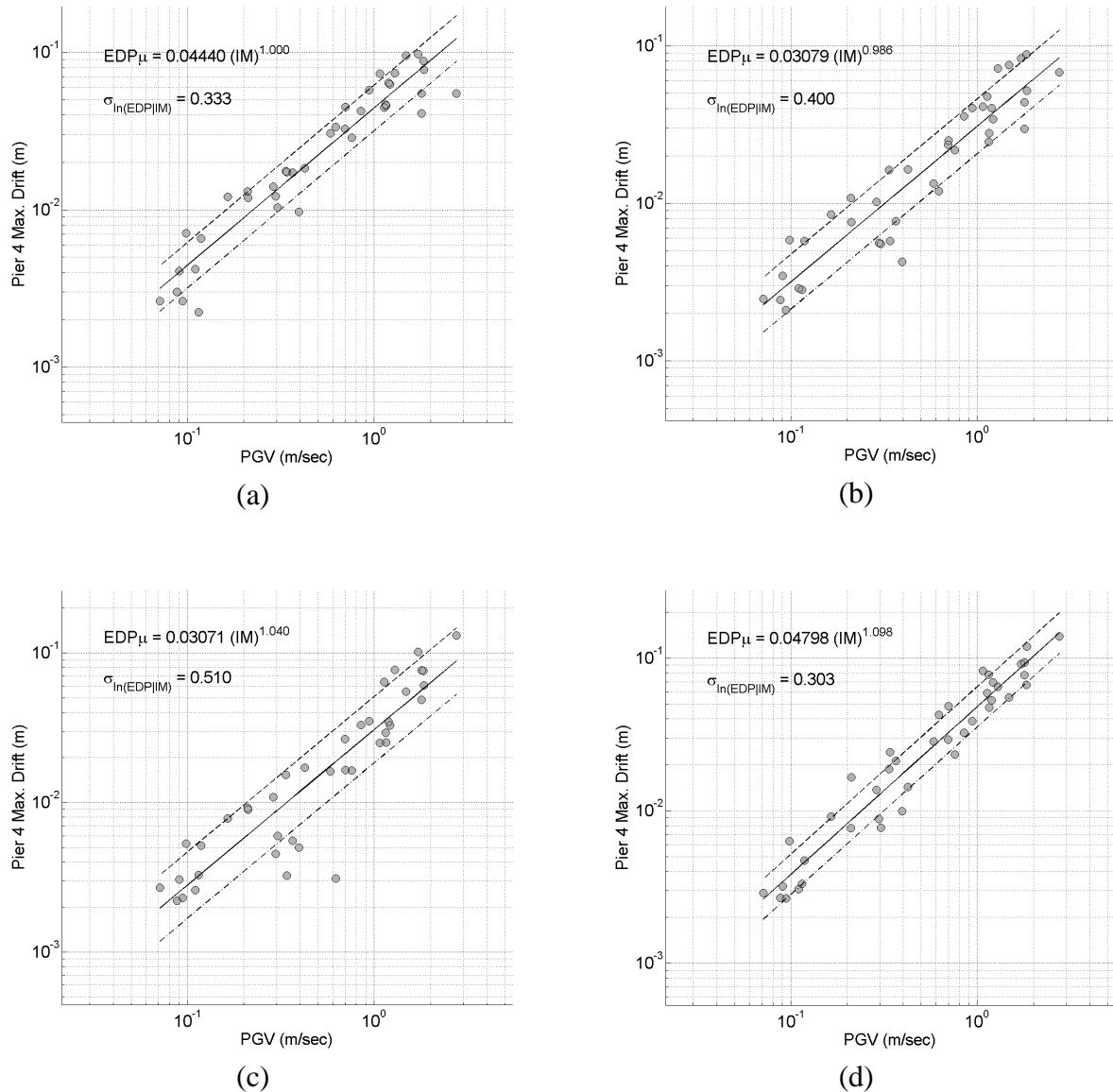


Fig. 7.18 Relationship between PGV and column drift for (a) Pier 1, (b) Pier 2, (c) Pier 3, and (d) Pier 4.

The pile force distribution and pile cap movement were significantly influenced by lateral spreading and the pattern of soil displacement with depth. This effect varied with ground motion intensity. Figures 7.19 and 7.20 show maximum bending moments and their locations for motions corresponding to all four hazard levels in Pile 0 at the left abutment, and Piles 4 and 5 at the right abutment. In Pile 0, maximum bending moments occurred for most motions at the interface between the clay and dense sand layers. In Pile 4, the maximum pile moment occurred, for small and moderate shaking, below the pile cap or at the interface between the surface clay and lower loose sand layers. However, for higher intensities, the maximum bending moment location moved down to the interface between the loose and dense sand layers (around 12 m depth). Similar patterns were observed in Pile 5. However, for moderate shaking (72-year return period, Motions 11–20 in Fig. 7.20(b)), the maximum bending moments occurred in the middle of the loose sand layer. This can be related to the fact that the upper portion of the loose sand layer was liquefied, while the lower portion was not fully liquefied for these strong motions. For stronger motions (i.e., 475- and 2475-year return periods, Motions 21–40 in Fig. 7.20(b)), the maximum pile bending moment reached the ultimate bending moment capacity.

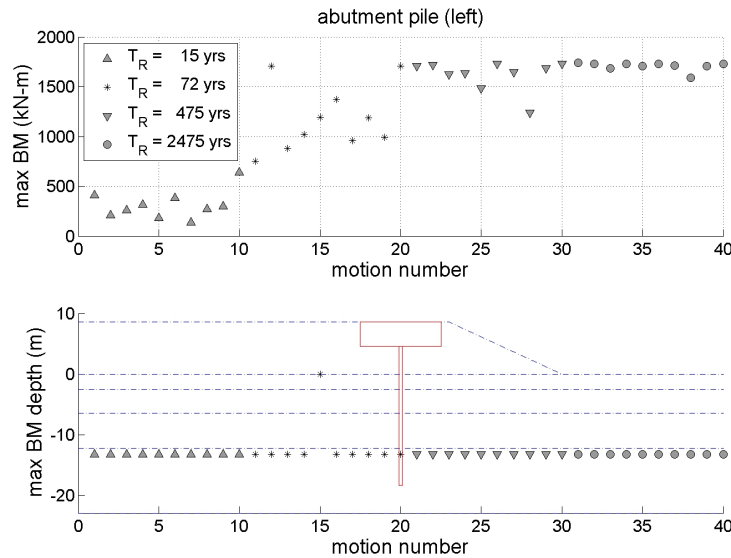


Fig. 7.19 Location of maximum pile bending moment in Pile 0 at left abutment.

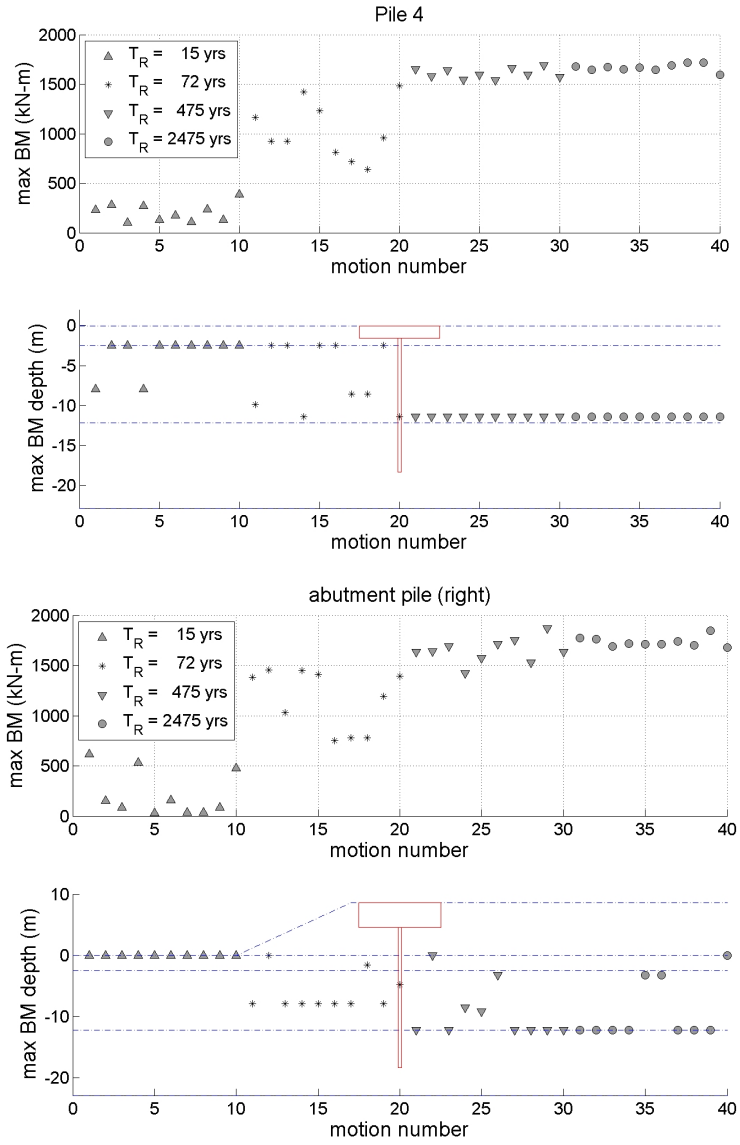


Fig. 7.20 Location of maximum pile curvatures in Piles 4 and 5 at right abutment.

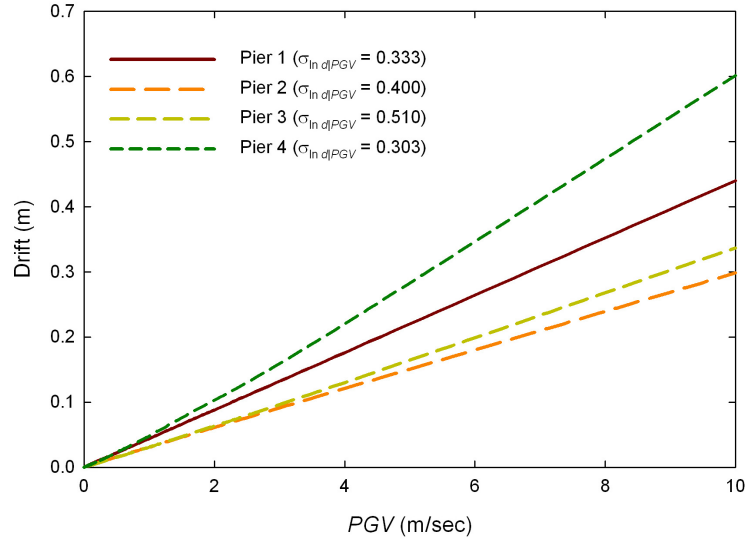


Fig. 7.21 Variation of median pier drift with PGV.

7.2.7.4 Simplified EDP-IM Model

In order to organize and process the large amounts of *EDP* data produced by the OpenSees simulations, the results of the simulations were interpreted in terms of a relatively simple power law model. The model is of the power law form

$$EDP = cIM^b \quad (7.11)$$

which has been found to approximate the response of structures with reasonable accuracy (refs). Table 7.13 presents a summary of the response model coefficients as interpreted in the simplified form of Equation (7.13).

Table 7.13 Summary of EDP hazard curve: exponential coefficient.

EDP symbol	coefficient <i>c</i>	coefficient <i>d</i>	EDP range
<i>C1</i> [drift,max]	7.8354e-07	-2.5698	0.2 - 9.7 (%)
<i>C2</i> [drift,max]	4.2444e-07	-2.4978	0.2 - 8.8 (%)
<i>C3</i> [drift,max]	1.2170e-06	-2.2352	0.2 - 13.1 (%)
<i>C4</i> [drift,max]	2.1292e-06	-2.2439	0.3 - 13.8 (%)
<i>P0</i> [drift,res]	5.7960e-04	-2.3869	0.000 - 0.562 (m)
<i>P1</i> [drift,res]	1.0018e-04	-2.0973	0.001 - 0.502 (m)
<i>P2</i> [drift,res]	1.2409e-04	-2.1365	0.000 - 0.346 (m)
<i>P3</i> [drift,res]	1.6531e-04	-1.4586	0.001 - 0.527 (m)
<i>P4</i> [drift,res]	9.0295e-04	-1.2342	0.000 - 1.198 (m)
<i>P5</i> [drift,res]	1.0782e-03	-1.4413	0.001 - 1.866 (m)
<i>EJ1</i> [gap,max]	1.2992e-05	-2.6119	0.004 - 0.567 (m)
<i>EJ2</i> [gap,max]	3.4581e-06	-3.4115	0.004 - 0.217 (m)
<i>BW1</i> [dx,max]	8.4257e-08	-8.0652	0.000 - 0.667 (m)
<i>BW2</i> [dx,max]	1.1128e-10	-11.382	0.000 - 0.317 (m)
<i>BA1</i> [dy,max]	1.0650e-07	-3.6588	0.013 - 0.125 (m)
<i>BA2</i> [dy,max]	7.6176e-06	-2.7629	0.015 - 0.274 (m)
<i>BP1</i> [dx,max]	2.2324e-04	-1.8777	0.004 - 0.589 (m)
<i>BP2</i> [dx,max]	4.8268e-04	-1.7349	0.003 - 0.997 (m)
<i>E1</i> [dx,res]	5.8392e-05	-2.8123	0.003 - 0.563 (m)
<i>E2</i> [dx,res]	9.7270e-04	-1.4806	0.002 - 1.840 (m)
<i>E1</i> [dy,res]	3.1000e-07	-3.6142	0.015 - 0.178 (m)
<i>E2</i> [dy,res]	1.0355e-05	-2.8483	0.018 - 0.293 (m)

7.3 SUMMARY

An extensive series of analyses were performed to analyze the response of the highway testbed bridge to a wide range of earthquake ground motions. The analyses required the development and validation of a detailed finite element model of the soil, foundations, bridge, and abutments. The finite element model accounted for the nonlinear, inelastic behavior of soil and structural materials, and considered interface behavior (both shear and normal, including separation and contact) for piles, pile caps, and abutments. The model was validated by a series of analyses using two ground motions before beginning an extensive set of analyses to define the variation of response under earthquake loading corresponding to different hazard levels.

The response of the soil-foundation-structure system was expressed in terms of a series of *EDPs* that described both structural and geotechnical aspects of the system. These included the

drift of each column, displacement of each pile cap, displacement of each expansion joint, displacement of each abutment backwall, vertical offset at each abutment due to approach embankment settlement, displacement of each bearing pad, and the vertical and horizontal movement of each approach embankment.

The responses to 10 ground motions at each of four hazard levels was found to be reasonably represented by a simple power law relationship between *EDP* and *IM*. The relative efficiencies of a series of candidate *IMs* were investigated; different *IMs* were observed to be most efficient for different *EDPs*, but PGV was selected as the single most useful *IM* for the purpose of response, damage, and loss estimation. Power law relationships between PGV and all of the selected *EDPs* were established; the fragility curves based on these *EDP-IM* relationships were used for subsequent estimation of damage and loss.

8 Foundation Damage and Loss

8.1 INTRODUCTION

The bridge response computed using OpenSees analyses and described in the preceding chapter provides a basis for estimating the recurrence rate of different levels of physical damage to the bridge. Such estimates of physical damage can provide the basis for subsequent loss estimation using the PEER PBEE framework described in Chapter 2.

In order to produce loss (*DV*) estimates that could be directly compared with the loss estimates produced by Mackie and Stojadinović (2007b) for the fixed-base bridge model, the loss model developed by Mackie and Stojadinović was used. The initial version of this loss model did not produce explicit damage estimates for all of the performance groups for which *EDPs* were computed. In order to investigate the effects of liquefaction-induced lateral spreading on foundation performance, damage and loss models were developed for the pile-supported bridge foundations. This chapter describes these models and the levels of physical foundation damage and loss they predicted. A more complete loss model for the entire structure, including the foundations, is described in Chapter 9.

8.2 DAMAGE AND LOSS PROBABILITY MATRIX APPROACH

In the absence of data on physical damage and loss in the early stages of the project, a discrete damage and loss probability estimation approach was developed. This approach involved the development of damage and loss probability matrices for the pile-supported bridge foundations.

8.2.1 Methodology

For each *EDP*, ranges corresponding to a discrete number of damage states (e.g., negligible, slight, moderate, severe, and catastrophic) were defined. A damage probability matrix, X , was

then defined such that its elements represented the probabilities of being in damage state j given that the *EDP* is in *EDP* range i .

$$X_{ij} = P[DM = dm_j | EDP = edp_i] \quad (8.1)$$

For the case of the previously listed five damage states, the damage probability matrix is represented in tabular form as shown in Table 8.1.

Table 8.1 Damage probability matrix.

Damage State, DM	Description	<i>EDP</i> range				
		edp_1	edp_2	edp_3	edp_4	edp_5
dm_1	Negligible	X_{11}	X_{12}	X_{13}	X_{14}	X_{15}
dm_2	Slight	X_{21}	X_{22}	X_{23}	X_{24}	X_{25}
dm_3	Moderate	X_{31}	X_{32}	X_{33}	X_{34}	X_{35}
dm_4	Severe	X_{41}	X_{42}	X_{43}	X_{44}	X_{45}
dm_5	Catastrophic	X_{51}	X_{52}	X_{53}	X_{54}	X_{55}

Because a given value of the *DM* can come from different *EDP* ranges (i.e., there is uncertainty in the *EDP-DM* relationship), off-diagonal terms are present in the damage probability matrix shown in Table 8.1. In this matrix it is required that the values in vertical

columns sum to unity, i.e., that $\sum_{i=1}^{N_{DM}} X_{ij} = 1.0$ for all j . This is equivalent to saying that the

damage for a given *EDP* must fall into one of the five damage states. The total probability theorem was then used to compute the probability of being in a given damage state using the conditional distribution of $DM|EDP$ and the distribution of *EDP* ranges, i.e.,

$$P[DM = dm_j] = \sum_{i=1}^{N_{EDP}} P[DM = dm_j | EDP = edp_i] P[EDP = edp_i] \quad (8.2)$$

Following a similar approach, a series of loss states, each of which were described by discrete *DV* values, were also defined; the *DV* selected for the foundation loss evaluation was taken as the fraction of replacement cost of the foundation under consideration, a quantity

referred to subsequently as the repair cost ratio, RCR . The loss probability matrix, Y , was defined such that the individual elements

$$Y_{jk} = P[DV = dv_k / DM = dm_j] \quad (8.3)$$

The loss probability matrix can be illustrated in tabular form as shown in Table 8.2.

Table 8.2 Loss probability matrix.

Loss state State, DM	Damage state				
	dm_1	dm_2	dm_3	dm_4	dm_5
dv_1	Y_{11}	Y_{12}	Y_{13}	Y_{14}	Y_{15}
dv_2	Y_{21}	Y_{22}	Y_{23}	Y_{24}	Y_{25}
dv_3	Y_{31}	Y_{32}	Y_{33}	Y_{34}	Y_{35}
dv_4	Y_{41}	Y_{42}	Y_{43}	Y_{44}	Y_{45}
dv_5	Y_{51}	Y_{52}	Y_{53}	Y_{54}	Y_{55}

Because uncertainty exists in the cost associated with a given damage state, a given value of DV can result from different damage states. Therefore, the total probability theorem can again be used to compute the probability of a particular loss level given the different damage states.

$$P[DV = dv_k] = \sum_{j=1}^{N_{DM}} P[DV = dv_k | DM = dm_j] P[DM = dm_j] \quad (8.4)$$

Substituting Equation (8.3) into Equation (8.4) allows calculation of losses directly from response quantities; i.e., $EDPs$

$$P[DV = dv_k] = \sum_{j=1}^{N_{DM}} \sum_{i=1}^{N_{EDP}} P[DV = dv_k | DM = dm_j] P[DM = dm_j | EDP = edp_i] P[EDP = edp_i] \quad (8.5)$$

or, substituting Equations (8.1) and (8.2) into (8.5),

$$P[DV = dv_k] = \sum_{j=1}^{N_{DM}} \sum_{i=1}^{N_{EDP}} X_{ij} Y_{jk} P[EDP = edp_i] \quad (8.6)$$

From this, the exceedance probability for a given cost level can be written as

$$P[DV > dv_k] = \sum_{k=k+1}^{N_{DV}} \sum_{j=1}^{N_{DM}} \sum_{i=1}^{N_{EDP}} X_{ij} Y_{jk} P[EDP = edp_i] \quad (8.7)$$

or

$$P[DV > dv_k] = \sum_{k=k+1}^{N_{DV}} \sum_{j=1}^{N_{DM}} \sum_{i=1}^{N_{EDP}} X_{ij} Y_{jk} \left(P[EDP > edp_i^-] - P[EDP > edp_i^+] \right) \quad (8.8)$$

where edp_i^- and edp_i^+ are the *EDP* values at the lower and upper bounds, respectively, of the i^{th} *EDP* range. To obtain a risk curve, the probabilities can be converted to exceedance rates using

$$\lambda_{DV}(dv_k) = \sum_{k=k+1}^{N_{DV}} \sum_{j=1}^{N_{DM}} \sum_{i=1}^{N_{EDP}} X_{ij} Y_{jk} \left[\lambda_{EDP}(edp_i^-) - \lambda_{EDP}(edp_i^+) \right] \quad (8.9)$$

The values in the square brackets of Equation (8.9) can be obtained from the *EDP* hazard curve.

8.2.2 Estimated Damage and Loss Probabilities

Detailed quantitative data on pile foundation damage during earthquake shaking is not readily available. There are relatively few case histories in which pile damage has been carefully documented, and relatively few of those include response or even ground motion information sufficient to accurately characterize *IMs* or *EDPs*. While model tests (shaking table and centrifuge) offer some promise for establishing more accurate damage models, difficulties in scaling the nonlinear, inelastic behavior of actual, full-scale pile materials down to model scale complicates their application to real problems.

For this project, foundation damage was correlated to foundation lateral displacement and five discrete damage states were defined in qualitative terms—negligible, minor, moderate, severe, and catastrophic. Using the result of a poll of experienced earthquake reconnaissance experts and a degree of judgment, foundation lateral displacement ranges were defined for each of the five damage states as shown in Table 8.3.

Table 8.3 *EDP* ranges corresponding to different damage states; where *EDP*=foundation lateral displacement.

<i>EDP</i> range	Damage state
< 4 cm	Negligible
4 – 10 cm	Minor
10 – 30 cm	Moderate
30 – 100 cm	Severe
> 100 cm	Catastrophic

Based on these definitions and the results of the permanent deformation poll, the damage probabilities shown in Table 8.4 were assigned.

Table 8.4 Damage probabilities

Damage State, DM	Description	EDP range				
		edp_1	edp_2	edp_3	edp_4	edp_5
dm_1	Negligible	0.95	0.05	0.00	0.00	0.00
dm_2	Slight	0.05	0.80	0.20	0.05	0.00
dm_3	Moderate	0.00	0.10	0.60	0.25	0.05
dm_4	Severe	0.00	0.05	0.15	0.55	0.10
dm_5	Catastrophic	0.00	0.00	0.05	0.15	0.85

A total of 11 loss states were defined for the foundations; the loss states corresponded to repair cost ratios of 0.0, 0.1, ..., 1.0. The loss probabilities assigned to each loss state are shown in Table 8.5.

Table 8.5 Loss probabilities.

Decision Variable, DV	Repair Cost Ratio	Damage State				
		Negligible, dm_1	Minor, dm_2	Moderate, dm_3	Severe, dm_4	Catastrophic, dm_5
dv_1	0.0	0.95	0.00	0.00	0.00	0.00
dv_2	0.1	0.05	0.15	0.20	0.00	0.00
dv_3	0.2	0.00	0.50	0.60	0.00	0.00
dv_4	0.3	0.00	0.20	0.15	0.00	0.00
dv_5	0.4	0.00	0.15	0.05	0.15	0.00
dv_6	0.5	0.00	0.00	0.00	0.50	0.00
dv_7	0.6	0.00	0.00	0.00	0.25	0.00
dv_8	0.7	0.00	0.00	0.00	0.10	0.00
dv_9	0.8	0.00	0.00	0.00	0.00	0.10
dv_{10}	0.9	0.00	0.00	0.00	0.00	0.20
dv_{11}	1.0	0.00	0.00	0.00	0.00	0.70

8.3 ESTIMATED FOUNDATION DAMAGE

The *EDP* hazard curves for the horizontal foundation displacement of each of the bridge foundations were used, along with the damage probability matrix shown in Table 8.4, to estimate damage levels associated with the computed response. Since the damage levels were expressed

in terms of discrete, qualitatively described damage states, the exceedance rates (and associated return periods) are presented in tabular form in Table 8.6.

Table 8.6 Tabular listing of mean annual rates of exceedance and return period for various damage states.

Damage State	Foundation											
	Left abut.		Pier 1		Pier 2		Pier 3		Pier 4		Rt. abut.	
	λ_{DV}	T_R										
Negligible, dm_1	1.0609	0.9	0.2796	3.6	0.0394	25	0.1007	10	0.1098	9.1	0.2108	4.7
Minor, dm_2	0.1003	10	0.0283	35	0.0047	214	0.0143	70	0.0166	60	0.0348	29
Moderate, dm_3	0.0333	30	0.0094	106	0.0016	640	0.0049	204	0.0056	178	0.0122	82
Severe, dm_4	0.0004	2279	0.0002	6112	0.0001	1919	0.0003	2885	0.0003	2870	0.0012	809
Catastrophic, dm_5	0	∞										

The values shown in Table 8.6 indicate that a moderate level of damage is much more likely to be exceeded at the left abutment (return period of 30 yrs) and much less likely to be exceeded at Pier 2 (return period of 640 yrs) than at the other foundation locations. A severe level of damage is much more likely to be exceeded at the right abutment (return period of 809 yrs) than at the other locations.

8.4 ESTIMATED FOUNDATION LOSSES

The *DM* hazard values for each of the bridge foundations were used, along with the damage and loss probability matrices described in the preceding section to estimate losses associated with foundation damage.

Figure 8.1 shows the loss risk curves that resulted from this procedure for the two abutment foundations and the foundations for each of the interior bridge piers. These curves indicate a relatively high level of risk, even at lower return periods; this result is not unexpected, given that a liquefiable soil profile in an area of very high seismicity is being considered. Table 8.6 summarizes the repair cost ratios at return periods of 100 and 1000 years.

Table 8.7 Estimated loss levels.

Foundation	100-yr RCR	1,000-yr RCR
Left abutment	0.62	0.77
Pier 1	0.46	0.71
Pier 2	0.24	0.53
Pier 3	0.35	0.67
Pier 4	0.37	0.69
Right abutment	0.52	0.93

As the curves of Figure 8.1 and tabulated values in Table 8.5 indicate, the estimated foundation losses are highest for the left abutment at the 100-years hazard level, and highest at the right abutment for the 1000-years hazard level. Pier 2, which is subjected to the lowest levels of lateral spreading-induced soil deformations, has significantly lower expected losses than do the other foundations at both hazard levels.

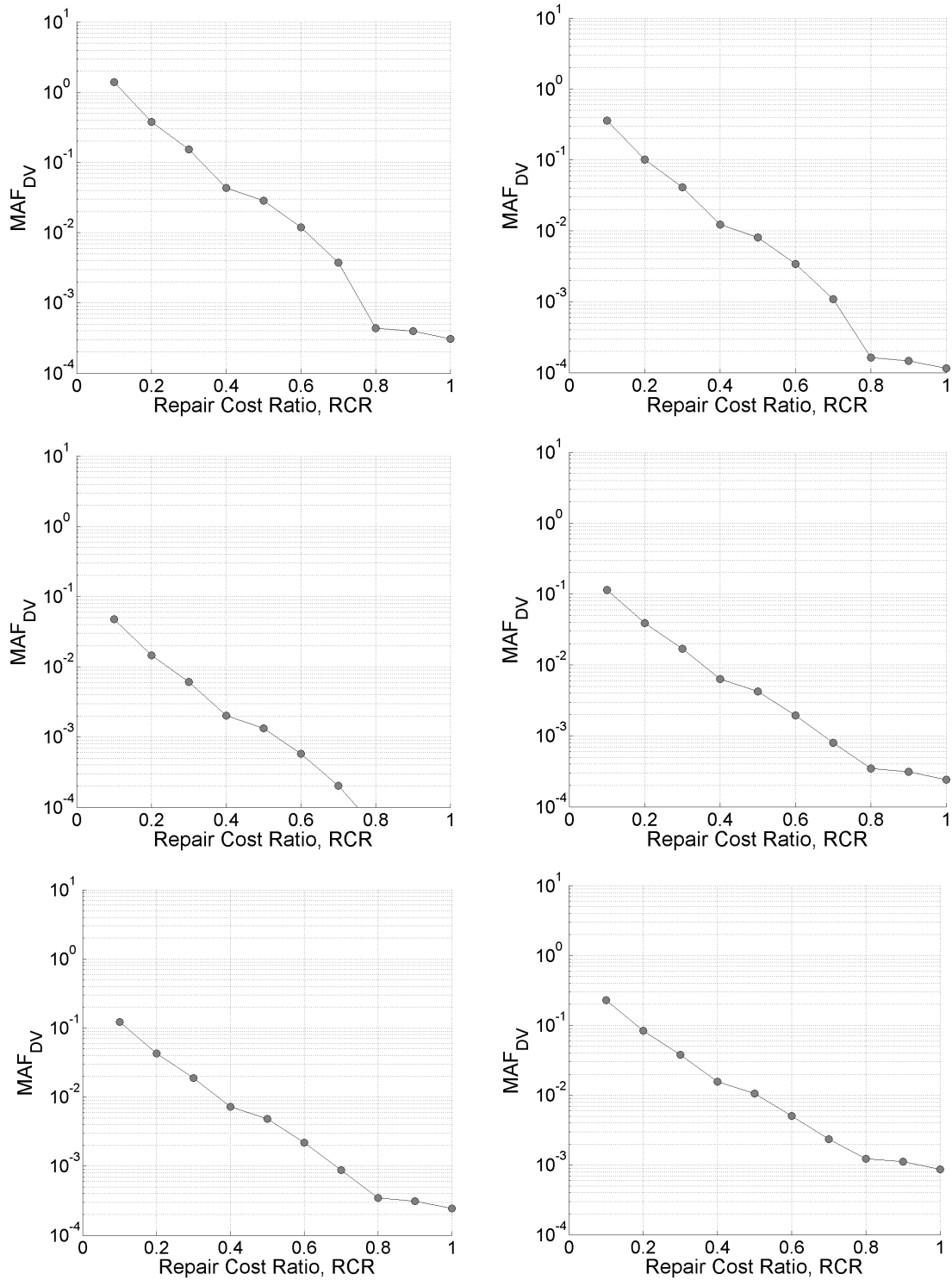


Fig. 8.1 Mean annual rates of exceedance of repair cost ratio, RCR, for different pile groups: (a) left abutment, (b)–(e) interior columns, and (f) right abutment. *DM* hazard curves for each pile group obtained considering most efficient *IM*: (a) *CAV*₅, (b) *PGV*, (c) *CAV*₅, (d) *PGA*, (e) *Ia*, (f) *CAV*₅.

8.5 SUMMARY

Using a procedure in which damage and loss probability matrices were developed for a small number of discrete damage states and a larger number of loss levels, the *EDP* hazard curves for each of the bridge foundations were used to estimate damage hazards and produce loss hazard curves. The relatively simple and monotonic relationship between damage and response and between loss and damage led to generally predictable results when interpreted in a relative sense—the foundations that experienced the highest levels of predicted response were observed to have the highest expected loss levels. However, the inclusion of uncertainty in damage and loss predictions allows quantitative estimation of the mean annual rates of exceedance of the different damage and loss levels.

9 Bridge Damage and Loss

9.1 INTRODUCTION

The bridge response computed using OpenSees analyses and described in Chapter 7 also provides a basis for estimating the recurrence rate of different levels of physical damage and loss for the entire bridge system. In order to facilitate comparisons of damage and loss for the testbed highway bridge considered in this research project with that of the same bridge under fixed-base conditions, the damage and loss model developed by Mackie and Stojadinović (2006) was modified to account for geotechnical/foundation-related damage and loss and then used to estimate total bridge damage and loss.

This chapter presents the results of a series of bridge damage and loss analyses, and examines the sensitivity of losses to various assumptions in the modeling of damage and loss. It also examines the question of how loss estimates would be affected by a lack of *EDP* information, as could be the case if a simpler response model was used.

9.2 DAMAGE MODELS

In order to estimate bridge damage, the main components of the bridge were divided into 21 performance groups. The most efficient *EDPs* were identified for each of the performance groups; the performance groups and *EDPs* are listed in Table 9.1. Multiple components were considered in some of the performance groups (four columns, for example, in the Column performance group). The following descriptions are based on Mackie et al. (2006).

Table 9.1 Performance groups and associated *EDPs*.

Performance Group	<i>EDP</i>
Column (4)	Maximum and residual tangential drift ratios
Expansion joint (2)	Longitudinal abutment displacement
Bearings (2)	Bearing displacement (absolute)
Back wall (2)	Back wall displacement
Approach slab (2)	Vertical abutment displacement
Deck segment (5)	Depth of spalling
Abutment pile groups (2)	Horizontal displacement
Interior pile groups (4)	Horizontal displacement

The column tangential drift ratio was computed as the maximum drift ratio in the longitudinal direction. The depth of spalling in the deck segments, which was computed from the strain profile along four segments on the left and right ends of the deck segment, was assumed to be indicative of the extent of deck spalling and roadway damage. The bearing displacement was taken as the maximum absolute displacement in the longitudinal direction. The vertical abutment displacement was assumed to control the slopes of the two approach slabs. The horizontal abutment displacement was used as an indication of the displacement demands on the expansion joints. The backwall displacement was measured at the top of the back wall and includes the effect of the soil behind the back wall. Horizontal displacement of the pile groups was measured at the pile cap level.

Damage models were developed for each performance group by characterizing the variation of median damage level and dispersion, i.e., $\sigma_{\ln DM|EDP}$, with *EDP*. The *DMs* for each performance group were divided into discrete damage states to which repair quantities were assigned. The number of damage states for each performance group varied depending, in part, on the number of different repair methods available; performance groups for which replacement was the only viable option, therefore, had only two possible damage states. The damage models for each of the performance groups are summarized in the following sections.

9.2.1 Columns

The highway testbed bridge had four spiral reinforced circular concrete columns, each 1.83 m (6 ft) in diameter and 15.2 m (50 ft) tall. Longitudinal reinforcement consisted of 52 #36 (#11) bars

with a total area of 337 cm² (52.24 in.²). The damage states for the columns corresponded to the limits for cover concrete spalling, rebar buckling and column failure.

Two damage models were used for the concrete columns—one based on maximum tangential drift (Table 9.2) and the other based on residual tangential drift (Table 9.3). The column damage models were obtained from the PEER structural performance database (<http://nisee.berkeley.edu/spd/>). An additional lower-level damage state was defined for the onset of column cracking. The repair methods for the column included injecting cracks with epoxy, replacing minor concrete spalls, steel column encasement for rehabilitation, and column replacement. The cost of column replacement was based on the average deck area per column.

Table 9.2 Column damage states based on maximum tangential drift ratio.

Damage State	Median <i>EDP</i> (Maximum drift ratio, %)	Dispersion ($\sigma_{\ln DMEDP}$)
Cracking	0.23	0.30
Spalling	1.64	0.33
Bar buckling	6.09	0.25
Failure	6.72	0.35

Table 9.3 Column damage states based on residual tangential drift ratio.

Damage State	Median <i>EDP</i> (Residual drift ratio, %)	Dispersion ($\sigma_{\ln DMEDP}$)
Cracking	0.50	0.30
Spalling	1.25	0.40
Bar buckling	2.00	0.40
Failure	6.72	0.35

9.2.2 Expansion Joints

The highway testbed bridge was modeled with expansion joints that extended over the widths (12 m) of both abutments. Two damage states were assumed for the expansion joint. The first limit was related to joint seal failure and the second was tied to the joint seal assembly. The expansion joint damage states are summarized in Table 9.4.

Table 9.4 Expansion joint damage states.

Damage State	Median <i>EDP</i> (Horizontal abutment displacement, cm)	Dispersion ($\sigma_{\ln DMEDP}$)
Seal failure	5.1	0.25
Assembly failure	10.2	0.25

9.2.3 Bearings

The testbed bridge was modeled with 5 cm (2 in.) high neoprene bearing pads supporting the girder webs at each abutment. The bearings were assumed to have yielded when a shear strain of 150% was reached and to have failed at a shear strain of 300%; replacement was considered to be the only repair option. The expansion joint damage states are summarized in Table 9.5.

Table 9.5 Bearing damage states.

Damage State	Median <i>EDP</i> (Horizontal abutment displacement, cm)	Dispersion ($\sigma_{\ln DMEDP}$)
Yielding	7.6	0.25
Failure	15.24	0.25

9.2.4 Back Walls

The back walls at each abutment were 1.8 m (6 ft) high and 30 cm (1 ft) thick. Backwall damage was related to the lateral displacement at the top of the wall. Two damage states beyond those at which expansion joint damage would occur were defined for the back wall—cracking, spalling, and failure. Mackie et al. (2006) noted that the backwall displacement demand model had high dispersion because the zero wall displacement that occurred prior to gap closure was followed by extremely large forces imparted to the wall upon closure. The abutment backwall damage states are summarized in Table 9.6.

Table 9.6 Abutment backwall damage states.

Damage State	Median <i>EDP</i> (Horizontal back wall displacement, cm)	Dispersion ($\sigma_{\ln DM/EDP}$)
Spalling	11.1	0.30
Failure	13.8	0.30

9.2.5 Approach Slabs

The bridge was assumed to be outfitted with 9 m (30 ft) long, 30 cm (12 in.) thick approach slabs at each abutment; the approach slabs were connected with dowel bars on the top of the abutment back wall and supported on full-width footings at their other ends. Hoppe (1999) cited approach slab rotation limits of 1/200 as affecting rider comfort, and 1/125 as triggering remedial measures. These limits correspond to vertical displacements of 4.5 cm (1.8 in.) for rider comfort and 7 cm (2.9 in.) for remedial measures. A high dispersion of 0.40 was assigned to the approach slab damage states due to lack of information about slab performance and limit states. The approach slab damage states are summarized in Table 9.7.

Table 9.7 Approach slab damage states.

Damage State	Median <i>EDP</i> (Vertical abutment displacement, cm)	Dispersion ($\sigma_{\ln DM/EDP}$)
Minor pavement failure	7.3	0.40
Major pavement failure	14.6	0.40
Approach slab failure	30.5	0.40

9.2.6 Deck Segments

The bridge had five deck segments, three covering the 45.7 m (150 ft) long internal spans and two covering the 36.6 m (120 ft) long external spans. Three damage states were defined in terms of depth of spalling (assumed to begin at 0.004 concrete strain). The depth of spalling was taken

as an indicator of the total amount of deck and roadway surface expected to have been damaged. Three damage states were defined as corresponding to 2%, 10%, and 25% spalling of the deck area. These threshold levels were chosen to correspond to condition state limits given in the *Caltrans Element Level Inspection Manual* (2000). The depth of spalling was taken from 15 cm (6 in.) above the top of the structural concrete to allow for a topping slab and new roadway. The bridge deck damage states are summarized in Table 9.8.

Table 9.8 Bridge deck damage states.

Damage State	Median <i>EDP</i> (Depth of spalling, cm)	Dispersion ($\sigma_{\ln DM EDP}$)
2% spalling		0.40
10% spalling		0.40
25% spalling		0.40

9.2.7 Pile Foundations

The bridge has a total of six pile group foundations, one supporting each abutment and one below each of the four interior columns. The abutment foundations consist of a group of six piles in a single row and the interior foundations are 2 x 3 pile groups. Pile cap horizontal displacements were shown to correlate very closely to maximum pile curvatures and displacements of 90 cm and 130 cm were selected, in consultation with Caltrans personnel, as median values for moderate and severe damage states. The pile foundation damage states are summarized in Table 9.9.

Table 9.9 Pile foundation damage states.

Damage State	Median <i>EDP</i> (Horizontal displacement, cm)	Dispersion ($\sigma_{\ln DM EDP}$)
Minor damage	90	0.40
Severe damage	130	0.40

9.3 REPAIR METHODS AND COSTS

The bridge response and damage models were used to estimate quantities of a series of repair items to which unit costs were assigned. The repair cost data were initially estimated from various Caltrans documents (Caltrans 2004; 2005) and then updated based on discussions with Caltrans personnel. The repair items and unit costs for each of the performance group damage states are presented in Tables 9.10–9.16.

The column repair methods included injecting cracks with epoxy, replacing minor concrete spalls, steel jacketing, and column replacement. Damage associated with residual column drift could be repaired by enlarging (a structurally undamaged column) to give the appearance of verticality, re-centering, or replacement. The repair method for expansion joint seal failure was replacement of the entire joint seal segment. The repair method for joint assembly failure consisted of replacement of the entire joint seal assembly. The failure of bridge bearing was assumed to require replacement of the bearings. The repair methods for abutment back walls included injecting cracks with epoxy, and repairing minor spalls, up to complete replacement. The repair methods assumed for the approach slab included injecting cracks with epoxy, replacing the concrete top cover, and removing and replacing the entire slab. Bridge deck repair was assumed to consist of surface refinishing. Foundation damage is repaired by adding new piles around the perimeter of the existing pile cap and expanding the existing pile cap to include the new piles.

Table 9.10 Column repair methods and costs.

Damage State	Repair Method	Unit	Repair Quantity	Unit Cost
Cracking	Inject cracks with epoxy	LF	200	\$80
	Replace minor spalls	SF	10	\$100
Spalling	Inject cracks with epoxy	LF	200	\$80
	Replace minor spalls	SF	94	\$100
Bar buckling	Inject cracks with epoxy	LF	200	\$80
	Replace minor spalls	SF	236	\$100
	Steel column casing	LF	50	\$2000
	Bridge bar reinforcement	KG	1562	\$2
Failure	Replace column	SF	6728	\$120

Table 9.11 Expansion joint repair methods and costs.

Damage State	Repair Method	Unit	Repair Quantity	Unit Cost
Seal failure	Replace joint seals	LF	39	\$90
Assembly failure	Replace joint seal assemblies	LF	39	\$900

Table 9.12 Bearing repair methods and costs.

Damage State	Repair Method	Unit	Repair Quantity	Unit Cost
Failure	Replace bearings	EA	3	\$3000

Table 9.13 Abutment backwall repair methods and costs.

Damage State	Repair Method	Unit	Repair Quantity	Unit Cost
Cracking	Inject cracks with epoxy	LF	45	\$80
Spalling	Inject cracks with epoxy	LF	45	\$80
	Replace minor spalls	SF	120	\$100
Failure	Replace back wall	LF	45	\$1000

Table 9.14 Approach slab repair methods and costs.

Damage State	Repair Method	Unit	Repair Quantity	Unit Cost
Cracking	Inject cracks with epoxy	LF	30	\$80
Pavement failure	Inject cracks with epoxy	LF	30	\$80
	Remove and replace roadway	CY	29	\$200
Slab failure	Remove and replace slab	SF	780	\$30

Table 9.15 Bridge deck repair methods and costs.

Damage State	Repair Method	Unit	Repair Quantity	Unit Cost
2% spalling	Refinish deck (interior span)	SF	117	\$13
	Refinish deck (exterior span)	SF	94	\$13
5% spalling	Refinish deck (interior span)	SF	585	\$13
	Refinish deck (exterior span)	SF	468	\$13
10% spalling	Refinish deck (interior span)	SF	1463	\$13
	Refinish deck (exterior span)	SF	1170	\$13

Table 9.16 Pile foundation repair methods and costs.

Damage State	Repair Method	Unit	Repair Quantity	Unit Cost
Moderate damage	Add piles	LF		\$90
	Drive piles	EA		\$12,000
Severe damage	Add piles	LF		\$90
	Drive piles	EA		\$12,000

9.4 ESTIMATED REPAIR COSTS

Based on the damage and loss models described in the preceding sections, a series of repair cost analyses were performed. The PEER methodology was initially used to compute repair cost hazard curves and to deaggregate those repair costs with respect to the various performance groups. Next, a series of sensitivity analyses were performed to investigate the effects of performance group median response and uncertainty reduction on total repair costs. Finally, a series of analyses were performed to investigate the effects of simplified geotechnical analyses on estimated total repair costs. The results of these analyses are described in the following sections.

9.4.1 Estimation of Total Repair Costs

A series of repair cost analyses were performed using the Matlab code developed by Mackie et al. (2006). The Mackie code is set up to produce conditional probabilities of various repair cost levels given an intensity measure, which was taken as peak velocity. The conditional probability of $DV|IM$ can be computed using the total probability theorem as

$$P[DV_i | IM_i] = \sum_{k=1}^{N_{DM}} \sum_{j=1}^{N_{EDP}} \sum_{i=1}^{N_{IM}} P[DV | DM_k] P[DM_k | EDP_j] P[EDP_j | IM_i] \quad (9.1)$$

Figures 9.1 and 9.2 show the IM hazard curve and the variation of median $DV|IM$ and median $\pm \sigma_{\ln DV|IM}$ with IM . The median repair cost can be seen to generally increase with increasing peak ground velocity, but can also be observed to exhibit discontinuities (i.e., local reductions) at various IM levels. These local reductions result from the elimination of certain repair items with increasing overall damage; for example, the amount of patching work required

to repair spalls on a concrete column drops to zero when damage is sufficiently high that column replacement becomes the preferred repair method. It should be noted that a vertical slice at any IM in Figure 9.2 can be used to develop a probability distribution for conditional repair cost. The median $DV|IM$ curve is relatively flat until the peak ground velocity exceeds about 30 cm/sec, which the seismic hazard curve indicates occurs at a return period of about 50 years, at which point it increases sharply. The median $DV|IM$ curve flattens out again at peak ground velocities of about 60–110 cm/sec at which point it rises steeply again.

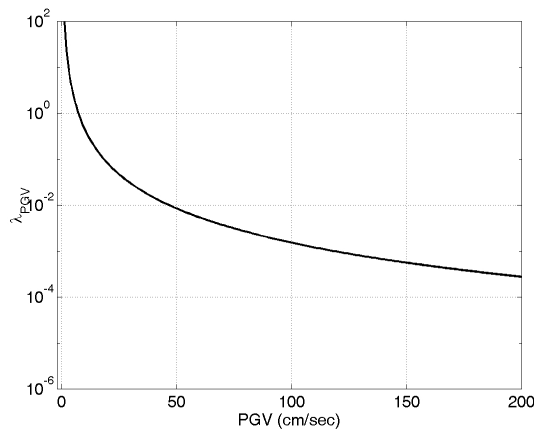


Fig. 9.1 *PGV hazard curve for highway testbed bridge site.*

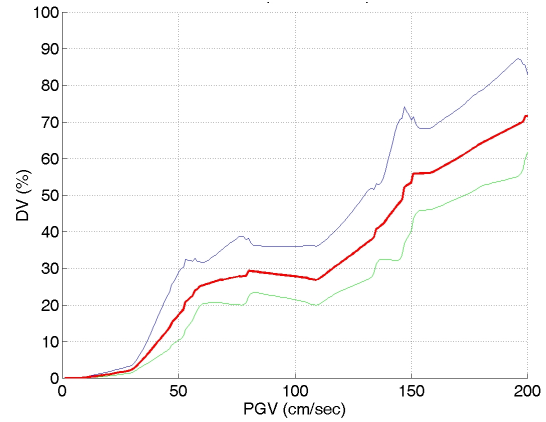


Fig. 9.2 *Distribution of $DV|IM$ (16th, 50th, and 84th percentile curves shown) for highway testbed bridge site for liquefaction case.*

9.4.1.1 Repair Cost Hazard Curves

The conditional distribution given by Equation (9.1) can be convolved with the IM hazard curve to produce a hazard curve for the decision variable, DV , as

$$\lambda_{DV}(dv_l) = \sum_{i=1}^{N_{IM}} P[DV > dv_l | IM = im_i] \Delta \lambda_{IM}(im_i) \quad (9.2)$$

Figure 9.3 shows the resulting total hazard curve for the repair cost ratio; the 100- and 1000-years repair cost ratios are 15% and 45%, respectively.

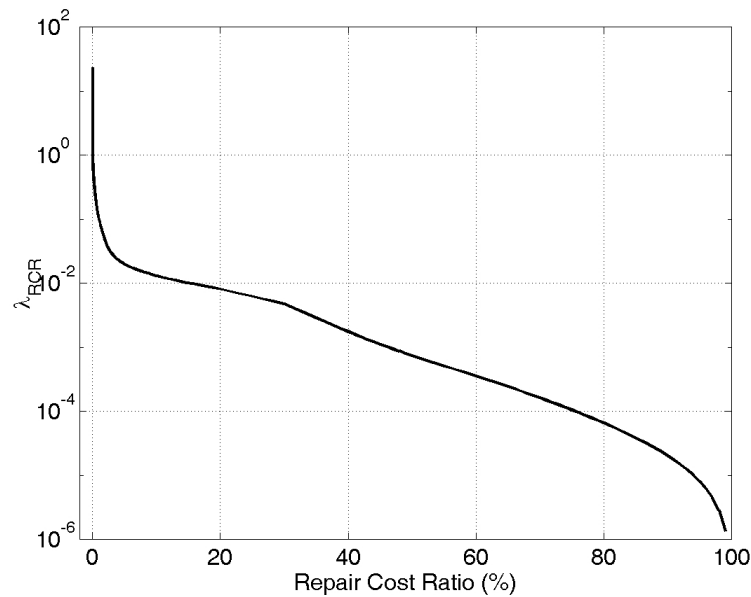


Fig. 9.3 Total repair cost ratio hazard curve for liquefaction case obtained from convolution of relationships shown in Figs. 9.1 and 9.2.

9.4.1.2 Deaggregation of Repair Cost

The Mackie code also provides repair cost deaggregation information. Deaggregated costs can be expressed conveniently in terms of the conditional $DV|IM$ plots. Figure 9.4 shows a series of deaggregated $DV|IM$ curves for various performance groups; the curves show that the relative contributions of the different performance groups and repair methods change, as would be expected, as the ground motion level changes. Figure 9.5 shows deaggregation data expressed in pie chart form for the 475-years hazard level.

Figure 9.5 shows that temporary superstructure support, followed by additional piling, produces the greatest contribution to repair costs at the 475-years hazard level. Note that temporary superstructure support resulting from severe column damage becomes significant at peak ground velocities of about 30 cm/sec and contributes strongly to the previously noted steepening of the overall median $DV|IM$ curve shown in Figure 9.2.

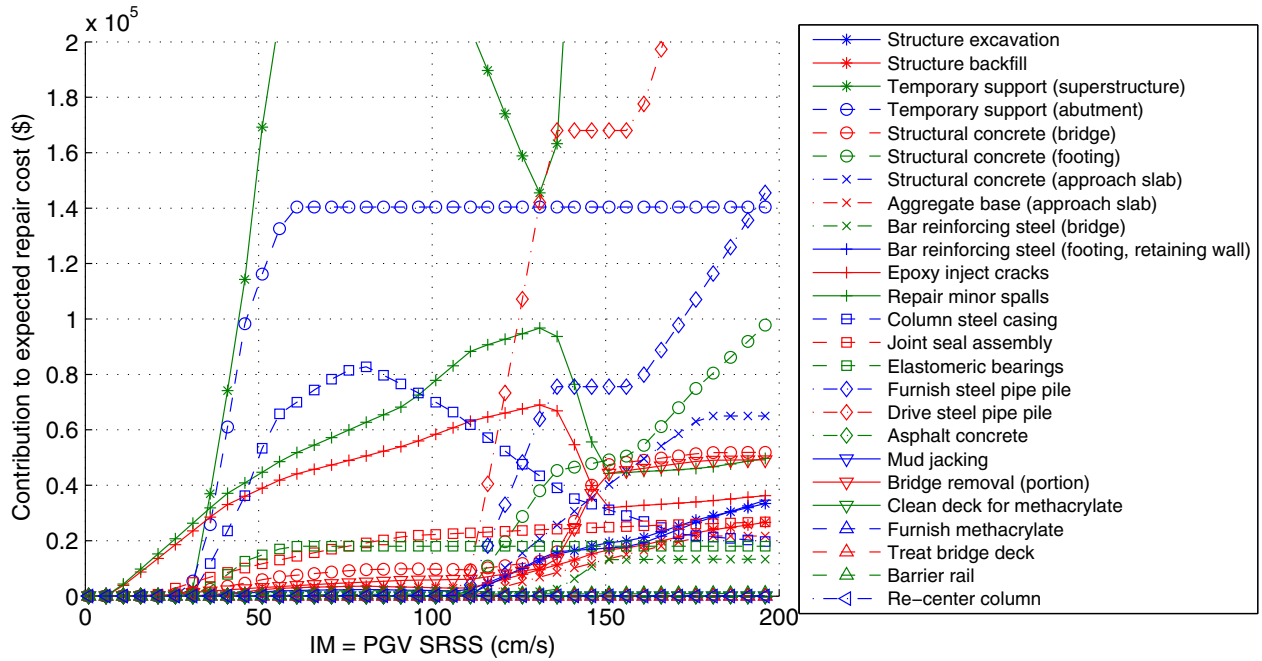


Fig. 9.4 Deaggregated conditional repair costs for testbed highway bridge in liquefaction case.

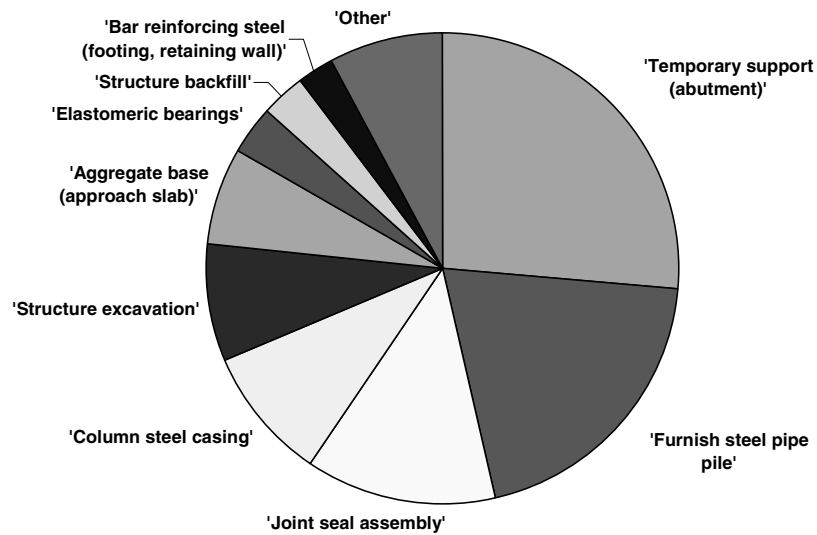


Fig. 9.5 Deaggregated conditional repair costs for testbed highway bridge for 475-yr return period in liquefaction case.

9.4.2 Sensitivity of Bridge Losses to Soil Conditions

This investigation has allowed a detailed characterization of bridge response, damage, and loss for the case of a typical highway bridge founded on liquefiable soils. The response has been shown to be significantly affected by the occurrence of liquefaction; the large foundation displacements observed in the response analyses are largely attributed to lateral spreading of the soils beneath and adjacent to the abutment slopes. These deformations induce bending demands on both pile foundations and bridge columns, and lead to potentially increased levels of displacement of approach slabs, expansion joints, etc.

9.4.2.1 Losses for Non-Liquefiable Soil Conditions

In order to better understand the contributions of liquefaction to the estimated bridge losses, a series of analyses were performed in which the bridge was supported by the same soil profile but without allowing the generation of excess pore pressure in saturated soils. The purpose of these analyses were to isolate the contributions of liquefaction by artificially modeling the soil as having the same initial stiffness as the liquefiable soil but not having the ability to generate pore pressure and liquefy.

Figure 9.6 shows the variation of median $DV|IM$ and median $\pm \sigma_{\ln DV|IM}$ with IM for the case of non-liquefiable soil. The median repair cost can be seen to generally increase with increasing peak ground velocity, but at a substantially slower rate than that shown in Figure 9.2. The increase in median repair cost ratio at peak ground velocities of about 30 cm/sec in Figure 9.2 does not exist for the non-liquefaction case, which indicates that liquefaction damage is expected to occur at about that peak velocity level. The median $DV|IM$ curve increases rapidly at peak ground velocities exceeding about 140 cm/sec, which corresponds to a return period of about 1,600 years. Figure 9.7 shows the repair cost hazard curve for the non-liquefiable soil case; the 100- and 1000-years repair cost ratios are about 6% and 20%, respectively. The repair cost ratio hazard curve slope changes in a manner that suggests higher repair costs at return periods of about 1,600 years.

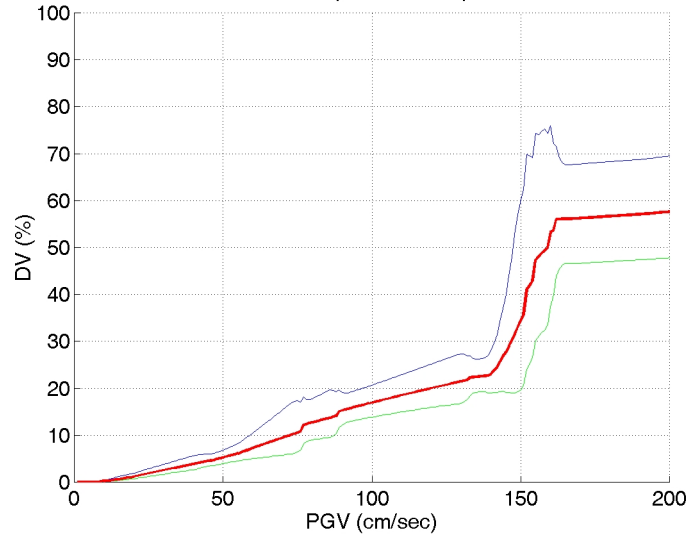


Fig. 9.6 Distribution of $DV|IM$ for highway testbed bridge site for non-liquefaction case.

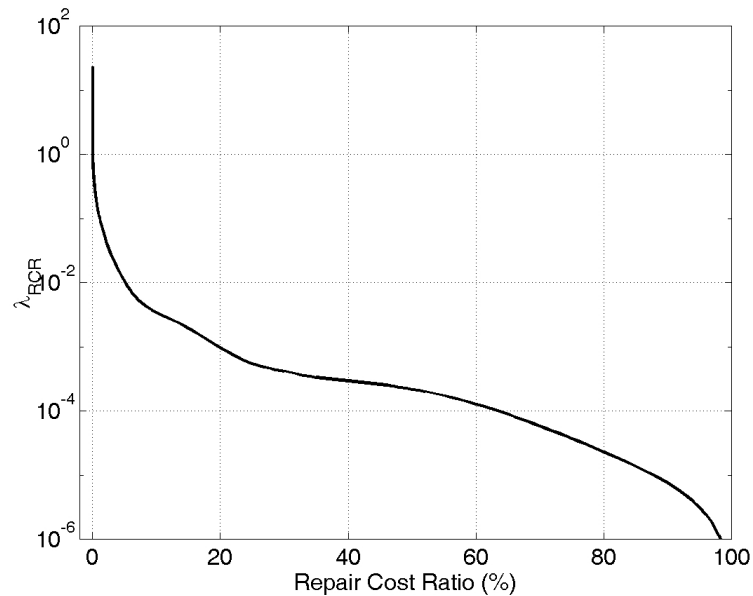


Fig. 9.7 Total repair cost ratio hazard curve for non-liquefaction case.

The deaggregation of conditional repair costs for the non-liquefaction case is shown in Figure 9.8. When liquefaction does not occur, the greatest contributors to repair cost are repairs of cracks and spalls at low ground motion levels (less than about 60 cm/sec), temporary support of the abutments at intermediate ground motion levels (approximately 65–140 cm/sec), and temporary support of the superstructure at higher ground motions levels (greater than about 150 cm/sec).

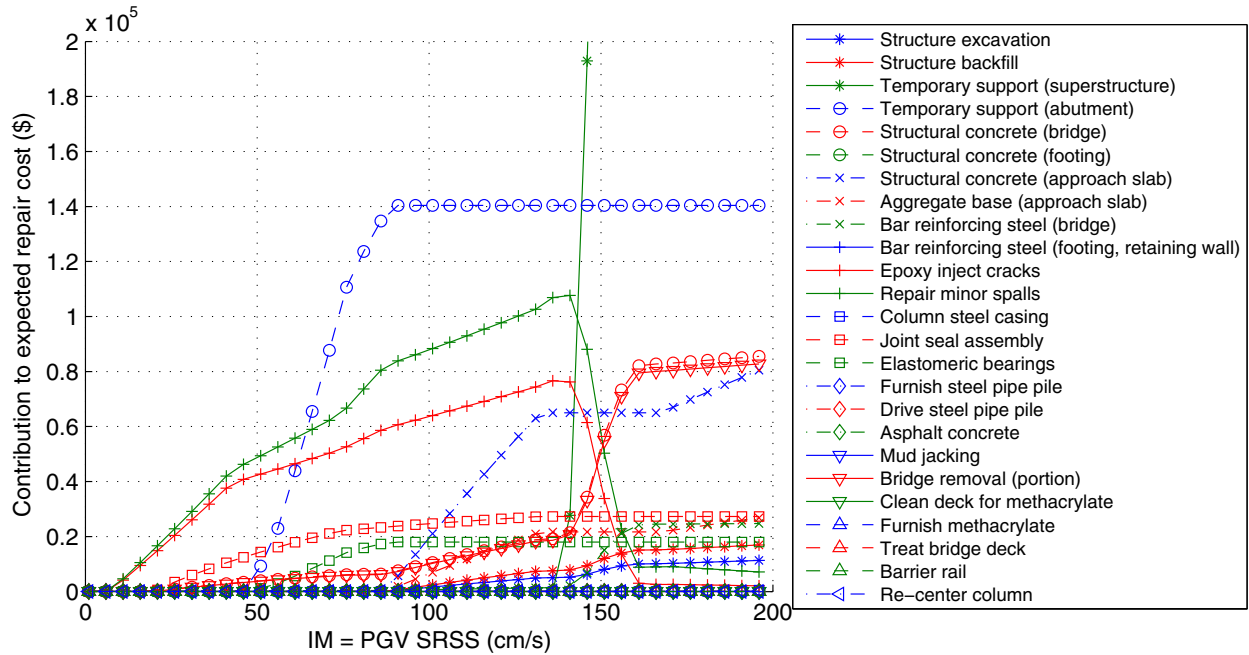


Fig. 9.8 Deaggregated conditional repair costs for testbed highway bridge in non-liquefaction case.

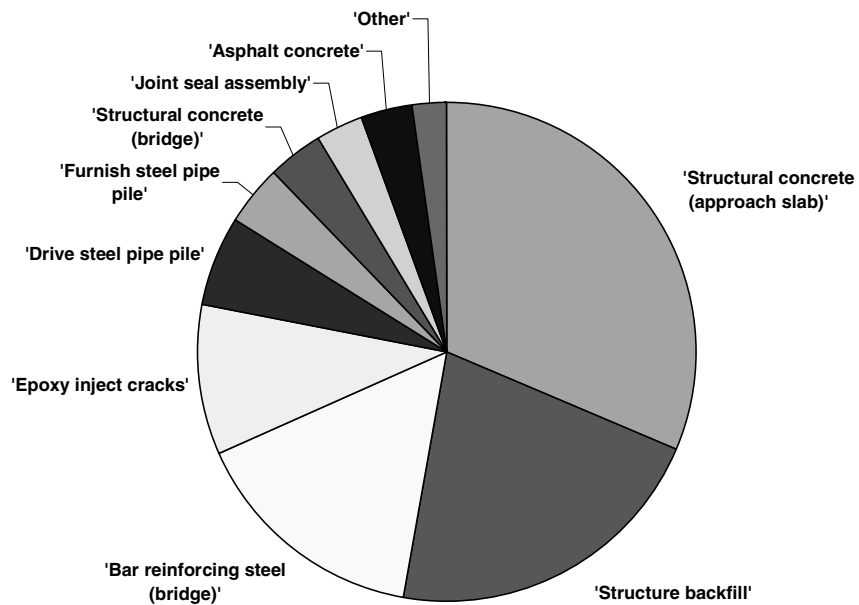


Fig. 9.9 Deaggregated conditional repair costs for testbed highway bridge for 475-yr return period in non-liquefaction case.

9.4.2.2 Losses for Fixed-Base Conditions

Another level of understanding of the geotechnical aspects of bridge loss can be gained by comparing bridge losses with liquefiable and non-liquefiable soils to those obtained when the highway testbed bridge is assumed to be supported on a rigid base; these conditions would be equivalent to assuming that the bridge site is underlain by intact bedrock. Mackie et al. (2006) performed a series of fixed-base analyses of the same bridge. These analyses model the response of the bridge to inertial loading without transient or permanent foundation deformations.

Figure 9.10 shows the variation of median $DV|IM$ and median $\pm \sigma_{\ln DV|IM}$ with IM for the fixed-base case. The median repair cost can be seen to generally increase with increasing peak ground velocity, but at a slower rate than that shown in Figures 9.2 and 9.6. Figure 9.11 shows the repair cost hazard curve for the non-liquefiable soil case; the 100- and 1000-years repair cost ratios are 7% and 26%, respectively.

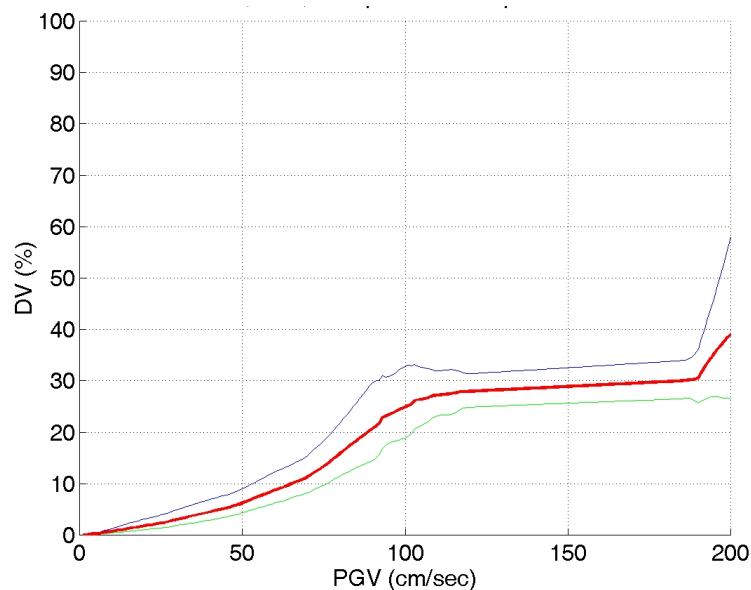


Fig. 9.10 Distribution of $DV|IM$ for highway testbed bridge site for fixed-base case

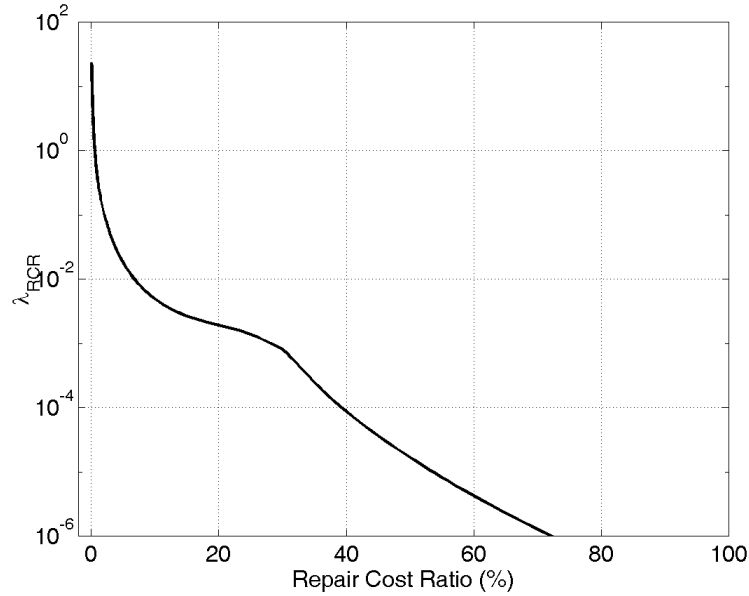


Fig. 9.11 Total repair cost ratio hazard curve for fixed-base case.

The deaggregation of conditional repair costs for the fixed-base case is shown in Figures 9.12 and 9.13. Temporary superstructure support is not significant for the fixed-base case until peak ground velocities are above about 190 cm/sec.

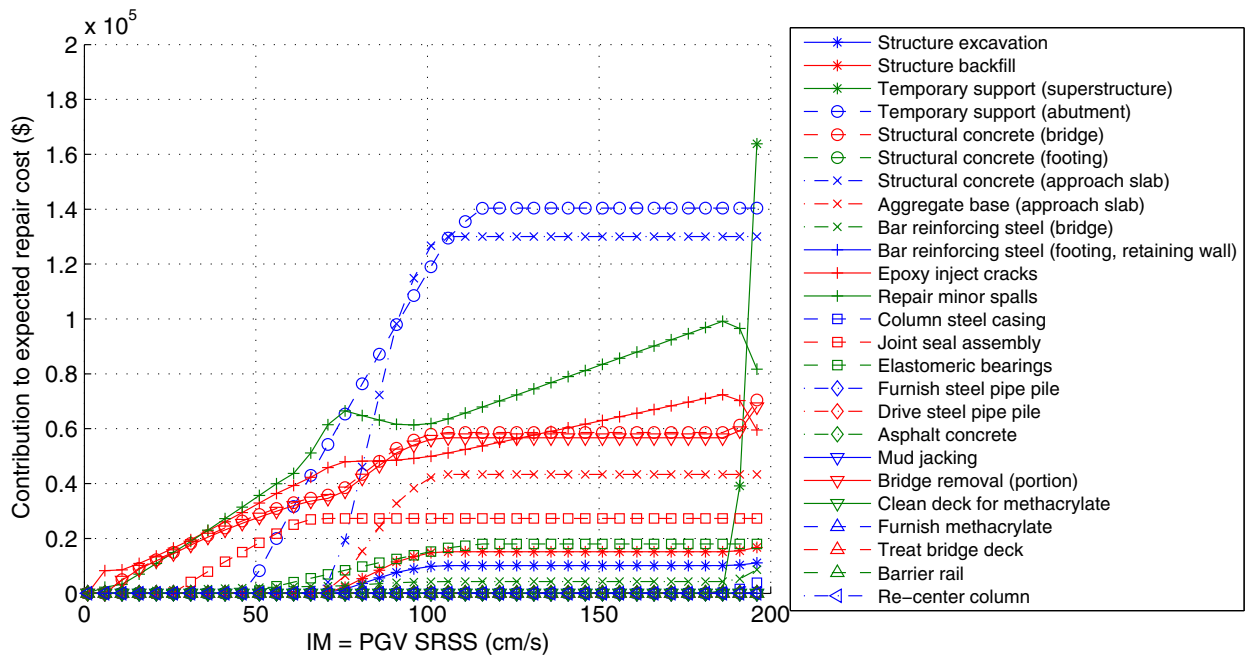


Fig. 9.12 Deaggregated conditional repair costs for testbed highway bridge in fixed-base case.

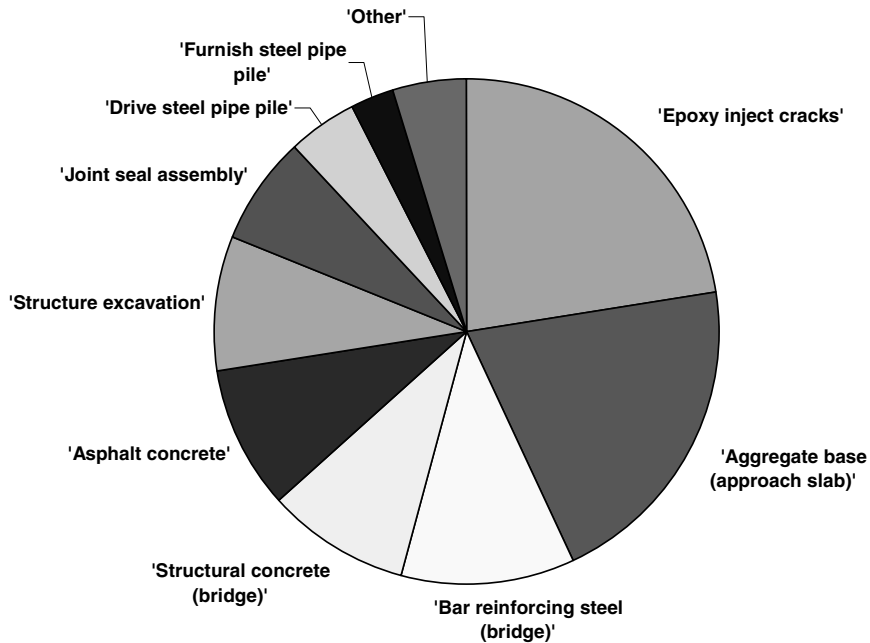


Fig. 9.13 Deaggregated conditional repair costs for testbed highway bridge for 475-yr return period.

9.4.2.3 Summary

The relative contributions of liquefaction and the ensuing deformations to bridge damage can be seen by comparing the total cost hazard curves shown in Figure 9.14. These curves indicate that the loss hazard is about the same for all three cases at return periods lower than about 50 years (i.e., λ_{DV} values greater than about 0.02 yr^{-1}). At longer return periods, the curves for Liquefaction and No Liquefaction diverge, indicating that the initiation of liquefaction for this site occurs with a return period of about 50 years. At a 100-year return period, losses for the Liquefaction case are more than twice as large as for the No Liquefaction case. The fixed-base case is actually more critical than the No Liquefaction case at this hazard level, indicating that inertial soil-structure interaction produces a beneficial reduction in structural demands at this level of shaking. Losses for the Liquefaction case remain at least about twice as large as for the No Liquefaction cases all the way to return periods of about 3,000 years; at greater return periods, the gap narrows, most likely due to increased deformations of the deeper clay layer that

occur at very strong input motion levels. The fixed-base losses increase at a much slower rate at return periods greater than about 1,000 years.

The analyses described in the preceding sections provide a great deal of insight into the mechanisms of damage and loss for the testbed highway bridge. By repeating the analyses with different soil behavior assumptions, the sensitivity of damage and loss to mechanisms such as soil liquefaction and lateral spreading, and even ground motion amplification can be identified. The occurrence of liquefaction at this site can be seen to contribute very strongly to losses at return periods encompassing those commonly used for the design of civil structures such as highway bridges. The curves shown below could be used to determine the financial benefits of improving the potentially liquefiable soils at this site to the point where liquefaction would not be triggered.

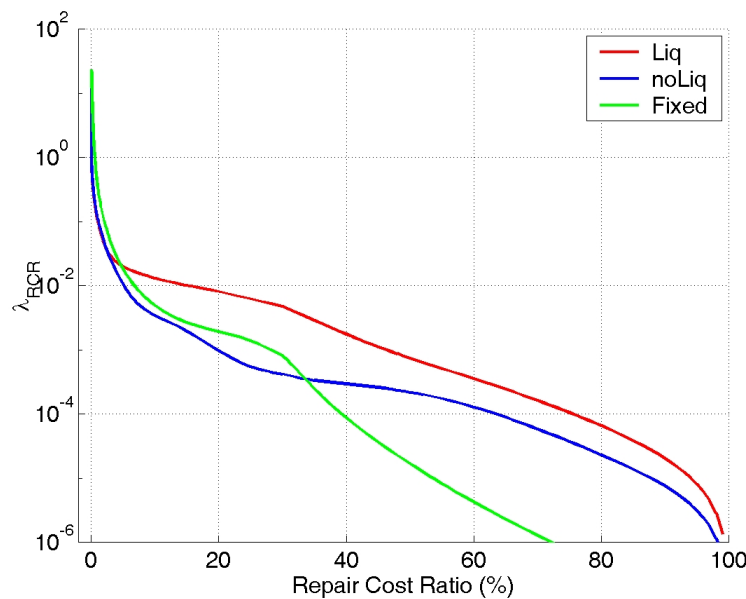


Fig. 9.14 Effect of different soil conditions on total repair cost ratio hazard curves.

9.4.3 Sensitivity of Bridge Losses to Uncertainty

The PEER framework for performance-based earthquake engineering shows very clearly how uncertainties affect response, physical damage, and losses at various hazard levels. In order to investigate the sensitivity of loss to uncertainty, the ground motion hazard curve for the highway testbed bridge site was convolved with the *DV|IM* hazard curve for different fractions of the total uncertainty shown in Figures 9.2 and 9.6. Uncertainties were increased and decreased by 50% of

the full uncertainty, and also taken down to nearly zero uncertainty, giving the fragility relationships shown in Figures 9.15 and 9.16 and the corresponding hazard curves shown in Figures 9.17 and 9.18.

These results suggest that the effects of uncertainty in $DV|IM$, i.e., the uncertainty in response, damage, and loss modeling are not particularly significant at short return periods. For the Liquefaction case, the hazard curve is not strongly affected by variations in uncertainty at return periods less than about 150 years. For the No Liquefaction case, the variation of uncertainty has a strong effect on DV hazards at return periods greater than about 5,000 years.

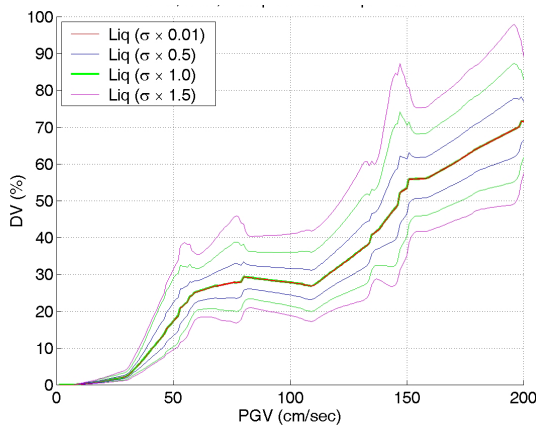


Fig. 9.15 $DV|IM$ relationship for liquefaction case with different fractions of actual uncertainty.

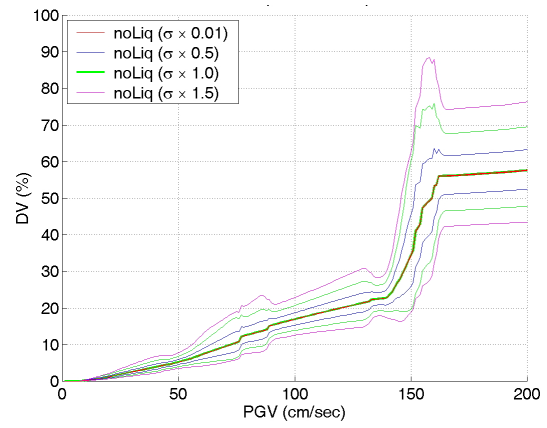


Fig. 9.16 $DV|IM$ relationship for non-liquefaction case with different fractions of actual uncertainty.

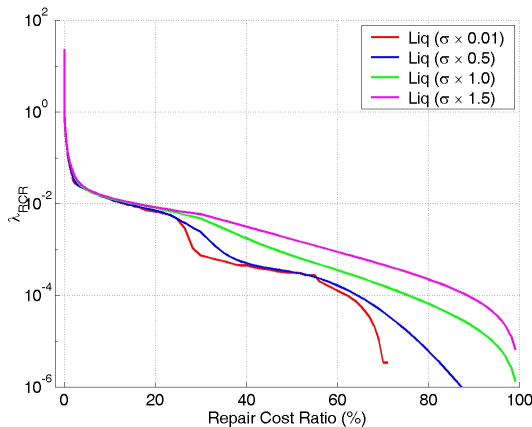


Fig. 9.17 Effects of different levels of uncertainty in $DV|IM$ on loss hazard for liquefaction case.

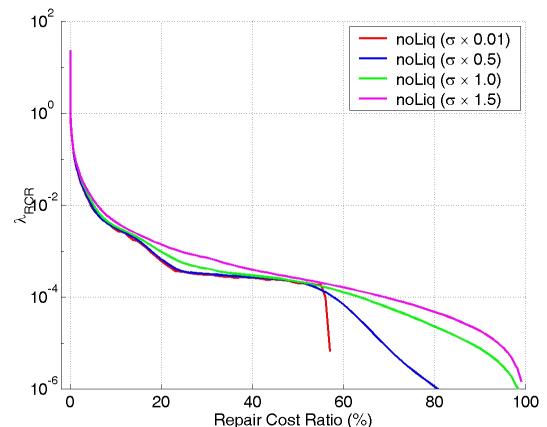


Fig. 9.18 Effects of different levels of uncertainty in $DV|IM$ on loss hazard for non-liquefaction case.

9.4.4 Implications for Simplified Response Analyses

The preceding section showed how differences in uncertainties can affect loss hazard curves. The uncertainties considered in that section were aggregated uncertainties, i.e., they reflect the uncertainties in response (given IM), damage (given EDP), and loss (given DM). Assuming independence of these intermediate quantities, the aggregated uncertainty is obtained by adding variances; hence, the aggregated uncertainty can be dominated by one or more of its constituent components.

Consider a situation in which an analysis is performed using a baseline value of response model uncertainty. In such a case, we can express the aggregated uncertainty as

$$\sigma_{\ln DV|IM-base}^2 = \sigma_{\ln EDP|IM-base}^2 + \sigma_{\ln DM|EDP}^2 + \sigma_{\ln DV|DM}^2 \quad (9.3)$$

Then, letting $\sigma_{\ln EDP|IM} = \alpha \sigma_{\ln EDP|IM-base}$, we can write

$$\sigma_{\ln DV|IM}^2 = \alpha^2 \sigma_{\ln EDP|IM-base}^2 + \sigma_{\ln DM|EDP}^2 + \sigma_{\ln DV|DM}^2 \quad (9.4)$$

If the uncertainties that contribute to loss uncertainty are all equal (i.e., $\sigma_{\ln EDP|IM-base}^2 = \sigma_{\ln DM|EDP}^2 = \sigma_{\ln DV|DM}^2$), then

$$\frac{\sigma_{\ln DV|IM}}{\sigma_{\ln DV|IM-base}} = \sqrt{\frac{2 + \alpha^2}{3}} \quad (9.5)$$

Therefore, a 50% increase in response uncertainty (i.e., $\sigma_{\ln EDP|IM} = 1.5 \sigma_{\ln EDP|IM-base}$), perhaps due to the use of simplified response models, would lead to a 19% increase in total uncertainty. According to Figure 9.17, this would lead to substantially increased loss predictions at return periods greater than about 200 years.

The question then becomes one of how large the response uncertainties are relative to damage and loss uncertainties for the subject structure. Current practice regarding the effects of ground failure on bridges such as the highway testbed bridge considered in this investigation typically revolves around the use of empirical or simplified analytical models to predict the permanent displacements of approach embankments. The Youd et al. (2002) empirical model for estimation of lateral spreading displacements is frequently used in practice; this model is based on interpretation of lateral spreading case histories from previous earthquakes. Although the uncertainty in this model has not been formally characterized, its authors note that about 90%

of its predicted displacement values fall within a factor of 2 of the observed values in the case history database. Assuming that the values are lognormally distributed, this would correspond to a dispersion of approximately $\sigma_{\ln EDP|IM} = 0.6$ in the prediction of approach embankment displacements. Newmark-type analyses are also used to estimate permanent slope displacements, although their applicability to soils in which pore pressures are generated is not straightforward. While no formal analyses of the uncertainty in such methods are available, the simplifications involved in these methods, along with record-to-record variability and the manner in which pore pressure generation is handled (or not handled) may well render their precision no better than the empirical methods.

The biggest difference between such simplified analyses and the detailed analyses conducted as part of this investigation, however, lies in the amount of information available to predict physical damage. In the detailed investigation, some 27 *EDPs* were explicitly calculated by OpenSees analysis and used to predict the required *DMs*. In simplified analyses, only two *EDPs* (the approach embankment displacements) are available for prediction of damage; some of the important damage mechanisms, however, are not related particularly closely to approach embankment displacements.

In order to obtain a sense of how much the additional information provided by a detailed analysis might improve loss estimates compared to a simplified analysis, a simple parametric analysis was performed. In this analysis, the uncertainties in response (i.e., $\sigma_{\ln EDP|IM}$) used in the previously described detailed analyses (Section 9.2) were adjusted to reflect the additional uncertainty that could exist in *DV|IM* if the *EDPs* were limited to approach embankment permanent displacements. The results of these analyses showed that the uncertainty in computed response was dominated by the uncertainties in damage (given response) and loss (given damage). In the end, with loss as the final metric of performance, the reduced uncertainty due to more accurate response modeling (given the assumption of equal median predictions) had a negligible effect on predicted losses. The analyses clearly showed, however, that errors in median response, as might be expected from simple analyses, would have a significant effect on computed losses; errors in median response, however, could not be predicted for the hypothetical testbed structure.

9.5 SUMMARY

This chapter illustrated the process by which earthquake-related losses could be estimated for the testbed bridge structure using the PEER PBEE methodology. The methodology was found to be effective in allowing estimation of loss hazard curves with consideration of uncertainties in ground motions, response, damage, and loss. The losses associated with liquefaction-induced deformations were included by explicitly modeling the liquefaction process, and the interaction of the structure with liquefied soils, using the OpenSees computer model.

By condensing the results of the response, damage, and loss model analyses, fragility curves for loss given ground motion intensity, i.e., $DV|IM$, could be computed. These fragility curves could then be combined with the seismic hazard curve to produce loss curves. The fragility curves showed a relatively irregular increase in loss with increasing intensity measure, thereby reflecting the onset and effects of physical phenomena such as liquefaction and shear failure. Response analyses were computed for cases in which liquefaction was modeled, and for which it was suppressed, and for a fixed-base support condition. Loss curves were computed for each of these cases.

Loss curves for each of the three cases reflect the physical mechanisms that lead to damage and loss under the various assumptions, and provide insight into the overall behavior of the soil-foundation-structure system. The loss curves exhibit irregular changes in slope, and consequently in shape, due to the irregularities in the $DV|IM$ fragility curves. The loss curve for the case in which liquefaction occurred, for example, becomes flatter at a return period of about 50 years due to the occurrence of liquefaction-related damage when ground motions reach sufficiently strong levels. In the case in which liquefaction was suppressed, the loss curve becomes flatter at a return period of about 1,600 years, which is when highly nonlinear response of the clay layer beneath the left side of the bridge begins to develop.

Earthquake-related losses are shown to be influenced by uncertainties in the prediction of ground motions, system response, physical damage, and economic loss. Uncertainties in ground motions are accounted for by a probabilistic seismic hazard analysis, which forms the input to a performance-based earthquake engineering evaluation. Uncertainties in response are related to uncertainties in the parameters required for response predictions and in the predictive models themselves. Different levels of response analysis require different input parameters and have different levels of model uncertainty; however, the model uncertainty inherent in either

simplified or detailed analyses has not been formally established. Nevertheless, it seems logical that detailed analyses will produce response estimates to which damage is more closely related than simplified analyses. When uncertainties in damage and loss estimation are large, however, the effects of different levels of uncertainty in response analyses may not have a significant effect on loss curves. This appears to be the case for the conditions studied in the analysis of the subject testbed bridge structure.

10 Summary and Conclusions

Performance-based earthquake engineering provides for the prediction of seismic performance of structures and facilities in terms that are useful to various stakeholders. The performance-based framework developed by PEER allows description of performance in terms that are useful to earth scientists, engineers, loss analysts, and facility owners/operators. It accounts for ground motions, system response, physical damage, and related losses in a systematic fashion that accounts for uncertainties in all of these factors. The primary goal of the research described in this report was to illustrate the manner in which the PEER framework could be used to evaluate the performance of a bridge underlain by liquefiable soils.

A detailed performance evaluation was undertaken for a hypothetical, but realistic, highway bridge founded on liquefaction-susceptible soils. Such conditions are relatively common for bridges in seismically active areas, but response has historically been difficult to evaluate using available computational tools. As a result, response evaluations have typically been performed using empirical or simplified computational models. The output of such models is limited, so their use in the direct estimation of physical damage is fraught with uncertainty. As a result, estimates of loss based on such estimates of physical damage are also affected by these high levels of uncertainty.

The detailed performance evaluation was based on response computations using the OpenSees computational platform; OpenSees allows high-level modeling of both the structural and geotechnical components of a bridge and its foundations, which then allows direct estimation of response variables to which physical damage is related. As a result, subsequent loss estimates can be based upon more accurate measures of physical damage.

10.1 SUMMARY

Following reviews of the basic concepts of performance-based earthquake engineering and soil-pile-structure interaction, a hypothetical highway testbed bridge and soil profile was defined. The bridge superstructure was taken to be identical to that analyzed under fixed-based conditions by Mackie and Stojadinović (2006). The soil profile was developed in coordination with Prof. Jonathan Bray and Dr. Christian Ledezma of UC Berkeley who were carrying out a parallel project based on the use of empirical and simplified analyses on the same bridge-soil system. The soil profile beneath the hypothetical testbed bridge included a shallow layer of liquefaction-susceptible soil of variable thickness. The liquefiable layer was thicker beneath the right abutment than the left abutment, but lateral spreading hazards were anticipated beneath both abutments and bridge approaches. The pile foundations required to support the bridge on the selected soil profile were designed by Dr. Ledezma.

The response of the bridge to earthquake loading was analyzed using a detailed OpenSees finite element model. The model captured details of the structural response, such as bearing response, abutment wall break-off, girder-abutment impact, etc., which are often not explicitly modeled in analyses that include soil response. The model also captured details of the geotechnical response, such as phase transformation behavior in liquefiable soils, nonlinear, inelastic pile-soil interaction, permanent soil deformations, etc., which are often not explicitly modeled in analyses that include structural response. While the OpenSees modeling effort went considerably beyond that normally used in contemporary practice, it provides a view of the types of analyses that are likely to become practical in the relatively near future.

The computed response was used to estimate various forms of physical damage, which were each divided into different damage states. The cost of repair for each damage state was then estimated. Convolving the response, damage, and loss models with a ground motion hazard curve allowed estimation of repair cost hazard curves. Cost hazard curves were also developed for cases in which pore pressure generation in potentially liquefiable soils was restricted; the difference between the cost curves with and without pore pressure generation provides insight into the effects of liquefaction on estimated repair costs. Repair cost curves were also generated for the fixed base model to allow the estimation of repair costs based solely on shaking-induced structural damage.

The research described in this report provides useful insights into the conceptual and practical factors that influence performance-based earthquake engineering evaluations, and demonstrates the benefits of performing such evaluations. By performing detailed response analyses, the *EDPs* that relate most closely to physical damage, and hence to repair costs, could be explicitly computed. The primary conclusions that could be drawn from this investigation include:

1. *The occurrence of liquefaction can cause sharply increased losses for a bridge subject to lateral spreading hazards.* The analyses performed in this research investigation showed that losses associated with liquefaction-induced permanent soil deformations were substantial. At even moderate return periods, losses were essentially doubled by the occurrence of liquefaction.
2. *Detailed modeling of soil-foundation-structure systems can provide more extensive and more accurate estimates of system response, which lead to improved damage and loss estimates.* The additional uncertainty in response that comes with the use of simplified response models leads to higher damage and loss estimates for a given hazard level. The extent to which eventual loss estimates are influenced by the accuracy of response estimates depends on the sensitivity of damage to response and of loss to damage, which vary from site-to-site and structure-to-structure.
3. *Selection of optimal IMs can lead to significant reductions in EDP uncertainty, particularly for aspects of response related to soil liquefaction.* The basic concept that response hazards are sensitive to the uncertainty in response predictions is well established. The resulting goal of working with *IMs* that are better predictors of response than other *IMs* follows naturally from that concept. The analyses performed in this investigation showed substantial differences in liquefaction-related *EDP* hazards when predicted by different *IMs*.
4. *Liquefaction-related hazards are better predicted by velocity-related IMs than acceleration-related IMs.* Response analyses performed for some 40 input motions representing four different *IM* hazard levels showed that velocity-related *IMs* such as peak ground velocity, Arias intensity, and CAV5 were significantly more efficient predictors of response than peak ground acceleration. This observation is consistent with the known facts that pore pressure generation in liquefiable soils is more closely related

to shear strain than shear stress, and that shear strain amplitudes are proportional to particle velocity in basic (linear) wave propagation.

5. *The use of detailed soil-foundation-structure interaction analyses can lead to useful insights into system behavior.* The response of a soil-foundation-structure system such as the highway testbed bridge studied in this investigation is complex and multi-faceted. Certain aspects of the response to certain input motions were strongly affected by interaction of all of the bridge/soil components. For example, the leftward lateral translation of the bridge deck observed in response to some input motions caused column drift ratios on the left side of the bridge to be greater than those on the right side even though the lateral spreading displacements on the right side of the bridge were greater than those on the left.
6. *Power law relationships can provide a good approximation to IM-EDP relationships even for complex soil-foundation-structure systems.* Relatively simple power law relationships were found to provide good median fits to *EDP-IM* data generated from extensive series of OpenSees analyses.
7. *Residuals from power law fits to response data were approximately lognormally distributed.* The residuals of *EDP|IM* from extensive series of OpenSees analyses were observed to be approximately lognormally distributed. This observation, along with that described in Item 4 above, allows the development of useful closed-form solutions for the *EDP* hazard.
8. *Record-to-record variability dominates the computation of response hazards.* Investigation of the effects of parametric uncertainty and spatial variability of soil properties showed that their contribution to response hazards was much lower than that of record-to-record variability. This emphasizes the importance of using efficient and sufficient *IMs* for response estimation, and of paying close attention to the selection and scaling of input motions for response analyses.

REFERENCES

- Abdoun T., Dobry R., O'Rourke T.O., and Goh S.H. (2003). Pile response to lateral spreads: Centrifuge modeling. *Journal of Geotechnical and Geoenvironmental Engineering, ASCE*, Vol. 129(No. 10):869–878.
- API (1993). Recommended practice for planning, designing and constructing offshore platforms. API Recommended Practice 2A (RP 2A), 20th Edition, Washington, D.C.
- Arulanandan R., Boulanger R.W., Kutter B.L., and Sluis W.K. (2000). New tool for shear wave velocity measurements in model tests. *Geotechnical testing journal*, Vol. 23(No. 4):444–453.
- Baecher G.B. and Christian J.T. (2003). *Reliability and Statistics in Geotechnical Engineering*. Prentice-Hall.
- Barton Y.O. and Finn W.D.L. (1983). Lateral pile response and p-y curves from centrifuge tests. *Proceedings of the 15th Annual Offshore Technology Conference, Houston, Texas*, (Paper 4502):503–508.
- Berber T.M. and Rollins K.M. (2005). Lateral subgrade moduli for liquefied sand under cyclic loading. *Seismic Performance and Simulation of Pile Foundations in Liquefied and Laterally Spreading Ground, Geotechnical Special Publication*, (No. 145):149–160.
- Berry M.P. and Eberhard M.O. (2003). Performance models for flexural damage in reinforced concrete columns. PEER Report No. 2003/18. Pacific Earthquake Engineering Research Center, University of California, Berkeley.
- Boulanger R.W., Chang D., Gulerce U., Brandenburg S.J., and Kutter B.L. (2005). Evaluation pile pinning effects on abutments over liquefied ground. *Seismic Performance and Simulation of Pile Foundations in Liquefied and Laterally Spreading Ground, Geotechnical Special Publication*, (No. 145):306–318.
- Boulanger R.W., Curras C.J., Kutter B.L., D.W. Wilson, and A. Abghari (1999). Seismic soil-pile-structure interaction experiments and analysis. *Journal of Geotechnical and Geoenvironmental Engineering, ASCE*, Vol. 125(No. 9):750–759.
- Boulanger R.W., Wilson D.W., Kutter B.L., Brandenburg S.J., and Chang D. (2004). Nonlinear FE analysis of soil-pile-interaction liquefying sand. *Proceedings, Geotechnical Engineering for Transportation Projects, Geotechnical Special Publication*, (No. 126): 470–478.

- Brandenberg S.J., Boulanger R.W., Kutter B.L., and Chang D. (2005). Behavior of pile foundations in laterally spreading ground during centrifuge tests. *Journal of Geotechnical and Geoenvironmental Engineering, ASCE*, Vol. 131(No. 11):1378–1391.
- Brandenberg S.J. (2005). *Behavior of Pile Foundations in Liquefied and Laterally Spreading Ground*. Ph.D. thesis, University of California, Davis.
- Briaud J.-L. and Smith T.D. (1983). Using the pressuremeter curve to design laterally loaded piles. *Proceedings of the 15th Annual Offshore Technology Conference, Houston, Texas*, (Paper 4502):495–502.
- Broms B.B. (1964). Lateral resistance of piles in cohesionless soils. *Journal of Soil Mechanics and Foundations Division*, Vol. 90(SM3):123–156.
- Broms B.B. (1964). Lateral resistance of piles in cohesive soils. *Journal of Soil Mechanics and Foundations Division*, Vol. 90(SM2):27–63.
- Brown D.A., Morrison C., and Reese L.C (1988). Lateral load behavior of pile group in sand. *Journal of Geotechnical and Geoenvironmental Engineering, ASCE*, Vol. 114(No. 11):1261–1276.
- Caltrans (2004). Caltrans seismic design criteria.
- Caltrans, (2004). Construction Statistics Based on Bid Openings, 2004. California Department of Transportation, Division of Engineering Services. http://www.dot.ca.gov/hq/esc/estimates/Construction_Stats_2004.xls
- Caltrans, (2005). Comparative Bridge Costs, January 2005. California Department of Transportation, Division of Structure Earthquake Engineering & Design Support
- Castello R.R. (1980). *Bearing Capacity of Driven Piles in Sand*. PhD thesis, Texas AM University, College Station, Texas.
- Chai Y.H. (2002). Flexural strength and ductility of extended pile-shafts. i: Analytical model. *Journal of Structural Engineering*, Vol. 128(No. 5):586–594.
- Chai Y.H. and Hutchinson T.C. (2002). Flexural strength and ductility of extended pile-shafts. ii: Experimental study. *Journal of Structural Engineering*, Vol. 128(No. 5):595–602.
- Cordova P. (2000). Development of a two-parameter seismic intensity measure and probabilistic seismic assessment procedure. PEER Report No.2000/10, 195–214. Pacific Earthquake Engineering Research Center, University of California, Berkeley.

- Cornell C. A. and Krawinkler H. (2000). Progress and challenges in seismic performance assessment. *PEER News*, April, pages 1–3.
- Coyle H. and Castello R. (1981). New design correlations for piles in sand. *Journal of Geotechnical Engineering Division, ASCE*, Vol. 107(No. GT7).
- Coyle H.M and Sulaiman I.H. (1967). Skin friction for steel piles in sand. *Journal of the Soil Mechanics and Foundation Division, ASCE*, Vol. 93(No. Sm-6).
- Curras C.J., Boulanger R.W., Kutter B.L., and Wilson D.W. (2001). Dynamic experiences and analysis of a pile-group-supported structure. *Journal of Geotechnical and Geoenvironmental Engineering, ASCE*, Vol. 127(No. 7):585–596.
- Deierlein G.G., Krawinkler H., and Cornell C.A. (2003). A framework for performance-based earthquake engineering. *Proceedings, 2003 Pacific Conference on Earthquake Engineering*.
- Dobry R., Taboada V., and Liu L. (1995). Centrifuge modeling of liquefaction effects during earthquakes. *Proc. 1st Intl. Conf. on Earthquake Geotechnical Engineering, K. Ishihara, ed., Tokyo, Japan*, Vol. 3:1291–1324.
- Duncan J.M. (2000). Factors of safety and reliability in geotechnical engineering. *Journal of Geotechnical and Geoenvironmental Engineering, ASCE*, Vol. 126(No. 4):307–316.
- Fleming W.G.K., Weltman A.J., and Randolph M.F. (1992). *Piling engineering*. Surrey University Press, London.
- Gazetas G. and Mylonakis G. (1998). Seismic soil-structure interaction: New evidence and emerging issues. *Geotechnical Earthquake Engineering and Soil Dynamics III, Geotechnical Special Publication*, Vol. 2(No. 75): 1119–1174.
- Gerolymos N. and Gazetas G. (2005). Phenomenological model applied to inelastic response of soil-pile interaction systems. *Soil and Foundations*, Vol. 45(No. 4): 119–132.
- Hamada M. (1992). Large ground deformations and their effects on lifelines: 1964 Nigata earthquake. *Case Studies of Liquefaction and Lifeline Performance During Past Earthquakes, Japanese Case Studies*. Technical Report NCEER-92-0001, NCEER, Buffalo, NY, USA., Vol. (1), 3.1–3.123.
- Harr M.E. (1987). *Reliability-Based Design in Civil Engineering*. McGraw-Hill.
- He L., Elgamal A., Abdoun T., Dobry R., Meneses J., Sato M., and Tokimatsu K. (2006). Lateral load on piles due to liquefaction-induced lateral spreading during one-g shake table experiments. *Proceedings of 8th National Conference on Earthquake Engineering, San Francisco, August 2006*.

- Hose Y., Silva P., and Seible F. (2000). Development of a performance evaluation database for concrete bridge components and systems under simulated seismic loads. *Earthquake Spectra*, Vol. 16(No. 2):413–442.
- Ilankatharan M., Kutter B., Shin H., Arduino P., and Kramer S.L. (2007). A demonstration of NEES system for studying soil-foundation-structure interaction: Centrifuge data report for test series mil02. and Environmental Engineering, University of California, Davis, California.
- Ilankatharan M., Kutter B., Shin H., Arduino P., and Kramer S.L. (2007). A demonstration of NEES system for studying soil-foundation-structure interaction: Centrifuge data report for test series mil03. and Environmental Engineering, University of California, Davis, California.
- Ilankatharan M., Kutter B.L., Shin H., Arduino P., Kramer S.L., Johnson N., and Sasaki T. (2006). Comparison of centrifuge and 1 g shake table models of a pile supported bridge structure. *Proceedings of the International Conference on Physical Modeling in Geotechnics, August*.
- Ilankatharan M., Sasaki T., Shin H., Kutter B., Arduino P., and Kramer S.L. (2005). A demonstration of NEES system for studying soil-foundation-structure interaction: Centrifuge data report for test series mil01. Rep. No. UCD/CGMDR-05/05, Ctr. for Geotech. Modeling, Dept. of civil and Environmental Engineering, University of California, Davis, California.
- Jalayer F. (2003). *Direct probabilistic Seismic Analysis: Implementating non-linear dynamic assessments*. PhD thesis, Stanford University, Stanford, California.
- Johnson N., Saiidi M., and Sanders D. (2006). Large-scale experimental and analytical seismic studies of a two-span reinforced concrete bridge system. Technical Report CCEER-06-02, University of Nevada, Reno.
- Jones A.L., Kramer S.L., and Arduino P. (2002). Estimation of uncertainty in geotechnical properties for performance-base earthquake engineering. PEER Report No.2002/16, Pacific Earthquake Engineering Research Center, University of California, Berkeley.
- JRA (2002). Specifications for highway bridges. Japan Road Association, Preliminary English Version, prepared by Public Works Research Institute (PWRI) and Civil Engineering Research Laboratory (CRL), Japan, November.

- Juirnarongrit T. and Ashford S.A. (2004). Analyses of pile responses based on results from full-scale lateral spreading test: Tokachi blast experiment. *Proceedings of 13th World Conference on Earthquake Engineering, Vancouver, Canada, August 1–6*.
- Kawamata Y., Ashford S.A., and Juirnarongrit T. (2006). Numerical simulation of deep foundations subjected to lateral spreading for Tokachi blast test. *Proceedings of 8th National Conference on Earthquake Engineering, San Francisco, August 2006*.
- Kerisel J. (1964). Deep foundations, basic experimental facts. Proceedings, Conference on Deep Foundations, Mexican Society of Soil Mechanics, Mexico City, Mexico, Vol.1, p.5.
- Ketchum M., Chang V., and Shantz T. (2004). Influence of design ground motion level on highway bridge cost. PEER Lifelines Project Number 6D01 Report, Pacific Earthquake Engineering Research Center, University of California, Berkeley.
- Kramer S.L. (1996). *Geotechnical Earthquake Engineering*. Prentice-Hall.
- Kramer S.L. (2006). Personal communications.
- Kramer S.L. and Mitchell R.A. (2006). Ground motion intensity measures for liquefaction hazard evaluation. *Earthquake Spectra*, Vol. 22(No. 2).
- Krawinkler H. (2002). A general approach to seismic performance assessment. *Proceedings, International Conference on Advances and New Challenges in Earthquake Engineering Research (ICANCEER), Hong Kong*.
- Krawinkler H. and Miranda E. (2004). Performance-based earthquake engineering. In Bozorgnia Y. and Bertero V., editors, *Earthquake Engineering from Engineering Seismology to Performance-Based Earthquake Engineering*. CRC Press.
- Kulhawy F.H. (1992). On the evaluation of static soil properties. *ASCE Geotechnical Special Publication*, (No. 31):95–115.
- Lacasse S. and Nadim F. (1996). Uncertainties in characterizing soil properties (plenary), uncertainty in the geologic environment, from theory to practice. *Proceeding of Uncertainty '96, Geotechnical Special Publication No.58*.
- Ledezma C.A. and Bray J.D. (2006). Peer bridge design of piles under the abutment.
- Ledezma C.A. and Bray J.D. (2006). Peer bridge pile design report.
- Ledezma, C.A. and Bray, J.D. (2007). “Performance-Based Earthquake Engineering Design Evaluation Procedure for Bridge Foundations Undergoing Liquefaction-Induced Lateral Spreading” PEER Report 2007/xx, Pacific Earthquake Engineering Research Center, Berkeley, California, 150 pp.

- Luco N. and Cornell C.A. (2001). Structure-specific scalar intensity measures for near-source and ordinary earthquake ground motions. *Earthquake Spectra*. Submitted for publication.
- Mackie K and Stojadinović B. (2003). Seismic demands for performance-based design of bridges. PEER Report No. 2003/16. Pacific Earthquake Engineering Research Center, University of California, Berkeley.
- Mackie K and Stojadinović B. (2005). Simplified application of the PEER methodology. <http://dodo.ce.berkeley.edu/mackie/Yr8/>.
- Mackie K., Wong J-M., and Stojadinović B. (2004). Method for post-earthquake highway bridge repair cost estimation. *Proceedings of 5th National Seismic Conference on Bridges and Highways, San Mateo, CA*.
- Mackie K.R. and Stojadinović B. (2005). Comparison of incremental dynamic, cloud, and stripe methods for computing probabilistic seismic demand models. *In Proceedings of the 2005 ASCE Structures Congress, April 20–24, New York, NY*.
- Mackie, K., Wong, J-M., and Stojadinović, B. (2006). "Method for post-earthquake highway bridge repair cost estimation." In *Proceedings of the 5th National Seismic Conference on Bridges and Highways, September 18–20. San Francisco, CA*.
- Mackie, K., and Stojadinović B, (2007). "Performance of Benchmark Bridge Structures," ASCE Structures Congress, Long Beach, CA. May 16–19 2007.
- Mackie, K.R., Wong, J.-M., Stojadinović, B. (2007). "Integrated Probabilistic Performance-Based Evaluation of Benchmark Reinforced Concrete Bridges," PEER Report 2007/xx, Pacific Earthquake Engineering Research Center, Berkeley, California, 202 pp
- Makido A. (2007). *Behavior of Spirally Reinforced Concrete Columns under Load Reversals*. PhD thesis, Purdue University.
- Maroney B.H. (1995). *Large scale bridge abutment tests to determine stiffness and ultimate strength under seismic loading*. Ph.D. thesis, University of California, Davis, CA.
- Matlock H. (1970). Correlations for design of laterally loaded piles in soft clay. *Proceedings of the II Annual Offshore Technology Conference, Houston, Texas, (OTC 1204):577–594*.
- Mokwa R.L. (1999). *Investigation of the Resistance of Pile Caps to Lateral Loading*. Ph.D. thesis, Virginia Polytechnic Institute.
- Mosher R.L (1984). Load transfer criteria for numerical analysis of axially loaded piles in sand. US Army Engineering Waterways Experimental Station, Automatic Data Processing Center, Vicksburg, Mississippi.

- NAVFAC (1982). Foundations and earth structures design manual 7.2. Department of the Navy, Naval Facilities Engineering Command, Alexandria, VA.
- Novak M. (1974). Dynamic stiffness and damping of piles. *Canadian Geotechnical Journal, ASCE*, Vol. 11: 574–598.
- O'Neill M.W. and Reese L.C (1999). Drilled shafts: construction procedures and design methods. Report FHWA-HI-88-042, US Department of Transportation, Federal Highway Administration, Office of Implementation, McLean, Virginia.
- Ovesen N.K. (1964). Anchor slabs, calculation methods and model tests. *Bulletin No. 16*. The Danish Geotechnical Institute, Copenhagen.
- Parker Jr., Fl and Reese L.C. (1969). Experimental and analytical studies of behavior of single piles in sand under lateral and axial loading. Research Report 117-2, Center for Highway Research, University of Texas, Austin, TX.
- Peck R.B., Hanson W.E., and Thornburn T.H. (1974). *Foundation engineering, 2nd Ed*. New York, Wiley.
- Petek K.A. (2006). *Development and Application of Mixed Beam-Solid Models for Analysis of Soil-Pile Interaction Problems*. Ph.D. thesis, University of Washington.
- Phoon K. and Kulhawy F.H. (1999). Characterization of geotechnical variability. *Canadian Geotechnical Journal, ASCE*, Vol. 36: 625–639.
- Poulos H.G. and Davis E.H. (1980). *Pile foundation analysis and design*. Wiley, New York.
- Randolph M.F. (1981). The response of flexible piles to lateral loading. *Geotechnique*, Vol. 31(No. 2):247–259.
- Ranf R.T. (2007). *Model Selection for Performanced-Based Earthquake Engineering*. PhD thesis, University of Washington.
- Reese L.C., Allen J.D., and Hargrove J.Q. (1981). Laterally loaded piles in layered soils. *Proceedings of the tenth international conference on soil mechanics and foundation engineering, Stockholm, Vol. 2, 819–822, 15–19 June*.
- Reese L.C., Cox W.R., and Koop F.D. (1974). Analysis of laterally loaded piles in sand. *Proceedings of the 6th Offshore Technology Conference, Houston, Texas, (2(OTC2080))*:473–485.
- Reese L.C., Cox W.R., and Koop F.D. (1975). Field testing and analysis of laterally loaded piles in stiff clay. *Proceedings of the 7th Offshore Technology Conference, Houston, Texas, (2(OTC2312))*:672–690.

- Reese L.C. and Van Impe W.F. (2001). *Single Piles and Pile Groups Under Lateral Loading*. A. A. Balkema, Rotterdam.
- Rollins K.M., T.M. Gerber, Lane D., and Ashford S.A. (2005). Lateral resistance of a full-scale pile group in liquefied sand. *Journal of Geotechnical and Geoenvironmental Engineering, ASCE*, Vol. 131(No. 1):115–125.
- SDC (2004). Caltrans seismic design criteria. http://www.dot.ca.gov/hq/esc/earthquake_engineering/SDC/SDCPage.html.
- Seed H.B. (1986). Design problems in soil liquefaction. *Journal of Geotechnical Engineering, ASCE*, Vol. 113 (No. 8):827–845.
- Seed H.B. and Harder L.F. (1990). SPT-based analysis of cyclic pore pressure generation and undrained residual strength. *Proceedings, H. Bolton Seed Memorial Symposium*,. University of California, Berkeley, Vol. 2, pp 351–376.
- Seed H.B and Idriss I.M. (1970). Soil moduli and damping factors for dynamic response analyses. Report EERC 70-10, Earthquake Engineering Research Center, University of California, Berkeley.
- Somerville P.G. (2000). Characterizing near fault ground motion for the design and evaluation of bridges. *Proceedings of the Third National Seismic Conference and Workshop on Bridges and Highways*.
- Stark T.D. and Mesri G. (1992). Undrained shear strength of sands for stability analysis. *Journal of Geotechnical Engineering, ASCE*, Vol. 118 (No. 11):1727–1747.
- Suzuki H., Tokimatsu K., and Ozawa G. (2006). Evaluation of group pile effects in non-liquefied and liquefied ground based on centrifuge model tests. *Proceedings of 8th National Conference on Earthquake Engineering, San Francisco, August 2006*.
- Tokimatsu K., Suzuki H., and Suzuki Y. (2001). Back-calculated p-y relation of liquefied soils from large shaking table tests. *Fourth International Conference on Recent Advances in Geotechnical Earthquake Engineering and Soil Dynamics*, (Paper No. 6.24):672–690. S. Prakash ed.
- Upsall, S.B. (2006). “Instrumental Intensity Scales for Geotechnical and Structural Damage,” Ph.D. Dissertation, University of Washington, Seattle, Washington, 403 pp.
- Vesic A.S. (1970). Tests on instrumented piles, Ogeechee river site. *Journal of the Soil Mechanics and Foundations Division, ASCE*, Vol. 96(SM2):pp 561– 584.

- Vijayvergiya V.N. (1997). Load-movement characteristics of piles. Proceedings of the Ports 77 Conference, Long Beach, California, ASCE.
- Wang S.-T. and Reese L.C. (1998). Design of pile foundation in liquefied soils. *Geotechnical Earthquake Engineering and Soil Dynamics III, Geotechnical Special Publication*, Vol. 2(No. 75): 1331–1343.
- Weaver T.J., Ashford S.A., and Rollins K.M. (2005). Response of 0.6 m cast-in-steel-shell pile in liquefied soil under lateral loading. *Journal of Geotechnical and Geoenvironmental Engineering, ASCE*, Vol. 131(No. 1):94–102.
- Wilson D.W. (1998). *Soil-Pile-Superstructure Interaction in Liquefying Sand and Soft Clay*. Ph.D. thesis, University of California, Davis.
- Wilson D.W., Boulanger R.W., and Kutter B.L. (2000). Observed seismic lateral resistance of liquefying sand. *Journal of Geotechnical and Geoenvironmental Engineering, ASCE*, Vol. 126(No. 10):898–906.
- Wood D.M. (2004). *Geotechnical Modeling, Applied Geotechnics Volume 1*. Spon Press.
- Wood S.L., Anagnos T., Eberhard M.O., Fenves G.L., Finholt T.A., Futrelle B., J.M. Jeremić, Kramer S.L., Kutter B.L., Matamoros A.B., McMullin K.M., Ramirez E.M., J.A. Rathje, Saiidi Sanders D.H. Stokoe K.H., M., and Wilson D.W. (2004). Using NEES to investigate soil-foundation-structure interaction. *Proceedings of 13th World Conference on Earthquake Engineering, Vancouver, Canada, August 1–6*.
- Yamazaki F. and Shinozuka M. (1988). Digital generation of non-gaussian stochastic fields. *Journal of Engineering Mechanics, ASCE*, Vol. 114(No. 7):1183–1197.
- Yang Z., Elgamal A., and Parra E. (2003). Computational model for cyclic mobility and associated shear deformation. *Journal of Geotechnical and Geoenvironmental Engineering, ASCE*, Vol. 129(No. 12):1119–1127.
- Zhang L., Silva F., and Grismala R. (2005). Ultimate lateral resistance to piles in cohesionless soils. *Journal of Geotechnical and Geoenvironmental Engineering*, Vol. 131(No. 1):78–83

Appendix: Implementation of PBEE

A.1 INTRODUCTION

The PEER PBEE methodology can be implemented in a number of different ways depending on the needs and perspective of the end user(s). One of the significant benefits of the methodology is that it is modular, i.e., it can be broken into different components so that performance can be explicitly described with respect to measures of response, damage, and loss.

This appendix presents a brief description of how the PEER methodology can be implemented for evaluation of the performance of a bridge founded on liquefiable soils. This description is intended to summarize the main steps in the evaluation process in a more concise form than that used to describe the investigation in the body of the report. Before undertaking such an evaluation, it is recommended that the entire report be read and understood.

A.2 THE PEER PBEE PROCESS

Before beginning, it is important to understand the basic building blocks of the PEER PBEE process. The process is illustrated schematically in Figure A.1. Earthquake loading is defined in terms of an intensity measure, IM . A response model is used to predict the response, EDP , from the intensity measure. A damage model is then used to predict the physical damage, DM , associated with the response. Finally, a loss model allows prediction of loss, DV , from the physical damage.

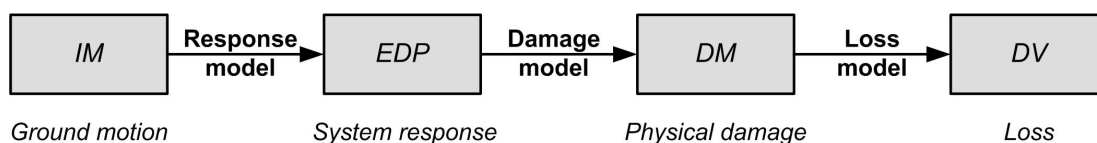


Fig. A.1 Schematic illustration of PEER PBEE components.

The intensity measure varies with exposure time in a manner commonly described by a seismic hazard curve, which is the result of a probabilistic seismic hazard analysis. In the PEER PBEE framework, the response is integrated (Eq. 2.1) over all values of the intensity measure—this means that the response of the system of interest must be computed for ground motions ranging from very weak (which may induce only elastic response) to very strong (which may induce highly nonlinear, inelastic response). The damage measure is integrated over all levels of response, so the selected damage model must be capable of predicting damage from both very low and very high levels of response. Finally, the decision variable is integrated over all levels of damage, so the loss model must predict losses from damage levels ranging from very low to very high.

The results of the response, damage, and loss models can be represented by fragility curves when each is expressed by a continuous random variable. This is the most common form of output for response models, but current damage and loss models are often expressed in discrete form; in such cases, their results can be expressed in terms of damage and loss probability matrices.

A.3 THE PROCEDURE

The remainder of this appendix provides a concise description of the major steps in a PEER framework-based PBEE evaluation of an existing structure. The structure used to illustrate the procedure is the bridge studied in this investigation, but the basic principles can be applied to any structure.

- 1. Look at the big picture.** Determine the purpose of the seismic evaluation and how the results will be used to make retrofit, replacement, or other decisions. Identify the basis on which such decisions will be made, i.e., define the decision variables. For illustration procedures, this appendix will assume that decisions will be made on the basis of direct economic losses, but other factors such as casualties, downtime, and indirect losses may also factor into the decision process.
- 2. Define potential other variables of interest.** Based on the decision variable(s), identify potential damage measures (DMs). The damage measures should be those that the decision variables are most closely related to. Identification of these variables may be

beyond the range of experience of a typical geotechnical or structural engineer; their identification may require consultation with construction estimators, insurance adjustors, or other professionals who are familiar with costs associated with repair of damage. Such professionals should be asked to estimate median costs and some measure of dispersion (e.g., the cost with 10% probability of exceedance, which, with the median cost can be used to estimate a distribution of loss given damage).

Potential response parameters should be defined with consideration of the damage measures, i.e., the response parameters (*EDPs*) should be those that correlate most strongly to the selected damage measures. For a substantial structure that can suffer more than one type of damage, multiple *EDPs* will be required. Finally, potential ground motion intensity measures (*IMs*) should be identified. The intensity measures should be those that response is most closely related to. It is important to recognize that the intensity measures must be those for which seismic hazard curves can be generated; this requires that an appropriate attenuation relationship be available for the *IM* of interest. For complex structures, multiple intensity measures (i.e., vector *IMs*) may provide an optimum prediction of response, particularly in situations where different physical phenomena (for example, soil liquefaction and structural vibration) strongly affect system response.

- 3. Develop and test a response model.** The response model will predict the desired *EDP* values given the selected *IMs*. Response models can range from empirical models to simplified analytical models to complex, detailed analytical models. An appropriate response model must use the identified *IMs* as inputs and produce the desired *EDPs* as outputs. In this appendix, the use of a nonlinear finite element response model is assumed.

Model development should consider the *EDPs* that are required for damage estimation. The complexity of the model should be adjusted so that these *EDPs* can be computed as accurately as the model is capable of doing. Aspects of the response that do not correlate to damage can be modeled in more approximate ways. For the bridge structure analyzed in this investigation, particular attention was paid to the liquefiable sands (i.e., using a constitutive model that was capable of capturing detailed aspects of liquefiable sand behavior such as phase transformation and dilation, and refining the mesh to allow development of anticipated damage mechanisms), the pile foundations

(i.e., defining p-y, t-z, and Q-z curves that would represent pile-soil interaction in all of the soils), the abutments (defining a breakable abutment backwall that would fracture in order to limit the axial loading on the bridge deck), the bridge bearings, and the boundary conditions.

The response model should be tested by analyzing the response to one or two input motions scaled to values ranging from very low (i.e., corresponding to short return periods for the site of interest) to very high (long return periods). The user should be confident that the model is stable and converging toward reasonable response predictions before proceeding further.

- 4. Define suite of input motions.** The response must be computed for appropriate input motions that reasonably represent the range of *IM* levels of interest at the site. The input motions should cover a range of shaking levels in order to define the response from low to high *IM* levels. For the investigation described in this report, ten ground motions corresponding to each of four return periods (for a total of 40 motions) were selected; attention was paid to ensure that at least one of these levels was low enough that liquefaction would not be triggered. The total number of motions required for the response analyses is not fixed—however, it is suggested that at least seven motions corresponding to each of at least three return periods be used. Definition of the input motions requires great care and may involve some level of scaling; procedures for ground motion selection are evolving in other PEER studies.
- 5. Perform and interpret results of response analyses.** Once the input motions have been defined, they should be applied to the response model for calculation of all *EDPs*. The *EDPs* should then be plotted vs *IMs*—log-log plots have proven useful for characterization of fragility behavior, since median *EDP-IM* behavior is often reasonably modeled by power law relationships (which plot linearly on log-log plots). At this stage, *EDPs* should be plotted against all potential *IMs* to determine which *IMs* are the most efficient predictors of the various *EDPs*; note that different *IMs* may be optimal for different *EDPs*. For example, Figure A.2 shows the variation of vertical embankment displacement at the right abutment with three *IMs*—peak ground velocity, Arias intensity, and CAV5. Power law relationships are appropriate for all three *IMs*, but the figure shows clearly that CAV5 is the most efficient predictor of this particular *EDP*. For a

different *EDP*, say Pier 4 maximum drift, Figure A.3 shows that peak velocity is the most efficient *IM*.

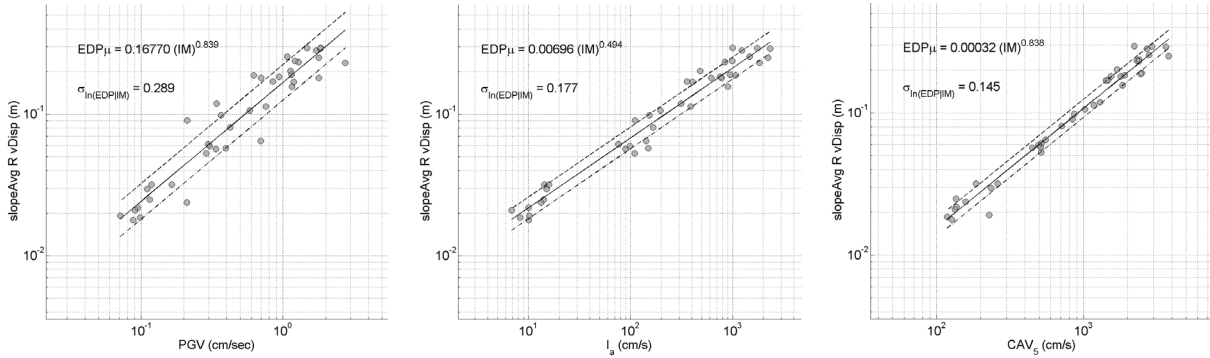


Fig. A.2 Variation of right abutment vertical displacement with (l-r) peak ground velocity, Arias intensity, and CAV_5 .

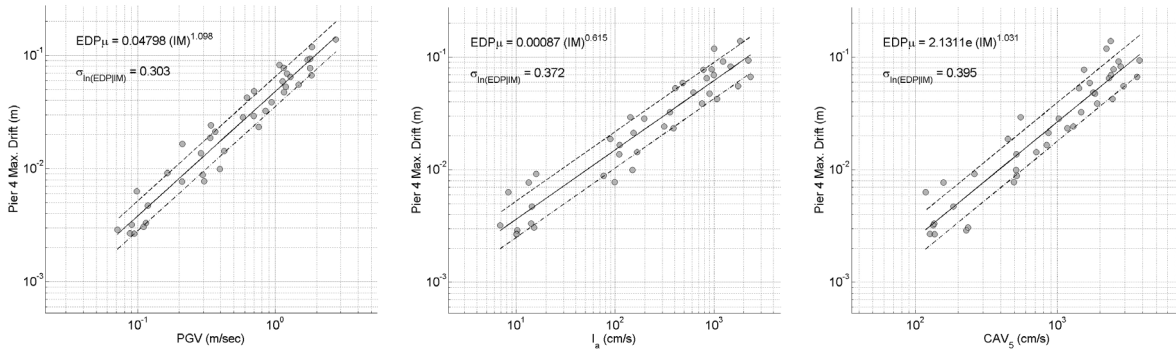


Fig. A.3 Variation of Pier 4 maximum drift with (l-r) peak ground velocity, Arias intensity, and CAV_5 .

6. Develop a damage model. The levels of damage resulting from different levels of response are predicted by damage models. For both fundamental and practical reasons, it is frequently difficult to characterize damage using smoothly varying continuous damage measures. Instead, a discrete number of damage limit states are usually defined, and the *EDP* levels corresponding to the different limit states estimated. In order to account for

uncertainties in capacities (i.e., the response levels corresponding to the different damage limit states), defining a damage model generally involves estimating the median *EDP* level and dispersion values at the boundaries between different limit states.

- 7. Develop a loss model.** The losses associated with different damage limit states are predicted by loss models. Loss models can be broken down into components associated with different repair methods. It should be noted that loss models may not be continuous and may not increase monotonically; for example, the cost of repairing cracks in a column by epoxy injection will drop to zero if the damage becomes so severe that a different repair method (or even column replacement) becomes more cost-effective.

The uncertainties associated with response, damage, and loss modeling have generally been found to be low relative to the uncertainty in ground motions. As a result, it may be convenient to collapse, or condense, the response, damage, and loss models into a single model that describes loss given ground motion, i.e., *DV|IM*. This condensation would take the form

$$P[DV > dv_l | IM = im_i] = \sum \sum P[DV > dv_l | DM = dm_k] P(DM > dm_k | EDP = edp_j) \times P[EDP > edp_k | IM = im_i] \quad (A.1)$$

This function actually describes a fragility surface, i.e., exceedance probabilities as a function of both *IM* and *DV*. Graphically, the fragility surface is shown in Figure A.4. It should be noted that the fragility curves are continuous and smooth in the *DV* dimension due to the assumption of lognormally distributed losses, but irregular in the *IM* direction due to the type of variability discussed in the preceding step.

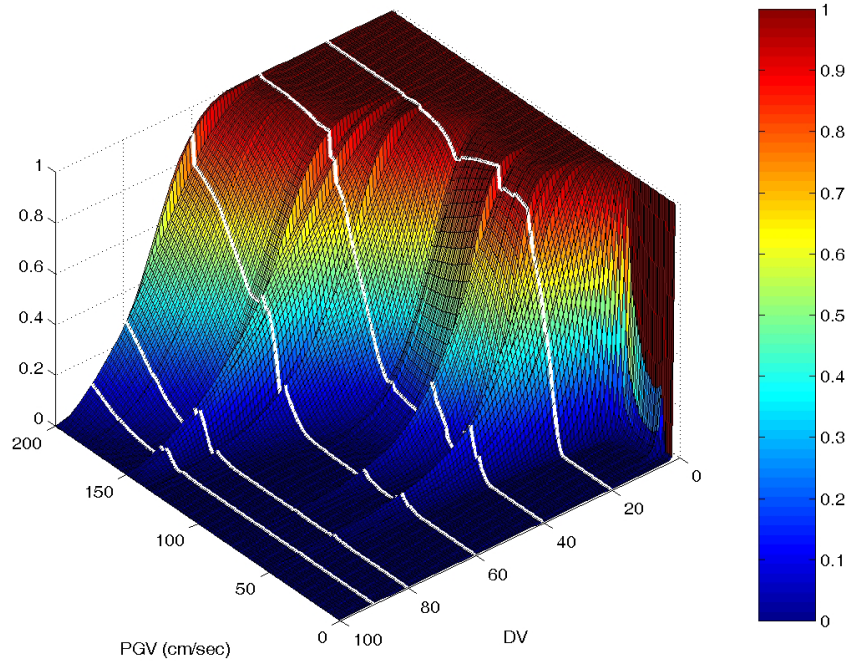


Fig. A.4 Fragility surface for testbed bridge. White lines indicate fragility curves for repair cost ratios of 20%, 40%, 60%, 80%, and 90%.

8. Compute loss curve. The condensed $DV|IM$ model can then be combined with an IM hazard curve to produce a loss curve using the following scheme

$$\lambda_{DV}(dv_l) = \sum_{i=1}^{N_{IM}} P[DV > dv_l | IM = im_i] \Delta \lambda_{IM}(im_i) \quad (A.2)$$

The integration over the IM hazard curve is carried out numerically, and produces a loss curve of the type shown in Figure A.5.

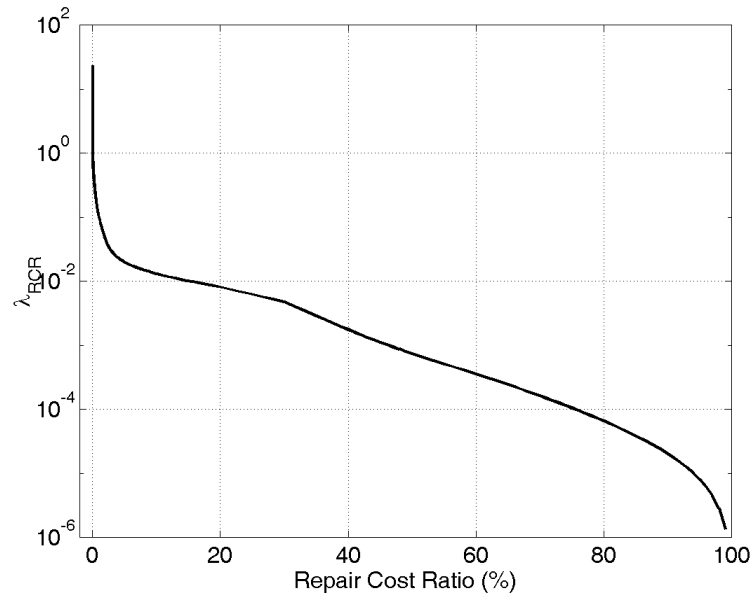


Fig. A.5 Loss curve for testbed bridge.

PEER REPORTS

PEER reports are available from the National Information Service for Earthquake Engineering (NISEE). To order PEER reports, please contact the Pacific Earthquake Engineering Research Center, 1301 South 46th Street, Richmond, California 94804-4698. Tel.: (510) 665-3405; Fax: (510) 665-3420.

- PEER 2008/07** *Using OpenSees for Performance-Based Evaluation of Bridges on Liquefiable Soils.* Stephen L. Kramer, Pedro Arduino, and HyungSuk Shin. November 2008.
- PEER 2008/06** *Shaking Table Tests and Numerical Investigation of Self-Centering Reinforced Concrete Bridge Columns.* Hyung IL Jeong, Junichi Sakai, and Stephen A. Mahin. September 2008.
- PEER 2008/05** *Performance-Based Earthquake Engineering Design Evaluation Procedure for Bridge Foundations Undergoing Liquefaction-Induced Lateral Ground Displacement.* Christian A. Ledezma and Jonathan D. Bray. August 2008.
- PEER 2008/04** *Benchmarking of Nonlinear Geotechnical Ground Response Analysis Procedures.* Jonathan P. Stewart, Annie On-Lei Kwok, Youssef M. A. Hashash, Neven Matasovic, Robert Pyke, Zhiliang Wang, and Zhaohui Yang. August 2008.
- PEER 2008/03** *Guidelines for Nonlinear Analysis of Bridge Structures in California.* Ady Aviram, Kevin R. Mackie, and Božidar Stojadinović. August 2008.
- PEER 2008/02** *Treatment of Uncertainties in Seismic-Risk Analysis of Transportation Systems.* Evangelos Stergiou and Anne S. Kiremidjian. July 2008.
- PEER 2008/01** *Seismic Performance Objectives for Tall Buildings.* William T. Holmes, Charles Kircher, William Petak, and Nabih Youssef. August 2008.
- PEER 2007/12** *An Assessment to Benchmark the Seismic Performance of a Code-Conforming Reinforced Concrete Moment-Frame Building.* Curt Haselton, Christine A. Goulet, Judith Mitrani-Reiser, James L. Beck, Gregory G. Deierlein, Keith A. Porter, Jonathan P. Stewart, and Ertugrul Taciroglu. August 2008.
- PEER 2007/11** *Bar Buckling in Reinforced Concrete Bridge Columns.* Wayne A. Brown, Dawn E. Lehman, and John F. Stanton. February 2008.
- PEER 2007/10** *Computational Modeling of Progressive Collapse in Reinforced Concrete Frame Structures.* Mohamed M. Talaat and Khalid M. Mosalam. May 2008.
- PEER 2007/09** *Integrated Probabilistic Performance-Based Evaluation of Benchmark Reinforced Concrete Bridges.* Kevin R. Mackie, John-Michael Wong, and Božidar Stojadinović. January 2008.
- PEER 2007/08** *Assessing Seismic Collapse Safety of Modern Reinforced Concrete Moment-Frame Buildings.* Curt B. Haselton and Gregory G. Deierlein. February 2008.
- PEER 2007/07** *Performance Modeling Strategies for Modern Reinforced Concrete Bridge Columns.* Michael P. Berry and Marc O. Eberhard. April 2008.
- PEER 2007/06** *Development of Improved Procedures for Seismic Design of Buried and Partially Buried Structures.* Linda Al Atik and Nicholas Sitar. June 2007.
- PEER 2007/05** *Uncertainty and Correlation in Seismic Risk Assessment of Transportation Systems.* Renee G. Lee and Anne S. Kiremidjian. July 2007.
- PEER 2007/04** *Numerical Models for Analysis and Performance-Based Design of Shallow Foundations Subjected to Seismic Loading.* Sivapalan Gajan, Tara C. Hutchinson, Bruce L. Kutter, Prishati Raychowdhury, José A. Ugalde, and Jonathan P. Stewart. May 2008.
- PEER 2007/03** *Beam-Column Element Model Calibrated for Predicting Flexural Response Leading to Global Collapse of RC Frame Buildings.* Curt B. Haselton, Abbie B. Liel, Sarah Taylor Lange, and Gregory G. Deierlein. May 2008.
- PEER 2007/02** *Campbell-Bozorgnia NGA Ground Motion Relations for the Geometric Mean Horizontal Component of Peak and Spectral Ground Motion Parameters.* Kenneth W. Campbell and Yousef Bozorgnia. May 2007.
- PEER 2007/01** *Boore-Atkinson NGA Ground Motion Relations for the Geometric Mean Horizontal Component of Peak and Spectral Ground Motion Parameters.* David M. Boore and Gail M. Atkinson. May 2007.
- PEER 2006/12** *Societal Implications of Performance-Based Earthquake Engineering.* Peter J. May. May 2007.
- PEER 2006/11** *Probabilistic Seismic Demand Analysis Using Advanced Ground Motion Intensity Measures, Attenuation Relationships, and Near-Fault Effects.* Polsak Tothong and C. Allin Cornell. March 2007.
- PEER 2006/10** *Application of the PEER PBEE Methodology to the I-880 Viaduct.* Sashi Kunnath. February 2007.

- PEER 2006/09** *Quantifying Economic Losses from Travel Forgone Following a Large Metropolitan Earthquake.* James Moore, Sungbin Cho, Yue Yue Fan, and Stuart Werner. November 2006.
- PEER 2006/08** *Vector-Valued Ground Motion Intensity Measures for Probabilistic Seismic Demand Analysis.* Jack W. Baker and C. Allin Cornell. October 2006.
- PEER 2006/07** *Analytical Modeling of Reinforced Concrete Walls for Predicting Flexural and Coupled-Shear-Flexural Responses.* Kutay Orakcal, Leonardo M. Massone, and John W. Wallace. October 2006.
- PEER 2006/06** *Nonlinear Analysis of a Soil-Drilled Pier System under Static and Dynamic Axial Loading.* Gang Wang and Nicholas Sitar. November 2006.
- PEER 2006/05** *Advanced Seismic Assessment Guidelines.* Paolo Bazzurro, C. Allin Cornell, Charles Menun, Maziar Motahari, and Nicolas Luco. September 2006.
- PEER 2006/04** *Probabilistic Seismic Evaluation of Reinforced Concrete Structural Components and Systems.* Tae Hyung Lee and Khalid M. Mosalam. August 2006.
- PEER 2006/03** *Performance of Lifelines Subjected to Lateral Spreading.* Scott A. Ashford and Teerawut Juirnarongrit. July 2006.
- PEER 2006/02** *Pacific Earthquake Engineering Research Center Highway Demonstration Project.* Anne Kiremidjian, James Moore, Yue Yue Fan, Nesrin Basoz, Ozgur Yazali, and Meredith Williams. April 2006.
- PEER 2006/01** *Bracing Berkeley. A Guide to Seismic Safety on the UC Berkeley Campus.* Mary C. Comerio, Stephen Tobriner, and Ariane Fehrenkamp. January 2006.
- PEER 2005/16** *Seismic Response and Reliability of Electrical Substation Equipment and Systems.* Junho Song, Armen Der Kiureghian, and Jerome L. Sackman. April 2006.
- PEER 2005/15** *CPT-Based Probabilistic Assessment of Seismic Soil Liquefaction Initiation.* R. E. S. Moss, R. B. Seed, R. E. Kayen, J. P. Stewart, and A. Der Kiureghian. April 2006.
- PEER 2005/14** *Workshop on Modeling of Nonlinear Cyclic Load-Deformation Behavior of Shallow Foundations.* Bruce L. Kutter, Geoffrey Martin, Tara Hutchinson, Chad Harden, Sivapalan Gajan, and Justin Phalen. March 2006.
- PEER 2005/13** *Stochastic Characterization and Decision Bases under Time-Dependent Aftershock Risk in Performance-Based Earthquake Engineering.* Gee Liek Yeo and C. Allin Cornell. July 2005.
- PEER 2005/12** *PEER Testbed Study on a Laboratory Building: Exercising Seismic Performance Assessment.* Mary C. Comerio, editor. November 2005.
- PEER 2005/11** *Van Nuys Hotel Building Testbed Report: Exercising Seismic Performance Assessment.* Helmut Krawinkler, editor. October 2005.
- PEER 2005/10** *First NEES/E-Defense Workshop on Collapse Simulation of Reinforced Concrete Building Structures.* September 2005.
- PEER 2005/09** *Test Applications of Advanced Seismic Assessment Guidelines.* Joe Maffei, Karl Telleen, Danya Mohr, William Holmes, and Yuki Nakayama. August 2006.
- PEER 2005/08** *Damage Accumulation in Lightly Confined Reinforced Concrete Bridge Columns.* R. Tyler Ranf, Jared M. Nelson, Zach Price, Marc O. Eberhard, and John F. Stanton. April 2006.
- PEER 2005/07** *Experimental and Analytical Studies on the Seismic Response of Freestanding and Anchored Laboratory Equipment.* Dimitrios Konstantinidis and Nicos Makris. January 2005.
- PEER 2005/06** *Global Collapse of Frame Structures under Seismic Excitations.* Luis F. Ibarra and Helmut Krawinkler. September 2005.
- PEER 2005/05** *Performance Characterization of Bench- and Shelf-Mounted Equipment.* Samit Ray Chaudhuri and Tara C. Hutchinson. May 2006.
- PEER 2005/04** *Numerical Modeling of the Nonlinear Cyclic Response of Shallow Foundations.* Chad Harden, Tara Hutchinson, Geoffrey R. Martin, and Bruce L. Kutter. August 2005.
- PEER 2005/03** *A Taxonomy of Building Components for Performance-Based Earthquake Engineering.* Keith A. Porter. September 2005.
- PEER 2005/02** *Fragility Basis for California Highway Overpass Bridge Seismic Decision Making.* Kevin R. Mackie and Božidar Stojadinović. June 2005.
- PEER 2005/01** *Empirical Characterization of Site Conditions on Strong Ground Motion.* Jonathan P. Stewart, Yoojoong Choi, and Robert W. Graves. June 2005.
- PEER 2004/09** *Electrical Substation Equipment Interaction: Experimental Rigid Conductor Studies.* Christopher Stearns and André Filiatrault. February 2005.

- PEER 2004/08** *Seismic Qualification and Fragility Testing of Line Break 550-kV Disconnect Switches.* Shakhzod M. Takhirov, Gregory L. Fenves, and Eric Fujisaki. January 2005.
- PEER 2004/07** *Ground Motions for Earthquake Simulator Qualification of Electrical Substation Equipment.* Shakhzod M. Takhirov, Gregory L. Fenves, Eric Fujisaki, and Don Clyde. January 2005.
- PEER 2004/06** *Performance-Based Regulation and Regulatory Regimes.* Peter J. May and Chris Koski. September 2004.
- PEER 2004/05** *Performance-Based Seismic Design Concepts and Implementation: Proceedings of an International Workshop.* Peter Fajfar and Helmut Krawinkler, editors. September 2004.
- PEER 2004/04** *Seismic Performance of an Instrumented Tilt-up Wall Building.* James C. Anderson and Vitelmo V. Bertero. July 2004.
- PEER 2004/03** *Evaluation and Application of Concrete Tilt-up Assessment Methodologies.* Timothy Graf and James O. Malley. October 2004.
- PEER 2004/02** *Analytical Investigations of New Methods for Reducing Residual Displacements of Reinforced Concrete Bridge Columns.* Junichi Sakai and Stephen A. Mahin. August 2004.
- PEER 2004/01** *Seismic Performance of Masonry Buildings and Design Implications.* Kerri Anne Taeko Tokoro, James C. Anderson, and Vitelmo V. Bertero. February 2004.
- PEER 2003/18** *Performance Models for Flexural Damage in Reinforced Concrete Columns.* Michael Berry and Marc Eberhard. August 2003.
- PEER 2003/17** *Predicting Earthquake Damage in Older Reinforced Concrete Beam-Column Joints.* Catherine Pagni and Laura Lowes. October 2004.
- PEER 2003/16** *Seismic Demands for Performance-Based Design of Bridges.* Kevin Mackie and Božidar Stojadinović. August 2003.
- PEER 2003/15** *Seismic Demands for Nondeteriorating Frame Structures and Their Dependence on Ground Motions.* Ricardo Antonio Medina and Helmut Krawinkler. May 2004.
- PEER 2003/14** *Finite Element Reliability and Sensitivity Methods for Performance-Based Earthquake Engineering.* Terje Haukaas and Armen Der Kiureghian. April 2004.
- PEER 2003/13** *Effects of Connection Hysteretic Degradation on the Seismic Behavior of Steel Moment-Resisting Frames.* Janise E. Rodgers and Stephen A. Mahin. March 2004.
- PEER 2003/12** *Implementation Manual for the Seismic Protection of Laboratory Contents: Format and Case Studies.* William T. Holmes and Mary C. Comerio. October 2003.
- PEER 2003/11** *Fifth U.S.-Japan Workshop on Performance-Based Earthquake Engineering Methodology for Reinforced Concrete Building Structures.* February 2004.
- PEER 2003/10** *A Beam-Column Joint Model for Simulating the Earthquake Response of Reinforced Concrete Frames.* Laura N. Lowes, Nilanjan Mitra, and Arash Altoontash. February 2004.
- PEER 2003/09** *Sequencing Repairs after an Earthquake: An Economic Approach.* Marco Casari and Simon J. Wilkie. April 2004.
- PEER 2003/08** *A Technical Framework for Probability-Based Demand and Capacity Factor Design (DCFD) Seismic Formats.* Fatemeh Jalayer and C. Allin Cornell. November 2003.
- PEER 2003/07** *Uncertainty Specification and Propagation for Loss Estimation Using FOSM Methods.* Jack W. Baker and C. Allin Cornell. September 2003.
- PEER 2003/06** *Performance of Circular Reinforced Concrete Bridge Columns under Bidirectional Earthquake Loading.* Mahmoud M. Hachem, Stephen A. Mahin, and Jack P. Moehle. February 2003.
- PEER 2003/05** *Response Assessment for Building-Specific Loss Estimation.* Eduardo Miranda and Shahram Taghavi. September 2003.
- PEER 2003/04** *Experimental Assessment of Columns with Short Lap Splices Subjected to Cyclic Loads.* Murat Melek, John W. Wallace, and Joel Conte. April 2003.
- PEER 2003/03** *Probabilistic Response Assessment for Building-Specific Loss Estimation.* Eduardo Miranda and Hesameddin Aslani. September 2003.
- PEER 2003/02** *Software Framework for Collaborative Development of Nonlinear Dynamic Analysis Program.* Jun Peng and Kincho H. Law. September 2003.
- PEER 2003/01** *Shake Table Tests and Analytical Studies on the Gravity Load Collapse of Reinforced Concrete Frames.* Kenneth John Elwood and Jack P. Moehle. November 2003.

- PEER 2002/24** *Performance of Beam to Column Bridge Joints Subjected to a Large Velocity Pulse.* Natalie Gibson, André Filiatrault, and Scott A. Ashford. April 2002.
- PEER 2002/23** *Effects of Large Velocity Pulses on Reinforced Concrete Bridge Columns.* Greg L. Orozco and Scott A. Ashford. April 2002.
- PEER 2002/22** *Characterization of Large Velocity Pulses for Laboratory Testing.* Kenneth E. Cox and Scott A. Ashford. April 2002.
- PEER 2002/21** *Fourth U.S.-Japan Workshop on Performance-Based Earthquake Engineering Methodology for Reinforced Concrete Building Structures.* December 2002.
- PEER 2002/20** *Barriers to Adoption and Implementation of PBEE Innovations.* Peter J. May. August 2002.
- PEER 2002/19** *Economic-Engineered Integrated Models for Earthquakes: Socioeconomic Impacts.* Peter Gordon, James E. Moore II, and Harry W. Richardson. July 2002.
- PEER 2002/18** *Assessment of Reinforced Concrete Building Exterior Joints with Substandard Details.* Chris P. Pantelides, Jon Hansen, Justin Nadauld, and Lawrence D. Reaveley. May 2002.
- PEER 2002/17** *Structural Characterization and Seismic Response Analysis of a Highway Overcrossing Equipped with Elastomeric Bearings and Fluid Dampers: A Case Study.* Nicos Makris and Jian Zhang. November 2002.
- PEER 2002/16** *Estimation of Uncertainty in Geotechnical Properties for Performance-Based Earthquake Engineering.* Allen L. Jones, Steven L. Kramer, and Pedro Arduino. December 2002.
- PEER 2002/15** *Seismic Behavior of Bridge Columns Subjected to Various Loading Patterns.* Asadollah Esmaeily-Gh. and Yan Xiao. December 2002.
- PEER 2002/14** *Inelastic Seismic Response of Extended Pile Shaft Supported Bridge Structures.* T.C. Hutchinson, R.W. Boulanger, Y.H. Chai, and I.M. Idriss. December 2002.
- PEER 2002/13** *Probabilistic Models and Fragility Estimates for Bridge Components and Systems.* Paolo Gardoni, Armen Der Kiureghian, and Khalid M. Mosalam. June 2002.
- PEER 2002/12** *Effects of Fault Dip and Slip Rake on Near-Source Ground Motions: Why Chi-Chi Was a Relatively Mild M7.6 Earthquake.* Brad T. Aagaard, John F. Hall, and Thomas H. Heaton. December 2002.
- PEER 2002/11** *Analytical and Experimental Study of Fiber-Reinforced Strip Isolators.* James M. Kelly and Shakhzod M. Takhirov. September 2002.
- PEER 2002/10** *Centrifuge Modeling of Settlement and Lateral Spreading with Comparisons to Numerical Analyses.* Sivapalan Gajan and Bruce L. Kutter. January 2003.
- PEER 2002/09** *Documentation and Analysis of Field Case Histories of Seismic Compression during the 1994 Northridge, California, Earthquake.* Jonathan P. Stewart, Patrick M. Smith, Daniel H. Whang, and Jonathan D. Bray. October 2002.
- PEER 2002/08** *Component Testing, Stability Analysis and Characterization of Buckling-Restrained Unbonded Braces™.* Cameron Black, Nicos Makris, and Ian Aiken. September 2002.
- PEER 2002/07** *Seismic Performance of Pile-Wharf Connections.* Charles W. Roeder, Robert Graff, Jennifer Soderstrom, and Jun Han Yoo. December 2001.
- PEER 2002/06** *The Use of Benefit-Cost Analysis for Evaluation of Performance-Based Earthquake Engineering Decisions.* Richard O. Zerbe and Anthony Falit-Baiamonte. September 2001.
- PEER 2002/05** *Guidelines, Specifications, and Seismic Performance Characterization of Nonstructural Building Components and Equipment.* André Filiatrault, Constantin Christopoulos, and Christopher Stearns. September 2001.
- PEER 2002/04** *Consortium of Organizations for Strong-Motion Observation Systems and the Pacific Earthquake Engineering Research Center Lifelines Program: Invited Workshop on Archiving and Web Dissemination of Geotechnical Data, 4–5 October 2001.* September 2002.
- PEER 2002/03** *Investigation of Sensitivity of Building Loss Estimates to Major Uncertain Variables for the Van Nuys Testbed.* Keith A. Porter, James L. Beck, and Rustem V. Shaikhutdinov. August 2002.
- PEER 2002/02** *The Third U.S.-Japan Workshop on Performance-Based Earthquake Engineering Methodology for Reinforced Concrete Building Structures.* July 2002.
- PEER 2002/01** *Nonstructural Loss Estimation: The UC Berkeley Case Study.* Mary C. Comerio and John C. Stallmeyer. December 2001.
- PEER 2001/16** *Statistics of SDF-System Estimate of Roof Displacement for Pushover Analysis of Buildings.* Anil K. Chopra, Rakesh K. Goel, and Chatpan Chintanapakdee. December 2001.

- PEER 2001/15** *Damage to Bridges during the 2001 Nisqually Earthquake.* R. Tyler Ranf, Marc O. Eberhard, and Michael P. Berry. November 2001.
- PEER 2001/14** *Rocking Response of Equipment Anchored to a Base Foundation.* Nicos Makris and Cameron J. Black. September 2001.
- PEER 2001/13** *Modeling Soil Liquefaction Hazards for Performance-Based Earthquake Engineering.* Steven L. Kramer and Ahmed-W. Elgamal. February 2001.
- PEER 2001/12** *Development of Geotechnical Capabilities in OpenSees.* Boris Jeremi . September 2001.
- PEER 2001/11** *Analytical and Experimental Study of Fiber-Reinforced Elastomeric Isolators.* James M. Kelly and Shakhzod M. Takhirov. September 2001.
- PEER 2001/10** *Amplification Factors for Spectral Acceleration in Active Regions.* Jonathan P. Stewart, Andrew H. Liu, Yoojoong Choi, and Mehmet B. Baturay. December 2001.
- PEER 2001/09** *Ground Motion Evaluation Procedures for Performance-Based Design.* Jonathan P. Stewart, Shyh-Jeng Chiou, Jonathan D. Bray, Robert W. Graves, Paul G. Somerville, and Norman A. Abrahamson. September 2001.
- PEER 2001/08** *Experimental and Computational Evaluation of Reinforced Concrete Bridge Beam-Column Connections for Seismic Performance.* Clay J. Naito, Jack P. Moehle, and Khalid M. Mosalam. November 2001.
- PEER 2001/07** *The Rocking Spectrum and the Shortcomings of Design Guidelines.* Nicos Makris and Dimitrios Konstantinidis. August 2001.
- PEER 2001/06** *Development of an Electrical Substation Equipment Performance Database for Evaluation of Equipment Fragilities.* Thalia Agnanos. April 1999.
- PEER 2001/05** *Stiffness Analysis of Fiber-Reinforced Elastomeric Isolators.* Hsiang-Chuan Tsai and James M. Kelly. May 2001.
- PEER 2001/04** *Organizational and Societal Considerations for Performance-Based Earthquake Engineering.* Peter J. May. April 2001.
- PEER 2001/03** *A Modal Pushover Analysis Procedure to Estimate Seismic Demands for Buildings: Theory and Preliminary Evaluation.* Anil K. Chopra and Rakesh K. Goel. January 2001.
- PEER 2001/02** *Seismic Response Analysis of Highway Overcrossings Including Soil-Structure Interaction.* Jian Zhang and Nicos Makris. March 2001.
- PEER 2001/01** *Experimental Study of Large Seismic Steel Beam-to-Column Connections.* Egor P. Popov and Shakhzod M. Takhirov. November 2000.
- PEER 2000/10** *The Second U.S.-Japan Workshop on Performance-Based Earthquake Engineering Methodology for Reinforced Concrete Building Structures.* March 2000.
- PEER 2000/09** *Structural Engineering Reconnaissance of the August 17, 1999 Earthquake: Kocaeli (Izmit), Turkey.* Halil Sezen, Kenneth J. Elwood, Andrew S. Whittaker, Khalid Mosalam, John J. Wallace, and John F. Stanton. December 2000.
- PEER 2000/08** *Behavior of Reinforced Concrete Bridge Columns Having Varying Aspect Ratios and Varying Lengths of Confinement.* Anthony J. Calderone, Dawn E. Lehman, and Jack P. Moehle. January 2001.
- PEER 2000/07** *Cover-Plate and Flange-Plate Reinforced Steel Moment-Resisting Connections.* Taejin Kim, Andrew S. Whittaker, Amir S. Gilani, Vitelmo V. Bertero, and Shakhzod M. Takhirov. September 2000.
- PEER 2000/06** *Seismic Evaluation and Analysis of 230-kV Disconnect Switches.* Amir S. J. Gilani, Andrew S. Whittaker, Gregory L. Fenves, Chun-Hao Chen, Henry Ho, and Eric Fujisaki. July 2000.
- PEER 2000/05** *Performance-Based Evaluation of Exterior Reinforced Concrete Building Joints for Seismic Excitation.* Chandra Clyde, Chris P. Pantelides, and Lawrence D. Reaveley. July 2000.
- PEER 2000/04** *An Evaluation of Seismic Energy Demand: An Attenuation Approach.* Chung-Che Chou and Chia-Ming Uang. July 1999.
- PEER 2000/03** *Framing Earthquake Retrofitting Decisions: The Case of Hillside Homes in Los Angeles.* Detlof von Winterfeldt, Nels Roselund, and Alicia Kitsuse. March 2000.
- PEER 2000/02** *U.S.-Japan Workshop on the Effects of Near-Field Earthquake Shaking.* Andrew Whittaker, ed. July 2000.
- PEER 2000/01** *Further Studies on Seismic Interaction in Interconnected Electrical Substation Equipment.* Armen Der Kiureghian, Kee-Jeung Hong, and Jerome L. Sackman. November 1999.
- PEER 1999/14** *Seismic Evaluation and Retrofit of 230-kV Porcelain Transformer Bushings.* Amir S. Gilani, Andrew S. Whittaker, Gregory L. Fenves, and Eric Fujisaki. December 1999.

- PEER 1999/13** *Building Vulnerability Studies: Modeling and Evaluation of Tilt-up and Steel Reinforced Concrete Buildings.* John W. Wallace, Jonathan P. Stewart, and Andrew S. Whittaker, editors. December 1999.
- PEER 1999/12** *Rehabilitation of Nonductile RC Frame Building Using Encasement Plates and Energy-Dissipating Devices.* Mehrdad Sasani, Vitelmo V. Bertero, James C. Anderson. December 1999.
- PEER 1999/11** *Performance Evaluation Database for Concrete Bridge Components and Systems under Simulated Seismic Loads.* Yael D. Hose and Frieder Seible. November 1999.
- PEER 1999/10** *U.S.-Japan Workshop on Performance-Based Earthquake Engineering Methodology for Reinforced Concrete Building Structures.* December 1999.
- PEER 1999/09** *Performance Improvement of Long Period Building Structures Subjected to Severe Pulse-Type Ground Motions.* James C. Anderson, Vitelmo V. Bertero, and Raul Bertero. October 1999.
- PEER 1999/08** *Envelopes for Seismic Response Vectors.* Charles Menun and Armen Der Kiureghian. July 1999.
- PEER 1999/07** *Documentation of Strengths and Weaknesses of Current Computer Analysis Methods for Seismic Performance of Reinforced Concrete Members.* William F. Cofer. November 1999.
- PEER 1999/06** *Rocking Response and Overturning of Anchored Equipment under Seismic Excitations.* Nicos Makris and Jian Zhang. November 1999.
- PEER 1999/05** *Seismic Evaluation of 550 kV Porcelain Transformer Bushings.* Amir S. Gilani, Andrew S. Whittaker, Gregory L. Fenves, and Eric Fujisaki. October 1999.
- PEER 1999/04** *Adoption and Enforcement of Earthquake Risk-Reduction Measures.* Peter J. May, Raymond J. Burby, T. Jens Feeley, and Robert Wood.
- PEER 1999/03** *Task 3 Characterization of Site Response General Site Categories.* Adrian Rodriguez-Marek, Jonathan D. Bray, and Norman Abrahamson. February 1999.
- PEER 1999/02** *Capacity-Demand-Diagram Methods for Estimating Seismic Deformation of Inelastic Structures: SDF Systems.* Anil K. Chopra and Rakesh Goel. April 1999.
- PEER 1999/01** *Interaction in Interconnected Electrical Substation Equipment Subjected to Earthquake Ground Motions.* Armen Der Kiureghian, Jerome L. Sackman, and Kee-Jeung Hong. February 1999.
- PEER 1998/08** *Behavior and Failure Analysis of a Multiple-Frame Highway Bridge in the 1994 Northridge Earthquake.* Gregory L. Fenves and Michael Ellery. December 1998.
- PEER 1998/07** *Empirical Evaluation of Inertial Soil-Structure Interaction Effects.* Jonathan P. Stewart, Raymond B. Seed, and Gregory L. Fenves. November 1998.
- PEER 1998/06** *Effect of Damping Mechanisms on the Response of Seismic Isolated Structures.* Nicos Makris and Shih-Po Chang. November 1998.
- PEER 1998/05** *Rocking Response and Overturning of Equipment under Horizontal Pulse-Type Motions.* Nicos Makris and Yiannis Roussos. October 1998.
- PEER 1998/04** *Pacific Earthquake Engineering Research Invitational Workshop Proceedings, May 14–15, 1998: Defining the Links between Planning, Policy Analysis, Economics and Earthquake Engineering.* Mary Comerio and Peter Gordon. September 1998.
- PEER 1998/03** *Repair/Upgrade Procedures for Welded Beam to Column Connections.* James C. Anderson and Xiaojing Duan. May 1998.
- PEER 1998/02** *Seismic Evaluation of 196 kV Porcelain Transformer Bushings.* Amir S. Gilani, Juan W. Chavez, Gregory L. Fenves, and Andrew S. Whittaker. May 1998.
- PEER 1998/01** *Seismic Performance of Well-Confined Concrete Bridge Columns.* Dawn E. Lehman and Jack P. Moehle. December 2000.

ONLINE REPORTS

The following PEER reports are available by Internet only at http://peer.berkeley.edu/publications/peer_reports.html

- PEER 2008/101** *Seismic Performance Objectives for Tall Buildings*. William T. Holmes, Charles Kircher, William Petak, and Nabih Youssef. August 2008.
- PEER 2007/101** *Generalized Hybrid Simulation Framework for Structural Systems Subjected to Seismic Loading*. Tarek Elkhoraibi and Khalid M. Mosalam. July 2007.
- PEER 2007/100** *Seismic Evaluation of Reinforced Concrete Buildings Including Effects of Masonry Infill Walls*. Alidad Hashemi and Khalid M. Mosalam. July 2007.